

# Search for Exotic Resonances in the Reaction $\bar{p}p \rightarrow \phi\phi$ in the Experiment PS202 at LEAR

Helen Korsmo



Thesis submitted in partial fulfillment of requirements to obtain the degree Doctor  
Scientiarum at the University of Oslo, Institute of physics.

November 1996

## Acknowledgements

A great number of people have helped me during my my affiliation with the JETSET experiment and the work with this thesis. I would like to express my gratitude to all of them.

Bjarne Stugu introduced me to the JETSET experiment when I started the work for my Cand. Scient. (masters) thesis in 1987. As my supervisor he gave me a very helpful introduction to the experiment, as well as to experimental particle physics in general. In 1990 Max Ferro-Luzzi, the leader of the CERN JETSET group, gave me the opportunity to stay for half a year at CERN as an associate, after obtaining my Cand. Scient. degree. This way I learned more about the JETSET experiment, both on the hardware and software side. During this period I benefited in particular from the cooperation and useful discussions with Staffan Ohlsson and Tom Fearnley.

After the half year at CERN I obtained a grant from the University of Oslo, to work for a Dr. Scient. degree here. My supervisor was professor Torleiv Buran.

I worked at the Physics Institute at the University in Oslo from 1991 to 1996 as a research associate. During this time I also made a number of trips to CERN and to Genoa. The Physics Institute in Oslo was very cooperative, and at several occasions they gave me extended exemption from my teaching duties, which allowed me to stay for long periods at CERN. I received financial support for travelling from the Norwegian Research Council.

During the years 1991 to 1994 I had a very fruitful cooperation with the Genoa group, working on various aspects of the data analysis. I was invited by Mario Macri to Genoa to work with his group at several occasions and received support from the Italian Istituto Nazionale di Fisica Nucleare (INFN) for staying there. In Genoa I worked with Maria Grazia Pia who played an instrumental role in developing the Genova-Oslo-Bari analysis chain, and I learned a lot from her systematic approach to data analysis. I have used several of her ideas in writing chapter 4 of this thesis. I also enjoyed working with Sajan Easo who was a member of the Genoa group for some time while I was there.

This thesis was written during the years 1995 and 1996, and I would like to thank three people who were particularly helpful during this period.

I am especially grateful to Rick Jones in the CERN group, who helped me with several practical points concerning data analysis and also read through the thesis and gave many comments and suggestions for improvements.

Special thanks to my friend James Gillies, who was not connected to the JETSET experiment or the University of Oslo but still found the time to read through drafts of the thesis and gave a number of useful comments.

My supervisor Torleiv Buran has given me invaluable help and support, in particular in the final year of preparing the thesis. I would like to thank him for this.

The work presented in this thesis is a result of the work of the whole JETSET collaboration. An account of some of the contributions to the data analysis are given in the introduction. There are also a number of others who built the detectors and kept the experiment running, who I have not mentioned by name. I would like to thank all the members of the JETSET collaboration, without whom this thesis would not have been possible.

Helen Korsmo  
Oslo, 20. November 1996



# Contents

<b>1</b>	<b>Introduction</b>	<b>1</b>
<b>2</b>	<b>Physics motivation of the JETSET experiment</b>	<b>4</b>
2.1	Theory of the colour force . . . . .	5
2.1.1	Quarks and colour . . . . .	5
2.1.2	The Lagrangian for QCD . . . . .	7
2.1.3	Asymptotic freedom and confinement . . . . .	9
2.1.4	Experimental evidence for QCD . . . . .	11
2.1.5	Summary of QCD . . . . .	11
2.2	The QCD spectrum . . . . .	12
2.2.1	Conventional states: mesons and baryons . . . . .	12
2.2.2	Spectroscopy of $q\bar{q}$ mesons . . . . .	14
2.2.3	Meson decays . . . . .	18
2.2.4	Exotic states: glueballs, hybrids, and molecules . . . . .	19
2.2.5	Predictions for gluonium spectroscopy . . . . .	21
2.2.6	Decay of glueballs . . . . .	25
2.2.7	Hybrid spectroscopy . . . . .	27
2.2.8	Hybrid decays . . . . .	27
2.2.9	Production of glueballs and hybrids . . . . .	28
2.2.10	Four-quark states . . . . .	33
2.2.11	Signatures for exotic states: how to spot a glueball . . . . .	33
2.2.12	Experimental status of gluonium searches . . . . .	35

2.3	The OZI rule as a glueball filter . . . . .	36
2.4	The reaction $p\bar{p} \rightarrow \phi\phi$ . . . . .	41
2.4.1	Is $p\bar{p} \rightarrow \phi\phi$ OZI-suppressed? . . . . .	42
2.4.2	Previous measurements of $p\bar{p} \rightarrow \phi\phi$ . . . . .	47
2.4.3	Results from $\phi\phi$ production experiments . . . . .	48
2.4.4	$J/\psi$ decay . . . . .	51
2.4.5	The $\xi$ resonance . . . . .	51
2.5	The JETSET physics Program . . . . .	54
2.5.1	$4K$ final states . . . . .	54
2.5.2	Measurement of $\bar{p}p \rightarrow \phi\phi \rightarrow 4K$ . . . . .	56
<b>3</b>	<b>Experimental method</b>	<b>65</b>
3.1	The antiproton beam and the gas jet target . . . . .	66
3.2	The detector . . . . .	73
3.3	Triggering . . . . .	97
3.4	The data acquisition system . . . . .	104
<b>4</b>	<b>Selection of the reaction <math>\bar{p}p \rightarrow 4K^\pm</math></b>	<b>105</b>
4.1	Data collected . . . . .	105
4.2	Data analysis . . . . .	108
4.2.1	Reduction . . . . .	108
4.2.2	Geometrical reconstruction of the events . . . . .	109
4.2.3	First step event selection . . . . .	118
4.2.4	Kinematical reconstruction of events . . . . .	119
4.3	Extraction of the $4K$ events . . . . .	125
4.3.1	General guidelines for $4K$ event selection . . . . .	125
4.3.2	Kinematical cuts . . . . .	125
4.3.3	Particle identification cuts . . . . .	132
4.3.4	The complete analysis chain. Final decision . . . . .	139
4.3.5	Background subtraction . . . . .	149
4.3.6	Statistics . . . . .	150
4.4	Acceptance . . . . .	150

<b>5</b>	<b>Extraction of <math>\phi\phi</math> events</b>	<b>160</b>
<b>6</b>	<b>Luminosity</b>	<b>169</b>
<b>7</b>	<b>Cross sections</b>	<b>173</b>
<b>8</b>	<b>Analysis of angular distributions</b>	<b>205</b>
<b>9</b>	<b>Conclusions</b>	<b>210</b>



# List of Tables

2.1	<i>Quantum numbers <math>J^{PC}</math> for mesons (quark-antiquark states).</i> . . . . .	13
2.2	<i>Quark assignments of established meson nonets.</i> . . . . .	14
2.3	<i>Scalar mesons with <math>J^{PC} = 0^{++}</math> below 2 GeV, with possible classifications and mass predictions from Godfrey and Isgur.</i> . . . . .	16
2.4	<i>Tensor mesons with <math>J^{PC} = 2^{++}</math> below 2 GeV, with possible classifications and mass predictions from Godfrey and Isgur.</i> . . . . .	18
2.5	<i><math>J^{PC}</math> values of two-gluon glueballs with different values of orbital angular momentum from the glue lego model.</i> . . . . .	21
2.6	<i>Glueball masses from a bag model.</i> . . . . .	23
2.7	<i>Possible quantum numbers for glueballs and hybrids in the bag model. Only hybrid states with the quarks in S-wave are shown.</i> . . . . .	23
2.8	<i>Measurement of OZI violation at LEAR</i> . . . . .	45
2.9	<i>States available to a proton-antiproton pair</i> . . . . .	59
2.10	<i>States available to a <math>\phi\phi</math> pair</i> . . . . .	60
2.11	<i>The first available transitions for <math>p\bar{p} \rightarrow \phi\phi</math>.</i> . . . . .	60
2.12	<i>The decay helicity amplitudes which are permitted to be nonzero for the various possible values of parity <math>P</math>, and signature <math>(-1)^J</math></i> . . . . .	64
2.13	<i>Allowed states for various values of the parameter <math>\beta</math>.</i> . . . . .	64
3.1	<i>Geometrical parameters for the beam pipe and beam pipe scintillators. The half-axes of the ellipse, thickness for each element, and the acceptance in polar angle for the scintillators are listed.</i> . . . . .	74
3.2	<i>Geometrical parameters for the forward detector</i> . . . . .	74
3.3	<i>Geometrical parameters for the barrel detector.</i> . . . . .	74
3.4	<i>Thickness and number of radiation lengths encountered by a particle passing through various elements of the JETSET detector.</i> . . . . .	75



3.5	<i>Azimuthal angles for the silicon strip detectors.</i>	96
3.6	<i>Cherenkov trigger conditions during the 1991 JETSET runs</i>	103
4.1	<i>1991 runs. Beam momenta, total centre-of-mass energy, number of 4K triggers, and number of events after reduction.</i>	106
4.2	<i>1992 runs. Beam momenta, total centre-of-mass energy, number of 4K triggers, and number of events after reduction.</i>	107
4.3	<i>1993 runs. Beam momenta, total centre-of-mass energy, number of 4K triggers, and number of events after reduction.</i>	107
4.4	<i>1994 runs. Beam momenta, total centre-of-mass energy, number of 4K triggers, and number of events after reduction.</i>	108
4.5	<i>Fraction of Monte Carlo and real events, with fit probability higher than 5%, before and after 4K selection cuts. beam momentum 1.5 GeV/c (1.6 GeV/c for <math>p\bar{p}\pi^+\pi^-</math>).</i>	122
4.6	<i>Number of real data events and Monte Carlo events passing trigger and 4K analysis cuts, at beam momentum 1.5 GeV/c.</i>	151
4.7	<i>Number of real data events and Monte Carlo events with <math>\phi\phi</math> fit probability higher than 5 % passing trigger and 4K analysis cuts, at beam momentum 1.5 GeV/c.</i>	152
4.8	<i>Number of real data events and Monte Carlo events passing trigger and 4K analysis cuts, at beam momentum 1.2 GeV/c.</i>	153
4.9	<i>Number of real data events and Monte Carlo events passing trigger and 4K analysis cuts, at beam momentum 1.9 GeV/c.</i>	154
4.10	<i>Number of real data events and Monte Carlo events passing trigger and <math>p\bar{p}\pi^+\pi^-</math> analysis cuts, at beam momentum 1.9 GeV/c.</i>	155
5.1	<i>Results from different methods of estimating the number of <math>\phi\phi</math> events in the event sample selected by the 4K analysis, for real data and Monte Carlo at a beam momentum 1.5 GeV/c.</i>	165
5.2	<i>Results from the channel likelihood fit for Monte Carlo data at beam momentum 1.4 GeV/c.</i>	167
6.1	<i>Momentum dependent factors for the luminosity determination by the beam attenuation method.</i>	171

# Chapter 1

## Introduction

The JETSET experiment was proposed in 1984 [?]. It was accepted by CERN in 1987 as PS202 (JETSET). The main purpose of the experiment was to search for exotic states of hadronic matter, such as glueballs and hybrids, by looking for structure in the reaction  $p\bar{p} \rightarrow \phi\phi$  in the energy range  $\sqrt{s} \approx 2.04\text{-}2.4\text{ GeV}$  (the lower limit corresponds to the  $\phi\phi$  threshold and the higher limit to the highest antiproton momentum from LEAR at 2.0 GeV/c). Since  $\phi$ -mesons are almost pure  $s\bar{s}$  (section 2.2.1), it was expected that  $p\bar{p} \rightarrow \phi\phi$  should be suppressed according to the OZI rule, an empirical rule which says that reactions with different valence quark flavours in the initial and final states will be strongly suppressed (section 2.3). According to QCD, the initial and final states are connected through an intermediate state of hard gluons in such reactions. Then the OZI rule can be understood as a consequence of asymptotic freedom. However, the suppression might be overcome if the reaction proceeds through a gluonic resonant intermediate state, a glueball (section 2.2.4).

An important part of the JETSET proposal was the use of an internal hydrogen cluster jet target, a technique which had first been used in the R704 experiment at CERN's Intersecting Storage Ring (ISR) [?, ?]. This technique gives a high integrated luminosity and an excellent momentum resolution. In the JETSET experiment the target intersected the antiproton beam in the Low Energy Antiproton Ring, LEAR, at right angles. The interaction area was surrounded by a detector especially designed to detect the kaons from the reaction  $p\bar{p} \rightarrow \phi\phi \rightarrow 4K^\pm$  and to remove background events. Also the reactions  $p\bar{p} \rightarrow \phi KK \rightarrow 4K^\pm$  and the non-resonant  $p\bar{p} \rightarrow 4K^\pm$  were detected.

The JETSET experiment was in operation from 1991 to 1994, and data were collected at a number of different beam momenta, or center of mass energies. So far the only results published are for cross sections at one beam momentum, 1.4 GeV/c, with data collected in July 1991 [?]. Preliminary results for the whole range of momenta have been shown at a number of conferences [?, ?, ?].

The cross sections and results from angular distribution presented in this thesis are the results of the most recent analysis done at the time of writing. However, work is still being done by members of the collaboration to improve the analysis. Particle identification procedures are being changed; there might also be other corrections done before the results are submitted for publication. We do not expect any major changes in the final results.

The most important result from JETSET is the  $p\bar{p} \rightarrow \phi\phi$  cross section, which is measured to be two orders of magnitude higher than expected from the OZI rule (see section 2.4.1 and the results in chapter 7, particularly figure 7.5). A broad resonant shape is observed. This could indicate glueball contributions, but there are alternative explanations of this reaction, which evade the OZI rule and could explain the results. These are discussed in section 2.4.1.

### Thesis outline

In this thesis I have endeavored to present as completely as possible the procedure that was followed to obtain the  $p\bar{p} \rightarrow \phi\phi$ , as well as the  $p\bar{p} \rightarrow \phi K K$  and  $p\bar{p} \rightarrow 4K^\pm$ , cross sections. The methods used to find the three factors necessary to calculate these cross sections (equation 7.1), the number of events for each reaction, the luminosity, and the acceptance, are described.

The results presented represent the work of the whole JETSET collaboration.<sup>1</sup> Some of the people who made contributions particularly important for this thesis are mentioned below.

In Chapter 2, I present the physics motivation for the JETSET experiment. This includes a discussion of the QCD spectrum, both of conventional states and of exotic states such as glueballs, hybrids, and four-quark molecules. Some indication of how to look for these exotic states are given, and existing candidates for these states discussed. The OZI rule is discussed in some detail, since the motivation for using the reaction  $p\bar{p} \rightarrow \phi\phi$  to search for glueballs was mainly its OZI-suppression. The possibility of other explanations than glueballs to the apparent OZI-violation observed in this channel is explored. At the end of the chapter, some comments about resonances and about information that can be obtained from angular distributions in this reaction are given.

The apparatus and trigger are described in chapter 3. The detector parts used in the experiment were built by institutes from Uppsala, Jülich, Freiburg, CERN, Genoa, and Illinois; the University of Genoa was responsible for the jet target system. The University of Oslo contributed parts of the hardware for the silicon detectors.

Chapter 4 describes the analysis to select  $4K$  events from the trigger sample. This includes first and second step event selection, track finding and fitting, kinematical reconstruction, and kinematical and particle identification cuts. Also described in this chapter are the background calculation procedures, and the acceptance calculations.

Two different analysis chain were developed in parallel for the purpose of finding the  $p\bar{p} \rightarrow 4K$  events, the Genoa-Oslo-Bari (GeOBa) analysis chain and the CERN analysis chain; they were later merged into a unified chain. I participated mainly in the development of the GeOBa chain. This work included straw tracker calibration, track and vertex fitting, and event display [?, ?, ?]. I also did acceptance and efficiency calculations for the cross section, using a GEANT Monte Carlo program that simulated the detector and the interactions occurring inside it. It was important to ascertain that the Monte Carlo program correctly simulated the data, for example the GHEISHA/FLUKA simulation programs for hadronic interaction were compared to see which one better reproduced the behaviour seen in our data [?]. I also used the Monte Carlo programs to determine detector and reconstructions resolutions and to test the effects of particle identification (PID) cuts [?], and of new detectors, for example the silicon barrel detectors [?].

---

<sup>1</sup>For a complete list of JETSET members, see [?]

A large number of my collaborators did important work on subjects discussed in chapter 4: Work on tracking was done by S. Ohlsson [?], S. Easo [?], and D. Drijard [?]. The PID procedures were mainly developed by groups from Cern and from Genoa [?, ?, ?]. In particular M. G. Pia and M. Ferro-Luzzi did important work on these routines. The  $\phi\phi$  fit was written by L. Bertolotto [?]. The Monte Carlo program used for acceptance calculations, and to set PID cuts, was mainly developed by M. G. Pia, B. Stugu, and P. Harris. [?, ?, ?, ?]. After a long period where the different analysis chains, using somewhat different tracking and PID routines, had been used and compared in the experiment, a unified chain was put together by R. Jones, S. Passaggio, and M. Lo Vetere [?]. This unified chain, with elements from both the GeOBa and the CERN analysis chains, is what is described here, and the output from this chain has been used to obtain the results.

I have tested the kinematical cuts and particle identification routines used to select the  $4K$  events in the unified analysis chain, and I show that they select primarily events of the type  $p\bar{p} \rightarrow 4K^\pm$ .

In chapter 5, I discuss how to extract the number of  $p\bar{p} \rightarrow \phi\phi$  events from the  $4K$  sample. Various methods for getting this number are compared; the conclusion is that the best estimate is obtained from using the channel likelihood method, a method that was implemented and tested for JETSET by A. Palano [?]. The relative admixtures of  $\phi\phi$ ,  $\phi KK$ , and nonresonant events were calculated with this method.

The determination of the luminosity, another necessary ingredient to calculate the cross section, is described in chapter 6. The luminosity was calculated by different methods, the Erlangen and Jülich groups made use of elastic events, and the group from Illinois calculated it from beam decay [?, ?, ?]. I contributed to one of the methods by simulating the silicon strip luminosity detectors and calculating the acceptance for the Erlangen luminosity monitor [?]. Since there was some discrepancy by the various methods in the run-to-run, and period-to-period relative luminosities, a relative luminosity determination was provided by R. Jones [?].

Chapter 7 gives a summary of the data analysis, with the number of events, calculated background, acceptance, and luminosities for all the beam momenta for the run periods in 1991 to 1993. The resulting cross sections for  $p\bar{p} \rightarrow \phi\phi$ , as well as  $p\bar{p} \rightarrow \phi KK$  and  $p\bar{p} \rightarrow 4K^\pm$ , are then calculated. The unified analysis chain, which ran on real data as well as Monte Carlo simulated data, was used to do the  $4K$  event selection to obtain these results.

The analysis of angular distributions is discussed in chapter 8. I have done a simple study of the angular distributions, to determine the parity  $P$  and signature  $(-1)^J$  of intermediate states in  $p\bar{p} \rightarrow \phi\phi$ . The conclusions are in agreement with the more complete partial wave analysis, done by A. Palano, in cooperation with R. Jones [?] .

Chapter 9 is the concluding chapter, where I interpret the results, and compare them with results from other experiments.

## Chapter 2

# Physics motivation of the JETSET experiment

According to the standard model of elementary particles, all matter is made of quarks and leptons. In addition there are gauge bosons which mediate the forces between these particles. The simplest gauge theory of forces is quantum electrodynamics (QED), which describes the interactions between charged particles. The gauge boson for this theory is the photon. Quantum chromodynamics (QCD) is the theory describing the strong force between quarks. It is called the colour force because we believe that quarks, in addition to electric charge, have another charge or degree of freedom, called colour, which is the source for these interactions. The gauge bosons for QCD are the eight gluons. Unlike QED, QCD is a **non-Abelian** theory, which means that the generators do not commute. This gives rise to interactions between coloured gluons; bound states of gluons (glueballs) and of quarks and gluons (hybrids) are possible. These types of matter are collectively known as exotics.

A positive identification of a glueball or a hybrid would confirm one of the most important distinctions between quantum chromodynamics and its parent theory, quantum electrodynamics, namely the nature of the relation between the charge associated with the interaction and the particle which mediates the interaction.

Of particular interest when looking for unconventional states of matter, such as glueballs, are those channels which do not have the same valence quark flavours in the initial and final states, for example  $p\bar{p} \rightarrow \phi\phi$ . According to the empirical OZI rule (section 2.3) these reactions should be suppressed, but the suppression might be overcome if the reaction goes through a gluonic resonant intermediate state.

In this chapter the experimental evidence for the quark model, and for colour and QCD, is described. This includes the properties of glueballs, such as their masses and decay modes, and possible production and discovery in experiments. The current experimental status of glueball searches is reviewed.

An account of the origin and meaning of the OZI rule, and how it applies to the reaction  $p\bar{p} \rightarrow \phi\phi$ , is given.

In the JETSET experiment the  $\phi$  is detected in the decay mode  $\phi \rightarrow K^+K^-$ ; the last part of the chapter describes the observables in the reaction  $p\bar{p} \rightarrow \phi\phi \rightarrow 4K^\pm$ , and how resonances can be identified, and their quantum numbers determined, in this reaction.

## 2.1 Theory of the colour force

### 2.1.1 Quarks and colour

In the early 1960s it was shown by Murray Gell-Mann and Yuwal Ne'eman that all the strongly interacting particles, or hadrons, that had been discovered so far could be classified in multiplets which were representations of the group  $SU(3)$  [?]. The multiplets could be interpreted as products of the fundamental 3 dimensional representation of  $SU(3)$ . Each multiplet contained particles with the same spin and parity but different values of isospin and strangeness (figure 2.1 shows baryon and meson multiplets). This classification led to the prediction of a new particle, named the  $\Omega^-$ , with spin  $3/2$  and strangeness  $-3$ , which was necessary to complete the spin  $3/2$  baryon decuplet. The discovery in 1963 of a particle with the predicted properties confirmed that  $SU(3)$  is the correct symmetry group for hadrons [?]. The quark model was put forward in 1964 by Murray Gell-Mann and George Zweig [?, ?]. They pointed out that the  $SU(3)$  structure could be explained by assuming that all the hadrons were built up of a triplet of quarks, which corresponds to the fundamental 3-dimensional representation of  $SU(3)$ , and a triplet of antiquarks, which corresponds to the conjugate representation. They proposed that all observed particles were either a combination of three quarks, making a baryon, or a quark and an antiquark, making a meson. Using group theory [?] one finds that this gives the observed multiplets of 1, 8, or 10 baryons, and 1 or 8 mesons (section 2.2.1).

The three quarks in the triplet have **flavours** up ( $u$ ), down ( $d$ ), and strange ( $s$ ). The up and down quarks make an isospin doublet with strangeness 0, and the strange quark is an isospin singlet with strangeness  $-1$  (see figure 2.2). The flavour  $SU(3)$  symmetry, which involves invariance of the Hamiltonian under rotations in flavour space, is only exact if differences in quark masses are ignored. Since the quark theory was first proposed in 1964, it has been found that three more quark flavours are needed to describe the observed particle spectrum, these are the charm ( $c$ ), bottom ( $b$ ), and top ( $t$ ) quarks.

A problem with the quark theory was the apparent violation of the Pauli exclusion principle. This principle states that a system of particles with half-integer spin must have an antisymmetric wavefunction. Several members of the baryon decuplet consist of three identical quarks in a symmetric configuration. The  $\Delta^{++}$  and  $\Delta^-$  have three up and three down quarks respectively, and the  $\Omega^-$  contains three strange quarks. The members of the decuplet have total spin  $3/2$ , which means that the three quarks have parallel spins and no orbital angular momentum, giving a symmetric total wavefunction.

In 1964 Greenberg [?] suggested that the quarks had another degree of freedom which he called **colour**. He postulated that there are three different colours (red, green and blue), which make up another  $SU(3)$  triplet (independent of  $SU(3)_{flavour}$ ) and that all observed particles are colour singlets, that is, invariant under  $SU(3)$  colour transformations. Combining three quarks in a  $SU(3)$  colour singlet gives an antisymmetric colour wave function, and reconciles the quark model with the Pauli principle.

The requirement that all the hadrons should be colour singlets also explained why the observed particles were either  $q\bar{q}$  or  $qqq$  combinations, since a singlet can be obtained by combining a colour triplet with an anticolour triplet, corresponding to a quark and an antiquark, or combining three colour triplets, corresponding to three quarks.

Greenberg's hypothesis also explained why a free quark, which should be relatively easy to

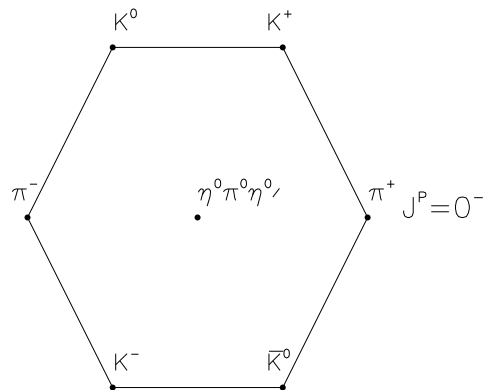
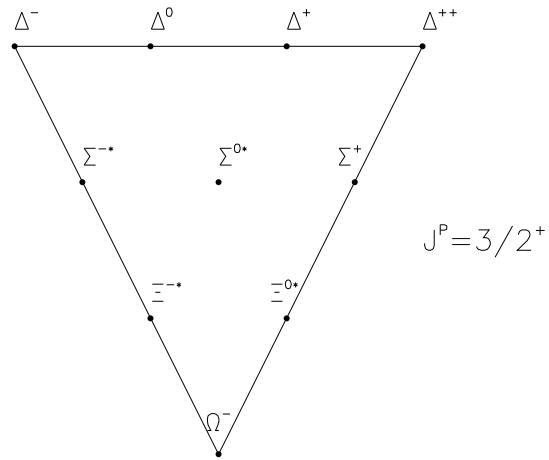
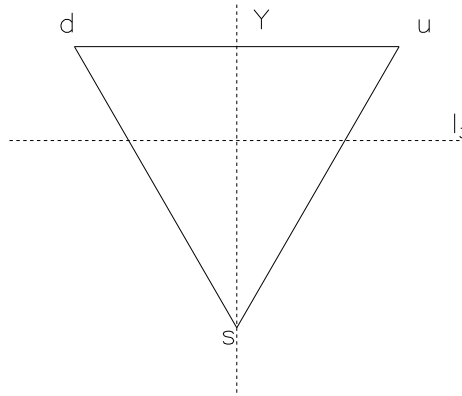


Figure 2.1:  $SU(3)$  multiplets of baryons (top) and mesons (bottom).

Figure 2.2: *The fundamental  $SU(3)$  triplet.*

identify due to its fractional charge, had not been observed. A single quark is coloured and therefore its wavefunction is not invariant under rotations in colour space.

Another piece of evidence for quark colour comes from studying the ratio

$$R = \frac{\sigma(e^+e^- \rightarrow \text{hadrons})}{\sigma(e^+e^- \rightarrow \mu^+\mu^-)} = \sum_{i=1}^{q\bar{q}\text{-pairs}} e_i^2 \quad (2.1)$$

in electron positron annihilations. The hadrons are assumed to be the result of an initial quark -antiquark pair being produced, and the sum is over the charges  $e_i$  of all the quark pairs accessible at that energy. To get a result in agreement with experiment [?], each quark flavour must be included 3 times, implying that any flavour comes in three different colours. The decay of the  $\pi^0$  to two photons also predicts three quark colours. The decay rate is proportional to the square of the number of quarks which can act as intermediate states in the decay, and therefore also proportional to the square of the number of quark colours,  $N_C$ . Comparison with experiment [?] gives  $N_C = 3$ .

### 2.1.2 The Lagrangian for QCD

The basic idea of QCD is that the colour charges are the sources of the strong, or chromodynamic, force between quarks. This force keeps quarks bound together in hadrons. When the theory was proposed in 1973 [?], it was known that the type of quantum field theories known as gauge theories could describe both the electromagnetic and weak interactions (QED and the Glashow-Weinberg-Salam theory), and it seemed natural to attempt to make a gauge theory for the strong interaction. Since quarks are fermions, the free Lagrangian for quarks is the Dirac Lagrangian

$$\mathcal{L}_0 = \bar{\Psi}(i\gamma^\mu\partial_\mu - m)\Psi, \quad (2.2)$$

where  $\Psi$  is a three component column vector in colour space. Here we consider only one flavour, for example the up quark, then  $\Psi$  is (by convention)

$$\Psi = \begin{pmatrix} u_{\text{red}} \\ u_{\text{blue}} \\ u_{\text{green}} \end{pmatrix}.$$



In QED, requiring local U(1) gauge invariance gives rise to electromagnetic interaction between charged particles. In QCD, invariance under local  $SU(3)_{colour}$  transformations of the form

$$\Psi(x) \rightarrow e^{i\alpha_a(x)T_a}\Psi(x), \quad (2.3)$$

where a summation over  $a$  is implied, and  $\alpha_a(x)$  is some function of  $x$ , is assumed. The generators  $T_a$  are a set of independent, traceless  $3 \times 3$  matrices, it is customary to choose  $T_a(a = 1, 8) = \lambda_a/2$ , the  $\lambda$ s are the eight  $3 \times 3$  Gell-Mann matrices. They satisfy the commutation relation

$$[T_a, T_b] = if_{abc}T_c. \quad (2.4)$$

The constants  $f_{abc}$  are the structure constants of the group. Since the generators  $T_a$  do not commute, the theory is non-Abelian. The Lagrangian in equation 2.2 is not invariant under the transformations 2.3. In order to get a gauge invariant Lagrangian we must do the replacement

$$\partial_\mu \rightarrow D_\mu = \partial_\mu - ig_s G_\mu^a T_a. \quad (2.5)$$

$D_\mu$  is called the covariant derivative. We have introduced the eight vector boson fields, or gluons,  $G_\mu^a$  which transform as

$$G_\mu^a \rightarrow G_\mu^a + \frac{1}{g_s} \partial_\mu \alpha_a + f_{abc} \alpha_b G_\mu^c. \quad (2.6)$$

$g_s$  is the strong coupling constant. The following Lagrangian is gauge invariant under the transformations 2.3 and 2.6.

$$\mathcal{L} = i\bar{\Psi}\gamma_\mu D^\mu\Psi + \bar{\Psi}m\Psi - \frac{1}{2}G_{\mu\nu}^a G_a^{\mu\nu}. \quad (2.7)$$

The last term is the gluon field self energy and  $G_{\mu\nu}^a$  is the field strength tensor

$$G_{\mu\nu}^a = \partial_\mu G_\nu^a - \partial_\nu G_\mu^a + g_s f_{abc} G_\nu^b G_\mu^c. \quad (2.8)$$

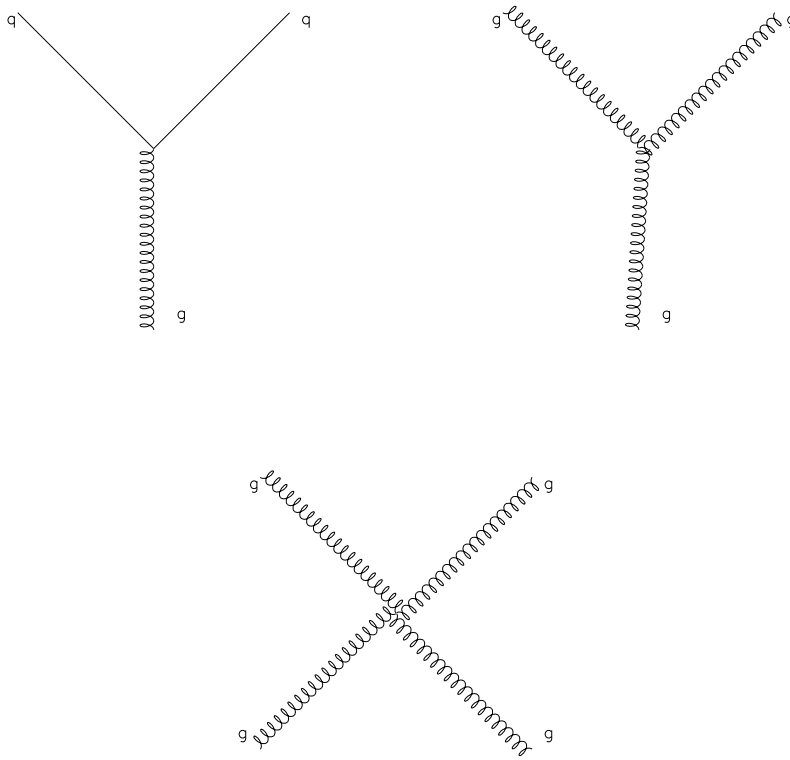
A mass term for the gluons,  $\frac{1}{2}G_\mu^a G_a^\mu$ , would not be consistent with gauge invariance, and therefore gluons should be massless.

The Lagrangian in equation 2.7 contains terms corresponding to couplings between quarks and gluons, and also self couplings of gluons. This gives three different QCD vertices, which are shown in figure 2.3. The self coupling of gluons arises from the non-Abelian nature of QCD and is the feature of this theory which makes it different from QED, where there is no coupling between the corresponding gauge bosons, the photons.

In order for the Lagrangian to be invariant under rotations in colour space the gluons must be an 8-dimensional representation of  $SU(3)_{colour}$ ; a product of the fundamental triplet  $\mathbf{3}$  and the conjugate triplet  $\bar{\mathbf{3}}$ , since  $\mathbf{3} \otimes \bar{\mathbf{3}} = \mathbf{8} \oplus \mathbf{1}$ . The singlet does not correspond to a gluon. The 8 gluons have colour charges  $r\bar{b}, b\bar{r}, r\bar{g}, g\bar{r}, b\bar{g}, g\bar{b}, (b\bar{b} - r\bar{r})/\sqrt{2}$ , and  $(r\bar{r} + b\bar{b} - 2g\bar{g})/\sqrt{6}$ .

In emitting a gluon, a quark or gluon can change its colour.

The complete QCD Lagrangian is a sum over all the six quark flavours. All the six flavours have identical couplings to gluons. It can be shown in QCD that the interaction between coloured particles is attractive for colour singlets, and less attractive or repulsive for other combinations, in agreement with Greenberg's hypothesis. Note that it is not sufficient for the state to be merely colourless(white) to be an observable. There are two colourless gluons in the octet but these are not colour singlets (invariant under  $SU(3)$  transformations).

Figure 2.3: *QCD vertices.*

### 2.1.3 Asymptotic freedom and confinement

The property of QCD called **asymptotic freedom** involves a decrease in the effective strength of the colour charges of quarks as the distance from which they are viewed decreases, and can be understood by the vacuum polarization of quarks and gluons. It was discovered in 1973 by Politzer, and independently by Gross and Wilczek, that this follows from QCD [?, ?, ?]. In QED the lowest order interaction, one-photon exchange, gives the,  $V(r) = -\frac{\alpha}{r}$ , Coulomb potential. Including one loop diagrams corresponding to virtual electron-positron pairs gives a **screening** effect, the interaction appears weaker at increasing distance or low four momentum transfer. The QCD interaction from one-gluon exchange gives a Coulomb potential of exactly the same form,  $V(r) = -\frac{\alpha_s}{r}$ . The one loop correction from quark- anti-quarks screens the colour charge, but the additional loops from virtual gluon pairs give the opposite effect, so the colour charge, and hence  $\alpha_s$ , increases with increasing distance. If the QCD coupling constant is defined as  $\alpha_s = g_s^2/4\pi$ ,  $\alpha_s$  varies with  $Q^2 = -q^2$ , where  $q^2$  is the four momentum squared transferred from incident to target particle, as

$$\alpha_s(Q^2) = \frac{12\pi}{(33 - 2n_f) \log(Q^2/\Lambda^2)}, \quad (2.9)$$

$n_f$  is the number of quark flavours, and

$$\Lambda^2 = \mu^2 \exp\left[\frac{-12\pi}{(33 - 2n_f)\alpha_s(\mu^2)}\right]. \quad (2.10)$$

$\Lambda$  has been measured by experiment to be about 0.1-0.5 GeV [?]. For  $Q^2 \gg \Lambda^2$  the coupling decreases toward asymptotic freedom, then the coupling is weak and perturbation theory can be applied. For small  $Q^2$  the coupling is large. In such cases it is not possible to use perturbation theory, and it is difficult to make exact predictions, for example about the masses of particles.

It is conjectured that quarks are permanently confined within hadrons, in such a way as to make only colour singlet states observable, but it is not yet proved that this **confinement** is a fundamental consequence of QCD. Intuitively one can imagine it as a consequence of the non-Abelian nature of QCD, which causes the field lines between two quarks to be coloured, and therefore to attract each other (figure 2.4). The consequence is that the force is constant, with the potential energy increasing with distance, so no finite amount of energy can separate the quarks. An effective potential between quarks and antiquarks of the form

$$V_{q\bar{q}}(r_{q\bar{q}}) = -\frac{4}{3} \frac{\alpha_s}{r} + br \quad (2.11)$$

has been frequently employed to give predictions of meson spectroscopy (section 2.2.2). The constant  $b$  is known as the string tension, and is numerically found to be approximately  $0.18 \text{ GeV}^2$  [?]. At large distances the linear confining term of the potential dominates.

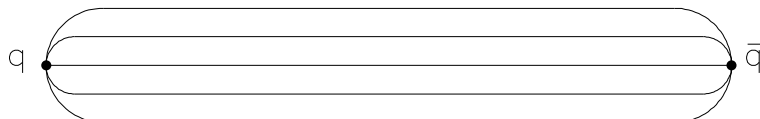


Figure 2.4: *Colour force field lines between quark and antiquark.*

### 2.1.4 Experimental evidence for QCD

Between 1968 and 1975 several experiments were performed which involved scattering of high energy electrons and neutrinos off protons [?, ?]. Such experiments are called deep inelastic scattering experiments because the electrons do not scatter coherently off the protons but interact with individual **partons** inside them, causing the protons to disintegrate.

These experiments gave a large amount of information about the quark structure of protons, in support of QCD. The **scaling behaviour** [?, ?] of the cross sections indicates scattering off point-like quarks with relatively weak interactions between them at short distances as expected from asymptotic freedom. Furthermore, the **momentum sum rules** in both electron- and neutrino- proton scattering suggest that quarks carry only about half of the total proton momentum, the rest is thought to be carried by gluons [?].

In another important type of experiments electrons and positrons annihilate, resulting in a large number of outgoing hadrons, appearing in two or three **jets** [?, ?]. This is explained by assuming that initially a quark-antiquark pair is produced,  $e^+e^- \rightarrow q\bar{q}$ , and additional quark-antiquark pairs are produced as the two initial quarks separate, giving rise to a large number of hadrons in two separate jets. The three-jet events give important evidence in support of the quark gluon picture, since they are interpreted as one of the initial quarks radiating a gluon, followed by the three particles flying off in separate directions, each resulting in a jet [?].

Another important prediction from QCD is that in addition to the known types of hadronic matter, mesons and baryons, exotic states like **glueballs**, **hybrids**, and possibly **four-quark systems** should be observed as free particles.

The discovery of a glueball would be a direct confirmation of the non-Abelian nature of QCD, since coloured gluons should be able to form bound colour singlet states of two or three gluons (see section 2.2.4).

### 2.1.5 Summary of QCD

In summary the following are the essential properties of QCD [?]:

- Quarks carry colour as well as electric charge. There are three colours: red, green, and blue.
- Colour is exchanged by eight bicoloured gluons. The gluons are massless and have spin 1.
- Quark-gluon interactions are computed by the same rules as electromagnetic interactions, QED, but substituting  $\sqrt{\alpha_s}$  for  $\sqrt{\alpha}$  at each vertex and introducing a colour factor.  $\alpha_s$  is the QCD coupling constant, which decreases as  $s$  increases. In other words, the  $q\bar{q}g$  vertex has the same structure as the  $e\bar{e}\gamma$  vertex.
- Since the gluons themselves carry colour charge, they can interact with other gluons. This means there are  $ggg$  and  $gggg$  vertices in the theory.

- At short distances (large  $s$ ),  $\alpha_s$  is sufficiently small to make it possible to compute colour interactions using the same perturbative techniques as in QED.
- It is believed that quarks and gluons are confined in colour singlets, although this has yet to be proven from QCD. In other words, only colour singlets can be observed as physical, free particles.

## 2.2 The QCD spectrum

In this section the various states corresponding to colour singlets are reviewed. The  $q\bar{q}$  mesons and  $qqq$  baryons described in section 2.1.1 have firm experimental support. There are also other combinations of quarks and gluons which give colour singlets. If the confinement hypothesis is correct, these should be observable as real physical particles [?]. Such exotic states have not been clearly identified up to now.

A survey of the hadronic spectrum and some candidates for exotic states is given. The conventional meson spectrum will be considered first, then the exotic states, which are the main topic of interest in this thesis. The study of mesons is important in order to be able to rule out the possibility of a glueball candidate being an ordinary meson. Also glueballs can mix with conventional mesons (section 2.2.12).

### 2.2.1 Conventional states: mesons and baryons

Almost all hadronic resonances can be interpreted as either  $q\bar{q}$  mesons or  $qqq$  baryons, the conventional hadrons. We will only consider  $SU(3)_{flavour}$ , that is, particles containing up, down, and strange quarks.

#### Mesons

One way to obtain a colour singlet is to combine the fundamental triplet of  $SU(3)_{colour}$ ,  $\mathbf{3}$  with the conjugate triplet  $\bar{\mathbf{3}}$

$$q \otimes \bar{q} = \mathbf{3} \otimes \bar{\mathbf{3}} = \mathbf{1} \oplus \mathbf{8}. \quad (2.12)$$

The singlet has the wavefunction

$$\psi_{colour} = (r\bar{r} + b\bar{b} + g\bar{g})/\sqrt{3}. \quad (2.13)$$

This is the colour wave function corresponding to the mesons. The flavour wave function is obtained by taking the product of the flavour triplet with the conjugate triplet. Both the singlet and octet correspond to observed particles. The singlet, which is invariant under rotations in  $SU(3)_{flavour}$ , is

$$\psi_{flavour}(1, I = 0, I_3 = 0) = (u\bar{u} + d\bar{d} + s\bar{s})/\sqrt{3}. \quad (2.14)$$

angular momentum $L$	spin singlet, $S = 0$	spin triplet, $S = 1$
0	$0^{-+}$	$1^{--}$
1	$1^{+-}$	$0^{++}, 1^{++}, 2^{++}$
2	$2^{-+}$	$1^{--}, 2^{--}, 3^{--}$
3	$3^{+-}$	$2^{++}, 3^{++}, 4^{++}$

Table 2.1: *Quantum numbers  $J^{PC}$  for mesons (quark-antiquark states).*

The singlet has isospin zero,  $I = 0$ . The octet consists of  $u\bar{d}, d\bar{u}, d\bar{s}, u\bar{s}, s\bar{d}, s\bar{u}$ , and two  $I_3 = 0$  states in the centre, one with  $I = 1$

$$\psi_{flavour}(8, I = 1, I_3 = 0) = (u\bar{u} - d\bar{d})/\sqrt{2}, \quad (2.15)$$

and one with  $I = 0$

$$\psi_{flavour}(8, I = 0, I_3 = 0) = (u\bar{u} + d\bar{d} - 2s\bar{s})/\sqrt{6}. \quad (2.16)$$

The physical isospin zero states are mixtures of the SU(3) octet and singlet states [?]. If the physical particle wave functions are called  $\beta$  and  $\beta'$ , and the singlet and octet wave functions denoted  $\alpha_0$  and  $\alpha_8$ , then

$$\begin{aligned} \beta &= \alpha_0 \cos \theta + \alpha_8 \sin \theta, \\ \beta' &= -\alpha_0 \sin \theta + \alpha_8 \cos \theta. \end{aligned} \quad (2.17)$$

The mixing angles are  $\theta \approx -11^\circ$  for the pseudoscalars,  $\theta \approx 40^\circ$  for the vectors, and  $\theta \approx 32^\circ$  for the tensors. It is therefore more useful to classify mesons in nonets than in octets and singlets. In the case of ideal mixing, one  $I = 0$  particle will be purely  $s\bar{s}$ , the other  $\frac{u\bar{u}+d\bar{d}}{\sqrt{2}}$ . This happens for  $\theta \approx 35.3^\circ$ . The vector mesons  $\phi$  and  $\omega$  are almost ideally mixed.

The quarks are spin 1/2 fermions and may couple to give a total spin of  $S = 0$  or  $S = 1$ . The total angular momentum is  $\vec{J} = \vec{L} + \vec{S}$ , the vector sum of the spin  $\vec{S}$  and orbital angular momentum  $\vec{L}$ . The parity of a fermion anti-fermion system is  $P = (-1)^{L+1}$ . The  $C$ -parity is a good quantum number only for states with  $Q=B=S=0$ , ( $Q$ =charge,  $B$ =baryon number,  $S$ =strangeness), that is, the states in the centre of the nonets. For such a state  $C = (-1)^{L+S}$ , where  $S$  and  $L$  are spin and orbital angular quantum numbers. Table 2.1 gives the possible  $J^{PC}$  values for mesons with orbital angular momentum 0, 1, 2, or 3. In table 2.2 some of the mesons in the scalar, pseudoscalar, vector and axial vector, and tensor fundamental nonets, with their usual quark assignments, are listed. In addition several of the nonets can have orbital excitations with higher  $L$ -values. For example the fundamental  $2^{++}$  nonet, has  $L = 1$ , but there is also an excited  $2^{++}$  nonet with  $L = 3$  as seen from table 2.1.  $L$  and  $S$  are not conserved quantum numbers, so different orbital configurations can mix. Parity conservation forbids mixing of even and odd  $L$  states, and then  $J$ -conservation requires that the spin  $S$  be unique, either 0 or 1. This leaves the possibility of mixing only for  $S = 1$  triplet states for which  $L = J \pm 2$ . There are also radial excitations, so all of the nonets will be repeated at higher mass [?].

$^{2S+1}L_J$	$J^{PC}$	$u\bar{u}, d\bar{d}, s\bar{s}$ $I = 0$	$u\bar{d}, u\bar{u}, d\bar{d}$ $I = 1$	$u\bar{s}, d\bar{s}$ $I = 1/2$
$^1S_0$	$0^{-+}$	$\eta, \eta'(958)$	$\pi$	$K$
$^3S_1$	$1^{--}$	$\phi(1020), \omega(783)$	$\rho(770)$	$K^*(892)$
$^1P_1$	$1^{+-}$	$h_1(1190)$	$b_1(1235)$	$K_1(1400)$
$^3P_0$	$0^{++}$	$f_0(1300), f_0(975)$	$a_0(980)$	$K_0^*(1350)$
$^3P_1$	$1^{++}$	$f_1(1285), f_1(1420)$	$a_1(1270)$	$K_1(1280)$
$^3P_2$	$2^{++}$	$f_2'(1525), f_2(1270)$	$a_2(1320)$	$K_2^*(1430)$

Table 2.2: Quark assignments (from [?]) of established meson nonets.

## Baryons

The other type of conventional hadron is obtained by making a colour singlet from the product of three fundamental triplets

$$q \otimes q \otimes q = 3 \otimes 3 \otimes 3 = 1 \oplus 8 \oplus 8 \oplus 10. \quad (2.18)$$

Here the colour singlet will be the antisymmetric wavefunction

$$\psi(\text{colour}) = (rgb - rbg + gbr - grb + brg - bgr) / \sqrt{(6)}, \quad (2.19)$$

which is the colour wavefunction corresponding to baryons. The details of the baryon wavefunctions are not important in this thesis, since we will mostly be concerned with states with baryon number  $B=0$ . The most important feature is that the product of flavour, spin, and space wave functions must always be symmetric, to make a total antisymmetric wave function.

### 2.2.2 Spectroscopy of $q\bar{q}$ mesons

The most successful models for predicting meson masses have been potential models. In a nonrelativistic quark potential model [?] the  $q\bar{q}$  wave functions are taken to be the solution of the Schrödinger equation with a potential which is a combination of a colour coulomb term from one gluon exchange (OGE), with a phenomenological linear confining term as in equation 2.11. In addition, to order  $\frac{v^2}{c^2}$  in the quark motion, one has the following spin dependent  $q\bar{q}$  Hamiltonian:

$$H_{spin-dep.} = +\frac{32\pi\alpha_s}{9m_q^2} \vec{S}_q \cdot \vec{S}_{\bar{q}} \delta(\vec{x}) + \frac{4\alpha_s}{m_q^2 r^3} (\vec{S}_q \cdot \hat{r} \vec{S}_{\bar{q}} \cdot \hat{r} - \frac{1}{3} \vec{S}_q \cdot \vec{S}_{\bar{q}}) \quad (2.20)$$

$$+ \frac{2\alpha_s}{m_q^2 r^3} \vec{L} \cdot \vec{S} - \frac{b}{2m_q^2 r} \vec{L} \cdot \vec{S}.$$

The first three terms are the spin-spin, tensor, and spin-orbit interactions, from the one gluon exchange term in the potential, the last term is an inverted spin-orbit term from the scalar linear confining interaction.

Figure 2.5: Prediction for isovector meson masses from the Godfrey-Isgur model. The dominant spectral composition and predicted masses of states in GeV are shown near solid bars representing their masses. Shaded areas correspond to the experimental masses and their uncertainties, normally taken from the Particle Data Group(1984). From [?].

The OGE spin-spin force, being a contact interaction, causes a large positive splitting between  $L = 0$  vector and pseudoscalar states. The spin-orbit interaction causes a splitting  $M_{J=L+1} > M_{J=L} > M_{J=L-1}$  for small  $L$  where the OGE term is largest, while for larger  $L$ , the scalar  $\vec{L} \cdot \vec{S}$  term dominates and the mass ordering will be inverted.

The tensor OGE interaction mixes spin triplet states related by  $\Delta L = 2$ .

The relativized model of Godfrey and Isgur [?] has a few minor modifications to this model, such as the use of  $H_{KE} = 2\sqrt{\vec{p}^2 + m_q^2}$  instead of the nonrelativistic energy term  $2m_q + p^2/m_q$ . The predictions of this model are shown in figure 2.5 for isovector mesons, figure 2.6 for strange mesons, and figure 2.7 for isoscalar mesons. This can be compared to the known states according to the Particle Data Group, 1994 [?]. We will consider scalar and tensor mesons. There are more states discovered with  $J^{PC} = 0^{++}$  and  $2^{++}$  than can fit into the  $q\bar{q}$  nonets. One possible explanation is that the extra states could be glueballs.



Figure 2.6: Prediction for strange meson masses from the Godfrey-Isgur model. The legend is as for figure 2.5. From [?].

$f_0(980)$	$f_0(1300)$	$f_0(1370)$	$f_0(1525)$	$f_0(1590)$	$f_J(1710)$
$1^3P_0$		$1^3P'_0$			$2^3P_0$
1090		1360			1760

$K_0^*(1430)$	$K_0^*(1950)$	$a_0(980)$
$1^3P_0$	$2^3P_0$	$1^3P_0$
1240	1890	1090

Table 2.3: Scalar mesons with  $J^{PC} = 0^{++}$  below 2 GeV from [?], with possible classifications and mass predictions from Godfrey and Isgur [?] in the third row. Masses are in MeV.

**Scalar mesons** (table 2.3) The two scalar  $K^0$ -mesons, and the isovector  $a_0(980)$  are in agreement with the predictions. Recently (1995), a new  $0^{++}$ ,  $I = 1$ , resonance has been found by Crystal Barrel, the  $a_0(1450)$  [?]. This resonance has been claimed to be the  $1^3P_0$  state [?], even if the mass is high compared to the 1090 MeV which is predicted by Godfrey and Isgur. There are a total of six isoscalar mesons with  $J^{PC} = 0^{++}$  if the  $f_j(1710)$ , with uncertain spin, is included. The model predicts two  $1^3P_0$  with masses 1090 MeV and 1360 MeV, and two  $2^3P_0$  states, masses 1780 MeV and 1990 MeV. There seems to be more scalar mesons at low mass than can be accommodated in the quark model.

Figure 2.7: Prediction for isoscalar meson masses from the Godfrey-Isgur model. The legend is as for figure 2.5. From [?].

$f_2(1270)$	$f_2(1430)$	$f_2(1520)$	$f'_2(1525)$	$f_j(1710)$	$f_2(1810)$
$1^3P_2$			$1^3P'_2$		$2^3P_2$
1280			1530		1820

$K_2^*(1430)$	$K_2^*(1980)$	$a_2(1320)$
$1^3P_2$	$2^3P_2$	$1^3P_2$
1430	1940	1310

Table 2.4: *Tensor mesons with  $J^{PC} = 2^{++}$  below 2 GeV from [?], with possible classifications and mass predictions from Godfrey and Isgur [?] in the third row. Masses are in MeV.*

**Tensor mesons** (table 2.4) The two  $K_2$  -mesons are unproblematic and have a good agreement with the predictions. The same applies to the isoscalar  $a_2(1320)$ .

However, a total of 9 isoscalars have been found with  $J^{PC} = 2^{++}$ . Below 2 GeV there are three unclassified states:  $f_2(1430)$ ,  $f_2(1520)$ , and  $f_j(1710)$ .

In addition there are three states above 2 GeV (not shown in the table),  $f_2(2010)$ ,  $f_2(2300)$ , and  $f_2(2340)$ .

Not all of the measured resonances can be explained as  $q\bar{q}$  states. A discussion of which of these states that could be interpreted as non  $q\bar{q}$  candidates is given in section 2.2.12. The meson resonances have traditionally been given  $q\bar{q}$  assignments based on flavour and  $J^{PC}$  quantum numbers, and masses. To be able to distinguish between  $q\bar{q}$  mesons and other hadronic states, it is also necessary to study their production and decay characteristics.

### 2.2.3 Meson decays

The OZI rule (section 2.3) can be used to make some simple predictions of the decay characteristics of ideally mixed mesons [?]. The  $s\bar{s}$  states will have a strong preference for decay to strange mesons, rather than to non-strange mesons, since a non-strange decay would involve annihilation of the  $s\bar{s}$  pair and hence be OZI-suppressed. On the other hand, states consisting of non-strange quark pairs can decay to strange mesons without violating the OZI rule. An example is the two tensor mesons  $f_2(1270)$  and  $a_2(1320)$ , which are thought to be isospin 0 and 1,  $u\bar{u}$  and  $d\bar{d}$  combinations, while the heavier  $f'_2(1525)$  is believed to be their  $s\bar{s}$  partner. This assignment is confirmed by the much larger branching fractions of  $f'_2(1525)$  to  $K\bar{K}$  final states than to  $\pi\pi$ , while  $f_2(1270)$  has a branching fraction ratio for  $\pi\pi : K\bar{K}$  of  $\approx 20 : 1$ . Taking phase space factors into account, this gives equal coupling to  $\pi$  and  $K$ . For heavier mesons such simple arguments may not always be valid. Decay of orbitally and radially excited states have nodes as a function of outgoing hadron momentum, which might lead to erroneous conclusions about flavour content.

Electromagnetic decays of mesons have characteristic properties [?]. The decay amplitude for decay to two photons would contain two electromagnetic vertices, and be of the form

$$A(q\bar{q} \rightarrow \gamma\gamma) \propto \langle q\bar{q} | e_q^2 | 0 \rangle, \quad (2.21)$$

this gives relative amplitudes

$$\langle f : a : f' | e_q^2 | 0 \rangle = \frac{(2/3)^2 + (-1/3)^2}{\sqrt{2}} : \frac{(2/3)^2 - (-1/3)^2}{\sqrt{2}} : (-1/3)^2, \quad (2.22)$$

and relative  $\gamma\gamma$  decay rates

$$?_{\gamma\gamma}(f : a : f') = 25 : 9 : 2. \quad (2.23)$$

The measured widths are

$$?_{\gamma\gamma}(f(1270) : a_2(1320) : f'(1525)) \approx 2.8 : 1.04 : 0.105, \quad (2.24)$$

which are in agreement with predictions, since there is some additional suppression of the  $s\bar{s}$  coupling due to the larger mass of the strange quark.

### 2.2.4 Exotic states: glueballs, hybrids, and molecules

In the same way as confinement predicts that a free quark can not be observed, a gluon can not be a free particle since it is not a colour singlet. However, it was pointed out in section 2.1.2 that the Lagrangian in equation 2.7 contains terms corresponding to self interactions between gluons. This means that the gluons can mutually interact and form bound states, glueballs.

The gluons form an 8 dimensional representation of  $SU(3)_{colour}$ . The products of two or three 8 dimensional representations will include colour singlets [?] :

$$\begin{aligned} g \otimes g &= 8 \otimes 8 = 1 \oplus 8_+ \oplus 8_- \oplus 10 \oplus 10^* \oplus 27, \\ g \otimes g \otimes g &= 8 \otimes 8 \otimes 8 = 1_+ \oplus 1_- \oplus \dots \end{aligned} \quad (2.25)$$

The plus and minus subscripts mean symmetric or antisymmetric combinations. This means that both  $gg$  and  $ggg$  can be expected to form observable physical particles.

Bound states of quarks and gluons, should also exist. A  $q\bar{q}g$  state would be a product of the  $\bar{q}q$  colour octet, and the gluon octet, and could therefore form a colour singlet:

$$q \otimes \bar{q} \otimes g = 3 \otimes \bar{3} \otimes 8 = (8 \oplus 1) \otimes 8 = 1 \oplus \dots, \quad (2.26)$$

while  $q\bar{q}gg$  would form a singlet in  $8 \otimes 8 \otimes 8$ . The mixed quark-gluon states are called hybrids and meiktons. They span complete flavour nonets and hence provide many possibilities for detection.

Four-quark states are also possible;  $q\bar{q}q\bar{q}$  can form a singlet as a product of the two meson octets :

$$q \otimes \bar{q} \otimes q \otimes \bar{q} = 3 \otimes \bar{3} \otimes 3 \otimes \bar{3} = (8 \oplus 1) \otimes (8 \oplus 1) = 1 \oplus \dots \quad (2.27)$$

Exotic states with nonzero baryon numbers like  $qqqg$  can also exist :

$$q \otimes q \otimes q \otimes g = 3 \otimes 3 \otimes 3 \otimes 8 = (10 \oplus 8 \oplus 8 \oplus 1) \otimes 8 = 1 \oplus \dots \quad (2.28)$$

With our current understanding of QCD there is no strict proof for the existence of any of these states of matter. However it appears that for most  $q\bar{q}q\bar{q}$  states, a separation into two separate mesons is energetically favoured; moreover, a rearrangement into two colour singlet  $q\bar{q}$  mesons can happen without interactions, so-called “fall-apart” [?].

The various types of exotic states can be classified in three different categories, saying nothing about their internal structure, but concentrating only on the observable quantities [?].

- **Exotic of the first kind:**

Quantum numbers not accessible to a  $q\bar{q}$  pair but possible for a multiquark state. These could be for instance  $Q=2, S=2$  etc. The absence of such states has been taken as evidence for the validity of the quark model.

- **Exotic of the second kind:**

These are states with quantum number combinations  $J^{PC}$  not accessible to  $q\bar{q}$  mesons, but that could be possible for glueballs or hybrids.

- **Exotic of the third kind:**

States with quantum numbers possible for a  $q\bar{q}$  system, but with the nonet already filled.

### Glueball and hybrid quantum numbers

Gluons are vector bosons with spin 1, so both glueballs and hybrids must have integer spin. The gluon colour octet transforms into itself under charge conjugation,  $8 = \bar{8}$ . Only the two colourless states in the centre of the octet will actually be eigenstates of the  $C$ -operator; analogous with photons they are assigned  $C = -1$ . The  $gg$  glueball will be a symmetric singlet in  $8 \otimes 8$  with  $C = 1$ . The three-gluon singlet will be overall antisymmetric in colour, but a pair of gluons must be in an octet, which is coupled either antisymmetrically or symmetrically. This can be seen from [?]:

$$\begin{aligned}(8 \otimes 8) \otimes 8 &= (1 \oplus 8_A \oplus 8_S \oplus \dots) \otimes 8 \\ 8_A \otimes 8 &= 1_A \oplus \dots \\ 8_S \otimes 8 &= 1_S \oplus \dots\end{aligned}$$

The charge conjugation for the antisymmetric ( $f_{abc}$ ) coupling of two gluons is  $C = +1$ , and for the symmetric ( $d_{abc}$ ) coupling it is  $C = -1$ .

In other words, two-gluon glueballs always have  $C = +1$ , while three-gluon glueballs can have either  $C = +1$ , or  $C = -1$ . Bose symmetry must be applied to find the possible  $J^{PC}$  combinations; the total wavefunction of several identical gluons must be overall symmetric. The different models (section 2.2.5) make different predictions about the allowed  $J^{PC}$ .

The spin of glueballs is a controversial topic. Free massless gluons will only exist in transverse polarisation, and in this case two  $S = 1$  gluons can only couple their spins to 0 or 2. Some authors claim that since gluons are not on the mass shell when confined to hadrons, all three polarisation states must be considered, giving  $S = 0, 1$ , or 2 for  $gg$  states [?]. Others say that this is not allowed, since the gluons are not genuine spin 1 mass quanta, and only transverse gluons appear in the Lagrangian [?].

L	$J^{PC}$
0	$0^{++}, 2^{++}$
1	$0^{-+}, 1^{-+}, 2^{-+}$
2	$0^{++}, 1^{++}, 2^{++}, 3^{++}, 4^{++}$
3	$1^{-+}, 3^{-+}, 4^{-+}$

Table 2.5:  $J^{PC}$  values of two-gluon glueballs with different values of orbital angular momentum from the glue lego model. From [?].

### 2.2.5 Predictions for gluonium spectroscopy

Several phenomenological and theoretical models have been put forward to predict quantum numbers and masses of glueballs:

- Glue lego
- The bag model
- Potential models
- Lattice QCD
- Flux tube models
- QCD sum rules

A summary of what the different models predict about glueball spectra is given below.

#### Glue lego

In this model [?] glueballs are constructed from building blocks, massive constituent gluons, in analogy with the simple quark model. The resulting colour singlet must be symmetric under interchange of any two gluon constituent labels.

i) **Two-gluon bound states.** The Bose symmetry condition gives

$$P_1 P_2 (-1)^L (-1)^{S-s_1-s_2} I = +1. \quad (2.29)$$

$P_1$  and  $P_2$  are the gluon parities and are -1 for vector gluons.

$S$  is the total glueball spin, and  $s_1$  and  $s_2$  the gluon spins.

$I = +1$  is the eigenvalue for interchange of gluon colour labels.  $L$  is the orbital angular momentum. The symmetry condition gives  $(L + S) = \text{even}$ . The possible two-gluon states are listed in table 2.5. The  $L = 1$   $gg$  state can have exotic  $J^{PC} = 1^{-+}$ .

ii) **Three-gluon bound states.** Only the ground state, with orbital angular momentum 0, will be considered. First the spin of two gluons are coupled,

$$1 \otimes 1 = (2 \oplus 0)(\text{symmetric}) \oplus 1(\text{antisymmetric}). \quad (2.30)$$

Next, the spin of the third gluon is coupled.  $S = 3$  can only be obtained from  $2 \oplus 1$  and must hence be symmetric.  $S = 0$  must come from  $1 \otimes 1$  and is antisymmetric.

The symmetric  $S = 3$  must couple to the symmetric colour  $d_{abc}$  with  $C = -1$ , in order to give a total symmetric wavefunction. The parity is negative for three vector gluons in S wave, giving  $J^{PC} = 3^{--}$ . The antisymmetric  $S = 0$  couples to antisymmetric colour  $f_{abc}$  with  $C = +1$ , so this state has  $J^{PC} = 0^{-+}$ . The spin 1 state is also symmetric, and requiring a symmetric wave function in this case, gives  $J^{PC} = 1^{--}$  [?].

The glue lego model makes no accurate predictions for the glueball masses, but the lowest mass  $gg$  states are predicted to be  $0^{++}$  and  $2^{++}$ , the excited states  $0^{-+}$ ,  $1^{-+}$ , and  $2^{-+}$  have higher masses. The lowest mass  $ggg$  states will be  $0^{-+}, 1^{--}$ , and  $3^{--}$ . The states with the same value of the orbital angular momentum will split because of spin-spin splitting, which is expected to be of the order of a hundred MeV.

## The Bag Model

In this model [?, ?] the quarks and gluons are confined to a spherical cavity, a bag, with a radius of about 1 fm. The boundary condition that no colour current flow across the bag surface gives two sets of modes for the massless gluons, transverse electric  $TE_j$ , and transverse magnetic  $TM_j$ . They have parities  $(-1)^{j+1}$  and  $(-1)^j$  respectively, where  $j$  is the total angular momentum of the gluon. The states of lowest angular momentum  $j = 1$ , will be  $TE_1$ ,  $J^P = 1^+$ , and  $TM_1$ ,  $J^P = 1^-$ .

The possible states are obtained by combining gluons in overall symmetric states that are colour singlets. Two-gluon states with minimum angular momentum will have parity +1 for the  $(TE)_1(TE)_1$  or  $(TM)_1(TM)_1$  combinations, and -1 for the  $(TE)_1(TM)_1$  combination. The ground state will be  $(TE)_1(TE)_1$ . Two identical gluons must have a wavefunction which is totally symmetric in spin-space-colour. Both the space and colour wave function are totally symmetric, and the spin function must be symmetric as well, giving possible spin 0 or 2, and  $J^{PC} = 0^{++}$  and  $2^{++}$  for the  $(TE)_1(TE)_1$  and  $(TM)_1(TM)_1$  states. The  $(TE)(TM)$  states need not obey the spin-statistics theorem since they do not contain two identical bosons, so the possible spin values could be 0, 1, or 2, giving  $J^{PC} = 0^{-+}, 1^{-+}, 2^{-+}$ .  $J = 1$ , which would give exotic quantum numbers, is only possible if the gluons in the bag are treated as massive spin 1 quanta with 3 helicity states.

If colour forces (spin-spin interactions) among the gluons are ignored, the following masses are predicted:  $M((TE)_1(TE)_1) \approx 1$  GeV,  $M((TE)_1(TM)_1) \approx 1.3$  GeV,  $M((TM)_1(TM)_1) \approx 1.6$  GeV.

Interactions between the gluons will shift the masses several 100 MeV. Also, unknown self-energies of the  $TE$  and  $TM$  state can shift the overall mass scale. Table 2.6 shows predictions for the  $gg$  glueball masses in the bag model. In order of increasing mass, the spectrum is  $M(0^{++}) < M(0^{-+}) < M(2^{++}) < M(2^{-+})$ .

The three-gluon states in the fundamental angular mode are  $(TE)_1(TE)_1(TE)_1$  with  $P = +1$ ,  $(TE)_1(TE)_1(TM)_1$  with  $P = -1$ ,  $(TE)_1(TM)_1(TM)_1$  with  $P = +1$ , and  $(TM)_1(TM)_1(TM)_1$

	$(TE)^2$		$(TE)(TM)$		$(TM)^2$	
$C_{TE}/C_{TM}$	$0^{++}$	$2^{++}$	$0^{-+}$	$2^{-+}$	$0^{++}$	$2^{++}$
1/2	670	1750			1930	2640
1	1140	2120	1440	2300	1550	2300
2	1560	2470			1330	1940

Table 2.6: *Glueball masses from a bag model. Masses are in MeV.  $C_{TE}, C_{TM}$  are gluon self energies with respect to cavity. From [?].*

$J^{PC}$	$q\bar{q}$	$gg$	$q\bar{q}g$	$ggg$
$0^{--}$	No	No		Yes
$0^{-+}$	$^1S_0$	$(TE)(TM)$	$^3S_1(TE)$	$(TM)(TM)(TM)$
$0^{+-}$	No	No		Yes
$0^{++}$	$^3P_0$	$(TE)(TE)$	$^3S_1(TM)$	$(TE)(TE)(TE)$
$1^{--}$	$^3S_1$	No	$^1S_0(TE)$	$(TM)(TM)(TM)$
$1^{-+}$	No	?	$^3S_1(TE)$	Yes
$1^{+-}$	$^1P_1$	No	$^1S_0(TM)$	$(TE)(TE)(TE)$
$1^{++}$	$^3P_1$	No	$^3S_1(TM)$	Yes
$2^{--}$	$^3D_2$	No		Yes
$2^{-+}$	$^1D_2$	$(TE)(TM)$	$^3S_1(TE)$	Yes
$2^{+-}$	No	No		Yes
$2^{++}$	$^3P_2$	$(TE)(TE)$	$^3S_1(TM)$	Yes

Table 2.7: *Possible quantum numbers for glueballs and hybrids in the bag model. Only hybrid states with the quarks in S-wave are shown.*

with  $P = -1$ . Identical gluons must be in a totally symmetric wavefunction. If the gluons are in a symmetric colour wave function, under interchange of two colour labels ( $C = -1$ ) the spin wave function must be symmetric and  $J = 1$  or  $3$  is obtained (as seen above). If they are in an antisymmetric colour wave function ( $C = +1$ ), the antisymmetric spin state  $J = 0$  is obtained. Thus possible states for  $(TE)_1(TE)_1(TE)_1$  are  $0^{++}, 1^{+-}, 3^{+-}$ , and for  $(TM)(TM)(TM)$  the same with opposite parities,  $0^{-+}, 1^{-+}, 3^{-+}$ .

By combining  $TE$  and  $TM$  gluons and adding angular excitations, all possible values of  $J^{PC}$  can be obtained for the three-gluon glueball. The masses for the  $3g$  glueballs are expected to be somewhat higher than the  $2g$  glueballs, and [?] gives approximately 1.4 GeV as the mass for the ground state  $(TE)_1(TE)_1(TE)_1$ .

The possible quantum numbers for glueballs and hybrids (section 2.2.7) in the bag model are shown in table 2.7.



### Potential models

These models assume two massive spin 1 gluons interacting through a potential. If the gluons interact via a breakable string, and the mass  $m_g$  is generated via the strong gluon forces, the potential is [?]

$$v(r) = 2m_g(1 - e^{-r/r_0}). \quad (2.31)$$

Another model [?] uses a long range confining scalar potential which is linear in the distance (similar to equation 2.11). In both models the lightest glueball has  $J^{PC} = 0^{++}$ , and from [?]  $M(0^{++}) = 1.23 \times 2m_g$ , where  $m_g$  is the unknown effective gluon mass. This mass can be estimated by finding the solutions for the relativistic bound state equations of a potential. The solutions have wavefunctions which have characteristic mass and length scales :

$$\begin{aligned} M_{\text{constituent}} &\approx \sqrt{a} \text{ GeV}, \\ \langle R \rangle_{\text{boundstate}} &\approx \frac{1}{\sqrt{a}} \text{ GeV}^{-1}. \end{aligned} \quad (2.32)$$

$a$  is the linear slope coefficient of the potential. Hadrons built from light quarks have typically  $a_q = 0.16 \text{ GeV}^2$ , giving  $M_q \approx 0.4 \text{ GeV}$  and  $\langle R \rangle \approx 0.5 \text{ fm}$ . Similarly,

$$m_g = \sqrt{a_g}, \quad (2.33)$$

where  $a_g$  is the coefficient for the long range linear potential between two gluons in the colour singlet. The forces between the colour **8** gluons are assumed to be stronger than the colour **3** quarks, so one expects  $a_g > a_q$ , and thus  $m_g > m_q$ .

The mass ordering in the potential models is the same as for the bag model:  $M(0^{++}) \approx M(0^{-+}) < M(2^{++}) \approx M(2^{-+})$ .

### Lattice QCD

In lattice gauge theory the non-perturbative aspects of QCD theory can be studied. The interactions between gluons are simulated by Monte Carlo programs by evaluating Feynman path integrals on a lattice and studying two-point correlation functions. According to the latest calculations [?, ?] the lightest state is the scalar ( $0^{++}$ ) with a mass

$$M(0^{++}) = \begin{cases} 1.550 \pm 50 \text{ GeV} [?] \\ 1.740 \pm 71 \text{ GeV} [?] \end{cases}$$

followed by the tensor which is estimated to have a mass

$$M(2^{++}) = \begin{cases} 2.270 \pm 100 \text{ GeV} [?] \\ 2.359 \pm 128 \text{ GeV} [?] \end{cases}$$

Next are  $0^{-+}, 2^{-+}, 1^{+-}, 3^{++}$ , and the radially excited  $0^{++}$ , which all have roughly twice the mass of the scalar glueball [?]. Exotic states like  $0^{--}$  have even higher masses. Lattice QCD results in the past have suffered from a mass scale uncertainty arising from the extrapolation from finite lattice spacing to the continuum. The results reported above represent major progress in controlling this systematic error.

### Flux tube model

In this model [?] quarkonium masses are calculated by joining quarks on lattice sites with tubes of colour flux. Glueballs are formed by removing the quarks and joining the ends of the flux tube. This model does not use glueballs made of constituent gluons, but determines the quantum numbers and masses from the various excitations (rotational, vibrational, and radial). The lightest glueball in this model is  $0^{++}$  with a mass of about 1.5 GeV. Next in order of mass are  $1^{+-}$ , and  $2^{+-}$ .

### QCD sum rules

The basic idea of this model [?, ?] is to form a two point function associated with a current carrying the same quantum numbers as the resonance being studied, and then extrapolate from the asymptotic high-momentum regime to low momentum where non-perturbative effects are present. The non-perturbative effects involve vacuum expectation values of the quark and gluon condensates, and will arise as powers of  $1/Q^2$  corrections to the asymptotic freedom regime.

Resonance formation is assumed to be due to current quarks or gluons interacting with the vacuum fluctuations of the fields. Ignoring instanton effects, results are in agreement with the lattice, bag, and potential models [?]. If instantons are included somewhat heavier glueballs are predicted [?].

#### 2.2.6 Decay of glueballs

The following are the expected decay properties of glueballs :

##### Widths

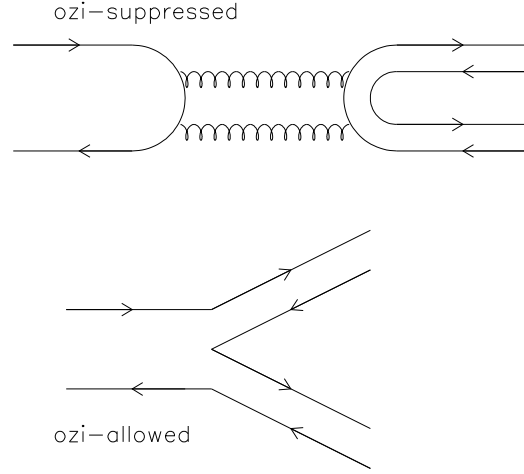
The width of glueballs was predicted to be about 10-30 MeV from the following relation [?]:

$$\Gamma_{gg} = \sqrt{\Gamma_{OZI} \times \Gamma_{hadron}}. \quad (2.34)$$

Where  $\Gamma_{OZI}$  and  $\Gamma_{hadron}$  are the widths of an OZI-suppressed, and an OZI allowed reaction (figure 2.8). The OZI rule is an empirical rule which says that reactions with different valence quark flavours in the initial and final states will be strongly suppressed (section 2.3). Such a reaction is for instance  $\phi \rightarrow \rho\pi$ , and the relation above follows if one assumes that this reaction has a glueball G as the dominant pole. However it is not clear whether this is valid in the low mass, non-perturbative regime of the glueballs.

##### Flavour independence

Glueballs are flavour singlets with isospin zero; they should preferentially decay to isoscalar flavour singlet states, with equal coupling to all flavours. Approximately equal branching

Figure 2.8: *OZI-suppressed and allowed decays.*

fractions to pseudoscalar pairs,  $gg \rightarrow \pi\pi$ ,  $gg \rightarrow \eta\eta$ ,  $gg \rightarrow \eta'\eta$  and  $gg \rightarrow K\bar{K}$ , and to pairs of vector mesons,  $gg \rightarrow \rho\rho$ ,  $gg \rightarrow \omega\omega$ , and  $gg \rightarrow \phi\phi$ , are expected.

Couplings should only depend on SU(3) isoscalar factors, phase space factors, and possible energy dependent terms [?].

If the gluon interaction is mass dependent, equal coupling to the up and down but not to the strange quark is expected. Perturbation theory predicts that the gluons have a stronger coupling to  $s$  quarks, than to  $u$  or  $d$  quarks [?].

### Quasi two body decays

Glueballs should obey  $C$ -parity for decays into mesons that are not  $C$ -eigenstates. Thus glueballs with  $C \pm 1$  have the following allowed decays to strange mesons [?]:

$$\begin{aligned} G^+ &\rightarrow K\bar{K}, K_V^*\bar{K}_V^*, K_T^*\bar{K}_T^*, \\ G^- &\rightarrow K_V^*\bar{K}, K_V^*\bar{K}_T \end{aligned} \quad (2.35)$$

$K$  is a pseudoscalar meson ( $C = +1$ )  $K_V$  is a vector ( $C = -1$ ), and  $K_T$  a tensor meson ( $C = +1$ ). A nonet of quarkonium states is not restricted by  $C$ -parity and can decay to the following final states,  $J^P$  permitting,

$$(q\bar{q}) \rightarrow K\bar{K}, K_V^*\bar{K}, K_V\bar{K}_V^*, K_T^*\bar{K}, \eta\eta'. \quad (2.36)$$

Glueballs, being flavour neutral, can decay both to states containing strange and non-strange quarks:

$$\begin{aligned} G^+ &\rightarrow \omega\omega, \phi\phi, \rho\rho, \pi\pi, \\ G^- &\rightarrow \omega\eta, \phi\eta, \rho\pi. \end{aligned} \quad (2.37)$$

Ideally mixed quarkonium is restricted by the OZI rule and will decay either to strange or nonstrange quarks:

$$\begin{aligned} (u\bar{u}, d\bar{d}) &\rightarrow \omega\omega, \omega\eta, \rho\rho, \\ (s\bar{s}) &\rightarrow \phi\phi, \phi\eta. \end{aligned} \quad (2.38)$$

A particle decaying into only one of the two classes of strange meson pairs in equation 2.35, but both types of channels in equation 2.38, would indicate a glueball.

### Suppressed radiative decays

Gluons have no electric charge, so they will not couple directly to photons. Reactions like  $gg \rightarrow \gamma\gamma$  will be first order forbidden, and therefore suppressed.

### 2.2.7 Hybrid spectroscopy

Hybrids are combinations of a  $q\bar{q}$  pair, with possible quantum numbers shown in table 2.1, and a gluon, with  $C = -1$ . Assuming no orbital angular momentum, that is, only  $S$  states for  $q\bar{q}$ , the following are the possible  $J^{PC}$  quantum numbers in the bag model (page 23):

$$\begin{aligned} {}^1S_0(0^{-+})(TE)(1^{+-}) &= 1^{-} \\ {}^3S_1(1^{--})(TE)(1^{+-}) &= 0^{-+}, 1^{-+}, 2^{-+} \\ {}^3S_1(1^{--})(TM)(1^{--}) &= 0^{++}, 1^{++}, 2^{++} \\ {}^1S_0(0^{-+})(TM)(1^{--}) &= 1^{+-} \end{aligned}$$

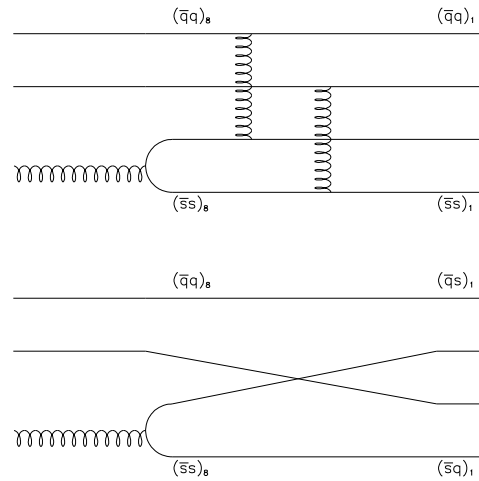
The lowest hybrid multiplet thus contain the exotic quantum numbers  $J^{PC} = 1^{-+}$ .

In the flux tube model there is also a degenerate set with reversed CP in the lowest hybrid multiplet [?]. In the constituent gluon model the lowest lying hybrid multiplet has (non-exotic) P-wave  $q\bar{q}$  quantum numbers  $J^{PC} = 0^{++}, 1^{++}, 2^{++}, 1^{+-}$  [?]; exotic  $J^{PC}$  can appear in excited multiplets. QCD sum rules have also been employed to study hybrids [?].

All the models predict the lightest hybrids to have masses of  $\approx 1.5 - 2$  GeV.

### 2.2.8 Hybrid decays

Figure 2.9 shows two different possibilities for hybrid decays involving strange mesons. The first step in both is  $(q\bar{q})_8g \rightarrow (q\bar{q})_8(s\bar{s})_8$ , the subscript 8 refers to colour octet. Then two colour singlet mesons can be formed either by rearrangement,  $(q\bar{s})_1(s\bar{q})_1$ , or by gluon exchange,  $(q\bar{q})_1(s\bar{s})_1$ . The second possibility has disconnected quark lines, it is therefore suppressed for conventional non-strange mesons and would be a decay signature for a hybrid. For example, a  $(u\bar{u} + d\bar{d})g$  hybrid with  $J^{PC} = 2^{++}$  would decay to both  $\omega\phi$  and  $\bar{K}^*K^*$  [?]. According to both flux tube and constituent gluon models, the lightest hybrids decay preferentially to pairs of one S-wave meson and one P-wave meson [?].

Figure 2.9: *Hybrid decay.*

### 2.2.9 Production of glueballs and hybrids

Gluonic states are expected to appear mostly in channels containing hard gluons, and not in processes where most of the momentum goes into the quarks [?]. According to QCD, a reaction containing  $n$  hard gluons has a rate proportional to  $(\alpha_s(s))^n$ .

Since the running coupling constant,  $\alpha_s$ , decreases with increasing energy  $s$  of the gluons, leading to asymptotic freedom (section 2.1.3), reactions with hard gluons are suppressed. In the presence of a glueball such suppression might be overcome.

The following are promising mechanisms for production of glueballs and hybrids [?] :

- Central production
- OZI-violating hadronic reactions
- $p\bar{p}$  annihilation
- $J/\Psi$  decay

#### Central production

Reactions like  $pp \rightarrow p_f(X_0)p_s$  at high energies are considered a good source for glueballs. The process is thought to be dominated by double pomeron exchange (figure 2.10). The pomeron has the same quantum numbers as the vacuum[?], and since it is believed that it has a large gluonic content, the final states  $X_0$  should have large gluon-gluon couplings.

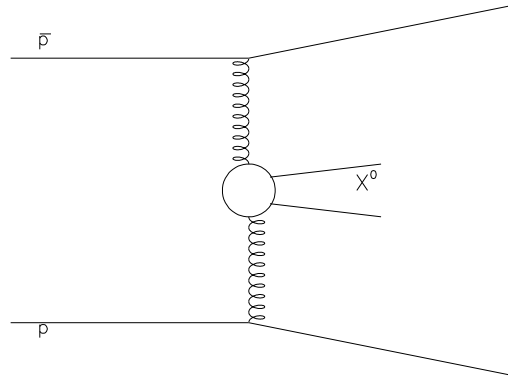


Figure 2.10: *Glueball production by central production.*

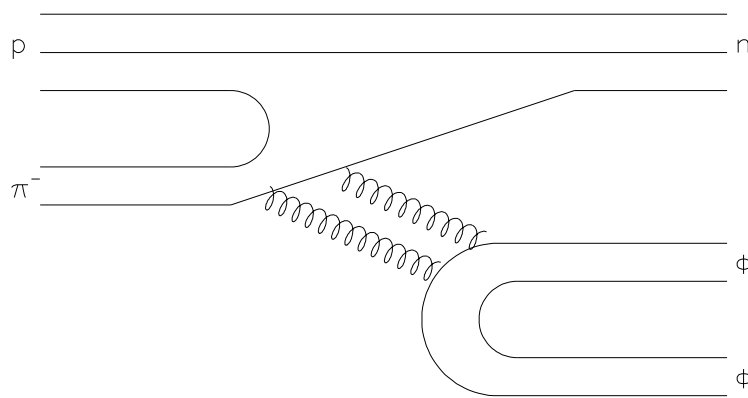


Figure 2.11: *Glueball production in the OZI-suppressed reaction  $\pi^- p \rightarrow \phi\phi n$ .*

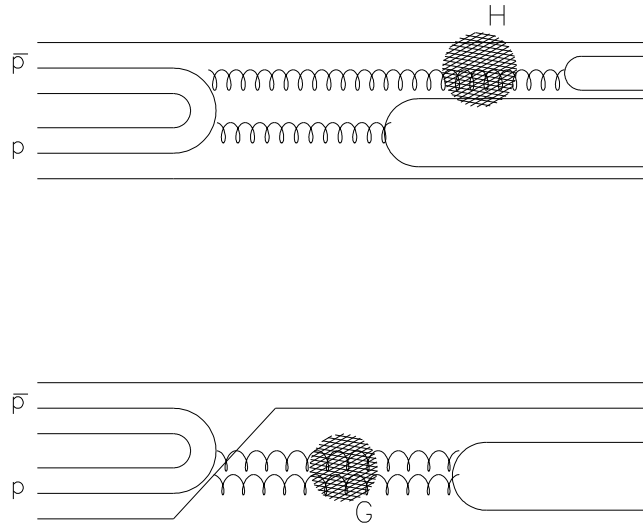


Figure 2.12: *Glueball and hybrid production in  $p\bar{p}$  annihilations.*

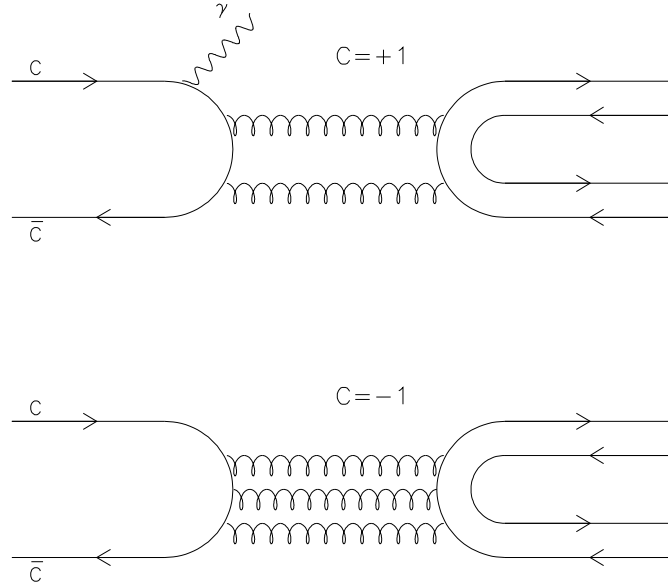
### OZI-suppressed reactions

Reactions with disconnected quark line diagrams are expected to be suppressed because of the OZI rule (section 2.3). One example is  $\pi^- p \rightarrow \phi\phi n$  (figure 2.11). In the case of ideal mixing there are no connected quark lines to the  $\phi\phi$  state since it consists only of strange quark-antiquark pairs not present in the initial state. It might therefore be created via the radiation of two or three hard gluons, which could resonate to form a glueball.

### Proton antiproton annihilation

In this type of reaction one or more quark-antiquark pairs annihilates into gluons. If some of the quark-antiquark pairs survive, there should be a good chance of producing hybrids. Annihilation at rest can occur from either S or P wave, which will couple to different resonances. Figure 2.12 shows some possibilities in  $p\bar{p}$  annihilation.

In the JETSET experiment, by concentrating on the reaction  $p\bar{p} \rightarrow \phi\phi$ , we were looking for  $p\bar{p}$  annihilation into an intermediate state of gluons only, produced by annihilation of all the initial quarks and antiquarks (figure 2.20).

Figure 2.13:  $J/\Psi$  decay.

### $J/\Psi$ decay

The  $c$  and  $\bar{c}$  quark annihilate through gluon emission (figure 2.13). In the radiative decay  $J/\Psi \rightarrow gg\gamma \rightarrow (q\bar{q})\gamma$  one of the quarks emits a photon before the quarks annihilate. This is a good source for hard gluons. The  $J/\Psi$  has  $J^{PC} = 1^{--}$ , and since the photon has  $C = -1$ , the glueball produced must have  $C = +1$ . From the lowest order diagrams shown in figure 2.14 one obtains the following relation [?]:

$$?(J/\Psi \rightarrow \gamma G) > ?(J/\Psi \rightarrow \gamma H) > ?(J/\Psi \rightarrow \gamma M), \quad (2.39)$$

where  $G$  is a glueball,  $H$  a hybrid,  $M$  a standard neutral meson.

The other possibility is the hadronic decay  $J/\Psi \rightarrow ggg \rightarrow (q\bar{q})(q\bar{q})$ . The intermediate state must consist of at least 3 gluons to give  $C = -1$ . The  $ggg$  state could produce two glueballs of opposite charge conjugation,  $G^+G^-$ . However, it is predicted that the masses of the  $G^-$  glueballs are on the order of 2 GeV, thus this reaction may be kinematically forbidden. Possible processes might be the decay to a glueball and a meson, or a hybrid and a meson. From the diagrams shown in figure 2.15 we expect [?]:

$$?(J/\Psi \rightarrow HM) > ?(J/\Psi \rightarrow GM) \approx ?(J/\Psi \rightarrow MM). \quad (2.40)$$

These perturbative estimates for the partial decay widths of exclusive decay channels are very approximate since final state interactions and interference effects have not been taken into account.



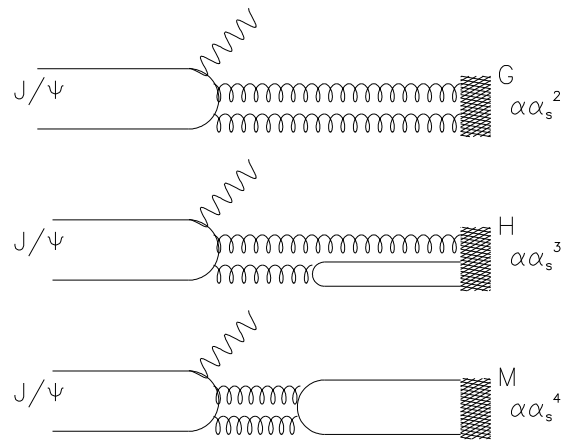


Figure 2.14: *Lowest order radiative  $J/\Psi$  decays, showing a strong coupling to exotic matter, particularly glueballs.*

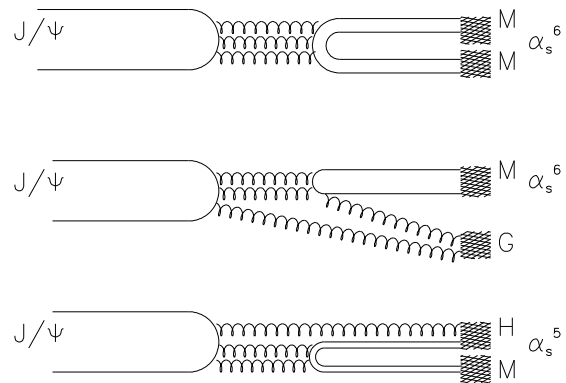


Figure 2.15: *Lowest order three-gluon  $J/\Psi$  decays, showing a strong coupling to exotic matter, particularly hybrids.*

### 2.2.10 Four-quark states

These states are of interest for JETSET, since it might be possible to produce them in the reaction  $p\bar{p} \rightarrow \phi\phi$ . The system  $q\bar{q}q\bar{q}$  can form an overall colour singlet (section 2.2.4), but such states are often likely to fall apart into more energetically favourable two-meson states. If the single four-quark cluster has a mass lower than the threshold for the two mesons, then “fall-apart” is not possible. An example of the latter case is the so-called  $K\bar{K}$  molecules. Weakly bound states of kaons and antikaons could be the ground state of a four-quark system,  $qs\bar{q}\bar{s}$  [?, ?]; the binding energy in this case is so small that the bound state is a molecule, that is, the average separation between mesons is greater than their size. The kaon and antikaon can form bound states with  $I = 0$ , and  $I = 1$ .

The scalar mesons  $f_0$  and  $a_0$  are candidates for such states, since they have masses just below  $K\bar{K}$  threshold and strong coupling to strange final states. Furthermore, it has been shown that neither  $\pi\pi$  nor  $\eta\eta$  have strong enough attraction to cause binding [?, ?].

Hybrid and four-quark states made of strange and/or charm quarks have been predicted to have widths of less than 50 MeV [?]. Four-quark states with only strange quarks,  $(s\bar{s}s\bar{s})$ , with  $J^{PC} = 0^{++}, 1^{+-}, 2^{++}$  could exist at masses around 2.3 GeV. The main decay mode for the  $2^{++}$  state would be  $\phi\phi$ , and for the  $1^{+-}$  state  $\eta\phi$  or  $\eta'\phi$ .

The following are some signatures for molecules [?]:

- $J^{PC}$  and flavour quantum numbers of an  $L = 0$  state. Due to the short range of the residual nuclear force, bound states with  $L > 0$  are unlikely to appear.
- Binding energy of maximum 50-100 MeV. This is calculated from the uncertainty principle, given that a minimum separation of 1 fm is necessary for the hadrons to maintain separate identities.
- Strong couplings to constituent channels above threshold.
- Anomalous electromagnetic coupling relative to expectations for quark-model states.

### 2.2.11 Signatures for exotic states: how to spot a glueball

The best signature for a non  $q\bar{q}$  state would be exotic quantum numbers not accessible for a conventional quark-antiquark meson. This could be an exotic of the first kind (accessible for molecules), or exotic of the second kind (exotic  $J^{PC}$ , accessible for glueballs and hybrids). For resonances with non-exotic quantum numbers, but with no place in a  $q\bar{q}$  nonet (exotic of the third kind), one will have to check with the quark model prediction to ascertain that the state is not a  $q\bar{q}$  state. The model of Godfrey and Isgur [?] gives prediction for masses for ground state and radially excited nonets. Also decay patterns not compatible with quark model predictions for  $q\bar{q}$  states (section 2.2.3) would indicate something other than a conventional meson.

Mass predictions as well as production and decay signatures for glueballs (section 2.2.4), hybrids (2.2.7), and molecules (2.2.10) have been given above.

For glueballs the following are the most important characteristics:

- Narrow widths for the lightest states (10-30 MeV).
- Preferential production in OZI-suppressed reactions and reactions involving hard gluons.
- Flavour singlet couplings.
- Selection rules as described in section 2.2.6 for quasi two-body decays.
- Suppressed radiative decays.
- Resonances that do not fit into existing  $q\bar{q}$  multiplets.
- Quantum numbers that are impossible for  $q\bar{q}$  mesons (exotic quantum numbers). This is the most unambiguous sign of a glueball.
- Gluons couple weakly to two-photon final states, but are copiously produced in radiative  $J/\Psi$  decays. This can be expressed in a “stickiness” coefficient [?]

$$S_x = \frac{?(J/\Psi \rightarrow \gamma X)/(\text{Phase Space})}{?(X \rightarrow \gamma\gamma)/(\text{Phase Space})}. \quad (2.41)$$

$S_x$  should be larger for glueballs than for ordinary mesons.

- The predicted masses are of the order 1.5-2 GeV, with  $0^{++}$  the lightest glueball, followed by the  $2^{++}$ .

A relevant question is why so few, if any, glueballs have been discovered during the last 40 years when so many mesons and baryons have been seen. There are several possible explanations:

- Perhaps glueballs do not exist at all. This would mean that QCD in its current formulation, is not the correct theory for describing strong interactions.
- Glueballs might be so broad that they can't be disentangled from  $q\bar{q}$  states.
- Even if glueballs are narrow enough to be observed, they might have been mistaken for normal quarkonium states.
- It is possible that pure glueballs don't exist, but that they mix with quark-antiquark states. This would give one more degree of freedom and another particle of the same quantum number, which could not fit into existing nonets.
- The reactions in which glueballs are produced have not yet been properly studied.

### 2.2.12 Experimental status of gluonium searches

Recently (1995), two new resonant states have gained prominence as glueball candidates, the  $f_0(1500)$  found by Crystal Barrel [?] and the  $\xi(2230)$  measured by the BES experiment [?] and others (section 2.3.6). The scalar candidate  $f_0(1500)$  has a mass and width of

$$\begin{aligned} M(f_0) &= 1520_{-55}^{+20} \text{ MeV}, \\ ?(f_0) &= 148_{-25}^{+20} \text{ MeV}. \end{aligned} \quad (2.42)$$

The tensor glueball candidate is probably the same as the  $\xi(2230)$  that has previously been seen by MarkIII in  $J/\Psi$  radiative decays. The BES experiment finds for the channel  $J/\Psi \rightarrow \gamma K_s^0 K_s^0$

$$\begin{aligned} M(\xi) &= 2232_{-16}^{+25} \pm 10 \text{ MeV}, \\ ?(\xi) &= 20_{-16}^{+25} \pm 10 \text{ MeV}. \end{aligned} \quad (2.43)$$

Similar masses and widths are seen in radiative decays to  $K^+ K^-$ ,  $p\bar{p}$ , and  $\pi\pi$ .

There are several arguments to support the gluonium interpretation of these states: The mass of the  $f_0$  is not consistent with the  $q\bar{q}$  prediction for a  $^3P_0$  nonstrange state, but is consistent with the mass predictions from lattice gauge theory for a scalar glueball. Also the width is quite narrow.

The ratio between the partial widths of decays to pseudoscalar pairs are [?]:

$$\frac{?(f_0(1500) \rightarrow \pi\pi : K\bar{K} : \eta\eta : \eta'\eta)}{\text{phase space} \times \text{form-factors}} = 1 : < 0.1(90\% \text{ C.L.}) : 0.27 \pm 0.11 : 0.19 \pm 0.08. \quad (2.44)$$

This is inconsistent with flavour symmetry, and seems to argue against a pure glueball interpretation, but might be consistent with a glueball mixed with  $q\bar{q}$  components [?] :

$$|G\rangle = |G_0\rangle + \xi \left( \frac{|u\bar{u} + d\bar{d}\rangle}{E(G_0) - E(d\bar{d})} + \frac{|s\bar{s}\rangle}{E(G_0) - E(s\bar{s})} \right), \quad (2.45)$$

where  $\xi$  is the mixing amplitude,  $E(G_0)$  and  $E(q\bar{q})$  are the masses of the relevant states. Since flavour symmetry is not exact,  $E(s\bar{s}) \neq E(d\bar{d})$ , decay into meson pairs of this state would violate flavour symmetry.

The  $f_0(1500)$  has been seen [?] in several of the production mechanisms mentioned for glueballs (section 2.2.9), radiative  $J/\Psi$  decays [?], central production  $pp \rightarrow p_f(X_0)p_s$  [?, ?], and  $p\bar{p}$  annihilation [?].

The  $\xi$  resonance, which has been seen in the gluon-rich  $J/\Psi \rightarrow \gamma X$  channel, has a narrow width and flavour symmetric coupling, both of which seem to favour a glueball rather than a  $q\bar{q}$  interpretation. Its mass is also consistent with the lattice gauge theory predictions for a  $2^{++}$  glueball (page 24).

According to the Particle Data Group [?] there are more states within certain multiplets than can be accounted for in the conventional quark model (section 2.2.2). Some of these could be either glueballs, hybrids, or four-quark molecules. For example, the  $0^{++}$  and  $2^{++}$  sectors have more isoscalars than can be accounted for. Three resonances that have often been mentioned as glueball candidates are the so-called  $g_{TS}$  or  $f_2(2010)$ ,  $f_2(2300)$ , and  $f_2(2340)$ , with  $J^{PC} = 2^{++}$ . They have been observed in the OZI-forbidden reaction  $\pi^- p \rightarrow \phi\phi n$ . Their

widths are larger than what is expected for glueballs, and they could also be the strange-antistrange quarkonium states,  $2^3P_2 s\bar{s}$ ,  $1^3F_2 s\bar{s}$ , and  $3^3P_2 s\bar{s}$  [?].

It will be impossible to identify a glueball or hybrid unambiguously without a complete understanding of light hadron spectroscopy. Further information about hadron spectroscopy and non  $q\bar{q}$  candidates can be found in references [?, ?, ?, ?].

### 2.3 The OZI rule as a glueball filter

The OZI rule was originally invented by Okubo [?], Zweig [?], and Iizuka [?] in order to explain the nearly ideal mixing for vector mesons (section 2.2.1), and the suppressed decay of  $\phi$ -mesons to pions.

The meson octet and singlet are mixed; SU(3) is broken so that the eigenstates of the mass Hamiltonian for the vector mesons are not the SU(3) isoscalar octet,  $\omega_8$ , and singlet,  $\omega_1$ . In the limit of ideal mixing the mixing angle is  $\theta = \theta_0 = \tan^{-1} \frac{1}{\sqrt{2}} = 35^\circ 16'$ , accordingly  $\phi$  is made only of  $s\bar{s}$  quarks and  $\omega$  of  $u\bar{u}$  and  $d\bar{d}$  quarks:

$$\begin{aligned}\phi &= (s\bar{s}) = \frac{1}{\sqrt{3}}\omega_1 - \sqrt{\frac{2}{3}}\omega_8, \\ \omega &= \frac{1}{\sqrt{2}}(u\bar{u} + d\bar{d}) = \sqrt{\frac{2}{3}}\omega_1 + \frac{1}{\sqrt{3}}\omega_8\end{aligned}\tag{2.46}$$

this follows if a rule is postulated:

$$\langle u\bar{u} + d\bar{d} | \hat{H}_0 | s\bar{s} \rangle \approx 0.\tag{2.47}$$

$\hat{H}_0$  is the mass part of the Hamiltonian, and its expectation value for members of the vector meson nonet can be calculated.

$$\begin{aligned}m(K^*)^2 &= \langle K^*(d\bar{s}) | \hat{H}_0 | K^*(d\bar{s}) \rangle = M_1^2 + m_d^2 + m_s^2 \\ m(\phi)^2 &= \langle \phi(s\bar{s}) | \hat{H}_0 | \phi(s\bar{s}) \rangle = M_1^2 + 2m_s^2 \\ m(\omega)^2 &= \langle \frac{1}{\sqrt{2}}(u\bar{u} + d\bar{d}) | \hat{H}_0 | \frac{1}{\sqrt{2}}(u\bar{u} + d\bar{d}) \rangle = M_1^2 + 2m_u^2\end{aligned}\tag{2.48}$$

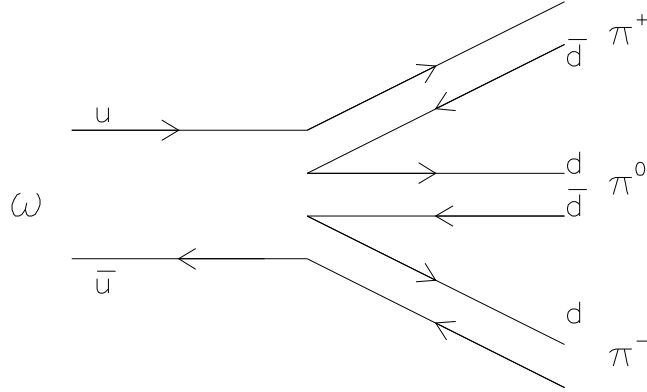
Here  $M_1$  is a common contribution to the mass coming from the  $^3S_1$  nature of the system (spin-spin splittings etc.), while  $m_d, m_s, m_u$  are the flavour contributions to the mass. <sup>1</sup> Ignoring the mass difference of the  $u$  and  $d$  quarks, the following mass formula is obtained:

$$m(\phi)^2 = 2m(K^*)^2 - m(\omega)^2.\tag{2.49}$$

This gives  $m(\phi) = 997$  MeV, which should be compared to the experimental value of 1019 MeV. If the  $\omega$  meson is ideally mixed it should have the same mass as the  $\rho$  meson, which has  $I = 1$ , and thus contains only up and down quarks. The  $\omega$  meson is 12 MeV heavier, suggesting a small admixture of  $s\bar{s}$  in its wavefunction.

---

<sup>1</sup>Okubo [?] used the squares of the masses in the mass formula which follows if one takes into account that the Hamiltonian for bosons, contains the square of the masses. Other authors have used a linear formula.

Figure 2.16: Quark line diagram for the OZI allowed process  $\omega \rightarrow 3\pi$ .

Evidence for the OZI rule also follows from the decays of the vector mesons. The decay  $\phi \rightarrow 3\pi$  is suppressed relative to  $\phi \rightarrow K\bar{K}$  even if it is favoured by phase space.

$$\frac{?(\phi \rightarrow 3\pi)}{?(\phi \rightarrow K\bar{K})} \approx \frac{1}{5}. \quad (2.50)$$

The example used by Okubo [?] was the ratio of the decay widths of  $\phi \rightarrow \pi^+\pi^-\pi^0$  and  $\omega \rightarrow \pi^+\pi^-\pi^0$ , which is

$$\frac{?(\phi \rightarrow \pi^+\pi^-\pi^0)}{?(\omega \rightarrow \pi^+\pi^-\pi^0)} = 0.074, \quad (2.51)$$

which gives a ratio of matrix elements, when phase space is taken into account, of

$$\frac{M(\phi \rightarrow \pi^+\pi^-\pi^0)}{M(\omega \rightarrow \pi^+\pi^-\pi^0)} \approx 0.10. \quad (2.52)$$

Figures 2.16, 2.17, and 2.18 show quark line diagrams of the decays  $\omega \rightarrow 3\pi$ ,  $\phi \rightarrow 3\pi$ , and  $\phi \rightarrow K\bar{K}$ , when  $\phi$  and  $\omega$  are ideally mixed. The  $\omega \rightarrow 3\pi$  and  $\phi \rightarrow K\bar{K}$  decays involve only continuous quark lines, while  $\phi \rightarrow 3\pi$  has the quark lines for the  $s$  and  $\bar{s}$  disjointed from the quark lines containing  $u$  and  $d$  quarks. The OZI rule simply says that diagrams of the type 2.17, which are called **hairpin** diagrams due to the resemblance of the  $s\bar{s}$  part of the diagram to a hairpin, are suppressed relative to diagrams of the type 2.16 and 2.18. If the part of the Hamiltonian responsible for decays is called  $\hat{H}'$ , then this can be written

$$\langle u\bar{u} + d\bar{d} | \hat{H}' | s\bar{s} \rangle \approx 0. \quad (2.53)$$

The OZI rule is experimentally well satisfied if it is defined terms of the single hairpin diagram suppression, where only one hairpin is disconnected from the rest of the diagram.

This can be tested by considering an exclusive reaction

$$A + B \rightarrow C_1 + C_2 + C_3 + \dots C_n + (s\bar{s}), \quad (2.54)$$

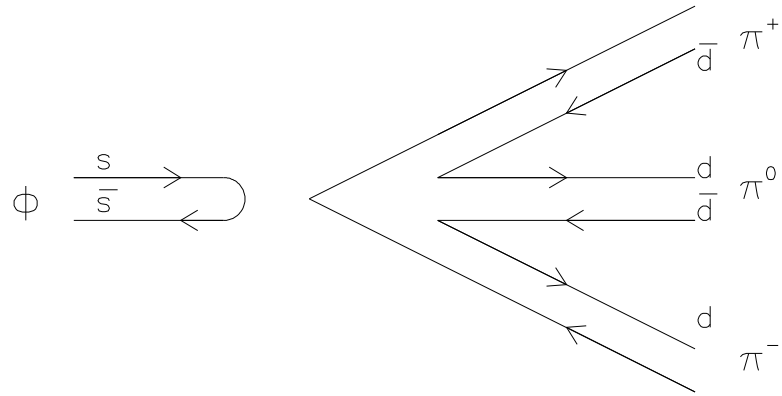


Figure 2.17: Quark line diagram for the OZI forbidden process  $\phi \rightarrow 3\pi$ .

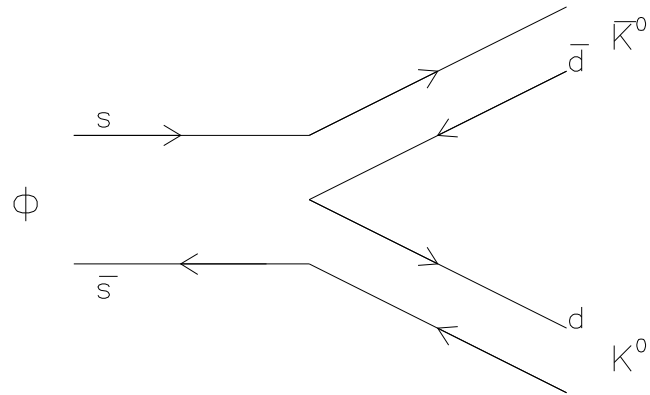


Figure 2.18: Quark line diagram for the OZI allowed process  $\phi \rightarrow K\bar{K}$ .

where all the particles  $A, B, C_1, C_2 \dots C_n$  do not contain strange quarks. The reaction must then proceed via a disconnected hairpin diagram and should ideally have a matrix element equal to zero. The ratio

$$Z = \frac{\sqrt{2}M[A + B \rightarrow C_1 + \dots C_n + (s\bar{s})]}{M[A + B \rightarrow C_1 + \dots C_n + (u\bar{u})] + M[A + B \rightarrow C_1 + \dots C_n + (d\bar{d})]}, \quad (2.55)$$

measures OZI violation, and should be much smaller than one [?]. In terms of the physical particles  $\phi$  and  $\omega$ , which are not ideally mixed,  $\theta \neq \theta_0$ , the ratio of matrix elements will be

$$\beta = \frac{M(A + B \rightarrow C_1 + C_2 + \dots \phi)}{M(A + B \rightarrow C_1 + C_2 + \dots \omega)} = -\frac{Z + \tan(\delta_V)}{1 - Z \tan(\delta_V)}. \quad (2.56)$$

Then  $\tan(\delta_V) = \tan(\theta - \theta_0)$  measures the known small OZI violation in the mass operator  $\hat{H}_0$ , and  $Z$  measures the amplitude of additional violation. The following 12 reactions of the hairpin type with known  $|\beta|^2$ , involving a vector meson  $V$ , can be used to determine  $Z$  and  $\delta_V$ :

$$\begin{aligned} V \rightarrow \rho\pi, \quad b_1 \rightarrow \pi V, \quad V \rightarrow \pi_0\gamma, \quad p\bar{p} \rightarrow \pi^+\pi^-V, \quad \pi N \rightarrow NV, \\ \pi^-p \rightarrow p\pi^-\pi^+\pi^-V, \quad pp \rightarrow ppV, \quad pp \rightarrow ppVn \times (\pi^+\pi^-). \end{aligned}$$

A global fit with all these reactions, setting  $Z = 0$ , gives  $\delta_V = \pm 5^\circ 43'$ , while the quadratic mass formula gives  $\delta_V = 4^\circ$ . On the other hand, setting a fixed  $\delta_V$  value corresponding to  $\tan \delta_V = 0.1$  gives us the fitted values  $\langle Z \rangle = 0$  and  $|Z| \leq 0.062$ . The conclusion is that the dynamical OZI violation is smaller than, or equal to, violation from mixing [?]. However, new measurements from LEAR indicate much larger  $Z$  - values [?, ?].

$$\frac{\sigma(\bar{n}p \rightarrow \pi^+\phi)}{\sigma(\bar{n}p \rightarrow \pi^+\omega)} = 0.11 \pm 0.015, \quad (2.57)$$

$$\frac{\sigma(\bar{p}n \rightarrow \pi^-\phi)}{\sigma(\bar{p}n \rightarrow \pi^-\omega)} = 0.13 \pm 0.025, \quad (2.58)$$

which gives  $|\beta|^2 \approx 0.12$ . For  $|Z|$  one can only obtain limits, since the phase of  $\beta$  is unknown:

$$0.25 < |Z| < 0.45. \quad (2.59)$$

Apparently a breaking of the OZI rule [?]. A possible explanation will be given in section 2.4.1.

The OZI rule is still not well understood on a theoretical basis. It may follow from asymptotic freedom, provided  $\alpha_s$  and  $\lambda$  are small enough.

In QCD, disconnected quark lines in OZI forbidden diagrams are bridged by the exchange of at least two or three hard gluons in colour singlet. Asymptotic freedom decouples quarks from gluons, which explains the OZI rule. In the OZI allowed processes with connected quark line diagrams, the creation and annihilation involves relatively soft gluons which have a stronger coupling to quarks.

A problem with this argument is that if the quark and antiquark annihilate into a large number of gluons, then each of them will be soft enough to make  $\alpha_s$  large and thus give a strong coupling. It is not clear why the process should be dominated by two or three gluon



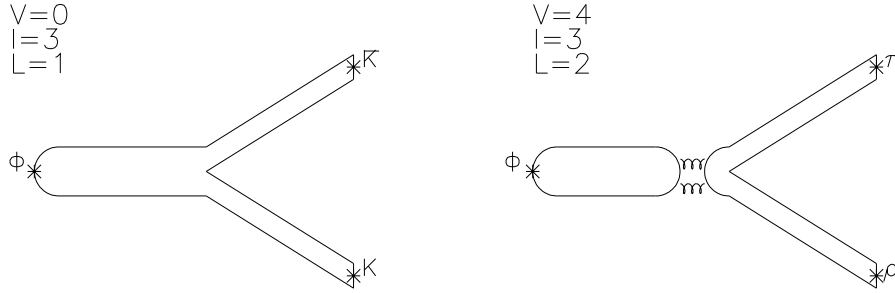


Figure 2.19: Representation of the processes  $\phi \rightarrow K\bar{K}$  (left), and  $\phi \rightarrow \rho\pi$  (right), in the  $1/N_C$  expansion.

exchanges. No satisfactory resolution to this problem has been found [?].

The OZI rule also follows to leading order in the large  $N_{colour}$  expansion [?]. In this simplified version of QCD, which follows when  $N_C \rightarrow \infty$  one can calculate the amplitude for a process as  $A \propto N^{-(V+2V')/2-I/2+L}$ , where  $V$  is the number of 3 way-vertices,  $V'$  the number of 4-way vertices,  $I$  is the number of insertions (external mesons), and  $L$  is the number of closed quark loops [?]. From this one can calculate the amplitude for  $\phi \rightarrow K\bar{K}$  and  $\phi \rightarrow \rho\pi$  (figure 2.19). The amplitude for the OZI-allowed process  $\phi \rightarrow K\bar{K}$  is proportional to  $\frac{1}{\sqrt{N}}$ , independent of the number of gluon exchanges. The OZI-suppressed process  $\phi \rightarrow \rho\pi$  has an amplitude proportional to  $\frac{1}{\sqrt{N^3}}$  if the disconnected quark loops are bridged by two gluons. Each gluon between disconnected loops gives an extra factor  $1/N$ . These results are general and result in OZI suppression for mesons. In the real world  $N_C = 3$ , and a  $1/N_C$  expansion must be carried out. It is not clear how these results carry over to baryons, since in a world of  $N_C$  colours each baryon must contain  $N_C$  quarks in order to obtain a colour singlet, and it is also possible that for baryons the sea of quark-antiquark pairs can not be ignored [?].

Both the asymptotic freedom, and the large  $N_{colour}$  expansion, gives rise to a more general OZI rule, where not only the single hairpin diagrams, but also other types of disconnected diagrams should be suppressed. For example both the reaction  $\pi^-p \rightarrow \phi n$  (single hairpin) and  $\pi^-p \rightarrow \phi\phi n$  (double hairpin) should be suppressed. The latter kind of reaction, with two hairpins disconnected from the rest of the diagram, has been used to hunt for glueballs decaying to  $\phi\phi$ , since even if quarks and gluons would normally be decoupled, a glueball resonance is expected to be strongly coupled.

Assuming approximately flavour independent couplings to  $u, d$  and  $s$  quarks, the decay widths of a glueball to  $\phi\phi$  or  $\omega\omega$  should be approximately equal. Discovering a glueball in a non-OZI suppressed reaction like  $\pi^-p \rightarrow \omega\omega n$  would however be difficult, since it would be masked by a background of non- gluonic processes. One can therefore regard the OZI rule as a glueball filter in reactions like  $\pi^-p \rightarrow \phi\phi n$ , where  $q\bar{q}$  states, but not glueballs, would be suppressed. Furthermore, the violation of the OZI rule should be particularly large when the  $\phi\phi$  system has the mass and quantum number of the glueball.

An example is the three resonances  $g_T(2120)$ ,  $g_T(2220)$  and  $g_T(2360)$  found by the experiment BNL-CCNY [?] (see also section 2.4.3). The most important argument for the glueball status of these resonances was the observation of a large violation of the OZI rule in  $\pi^-p \rightarrow \phi\phi n$  [?].

Lipkin [?] has questioned the validity of the OZI rule for processes described by diagrams which are not of the single hairpin type, and where the smallest disconnected piece has quark lines from two or more hadrons. For example,  $\pi^-p \rightarrow \phi\phi n$  is related by crossing to the non-suppressed reaction  $\phi n \rightarrow \phi\pi^-p$ , which is elastic  $\phi$  nucleon scattering with additional pion production. It should therefore not be suppressed, and there is some experimental evidence to support this [?].

The theoretical justification of Lipkin's argument was questioned by Lindenbaum [?]. The two reactions, the OZI-suppressed  $\pi^-p \rightarrow \phi\phi n$ , and the elastic scattering  $\phi n \rightarrow \phi\pi^-p$  would take place in two different kinematical and physical regions, and the two reactions cannot be simply related without knowing everything about analytic continuity, singularities involved, etc.

## 2.4 The reaction $p\bar{p} \rightarrow \phi\phi$

The reaction  $p\bar{p} \rightarrow \phi\phi$ , should be an ideal hunting ground for glueballs for the following reasons [?]: If we assume that the proton(antiproton) consists only of  $uud$  ( $\bar{u}\bar{u}\bar{d}$ ), and the  $\phi$  meson is ideally mixed, so it is pure  $s\bar{s}$ , the simplest way to imagine this process is that the three quark-antiquark pairs annihilate, producing first an intermediate state with at least two gluons in a colour singlet state, followed by the production of two  $s\bar{s}$  pairs (figure 2.20). This process, with its disconnected quark lines, should be OZI-suppressed, but the suppression could be overcome if the reaction proceeds via a gluonic resonant state. The possibility of

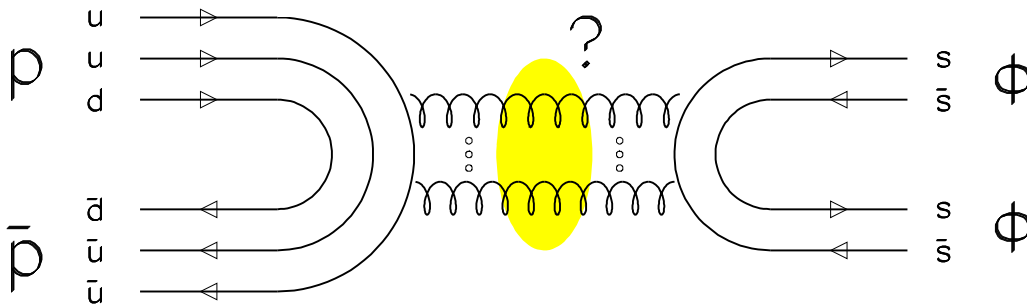


Figure 2.20: The process  $p\bar{p} \rightarrow \phi\phi$ .

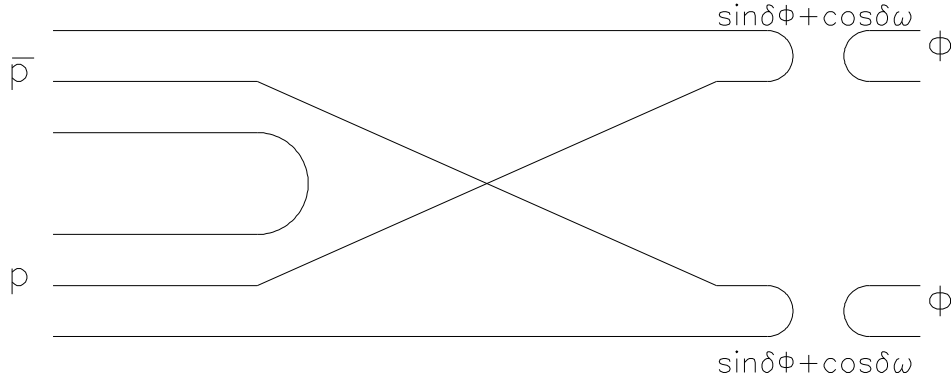


Figure 2.21: *The process  $p\bar{p} \rightarrow \phi\phi$  through  $\omega - \phi$  mixing.*

evading the OZI rule in  $p\bar{p} \rightarrow \phi\phi$  is discussed below.

Glueballs are expected to couple particularly strongly to strange quarks, compared to the lighter  $u$  and  $d$  [?]. Previous measurements (section 2.4.3) might have found gluonic resonances in the  $\phi\phi$  channel.

An overview of previous measurements of  $\phi\phi$  in formation and production experiment, as well as other resonances of interest in the relevant energy region, is given at the end of this section.

#### 2.4.1 Is $p\bar{p} \rightarrow \phi\phi$ OZI-suppressed ?

The use of the OZI rule as a glueball filter was discussed in the preceding section. In this section we will inquire whether OZI suppression is valid in our specific case,  $p\bar{p} \rightarrow \phi\phi$ . The final state contains two hairpin loops, and will therefore be suppressed, and a good glueball filter if the OZI rule is generally valid, but not if it only applies to single hairpin diagrams. It is possible that the OZI rule, even if it is generally valid, can be evaded in the reaction  $p\bar{p} \rightarrow \phi\phi$ , by proceeding via the connected quark line diagrams described below.

##### $\omega - \phi$ mixing

Because of the departure from ideal mixing, the  $\phi$  meson contains a small admixture of nonstrange mesons,

$$\phi = \cos\delta_V(s\bar{s}) + \sin\delta_V(u\bar{u} + d\bar{d}), \quad (2.60)$$

where  $\delta_V = \theta - \theta_0$ , the difference between the real and ideal mixing angle for the vector mesons. If the reaction  $p\bar{p} \rightarrow \phi\phi$  proceeds only through the nonstrange component of the  $\phi$  (figure 2.21), the amplitude for this reaction should be

$$\langle p\bar{p} | \hat{H}' | \phi\phi \rangle \propto \sin^2 \delta_V, \quad (2.61)$$

if both  $\phi$ s are produced by independent OZI-violating couplings. The  $\omega$  meson is mostly

$u\bar{u}, d\bar{d}$ :

$$\omega = \sin\delta_V (s\bar{s}) + \cos\delta_V (u\bar{u} + d\bar{d}), \quad (2.62)$$

so the reaction  $p\bar{p} \rightarrow \omega\omega$  has an amplitude  $\propto \cos^2 \delta_V$ . The singlet-octet mixing angle is  $\theta \approx 39^\circ$ , then  $\delta_V \approx 4^\circ$ , and

$$\frac{\sigma(p\bar{p} \rightarrow \phi\phi)}{\sigma(p\bar{p} \rightarrow \omega\omega)} = \tan^4 \delta_V \approx 2.5 \cdot 10^{-5}. \quad (2.63)$$

If  $\sigma(p\bar{p} \rightarrow \omega\omega)$  is estimated to be about  $0.5 \text{ mb}$ ,<sup>2</sup> a cross section  $\sigma(p\bar{p} \rightarrow \phi\phi) \approx 10 \text{ nb}$  is obtained.

### Strangeness in the proton

According to the naive constituent quark model considered so far, the proton wave functions contains two  $u$  quarks and one  $d$  quark. Perturbative QCD predicts that that the proton should also contain a sea of quark-antiquark  $u, d$ , and  $s$  pairs, and gluons, which will be revealed at large momentum transfers, or small distances. Various experimental evidence now indicates that already at small momentum transfers, these non-naive constituents can be observed [?].

The pion nucleon sigma term,

$$\sum^{\pi N} = \frac{1}{2}(m_u + m_d) \langle p|(u\bar{u} + d\bar{d})|p \rangle, \quad (2.64)$$

is about a factor of two larger than expected from setting  $\langle p|s\bar{s}|p \rangle = 0$ ; the experimental value [?] indicates

$$\frac{\langle p|s\bar{s}|p \rangle}{\langle p|(u\bar{u} + d\bar{d})|p \rangle} \approx 0.2. \quad (2.65)$$

Also data from deep inelastic scattering on the polarized structure function  $g_1^\nu$  [?, ?, ?] indicates a significant strange quark component in the proton, with

$$\Delta s = -0.10 \pm 0.02 \quad (2.66)$$

the fraction of the proton spin carried by strange quarks and antiquarks.

From the theoretical point of view, recent lattice QCD calculations indicate  $\Delta s \approx -0.10$  in the proton [?].

To estimate the amplitude of strangeness production in  $p\bar{p}$  annihilation, the proton wave function can be written [?, ?]

$$|p \rangle = x \sum_{X=0}^{\infty} |uudX \rangle + z \sum_{X=0}^{\infty} |uuds\bar{s}X \rangle, \quad (2.67)$$

where  $X$  stands for any number of gluons and light  $q\bar{q}$  pairs, and the condition  $|x|^2 + |z|^2 = 1$  holds (the admixture of more than one  $s\bar{s}$  pair is neglected). There are two different diagrams for producing a state with open or hidden strangeness from the  $s\bar{s}$  content in the proton,

<sup>2</sup>We assume that the  $p\bar{p} \rightarrow \omega\omega$  is 10% of the total  $p\bar{p} \rightarrow 2\pi^+ 2\pi^- 2\pi^0$  cross section, which is measured to be approximately  $5 \text{ mb}$  [?].

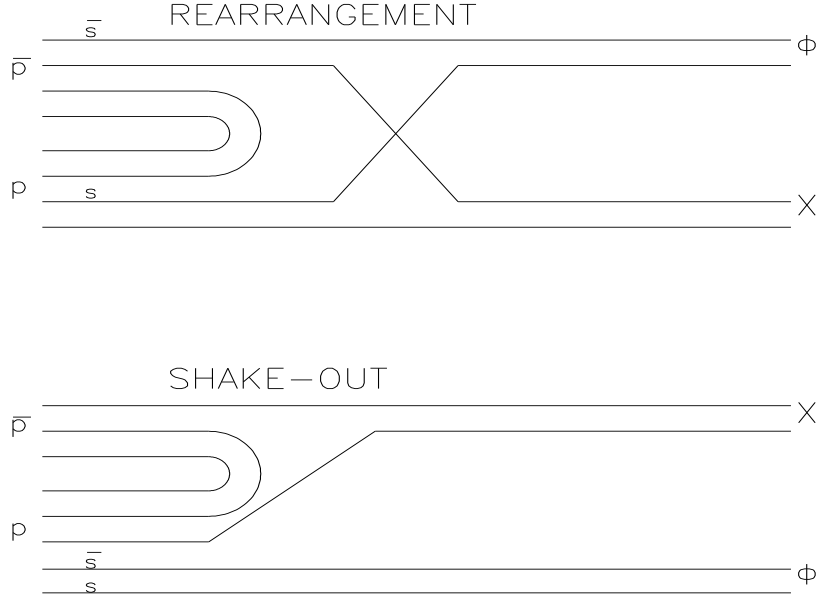


Figure 2.22: *Shake-out and rearrangement diagrams for the process  $p\bar{p} \rightarrow s\bar{s} + X$ .*

the shake-out diagram and the rearrangement diagram (figure 2.22). The amplitude for  $p\bar{p}$  annihilation into a state with open or hidden strangeness via the shakeout diagram is

$$A(p\bar{p} \rightarrow s\bar{s} + X) \approx 2\text{Re}(xz^*)P(s\bar{s}). \quad (2.68)$$

The amplitude for producing a  $s\bar{s}$  state via rearrangement is

$$A(p\bar{p} \rightarrow s\bar{s} + X) \approx |z|^2 T(s\bar{s}). \quad (2.69)$$

$P(s\bar{s})$  and  $T(s\bar{s})$  are factors which depend on the initial and final states. The ratio  $R$  is defined [?]

$$R = \frac{\sigma(A + B \rightarrow \phi X)}{\sigma(A + B \rightarrow \omega X)} = \left( \frac{Z - \tan \delta}{1 - Z \tan \delta} \right)^2 (\text{phase space}). \quad (2.70)$$

Table 2.8 shows some results from measurement of  $R$  for various final states measured at LEAR in proton-antiproton annihilation at rest [?]. The  $Z$  values obtained from these data are much larger than what have been observed previously [?]. The  $\phi$  enhancement in these data are much larger than in  $\pi p$ ,  $pp$ , or higher energy  $p\bar{p}$  annihilation. The large enhancement of  $\phi\pi$  production appears to be restricted to S-wave with no large deviation from naive OZI predictions in any P-wave annihilation channel.

A theoretical model to explain the LEAR results is the Polarized Vacuum model [?], which takes into account the following :

Final state	$R \cdot 10^3$	$ Z \%$	Experiment
$\phi\gamma$	$250 \pm 89$	$42 \pm 8$	Crystal barrel
$\phi\pi^0$	$96 \pm 15$	$24 \pm 2$	Crystal barrel
$\phi\pi^-$	$83 \pm 25$	$22 \pm 4$	Bubble chamber
$\phi\pi^+$	$110 \pm 15$	$26 \pm 2$	Obelix
$\phi\rho$	$6.3 \pm 1.6$	$1.4 \pm 1.0$	Asterix
$\phi\rho$	$7.5 \pm 2.4$	$2.1 \pm 1.2$	Asterix
$\phi\omega$	$19 \pm 7$	$7 \pm 4$	Asterix

Table 2.8: Measurement of OZI violation at LEAR.  $R$  and  $Z$  are defined in equation 2.70 (from [?]).

- Sum rules indicate that the vacuum is strange, that is, the density of strange quarks in the vacuum is high

$$\langle 0 | s\bar{s} | 0 \rangle = (0.8 \pm 0.1) \langle 0 | q\bar{q} | 0 \rangle . \quad (2.71)$$

The vacuum pairs are in  $J^{PC} = 0^{++}, S = 1, {}^3P_0$  triplet state .

- The masses of  $J^{PC} = 0^{-+}$  mesons are small at hadronic scale,  $M(\pi) \ll M(\rho)$  etc., from this one concludes that there exists a strong effective attraction between quark and antiquark in S-wave, spin singlet  ${}^1S_0, J^{PC} = 0^{-+}$  state.

When the basic  $|uud\rangle$  proton state is immersed in the vacuum there will be a strong attraction in the  $S = 0$  state of an  $\bar{s}q$  pair, which will generate an admixture of negatively polarized  $s\bar{s}$  pairs, with opposite spin of the proton. This result is consistent with the deep inelastic scattering results from above. The implications for  $p\bar{p} \rightarrow \phi X$  is that the shakeout diagram is forbidden, since the vacuum pair has  $J^{PC} = 0^{++}$ , while the  $\phi$  meson has  $J^{PC} = 1^{--}$ . The rearrangement diagram is favoured. It has been observed that  $\phi$  production is favoured from spin triplet  $p\bar{p}$  states, as predicted from this model.

The expected cross-section for the reaction  $p\bar{p} \rightarrow \phi\phi$  if it proceeds through the strange component of the proton ( $X = \phi$ ) is:

$$\sigma(p\bar{p} \rightarrow \phi\phi) \approx |z|^4 \sigma(p\bar{p} \rightarrow \omega\omega) \approx 0.8 \mu\text{b}, \quad (2.72)$$

where we have set  $|z|^2 \approx 4\%$ , and  $\sigma(p\bar{p} \rightarrow \omega\omega)$  to be about 0.5 mb. For the rearrangement to take place, the two protons must be in spin triplet,  $S_{p\bar{p}} = 1$ . The two  $\phi$  mesons will be produced with parallel spins,  $S_{\phi\phi} = 2$ , and for production close to threshold be in relative S wave. If the  $\phi\phi$  system is produced through the strangeness content of the nucleon, it will have quantum numbers  $J^{PC} = 2^{++}$ .

### Two meson intermediate states

The requirement that the S-matrix is unitary [?],  $S^\dagger S = 1$ , leads to the unitarity relation

$$\text{Im}M(i \rightarrow f) = \sum_n M^*(f \rightarrow n)M(i \rightarrow n)\delta(E - E_n), \quad (2.73)$$

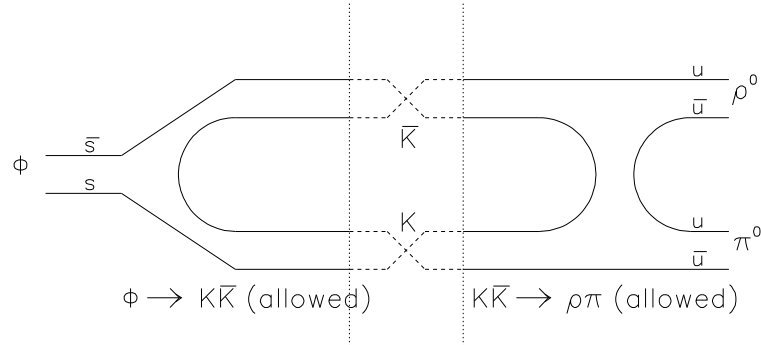


Figure 2.23: The reaction  $\phi \rightarrow K\bar{K} \rightarrow \pi^- \rho$ .

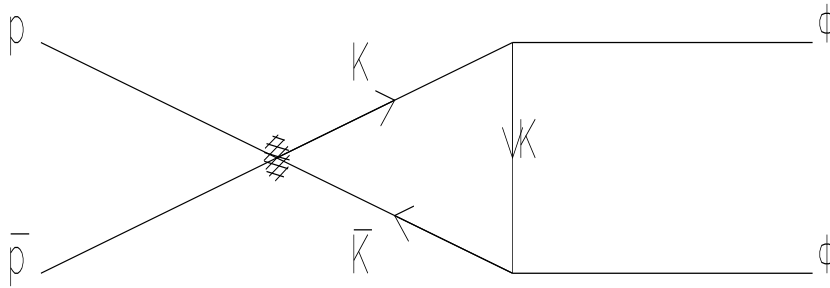


Figure 2.24: Triangle diagram for the reaction  $p\bar{p} \rightarrow K\bar{K} \rightarrow \phi\phi$ .

where the sum is over all intermediate states. For example, the OZI forbidden  $\phi \rightarrow \rho\pi$  could go through the intermediate state  $K\bar{K}$  as shown in figure 2.23 which is a combination of two OZI allowed processes. It is not presently understood how the OZI rule fits with unitarity. To get the necessary OZI suppression it seems necessary to invoke some kind of cancellation effect that only appears when the reaction  $i \rightarrow f$  is OZI-suppressed and not when it is OZI allowed. At present it is not known how to calculate this from first principles.

The calculated contribution to the  $p\bar{p} \rightarrow \phi\phi$  cross section from two meson intermediate states, like  $p\bar{p} \rightarrow K\bar{K} \rightarrow \phi\phi$  (figure 2.24) varies with energy from  $0.6 \mu\text{b}$  to  $3.0 \mu\text{b}$  (figure 2.25).

The reaction will only take place through the  $K\bar{K}$  intermediate state if the initial spin  $S_{p\bar{p}} = 1$ . Bose statistics requires the final state to have  $S_{\phi\phi} = 0$  or 2 [?].

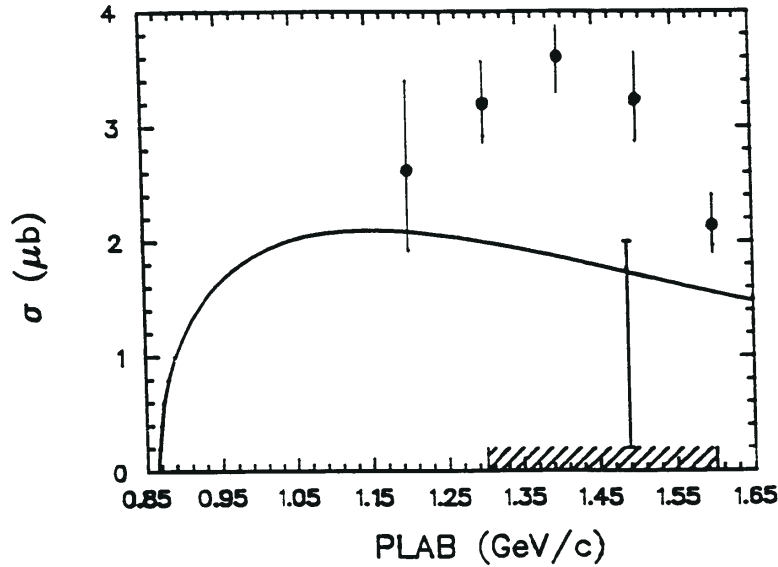


Figure 2.25: Energy dependence of the total cross section for  $p\bar{p} \rightarrow \phi\phi$  by the  $K\bar{K}$  intermediate state (from [?]).

### Gluonic or other resonant states

The process shown in figure 2.20 is suppressed by a factor  $\alpha_s^2$ , or  $1/N$  according to the large  $N_C$  expansion, but if a narrow glueball exists, then it might resonate at some invariant mass of the  $\phi\phi$  system, which will result in a strong coupling in the vicinity of  $\sqrt{s}$  for the resonance. However, as we have seen, there are many other processes that might possibly mask this one, so that glueballs, even if produced in this reaction, might be difficult to detect.

It is also possible that the system could resonate in  $q\bar{q}$  to form ordinary mesonic resonances, or in  $q\bar{q}q\bar{q}$  to form a four-quark molecule, or form a hybrid state like  $q\bar{q}g$ .

#### 2.4.2 Previous measurements of $p\bar{p} \rightarrow \phi\phi$

The reaction  $p\bar{p} \rightarrow \phi\phi$  has been measured twice before. An ANL bubble chamber experiment measured a  $p\bar{p} \rightarrow K^+K^-K^+K^-$  cross-section of  $3.8 \pm 1.7 \mu b$  over a range of incident momenta from 1.6 to 2.2 GeV/c, collecting six events in total. The  $\phi\phi$  production cross-section was estimated to be about  $2 \mu b$  [?]. The CERN ISR experiment R704 found 83 events of the type  $p\bar{p} \rightarrow \phi\phi \rightarrow K^+K^-K^+K^-$  at a centre of mass energy  $\sqrt{s} = 2.989$  GeV. After correcting for the branching fraction  $BR(\phi \rightarrow K^+K^-) = 0.495$ , a cross section  $\sigma(p\bar{p} \rightarrow \phi\phi) = 25.0 \pm 8.3$  nb was obtained [?].



### 2.4.3 Results from $\phi\phi$ production experiments

Several experiments have performed measurements on hadronic production of  $\phi\phi$  pairs:

- The reaction  $\pi^- p \rightarrow \phi\phi n$  has been measured in several experiments at the MPS facility at BNL-AGS using a 22 GeV pion beam [?].
- The OMEGA spectrometer at CERN-SPS also measured  $\pi^- p \rightarrow \phi\phi n$ , using a 16 GeV/c beam [?].
- The experiment WA67, also using the OMEGA spectrometer at CERN-SPS, measured the inclusive reaction  $\pi^- Be \rightarrow \phi\phi X$  [?, ?].
- The experiment E623 studied the reaction  $pN \rightarrow \phi\phi X$ , using a 400 GeV/c proton beam from the FNAL main ring [?].
- The reaction  $K^- p \rightarrow \phi\phi\lambda$  was measured at SLAC using the LASS spectrometer in an 11 GeV/c beam [?].
- Central production of neutral states was studied with the experiment WA76 using the OMEGA spectrometer [?]. Both  $\pi^+ p \rightarrow \pi^+(X^0)p$  at 85 GeV/c and  $pp \rightarrow p(X^0)p$  at 85 GeV/c and 300 GeV/c were studied. These processes are presumed to take place by double Pomeron exchange. Among the final states studied were those with  $X^0 = \phi\phi, K^+K^-\phi$ , and  $K^+K^-K^+K^-$ .

The data obtained in  $\phi\phi$  hadronic production up to about 2.5 GeV/c invariant mass were all consistent with the production mostly taking place in  $J^P = 2^+$  wave, at least they were not inconsistent with this assignment. Some of the experiments (BNL-CCNY, WA76, WA67) found evidence for broad ( $\Gamma \approx 100 - 200$  MeV) resonances. These experiments also found that the ratio of  $\phi\phi$  to  $\phi KK$ , and  $4K$  final states were larger than expected from the OZI rule. The most outstanding results were the result from the BNL experiments, where several glueball resonances were claimed.

#### The $g_T$ resonances

The BNL/CCNY group studied the following reactions in four generations of experiments [?]:

$$\begin{aligned} \pi^- p &\rightarrow \phi\phi n, \\ \pi^- p &\rightarrow \phi K^+ K^- n, \\ \pi^- p &\rightarrow K^+ K^- K^+ K^- n. \end{aligned} \tag{2.74}$$

The  $\phi$  mesons were detected from the decay  $\phi \rightarrow K^+ K^-$ , so the final state measured was always  $K^+ K^- K^+ K^- n$ . Figure 2.26 shows the invariant mass of a pair of  $K^+ K^-$ , against the other pair (two mass combinations for each event). In this plot the density of  $\phi\phi$  events is seen to be larger than  $K^+ K^- K^+ K^-$  by a factor of 1000, and a factor 50 larger than  $K^+ K^- \phi$ . This is in disagreement with the OZI rule, since  $\pi^- p \rightarrow \phi\phi n$  is OZI forbidden,

Figure 2.26: Scatterplot of  $K^+K^-$  effective masses in the reaction  $\pi^-p \rightarrow K^+K^-K^+K^-n$  (from [?]).

(figure 2.11), while  $\pi^-p \rightarrow \phi K^+K^-n$  and  $\pi^-p \rightarrow K^+K^-K^+K^-n$  are OZI allowed (figure 2.28). The experiment found 6658  $\pi^-p \rightarrow \phi\phi n$  events which were analysed with a partial wave analysis including all 114 waves with  $J \leq 6$ , and  $L \leq 4$ . Three sets of partial waves, all with  $J^{PC} = 2^{++}$  were found to describe all the data: The unitary K-matrix formalism was used to fit the partial waves. Three K-matrix poles were necessary to fit the data. This corresponds to the following Breit-Wigner resonance parameters (figure 2.27).

$$\begin{aligned} M_1 &= 2011 \pm 69 \text{ MeV}, \Gamma_1 = 202 \text{ MeV} \pm 6 \text{ MeV} \text{ ( S wave, 45\% of data),} & (2.75) \\ M_2 &= 2297 \pm 28 \text{ MeV}, \Gamma_2 = 149 \text{ MeV} \pm 41 \text{ MeV} \text{ ( D wave, 20\% of data),} \\ M_3 &= 2339 \pm 55 \text{ MeV}, \Gamma_3 = 319 \text{ MeV} \pm 75 \text{ MeV} \text{ ( D wave, 35\% of data),} \end{aligned}$$

The apparent breakdown of the OZI rule led to the claim that the three resonances must be tensor glueballs [?]. They were labelled  $g_T$  ( $f_2$  by the Particle Data Group [?]). A glueball would be expected to have a strong coupling in spite of OZI suppression. In section 2.3 the debate about whether such double hairpin processes are really suppressed was mentioned. Failure to detect these resonances in other gluon-rich channels (section 2.4.4), as well as their widths, which are broader than expected for glueballs, makes the glueball interpretation less likely. One possible explanation of these states could be that the process proceeds through the strange sea quark component of the proton (figure 2.29), and that the  $g_T(f_2)$  resonances are  $s\bar{s}$  excited quarkonium.

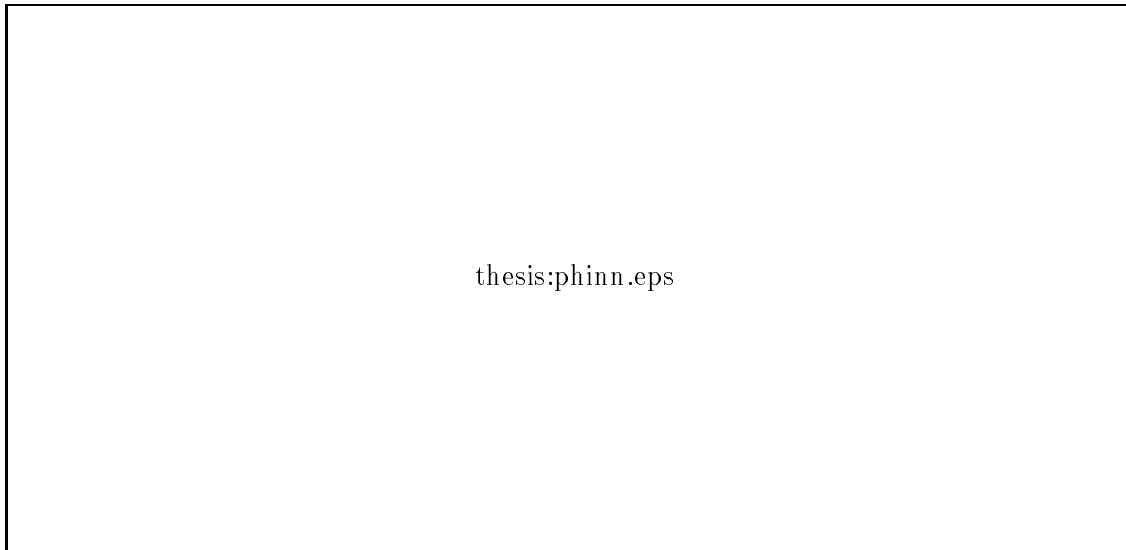


Figure 2.27: Results from  $\pi^- p \rightarrow \phi\phi n$ . a) Acceptance corrected  $\phi\phi$  mass spectrum, b) intensity for the three  $J^{PC} = 2^{++}$  waves (from [?]).

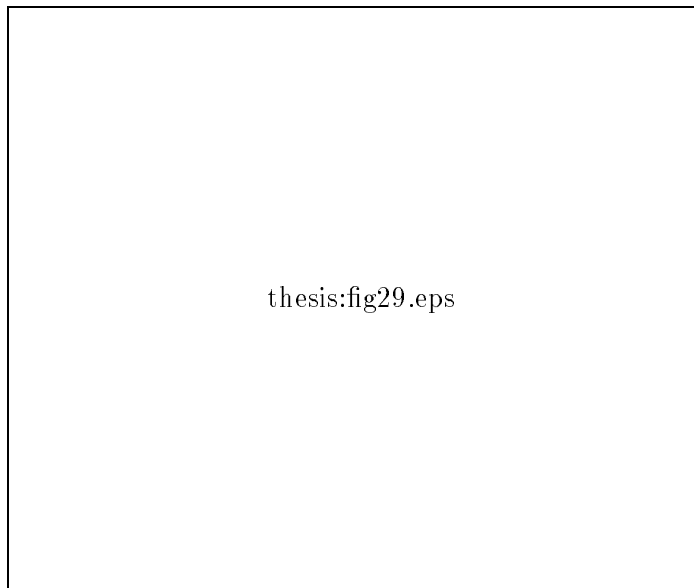


Figure 2.28: The reactions  $\pi^- p \rightarrow K^+ K^- K^+ K^- n$  (top) and  $\pi^- p \rightarrow \phi K^+ K^- n$  (bottom), which are not OZI-suppressed.



Figure 2.29: *The reaction  $\pi^-p \rightarrow \phi\phi n$  through strangeness component of the proton.*

#### 2.4.4 $J/\psi$ decay

Two experiments have studied radiative  $J/\psi$  decay,  $J/\Psi \rightarrow \phi\phi\gamma$ , following the resonance formation  $e^+e^- \rightarrow J/\Psi$ . Both  $K^+K^-K^+K^-$  and  $K^+K^-K_S K_L$  final states were studied. The experiment DM2 at Orsay-DCI [?] found an enhancement in the  $\phi\phi$  invariant mass spectrum near threshold, consistent with resonance parameters

$$M = 2238 \text{ MeV} \pm 7 \text{ MeV}, \Gamma = 80 \text{ MeV} \pm 30 \text{ MeV}, \quad (2.76)$$

while the experiment Mark III at SLAC-SPEAR [?] found a resonance structure with

$$M = 2222 \text{ MeV} \pm 27 \text{ MeV}, \Gamma = 150 \text{ MeV} \pm 30 \text{ MeV}. \quad (2.77)$$

Both experiments found that the resonance state had dominantly  $J^P = 0^-$ . The results from these experiments are in contrast to what is observed in hadronic  $\phi$  pair production. It is interesting to speculate why these processes show so different characteristics. Possibly glueballs can be produced in both  $J/\Psi$  decay and hadronic production, but the hadronic  $\phi\phi$  production could be dominated by other processes (section 2.3.2), and thus render the glueballs invisible.

#### 2.4.5 The $\xi$ resonance

An interesting resonance in the mass region investigated by JETSET is the narrow state  $f_4(2230)(\xi(2230))$  with [?]

$$M = 2225 \text{ MeV} \pm 6 \text{ MeV}, \Gamma = 38_{-13}^{+15}. \quad (2.78)$$

This resonance might have been observed in several experiments, while others have searched for it with no success.

- The first evidence for this state came from the MarkIII experiment at Spear [?] in radiative  $J/\psi$  decays,  $J/\Psi \rightarrow \gamma\xi$ , with the  $\xi$  subsequently decaying to  $K^+K^-$  or  $K_0^S K_0^S$ .  $M = 2231 \pm 13 \text{ MeV}$ ,  $\Gamma = 22 \pm 23 \text{ MeV}$ , and  $J^{PC} = \text{even}^{++}$ . No signal was seen in other two-meson decay modes.

- The LASS Spectrometer at SLAC investigated the reactions  $K^-p \rightarrow K_s K_s \Lambda$ , and  $K^-p \rightarrow K^- K^+ \Lambda$ . A resonance with  $M = 2209 \pm 16$  MeV,  $\Gamma = 60 \pm 82$  MeV, and likely  $J^{PC} = 4^{++}$  was found [?, ?].
- The DM2 experiment did not find evidence for the  $\xi$  resonance by searching the same production and decay channels as MarkIII [?].
- The experiments PS170 [?] and BNL-AGS [?] looked for direct formation of the  $\xi(2230)$  in  $p\bar{p}$  interactions. No evidence for  $\xi$  formation was found.
- A search for the  $\xi$  in  $p\bar{p} \rightarrow K_s K_s$  in the experiment PS185 at LEAR also gave a negative result [?].
- Production of neutral hadrons in  $\pi^- p \rightarrow X^0 n$ , decaying into multi-photon final states, was studied by GAMS(CERN-IHEP). A resonant structure was seen with  $M = 2220 \pm 10$  MeV, decaying into  $\eta\eta'$  and with  $J \geq 2$  [?].
- The BES experiment has found evidence for the  $\xi$  in  $J/\Psi$  radiative decays, with the  $\xi$  decaying to  $K^+ K^-$ ,  $K_0^S K_0^S$ ,  $p\bar{p}$ , and  $\pi^+ \pi^-$  [?].

The  $J^{PC}$  for this resonance is either  $2^{++}$ , or  $4^{++}$ , and it has isospin zero. A possible interpretation is that it is a  ${}^3F_2$ , or  ${}^3F_4$   $s\bar{s}$  state, the mass of these states should lie in the  $\xi$  mass region (section 2.2.2), and it has also been predicted that their widths should be particularly small, since they have a limited number of decay modes.

The  $\xi$  could also be a glueball, as pointed out in section 2.2.12. The results from BES favour this interpretation, since approximately flavour symmetric couplings are observed [?] :

$J/\Psi \rightarrow \gamma K_s^0 K_s^0$  :

$$\begin{aligned} M(\xi) &= 2232_{-16}^{+25} \pm 10 \text{ MeV}, \\ ?(\xi) &= 20_{-16}^{+25} \pm 10 \text{ MeV}, \\ Br(J/\Psi \rightarrow \gamma\xi)Br(\xi \rightarrow K_s K_s) &= (2.7_{-0.9}^{+1.1} \pm 1.0) \cdot 10^{-5}. \end{aligned} \quad (2.79)$$

$J/\Psi \rightarrow \gamma K^+ K^-$  :

$$\begin{aligned} M(\xi) &= 2230_{-7}^{+6} \pm 12 \text{ MeV}, \\ ?(\xi) &= 20_{-15}^{+20} \pm 12 \text{ MeV}, \\ Br(J/\Psi \rightarrow \gamma\xi)Br(\xi \rightarrow K^+ K^-) &= (3.3_{-1.3}^{+1.6} \pm 1.1) \cdot 10^{-5}. \end{aligned} \quad (2.80)$$

$J/\Psi \rightarrow \gamma p\bar{p}$  :

$$\begin{aligned} M(\xi) &= 2235 \pm 4 \pm 5 \text{ MeV}, \\ ?(\xi) &= 15_{-9}^{+12} \pm 9 \text{ MeV}, \\ Br(J/\Psi \rightarrow \gamma\xi)Br(\xi \rightarrow p\bar{p}) &= (1.5_{-0.5}^{+0.6} \pm 0.5) \cdot 10^{-5}. \end{aligned} \quad (2.81)$$

$J/\Psi \rightarrow \gamma \pi^+ \pi^-$  :

$$\begin{aligned} M(\xi) &= 2235_{-6}^{+4} \pm 10 \text{ MeV}, \\ ?(\xi) &= 19_{-11}^{+13} \pm 12 \text{ MeV}, \\ Br(J/\Psi \rightarrow \gamma\xi)Br(\xi \rightarrow \pi^+ \pi^-) &= (5.6_{-1.6}^{+1.8} \pm 1.4) \cdot 10^{-5}. \end{aligned} \quad (2.82)$$

Figure 2.30: *Invariant mass spectra for  $\pi^+\pi^-$ ,  $K^+K^-$ ,  $K_s^0K_s^0$ , and  $p\bar{p}$  in  $J/\psi$  radiative decays from the BES experiment. From [?].*

Note that the  $\xi$  is observed to couple both to  $p\bar{p}$  and  $K_s K_s$ . It can be seen clearly in both of the invariant mass spectra (figure 2.30). This should be compared to the results from PS185 [?] where no evidence for the  $\xi$  was found in  $p\bar{p} \rightarrow K_s K_s$ , either in the excitation function or in the angular distributions. An upper limit  $Br(p\bar{p} \rightarrow \xi)Br(\xi \rightarrow K_s K_s) \approx 2 \cdot 10^{-5}$  was found. This indicates that both of these branching fractions are of the order of less than one percent.

## 2.5 The JETSET physics Program

The JETSET Physics program involved the spectroscopy of hadronic states, including possible glueballs, hybrids, and multiquark states in the mass region 1.96 to 2.4 GeV. Emphasis was put on the exclusive reactions  $p\bar{p} \rightarrow \phi\phi$ ,  $\omega\omega$ , and  $\phi\omega$ , and also on  $p\bar{p} \rightarrow K\bar{K}$ , using antiprotons from CERN's LEAR with momentum up to 2 GeV/c. Of special interest was the OZI-forbidden reaction  $p\bar{p} \rightarrow \phi\phi$ , supposedly a good source for glueballs. Also the inclusive reaction  $p\bar{p} \rightarrow \phi\phi\pi^0$  was interesting, since exotic quantum numbers was possible for the the  $\phi\phi$  system this way [?].

As described in the previous section, interesting resonances have been observed by other experiments in the  $\phi\phi$  system in the relevant energy range, both in production experiments and in  $J/\Psi$  decay. We also wanted to look for the  $\xi$  resonance observed by BES and others (section 2.4.5). The detector and the experimental technique are described in the next chapter. The  $\phi$  mesons were detected in their decay  $\phi \rightarrow K^+ K^-$  (branching fraction 49.1 % according to [?]), and the detector was specially designed to detect the reaction  $\bar{p}p \rightarrow \phi\phi \rightarrow 4K$ .

### 2.5.1 $4K$ final states

Four kaon final state can be obtained from proton-antiproton annihilation in the three following ways:

- $p\bar{p} \rightarrow 4K^\pm$  (nonresonant),
- $p\bar{p} \rightarrow \phi K K \rightarrow 4K^\pm$ ,
- $p\bar{p} \rightarrow \phi\phi \rightarrow 4K^\pm$ ,

shown in figure 2.31<sup>3</sup>. According to the isobar model [?] the reaction  $\bar{p}p \rightarrow 4K^\pm$  will proceed mostly through two meson intermediate states. For the four kaon final state near threshold this corresponds to  $2\phi$  production, but also  $f_0(980)$ ,  $f_2(1270)$ ,  $f_0(1300)$ , and  $a_2(1320)$ .

The reaction  $\bar{p}p \rightarrow \phi\phi \rightarrow 4K$  should be suppressed relative to the processes with intermediate states consisting of nonstrange mesons because of the OZI rule. According to the Particle Data Group [?] the  $f_0, f_2$ , and  $a_2$  meson resonances have much larger width than the  $\phi$ , and they will not be distinguishable from  $4K$  phase space.

Only reactions going through two  $\phi$  mesons will be OZI-suppressed, so  $\bar{p}p \rightarrow \phi\phi \rightarrow 4K$  is

---

<sup>3</sup>Events from these reactions will frequently be denoted just as  $4K, \phi K K$ , and  $\phi\phi$  events, respectively, in the rest of the text.

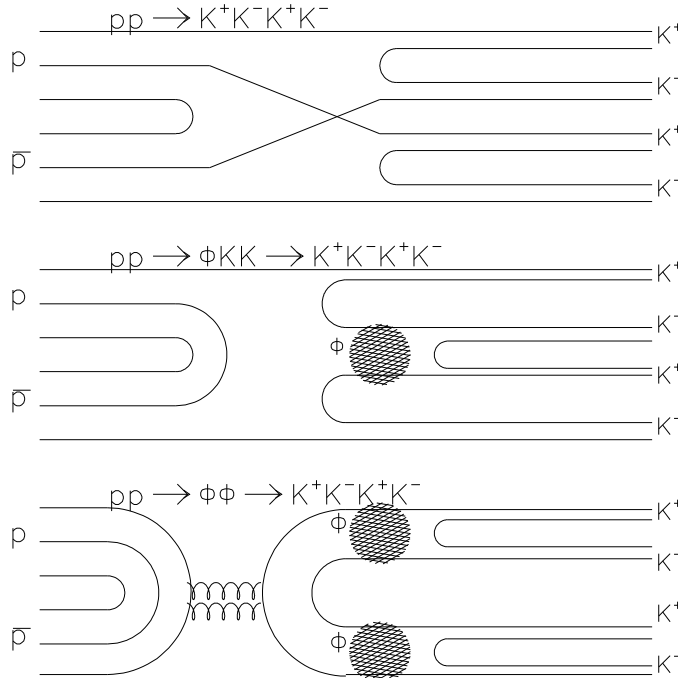


Figure 2.31: Reactions with four kaon final states in proton antiproton annihilations.

expected to have a small cross section compared to  $\bar{p}p \rightarrow 4K^\pm$ .

The experiment measured the cross section for the three reactions as a function of incident beam momentum. The total cross section for each value of the beam momentum, or total energy  $\sqrt{s}$ , was calculated from the formula

$$\sigma = \frac{N_{events}}{A \cdot L}. \quad (2.83)$$

$N_{events}$  is the total number of  $\phi\phi$ ,  $\phi KK$ , or  $4K$  events, at the particular beam momentum setting, with the background subtracted.

$A$  is the acceptance times efficiency of the detector, trigger and analysis, and  $L$  is the integrated luminosity at that beam momentum.

One way to distinguish between the  $\phi\phi$ ,  $\phi KK$ , and  $4K$  events is to study the invariant mass plots (Goldhaber plots) of one kaon pair versus the other. Since the charges of the particles are unknown, three combinations are possible:

$(K_1, K_2)vs(K_3, K_4)$ ,  $(K_1, K_3)vs(K_2, K_4)$ , and  $(K_1, K_4)vs(K_2, K_3)$ . Figure 2.32 show what these plots look like for the three reactions using Monte Carlo events. Also shown are the projection of the Goldhaber plot when the other entry lies within  $m_\phi \pm 20$  MeV (within the two “ $\phi$  bands” indicated in the scatterplots). For  $\phi\phi$  events this removes most of the combinatorial background and leaves only the  $\phi$  peak. The projections of the Goldhaber plot outside the  $\phi$  bands are shown in figure 2.33. The  $\phi$  peak is seen only for the  $\phi KK$  events.



clearpage

### 2.5.2 Measurement of $\bar{p}p \rightarrow \phi\phi \rightarrow 4K$

The following are the most important quantities to be measured in the reaction  $\bar{p}p \rightarrow \phi\phi \rightarrow 4K$  by JETSET:

- The total cross section for the reaction  $\bar{p}p \rightarrow \phi\phi$  at each beam momentum, or total CMS energy.
- The differential cross section, or angular distribution, of the  $\phi$  mesons.
- The angular distribution of the four K mesons.

From this, information about possible resonances and their quantum numbers can be obtained.

### Resonances

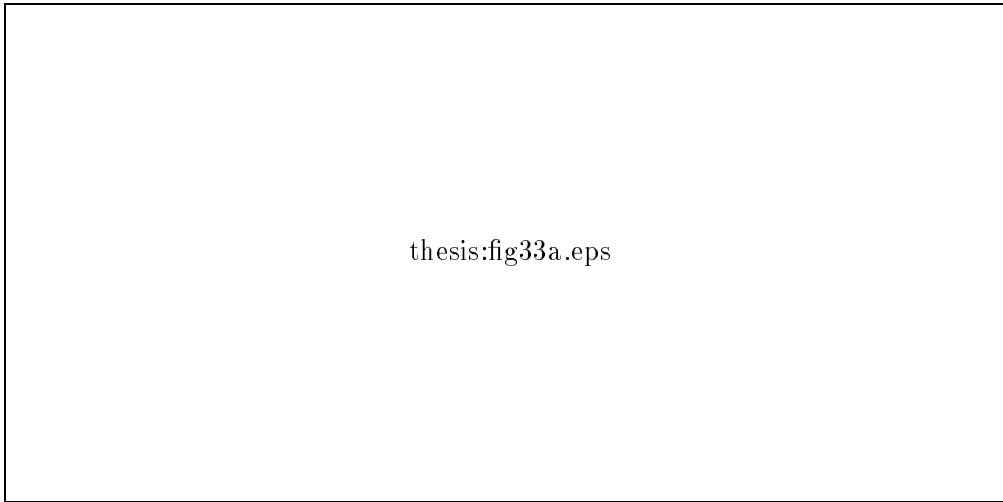
One of the most important physics goals of the JETSET experiment was the search for strong interaction resonances in the reaction  $\bar{p}p \rightarrow \phi\phi$ . Such resonances correspond to poles in the hadronic scattering amplitude near the real (physical) axis. Each pole corresponds to an unstable bound state whose decays to lighter hadrons is responsible for the singularity, and can be assigned unique quantum numbers for conserved quantities such as spin ( $J$ ), parity ( $P$ ), charge-conjugation parity ( $C$ ), isospin ( $I$ ), strangeness ( $S$ ), and for  $S=0$ ,  $G$ -parity ( $G$ ). In a formation experiment like JETSET, these resonances would enter as intermediate states  $X$  in the reaction  $p\bar{p} \rightarrow X \rightarrow \phi\phi$ . The presence of  $X$  would be indicated by some special behavior of the reaction parameters when  $s = M_X^2$ , including a peak in the total cross section and a phase shift passing through  $90^\circ$  [?]. In general there may be more than one  $X$  contributing to the reaction at a given incident  $\bar{p}$  momentum, in which case the amplitude from each pole must be added coherently.

The total cross section for an inelastic reaction with two particles in the initial state and two particles in the final state, averaged over spin orientations and integrated over scattering angles can be expressed as [?, ?]:

$$\sigma_{fi} = \sum_J \frac{\pi}{k^2} \frac{(2J+1)}{(2S_1+1)(2S_2+1)} \sum_{LlSs} |S_{cls,CLS}^J(k)|^2, \quad (2.84)$$

where  $k$  is the momentum of either of the two initial state particles in the centre-of-mass system,  $S_1$  and  $S_2$  are the spins of the two initial state particles,  $J$  is the total angular momentum,  $S_{cls,CLS}^J(k)$  is the S-matrix element,  $L, l, S, s$  are initial and final state orbital angular momenta and spin, and  $C, c$  signify other channel quantum numbers.

This is a sum over the contributions from all the possible partial waves, where each wave is denoted by its total angular momentum,  $J$ , and the initial and final states spin,  $S, s$ , and orbital angular momenta  $L, l$ .



thesis:fig33a.eps

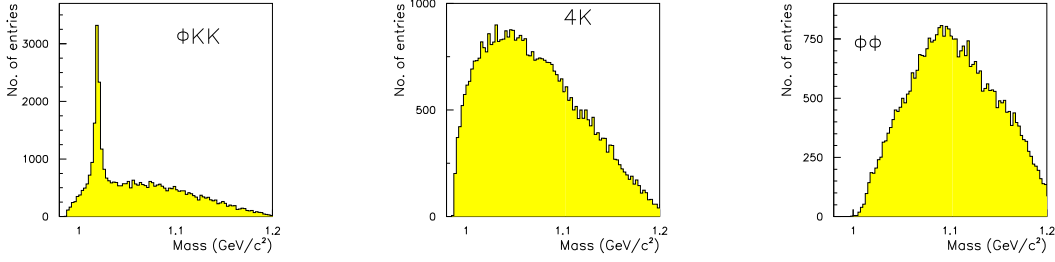


Figure 2.33: Invariant mass, when other is not  $\phi$  (the generated momenta from Monte Carlo simulated events are used).

The possible quantum numbers for partial waves in the reaction  $\bar{p}p \rightarrow \phi\phi$  are given in table 2.11.

The S-matrix elements are parameterized as

$$S_{cls,CLS}^J(k) = S_{fi} = \eta_{fi} e^{2i\delta_{fi}} \quad (2.85)$$

where  $\eta_{fi}$  is the absorption parameter and  $\delta_{fi}$  the phase angle.

The partial wave analysis finds the magnitude and phase of each partial wave, the interference between the waves and the interference with non-resonant background.

If a given reaction has a predominant contribution to the cross section from a single state  $J$  and a given  $L, l, S, s$ , then :

$$\sigma_{fi} = \frac{\pi}{k^2} \frac{(2J+1)}{(2S_1+1)(2S_2+1)} |S_{cls,CLS}^J(k)|^2. \quad (2.86)$$

If the reaction goes through a resonance in this partial wave the contribution to the total cross section from this wave has the form [?, ?]:

$$\sigma_{fi} = \frac{\pi}{k^2} \frac{(2J+1)}{(2S_1+1)(2S_2+1)} \frac{?_i ?_f}{(E - E_0)^2 + ?^2/4}, \quad (2.87)$$

where  $?_i, ?_f$ , and  $?$  are the partial decay widths into initial and final states, and the total resonance width. This is the Breit-Wigner formula for a resonance with mass  $m = E_0$ , and half width  $?/2$ .

In addition, the phase should move rapidly from 0 to 180 degrees in the vicinity of a resonance, going through 90 degrees at mid resonance [?]. This phase movement can be observed by taking the phase difference between the resonating wave and another, nonresonating, reference wave.

### Available quantum numbers for transitions

Conservation of angular momentum, parity and  $C$ -parity, and the Bose statistics for  $\phi$  mesons, puts a limit on the values of total angular momentum  $J$ , and spin and orbital angular momentum in the initial and final state, for the reaction  $p\bar{p} \rightarrow \phi\phi$ .

L	S	$J^{PC}$	$^{2S+1}L_J$
0	0	$0^{-+}$	$^1S_0$
0	1	$1^{--}$	$^3S_1$
1	0	$1^{+-}$	$^1P_1$
1	1	$0^{++}$	$^3P_0$
1	1	$1^{++}$	$^3P_1$
1	1	$2^{++}$	$^3P_2$
2	0	$2^{-+}$	$^1D_2$
2	1	$1^{--}$	$^3D_1$
2	1	$2^{--}$	$^3D_2$
2	1	$3^{--}$	$^3D_3$
3	0	$3^{+-}$	$^1F_3$
3	1	$2^{++}$	$^3F_2$
3	1	$3^{++}$	$^3F_3$
3	1	$4^{++}$	$^3F_4$
4	0	$4^{-+}$	$^1G_4$
4	1	$3^{--}$	$^3G_3$
4	1	$4^{--}$	$^3G_4$
4	1	$5^{--}$	$^3G_5$

Table 2.9: States available to a proton-antiproton pair, when the orbital angular momentum is 0 to 4. The isospin can be 0 or 1, and the  $G$ -parity  $\pm 1$ . From [?].

The possible quantum numbers for a  $p\bar{p}$  combination are given in table 2.9. The total spin  $S$  can be 0 or 1, the parity is  $P = (-1)^{L+1}$ , the  $C$  and  $G$  parities are  $C = (-1)^{L+S}$  and  $G = (-1)^{L+S+I}$ , and the isospin  $I$  is either 0 or 1. These quantum numbers are the same as those that are available for a  $q\bar{q}$  pair (table 2.1).

The final  $\phi\phi$  state consists of two bosons and must be a totally symmetric product wave function of space, spin and isospin. The  $\phi$  meson has  $I = 0$ , and  $J^{PC} = 1^{--}$ , so the total spin can be  $S=0, 1$ , or  $2$ , with  $L$ =even, odd, even, and parity  $P = (-1)^L$ . Both  $C$  and  $G$  parities are positive. This gives the available states listed in table 2.10.

Then conservation of total angular momentum, parity and  $C$ -parity give the possible transitions for  $p\bar{p} \rightarrow \phi\phi$  listed in table 2.11.

L	S	$J^{PC}$	$^{2S+1}L_J$
0	0	$0^{++}$	$^1S_0$
0	2	$2^{++}$	$^5S_2$
1	1	$0^{-+}$	$^3P_0$
1	1	$1^{-+}$	$^3P_1$
1	1	$2^{-+}$	$^3P_2$
2	0	$2^{++}$	$^1D_2$
2	2	$0^{++}$	$^5D_0$
2	2	$1^{++}$	$^5D_1$
2	2	$2^{++}$	$^5D_2$
2	2	$3^{++}$	$^5D_3$
2	2	$4^{++}$	$^5D_4$
3	1	$2^{-+}$	$^3F_2$
3	1	$3^{-+}$	$^3F_3$
3	1	$4^{-+}$	$^3F_4$

Table 2.10: States available to a  $\phi\phi$  pair when the orbital angular momentum is 0 to 4. The isospin is always 0.  $L+S$  is always even, and  $C=G=+1$ . From [?].

$p\bar{p}$	$J^{PC}$	$\phi\phi$
$^3P_0$	$0^{++}$	$^1S_0, ^5D_0$
$^1S_0$	$0^{-+}$	$^3P_0$
$^3P_1$	$1^{++}$	$^5D_1$
$^3P_2, ^3F_2$	$2^{++}$	$^5S_2, ^1D_2, ^5D_2, ^5G_2$
$^1D_2$	$2^{-+}$	$^3P_2, ^3F_2$
$^3F_3$	$3^{++}$	$^5D_3, ^5G_3$
$^3F_4, ^3H_4$	$4^{++}$	$^5D_4, ^1G_4, ^5G_4, ^5I_4$
$^1G_4$	$4^{-+}$	$^3F_4, ^3H_4$

Table 2.11: The first available transitions for  $p\bar{p} \rightarrow \phi\phi$ . From [?].

Figure 2.34: *Angles in  $\bar{p}p \rightarrow \phi\phi$  in the centre-of-mass system. From [?].*

#### Angles in $p\bar{p} \rightarrow \phi\phi \rightarrow 4K$

When studying angular distributions in the reaction  $\bar{p}p \rightarrow \phi\phi \rightarrow 4K$ , the following angles, defined in figures 2.34 and 2.35, are of interest:

- $\Theta, \Phi$ , polar and azimuthal angles for one of the  $\phi$  mesons in the centre of mass system of the proton and antiproton.
- $\theta_1, \phi_1, \theta_2, \phi_2$ , polar and azimuthal angles for one of the  $K$ -mesons in the rest frame of each  $\phi$  meson.
- It is also useful to define  $\chi = \phi_1 + \phi_2$ , the azimuthal angle between the decay planes of the  $\phi$ 's.

Figure 2.35: *Angles in  $\bar{p}p \rightarrow \phi\phi \rightarrow 4K$ , showing the decay of the  $\phi\phi$  pair in the rest frame of one of the  $\phi$ s. Only the positive kaons are shown. From [?].*

Important information concerning the existence and nature of intermediate resonances can be inferred by studying the angular distributions of the outgoing  $K$ -mesons.

If the reaction goes through an intermediate state  $X$ ,  $p\bar{p} \rightarrow X \rightarrow \phi\phi \rightarrow 4K^\pm$ , the angular distributions of the four outgoing  $K$ -mesons will depend on the spin and parity of the kaons, the  $\phi$  mesons, and the intermediate state  $X$ , and the dynamics of the transitions.

Apart from any assumptions concerning hypothetical intermediate resonances  $X$ , the final-state angular distributions can be decomposed into components of definite orbital angular momentum, spin, and total angular momentum in the final  $\phi\phi$  state. In regions where the total cross section indicates resonant behaviour, one can then look in the partial wave decomposition for a single combination of  $J, P, C$  that is responsible for the peak.

### Spin and parity determination in $\phi\phi$ decay

A simple connection between the angle  $\chi$  and the spin and signature of a resonant state decaying to  $\phi\phi$  can be found by integrating the angular distributions. In the helicity basis the angular distribution for a definite  $J$  value is given by [?, ?]

$$\begin{aligned}
 I(\Theta, \Phi, \theta_1, \phi_1, \theta_2, \phi_2) = & \\
 \sum_{M, M', \lambda_1, \lambda_2, \lambda'_1, \lambda'_2} & \rho_{MM'} D_{M, \lambda}^{J*}(\Phi, \Theta, -\Phi) D_{M', \lambda'}^J(\Phi, \Theta, -\Phi) A_{\lambda_1, \lambda_2} A_{\lambda'_1, \lambda'_2}^* \\
 & D_{\lambda_1, 0}^{1*}(\phi_1, \theta_1, -\phi_1) D_{\lambda'_1, 0}^1(\phi_1, \theta_1, -\phi_1) \\
 & D_{\lambda_2, 0}^{1*}(\phi_2, \theta_2, -\phi_2) D_{\lambda'_2, 0}^1(\phi_2, \theta_2, -\phi_2). \tag{2.88}
 \end{aligned}$$

- $\lambda_1, \lambda_2$  are the helicities for the  $\phi$ -mesons,  $0, \pm 1$  ( $\phi$  has spin 1), and  $\lambda = \lambda_1 - \lambda_2$ .
- $A_{\lambda_1, \lambda_2}$  is the amplitude for production of two  $\phi$ s with helicities  $\lambda_1, \lambda_2$ . The  $A_{00}$  factors from the  $\phi$  decay to spinless kaons are constants and have been omitted.
- $M$  is the  $z$ -component of  $J$ .
- $\rho_{MM'}$  is initial density matrix of the particles decaying into  $\phi\phi$ .
- $A_{\lambda_1, \lambda_2}$  is the amplitude for production of two  $\phi$ s with helicities  $\lambda_1, \lambda_2$ .
- $D_{M, \lambda}^J$  is a  $D$ -matrix element [?].

The helicity amplitudes  $A_{\lambda_1, \lambda_2}$  depend on the  $J^P$  of the intermediate resonance. Without explicitly calculating the amplitudes, several constraints on the amplitudes can be obtained from the following two equations [?]:

$$A_{-\lambda_1 - \lambda_2} = P(-1)^J A_{\lambda_1, \lambda_2}, \tag{2.89}$$

$$A_{\lambda_1, \lambda_2} = (-1)^J A_{\lambda_2, \lambda_1}. \tag{2.90}$$

The quantity  $(-1)^J$  is called the *signature* of the state. Equation 2.89 is required from parity conservation, while equation 2.90 is implied from the identity of the two  $\phi$ s. For certain values of the parity and signature, equations 2.89 and 2.90 are incompatible, forcing the corresponding  $A_{\lambda_1, \lambda_2}$  to vanish. The decay helicity amplitudes which are permitted to be nonzero for the various possible values of parity  $P$ , and signature  $(-1)^J$  are shown in table 2.12.

By integrating over all the other angles in equation 2.88, and summing over helicities, we obtain the following equation for the distribution of the angle  $\chi$  [?]:

$$I(\chi) = 1 + \beta \cos 2\chi, \tag{2.91}$$

The parameter  $\beta$  is a function of the helicity amplitudes :

$$\beta = \frac{2P|A_{11}|^2}{2|A_{11}|^2 + |A_{00}|^2 + 4|A_{01}|^2 + 2|A_{1-1}|^2} \tag{2.92}$$

The parameter  $\beta$  gives information about the possible quantum numbers; it can be seen from the expression for  $\beta$ , and table 2.12, that if  $\beta \neq 0$ , then  $(-1)^J = 1$ , and the sign of  $\beta$  gives the parity of the state.



$P$	$(-1)^J$	Nonvanishing amplitudes
-1	-1	$A_{10} = A_{-10} = -A_{01} = -A_{0-1}$
+1	-1	$A_{10} = -A_{-10} = -A_{01} = A_{0-1}$ $A_{1-1} = A_{-11}$
-1	+1	$A_{10} = A_{01} = -A_{-10} = -A_{0-1}$ $A_{1-1} = A_{-11}$
+1	+1	$A_{10} = A_{01} = A_{-10} = A_{0-1}$ $A_{1-1} = A_{-11}$ $A_{11} = A_{-1-1}$ $A_{00}$

Table 2.12: *The decay helicity amplitudes which are permitted to be nonzero for the various possible values of parity  $P$ , and signature  $(-1)^J$ . From [?].*

Parameter values	Allowed states
$\beta > 0$	$(-1)^J = P = 1$
$\beta < 0$	$(-1)^J = 1, P = -1$

Table 2.13: *Allowed states for various values of the parameters  $\beta$ . From [?, ?].*

## Chapter 3

# Experimental method

In the previous chapter it was shown why the reaction  $\bar{p}p \rightarrow \phi\phi$  is an interesting channel to study when looking for exotic states of matter, such as glueballs. A better understanding of the OZI rule may also be obtained, as well as new evidence for strangeness in the proton.

To search for gluonic resonances in  $\bar{p}p \rightarrow \phi\phi$ , a well focused antiproton beam with well determined momentum of about 1-2 GeV, changeable in small steps, was required. A high luminosity of proton-antiproton collisions was necessary to get sufficient statistics for these low cross section reactions at each value of the beam momentum. These conditions were obtained by inserting an internal hydrogen gas jet target into LEAR, the low-energy antiproton ring, at CERN. The stochastically cooled antiproton beam annihilated in flight onto the the gas jet, which crossed the LEAR beam at a perpendicular angle.

This technique is especially suitable to search for narrow resonances and measure their masses and widths with high precision. In a formation experiment of this kind, the parameters of a sufficiently narrow resonance can be extracted from the excitation curve obtained by stepping the beam momentum across the resonance. The precision on the measurement of the central mass and width of the resonance is then related only to the accurate knowledge of the energy of the initial state, depending on machine parameters, not on detector resolutions. The stochastically cooled antiproton beam had a momentum spread of  $\Delta p/p \approx 10^{-3}$ , giving a precision of the invariant mass of the  $p\bar{p}$  system of the order of 1 MeV. The internal target technique took full advantage of this small momentum spread, compared to an external target, since extracting the beam from the ring would disturb it, and hence increase the uncertainty of the momentum. The density of the target was low enough to not blow up the beam too quickly. The disturbances of the beam from the relatively low density target were small enough to be corrected by the focusing magnets and the stochastic cooling system, thus the same beam of antiprotons could be used for several days. Since the beam circulated the LEAR ring at a frequency of  $\approx 3 \cdot 10^6$  Hz, a much higher luminosity was achieved than with an external target, where the beam is spilled.

The beam momentum was varied from 0.6 GeV/c to 2.0 GeV/c, corresponding to a centre of mass energy of 1.96 GeV to 2.43 GeV. This is an energy area where several interesting states have been seen by other experiments.

In JETSET the  $\phi$  mesons were detected in the decay  $\phi \rightarrow K^+K^-$ , giving a four kaon final state.

Figure 3.1: *Antiproton production for LEAR (from [?]).*

The detector had to be able to filter out the large amounts of background events at the trigger level and to recognize  $\phi\phi$  events offline.

In addition to the OZI suppressed reaction  $\bar{p}p \rightarrow \phi\phi \rightarrow K^+K^-K^+K^-$  we were also interested in the non OZI suppressed reactions  $\bar{p}p \rightarrow \phi KK \rightarrow K^+K^-K^+K^-$  and  $\bar{p}p \rightarrow K^+K^-K^+K^-$ , since studying the latter two reactions would help in understanding the mechanisms involved in the production of  $\phi\phi$  in the  $p\bar{p}$  annihilations.

The main physics goal of the experiment was to measure the cross section as a function of energy of these three reactions.<sup>1</sup>

### 3.1 The antiproton beam and the gas jet target

#### The antiproton beam

The antiprotons for LEAR [?, ?] were produced by bombarding 26 GeV/c protons from the proton synchrotron, PS, on a tungsten target. Antiprotons with a momentum of about 3.5 GeV/c were selected by dipole magnets to the AAC, Antiproton Accumulating Complex.

---

<sup>1</sup>Other channels of interest in the  $p\bar{p}$  annihilations were  $K_0^s K_0^s$ , which is also an interesting channel to look for glueballs,  $\phi\omega$ , and  $\phi\phi\pi^0$ . The latter is particularly interesting since it is a way to obtain exotic quantum numbers for the  $\phi\phi$  state [?]. These physics channels are the subject of other theses from this experiment and will not be treated here.

Figure 3.1 shows the layout of the antiproton production system. The AAC consisted of the Antiproton COLlector ring, ACOL, and the Antiproton Accumulator, AA. Here the antiprotons were collected, accumulated, and stochastically cooled. Stochastic cooling is a method to give uniform momenta to the antiprotons. A pickup coil measured the average deviation of particles from the ideal orbit, and a correction signal was transmitted across the ring. The correction signal arrived faster than the antiprotons, which had to go around the arc, and was used to modulate the field at the far side and deflect straying particles back towards the central orbit. When the bunch circulating in the AA contained about  $4 \cdot 10^{10}$  antiprotons with momentum 3.5 GeV/c, a bunch of typically  $4 \cdot 10^9$  was transferred to the PS, where it was decelerated to 0.609 GeV/c, before it was sent into the LEAR ring, where the beam momentum could be varied between 0.6 GeV/c and 2 GeV/c. Continuous stochastic cooling gave a low momentum uncertainty,  $\frac{\Delta p}{p} \approx 10^{-3}$ . Low beta quadrupoles focused the beam. The orbit length in LEAR was 78.12 m. At a beam momentum 1.5 GeV/c, the  $\bar{p}$  revolution frequency in LEAR was  $\nu = v/l \approx 0.85c/78.12\text{m} \approx 3.26 \cdot 10^6$  Hz. In figure 3.2 the LEAR ring is shown, with the location of JETSET in the south straight section, low beta quadrupoles to focus the beam, and stochastic cooling system.

Figure 3.2: *The LEAR ring (from [?]).*

### The LEAR beam pipe

In the region where JETSET was located LEAR was equipped with a special vacuum chamber around the interaction region. The chamber size was dictated by machine parameters at injection time.

It had an elliptical transverse section, with horizontal and vertical half-axes of 7.8 and 3.8 cm respectively, and extended 30 cm downstream of the target. The constraints imposed by the size of the vacuum chamber limited the geometrical acceptance of the detector to polar angles  $\theta > 10^\circ$ . Before reaching the detector the particles had to travel some distance and traverse the wall of the chamber. The vacuum chamber design and thickness (300  $\mu\text{m}$  of corrugated stainless steel) was a compromise between the constraints imposed by the machine operation and the requirement to minimize the effect of multiple scattering on particles traversing it; however, it represented the main source of multiple scattering in the JETSET set-up that contributed to the perturbation of track directions and ultimately degraded reconstruction resolution.

### The Gas jet target

The target for the experiment consisted of a molecular hydrogen cluster jet (figure 3.3), which crossed the LEAR vacuum pipe where it interacted with the antiproton beam (figure 3.5). The system was installed in the straight section SL2 of the LEAR ring. The basic principle of operation consisted in the expansion of molecular hydrogen kept at low temperature and high pressure, which created an intense supersonic flow of clusters of  $\text{H}_2$  molecules. The jet was oriented in the horizontal plane and intersected the antiproton beam perpendicularly. The gas jet was formed in a trumpet-shaped nozzle with temperature and pressure close to those of the phase-transition to liquid. Due to Van der Waals forces a clustering of the molecules took place. The generated beam thus consisted of large clusters of hydrogen molecules. To collimate the jet, it was passed through three slits before reaching the vacuum pipe. This provided a low-mass pure gaseous hydrogen target in the interaction region, with a density up to  $\rho = 10^{13}$  atoms/cm<sup>2</sup> and diameter of 8 mm. The nozzle was 80 cm away from the interaction region. After traversing the vacuum pipe, the gas was absorbed by a sink pump system. This type of target had earlier been used in the ISR experiment R704 and was modified for use in JETSET [?, ?].

### The $p\bar{p}$ interactions

The combination of a thin target with an intense antiproton beam fully exploited the small momentum spread of the machine. Different from all other experiments at LEAR, the JETSET experiment used an internal target, which crossed the LEAR beam pipe. This was made possible by the LEAR stochastic cooling system, which compensated for the perturbation of the coasting antiproton beam from the gas jet target. The transverse stochastic cooling kept the transverse dimensions of the beam smaller than those of the jet in spite of the Coulomb scattering of antiprotons with the hydrogen jet. The longitudinal stochastic cooling compensated for energy losses to maintain a good momentum resolution and to keep the beam on its nominal orbit.



Figure 3.3: *The jet target. The source is at the bottom, the sink at the top of the picture (from [?]).*

When a resonant state is produced in a  $p\bar{p}$  interaction, its mass is given by the invariant mass of the  $p\bar{p}$  system. Since the protons were practically at rest, the invariant mass was

$$M = \sqrt{(E_{\bar{p}} + m_p)^2 - \vec{p}_{\bar{p}}^2} = \sqrt{2m_p^2 + 2m_p\sqrt{m_p^2 + \vec{p}_{\bar{p}}^2}}. \quad (3.1)$$

$E_{\bar{p}}$  and  $p_{\bar{p}}$  are the antiproton total energy and momentum,  $m_p$  the proton(antiproton) mass. The uncertainty in the mass arises from the antiproton momentum resolution  $\Delta p_{\bar{p}}$ :

$$\Delta M = \frac{m_p p_{\bar{p}}}{M\sqrt{m_p^2 + p_{\bar{p}}^2}} \Delta p_{\bar{p}}. \quad (3.2)$$

Thus the antiproton momentum resolution of about  $\frac{\Delta p}{p} \approx 10^{-3}$  translated into an experimental invariant-mass resolution of less than 1 MeV.

The intersection region of the LEAR beam with the internal jet target was 8 mm  $\times$  6 mm  $\times$  8 mm (fwhm).

At a momentum of 1.5 GeV/c the revolution frequency of the antiprotons in LEAR was  $\nu = 3.24$  MHz. With a jet density of up to  $\rho = 10^{13}$  atoms/cm<sup>2</sup>, and an unbunched beam initially consisting of  $N_0 = 4 \cdot 10^{10}$  antiprotons, a peak luminosity of  $\mathcal{L}_0 = \rho\nu N_0 \approx 10^{30}$  cm<sup>-2</sup>s<sup>-1</sup> was achieved. The hadronic  $p\bar{p}$  total cross section is  $\sigma = 100$  mb in the relevant energy range, which gives a hadronic interaction rate up to  $\frac{dN}{dt} = \sigma\mathcal{L}_0 = 10^5$  Hz. This influenced the beam lifetime  $\tau$  in the machine, which caused the luminosity to decrease in time. Assuming no losses in the machine except those due to hadronic interactions and coulomb scattering in the hydrogen jet, the beam lifetime can be estimated. The number of particles in the beam were  $N(t) = N_0 e^{-\rho\nu\sigma_a t} = N_0 e^{-t/\tau}$ , where  $N_0$  is the initial number of antiprotons in the beam,  $\sigma_a$  is the total cross section for absorption and elastic coulomb scattering, and  $\tau$  is the lifetime.  $\sigma_a = 100$  mb gives  $\tau = (\rho\nu\sigma_a)^{-1} \approx 89$  hours. This way a typical beam lifetime of a few days was achieved. If no problems occurred, the experiment ran at a fixed momentum setting, using the same beam for several days. Then a new antiproton beam was injected, and tuned to the required energy setting.

The longitudinal stochastic cooling also allowed a scan in small steps of  $\sqrt{s}$ , for example to search for a specific resonance.

As the luminosity decreased with time as  $\mathcal{L} = \mathcal{L}_0 e^{-t/\tau}$ , in 24 hours the integrated luminosity was  $\int_0^{24h} \mathcal{L} dt \approx 7.5 \cdot 10^{10}$  b<sup>-1</sup>, if the beam initially contained  $4 \cdot 10^{10}$  antiprotons. Assuming a  $p\bar{p} \rightarrow \phi\phi$  cross section of 1  $\mu$ b there would be a maximum of  $7.5 \cdot 10^4$   $p\bar{p} \rightarrow \phi\phi$  interactions in one day, with 25 % of them in a  $4K$  final state, since  $BR(\phi \rightarrow K^+K^-) = 0.49$  [?] .

Figure 3.4 shows cross sections of various  $p\bar{p}$  reactions in the relevant energy range. A large part of the pionic background had to be filtered out at the triggering level since only about 100 events could be written to tape each second.

The requirements of the detector were fast on-line triggering, good precision tracking with a minimum of multiple scattering, and photon detection, to select the desired signal out of the large number of background reactions.

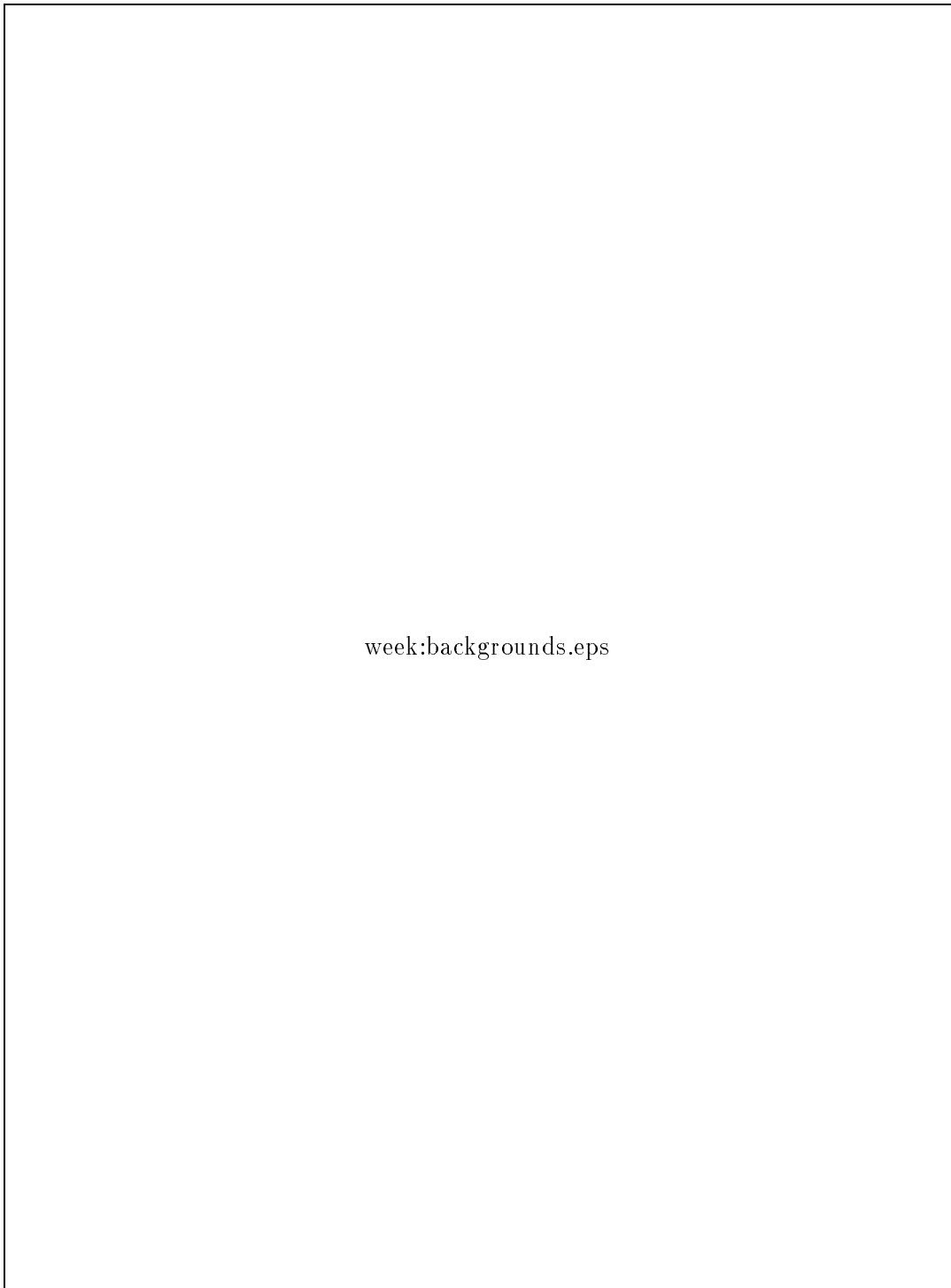


Figure 3.4: *Cross-sections of the main four-track backgrounds in the energy range accessible to JETSET (from [?]).*





Figure 3.5: *The JETSET detector. The hydrogen cluster jet target which was lying in the horizontal plane is shown with the source at the bottom of the picture (1), and the sink at the top (2). The antiproton direction is from left to right.*

## 3.2 The detector

The detector was designed especially to measure the reaction  $\bar{p}p \rightarrow \phi\phi \rightarrow 4K$ . The final state kaons' momenta were in the range 200 MeV/c to 1 GeV/c, which required a compact apparatus to minimize the losses due to kaon decays. The volume of the whole detector was  $\approx 1m^3$ . It was divided into a barrel and a forward part, where the forward part covered polar angles from 15 degrees to 45 degrees, and the barrel part the angles between 45 degrees and 135 degrees. The azimuthal coverage was almost 360 degrees, limited only by the jet target fixtures. This covered most of the important angular region except the very forward part, which was occupied by the vacuum chamber surrounding the interaction volume.

The JETSET detector is shown in figure 3.5. The trigger system for the experiment consisted of

- 60 scintillator strips adjacent to the beam pipe,
- 48 Cherenkov liquid threshold counters,
- 24 barrel gamma veto counters made of lead and scintillating fibers,
- an outer scintillator array in the barrel and forward regions containing 144 elements.

The trigger rejected most of the pionic background and reduced the event rate from  $\approx 100$  kHz to 100 Hz. The following characteristics of the  $4K$  signal were used in the trigger (section 3.3): All the events have four prongs, which are always forward of 65 degrees in the lab frame, three of them being forward of 45 degrees. All the particles have a moderate  $\beta = \frac{v}{c}$  value. Reactions like  $p\bar{p} \rightarrow \pi^+\pi^-K^+K^-$  and  $p\bar{p} \rightarrow \pi^+\pi^-p\bar{p}$  have signatures similar to good events, and these had to be filtered out offline.

The main idea of the offline analysis was to do a precise tracking of the four particles, and then reconstruct the momenta assuming the particles were kaons. The detector was not equipped with a magnet, so the momenta were not measured directly. The tracking was done with 2400 cylindrical drift chambers, or “straws”.

The detector also contained 3700 silicon pad counters for energy loss measurement (dE/dx counters). The event was accepted as a  $4K$  event if the response of the Cherenkov and dE/dx silicon counters corresponded to the reconstructed momenta. The forward part also contained an electromagnetic calorimeter consisting of 300 counters made of lead and scintillating fibers. This was used to reconstruct  $\pi^0$  for the  $\phi\phi\pi^0$  events, and veto events with neutral particles in the  $\phi\phi$  analysis.

Tables 3.1, 3.2, and 3.3 show the geometrical parameters for the detector elements in the forward and barrel region, where the origin of our coordinate system is defined as the interaction point where the antiproton beam crosses the hydrogen jet. The  $z$ -axis is parallel to the beam, the positive direction pointing in the same way as the antiproton momentum. The  $x$  and  $y$  axes follow the horizontal and vertical directions perpendicular to the beam respectively.

The number of radiation lengths encountered by a particle traversing various parts of the detector is shown in table 3.4.

Element	$(A, B)_{center}$ (cm)	thickness(cm)	$\theta_{acc}$
Beam pipe	A= 7.8, B=3.8	0.03	
Barrel pipe scintillator	A = 8.5, B = 4.3	0.2	45° – 65°
Forward pipe scintillator	A = 8.5, B = 4.3	0.2	15° – 45°

Table 3.1: Geometrical parameters for the beam pipe and beam pipe scintillators. The half-axes of the ellipse, thickness for each element, and the acceptance in polar angle for the scintillators are listed.

Detector	$Z_{entrance}$ (cm)	$Z_{exit}$ (cm)	$R_{inner}$ (cm)	$R_{outer}$ (cm)	$\theta_{acc}$
Outer scintillator:					
Layer 1 ( $\phi$ -segments)	57.0	57.5	A=8.8, B=4.8	58.0	11° – 45°
Layer 2 (spirals)	58.0	58.5			
Layer 3 (spirals)	59.0	59.5			
Straw tube tracker:					
x-chamber 1	20.38	22.78	A=8.8, B=4.8	28.4	16° – 54°
y-chamber 1	23.10	25.50			
x-chamber 2	25.77	28.27			
y-chamber 2	28.55	30.95			
Silicon dE/dx	31.3	34.6	A=8.8, B=4.8	28.3	14° – 42°
Threshold Cherenkov	52.3	54.7	9.0	52.3	16° – 45°
Rich	36.8	46.8	A=9.6, B=6.4	30.0-40.3	15° – 39°
E/M calorimeter	62.0	82.0	9.7	69.0-73.0	9° – 48°

Table 3.2: Geometrical parameters for the forward detector. In this table, the z-coordinate for entrance and exit of the detector, inner and outer radius, and the coverage in polar angle is shown. Each detector element had a hole in the middle to make room for the elliptical beampipe, which was either elliptical(scintillators), rectangular(straws,silicon,Rich), or circular (calorimeter, Cherenkov). For the two former cases the halfaxis, or rectangle sides A and B are given, and the acceptance in polar angle depends on the azimuthal angle for the track.

Detector	$Z_1$ (cm)	$Z_2$ (cm)	$R_{inner}$ (cm)	$R_{outer}$ (cm)	$\theta_{acc}$
Outer scintillator:					
Layer 1 (straight)	-35.0	+35.0	35.0	35.5	45° – 135°
Layer 2 (helical)			36.0	36.5	
Layer 3 (helical)			37.0	37.5	
Straw tube tracker	-26.8	+18.8	A=8.8, B=4.8	18.5	25° – 162°
Threshold Cherenkov	-31.0	+32.0	30.0	30.	43° – 136°
Barrel $\gamma$ veto	-39.0	+39.0	39.0	48.3	45° – 135°

Table 3.3: Geometrical parameters for the barrel detector. The longitudinal position (z-coordinates for beginning and end of detector), inner and outer radius, and coverage in polar angle is shown. The barrel straw tracker had an elliptical hole in the middle, and the ellipse half-axes are given in the table, the angular acceptance depended on the azimuthal angle for the track.

Element	Material	Thickness, $X$ (cm)	Rad.length, $X_0$ (cm)	$X/X_0$
Beam pipe	Steel	0.03	1.760	1.7 %
Beam pipe scintillator	Plastic	0.2	47.8	0.4 %
Straw tube walls	Aluminium	0.006	8.9	0.07 %
dE/dx	Silicon	0.03	9.36	0.3 %
dE/dx	Circuit board			2.7 %
Threshold Cherenkov	Water	2.0	36.1	5.5%
Threshold Cherenkov	Freon	2.0	18.6	10.8 %
Cherenkov walls	Plexiglass	0.3	34.4	0.9 %
Rich radiator	Quartz	1.0	11.7	8.5 %
Barrel endcap	Aluminium	0.2	8.9	2.2%
E/M calorimeter	Lead+scint.+epoxy	20.0	1.61	12.5
Barrel $\gamma$ veto	Lead +scint.	9.3	1.55	6.0

Table 3.4: *Thickness and number of radiation lengths encountered by a particle passing through various elements of the JETSET detector.*

### The trigger scintillators

A system of 60 scintillator counters arranged around the beam pipe (pipe scintillators [?]), and a hodoscope consisting of three layers of scintillators outside the Cherenkov counters (forward and barrel outer scintillators, also called “Jülich scintillators” [?]) were used to determine the charged multiplicity for the trigger.

The 60 beam pipe scintillators were arranged in two quasi-elliptical layers parallel to the beam pipe. The inner layer (barrel pipe scintillators) consisted of 20 elements, 2 cm wide, and covering  $360^\circ$  in azimuthal angle  $\phi$  and  $45^\circ - 65^\circ$  in polar angle  $\theta$ . The outer layer (forward pipe scintillators) consisted of 40 elements, 1 cm wide, and covering  $360^\circ$  in azimuthal angle, and  $15 - 45^\circ$  in polar angle. All the scintillators were 0.2 cm thick. Each element covered an azimuthal angle  $\phi$  varying from approximately 6 degrees to 14 degrees (figure 3.6). To cover the same angular region in  $\theta$  around the ellipse, the scintillator elements had varying lengths along the beam direction (figure 3.7). The light was collected by plexiglass light guides with the same width as the scintillator elements but 3 mm thick, connected to photomultipliers. The signals were fed into 16-channel discriminators, which gave an analogue output signal proportional to the number of input signals above threshold. By daisy-chaining all the units of the barrel pipe scintillators a signal proportional to the total multiplicity of the counters was obtained. The forward pipe scintillators were daisy-chained in the same way.

The barrel outer scintillators (figure 3.8), positioned outside the barrel threshold Cherenkovs, had one layer of 24 straight scintillators parallel to the beam pipe, and two helical layers, twisted in opposite directions, with 12 scintillators in each. This gave 288 independently sensitive regions or **pixels**. The forward detector (figure 3.9) was positioned downstream of the forward Cherenkov counters, and contained one layer with 48 wedge shaped elements and two layers each with 24 spirally shaped detectors curved in opposite directions, which gave a total of 960 pixels (figure 3.10). The outer scintillators were made of 5 mm Bicron “BC404” material [?]. They were read out by photomultipliers connected both to TDC and ADC readout electronics.

In addition to being used for triggering the scintillators were also used for offline trackfinding, and the beam pipe scintillators were used as timing devices. The signal from the pipe

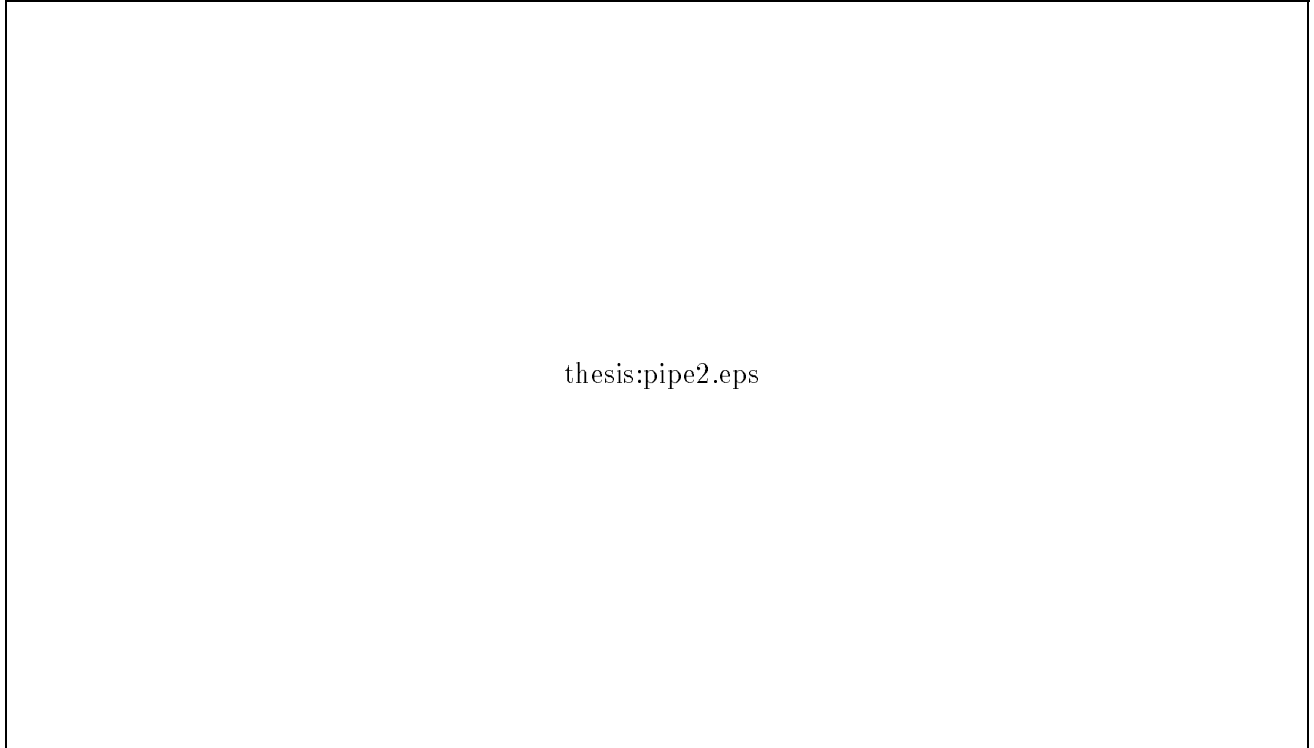


Figure 3.6: *Azimuthal coverage of the beam pipe scintillators across the beam pipe for one quadrant of the outer layer (from [?]).*

scintillator was used to start the TDCs for the straw tracker and the rest of the detector. The optimum resolution of the time signal for the pipe scintillators was measured to be about 0.15 ns at Cern's T11 East hall test beam [?]. When being used as trigger detectors in the experiment the resolution was smeared out because of the variations of the impact point along the scintillator length. In this case the time resolution was about 1 ns.

The time resolution of the outer scintillators, when they were used in the experiment, was about 2 ns for the straight counters, somewhat higher for the curved elements.

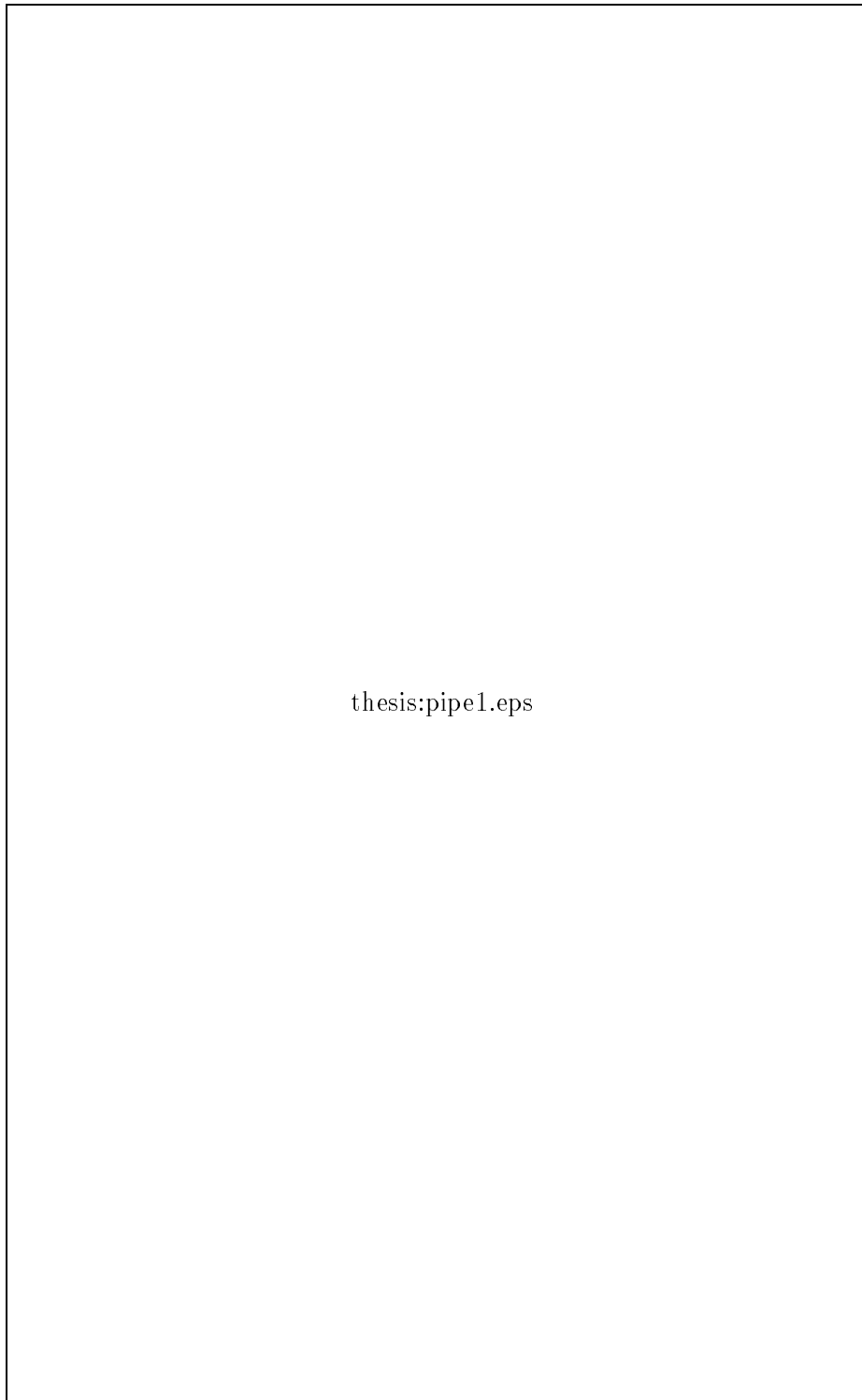


Figure 3.7: *Azimuthal extension of the beam pipe scintillators vs. length along beam direction (from [?]).*

Figure 3.8: *The outer scintillator hodoscope, barrel system (from [?]).*

Figure 3.9: *The three layers of the forward outer scintillator hodoscope (from [?]).*



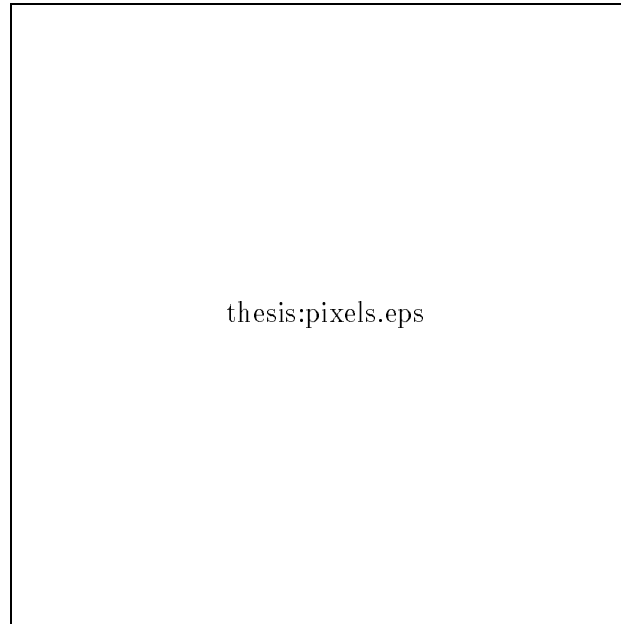


Figure 3.10: *The pixel structure of the forward scintillator hodoscope (from [?]).*

### The forward and barrel straw trackers

The purpose of the forward and barrel straw trackers was to give tracking information from drift-time and charge division measurements for the offline analysis. The barrel tracker [?] gave both transverse ( $r, \phi$ ), and longitudinal ( $z$ ) coordinates for particles with  $\theta > 30^\circ$ , thereby giving full three-dimensional information about the track coordinates. The forward tracker [?] measured the  $zx$  and  $zy$  projections of tracks with  $\theta < 45^\circ$ .

The trackers consisted of cylindrical drift tubes (straws) glued together. The distance of the track from the wire was determined by measuring the drift time of the ionized electrons. By using analog readout on both ends of the resistive wire, the longitudinal position was determined from charge division.

Each of the drift tubes had a diameter of 0.8 cm, with a central anode wire of  $30 \mu\text{m}$  stainless steel and resistance  $1k\Omega/m$ . The tubes were made of aluminium with a wall thickness of  $60 \mu\text{m}$ . The gas was 50 % Ar, 50 %  $CO_2$ , at atmospheric pressure. A particle traversing one straw would encounter about  $10^{-3}$  radiation lengths, so there was little multiple scattering inside the tracker. The straw chambers were positioned just outside the pipe scintillators.

The barrel tracker (figure 3.12) contained 1400 straws running parallel to the beam. They were mounted on aluminium endplates and had a length of 43.6 cm. To allow for entry of the jet, 100 of the straws were split into two separated but electrically connected sections (barrel inserts). The inner boundary of the barrel straw tracker had an oval shape determined by the size of the beam pipe and the thickness of the beam pipe scintillators surrounding the pipe. The barrel tracker readout was done from the barrel rear end plates. The straws were connected to preamplifiers by coaxial cables with a resistance of  $85 \Omega$ . They were connected in pairs at the forward end by means of  $50 \Omega$  jumper resistors to form a single

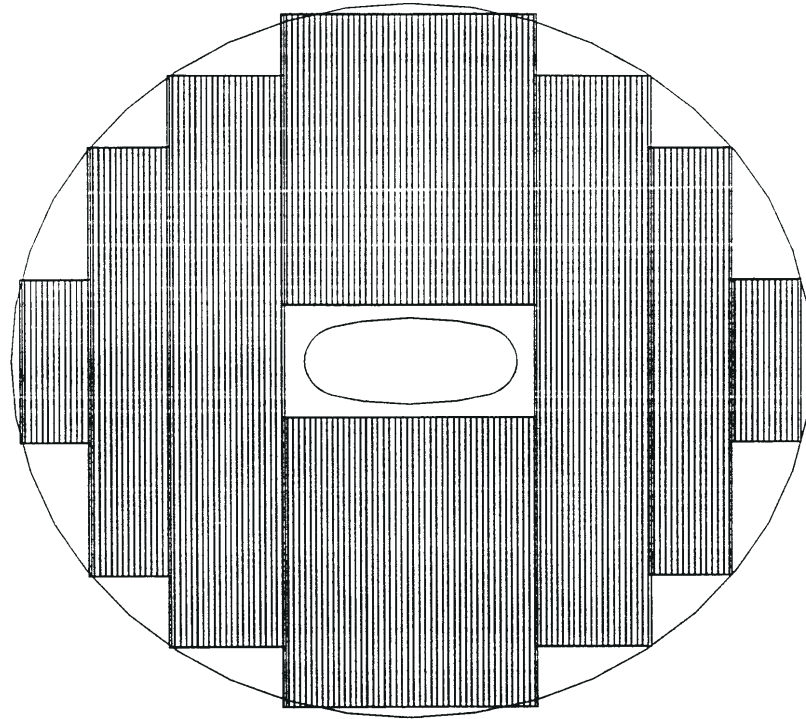


Figure 3.11: *Plan view of single forward tracker plane with straws parallel to the  $y$  direction, hence measuring the  $x$  coordinate (from [?]).*

charge division system (figure 3.16). The barrel tracker had both ADC and TDC readout. Thus the transverse coordinate could be obtained from the TDC signal, and the longitudinal coordinate from the ADC signal by the method of charge division.

The forward tracker (figure 3.11) contained about 1000 tubes, and was mounted in 12 layers perpendicular to the beam axis, 6 layers with the straws parallel to the  $x$ -direction, and 6 layers parallel to the  $y$ -direction. The layers were divided into 2  $x$ -chambers and 2  $y$ -chambers. Each forward layer was made of several blocks of straws with varying length to give an approximately circular perimeter, with a rectangular hole for the beampipe in the middle. The electronic readout for the forward tracker was placed at a distance of about 2 m from the counter. These straws were also connected to preamplifiers by  $85\ \Omega$  coaxial cables and had TDC readout, but no ADC. From the TDC signal the transverse coordinate, either  $x$  or  $y$ , could be determined. Since there was no analog readout, there was no measurement of the longitudinal coordinate of these straws.

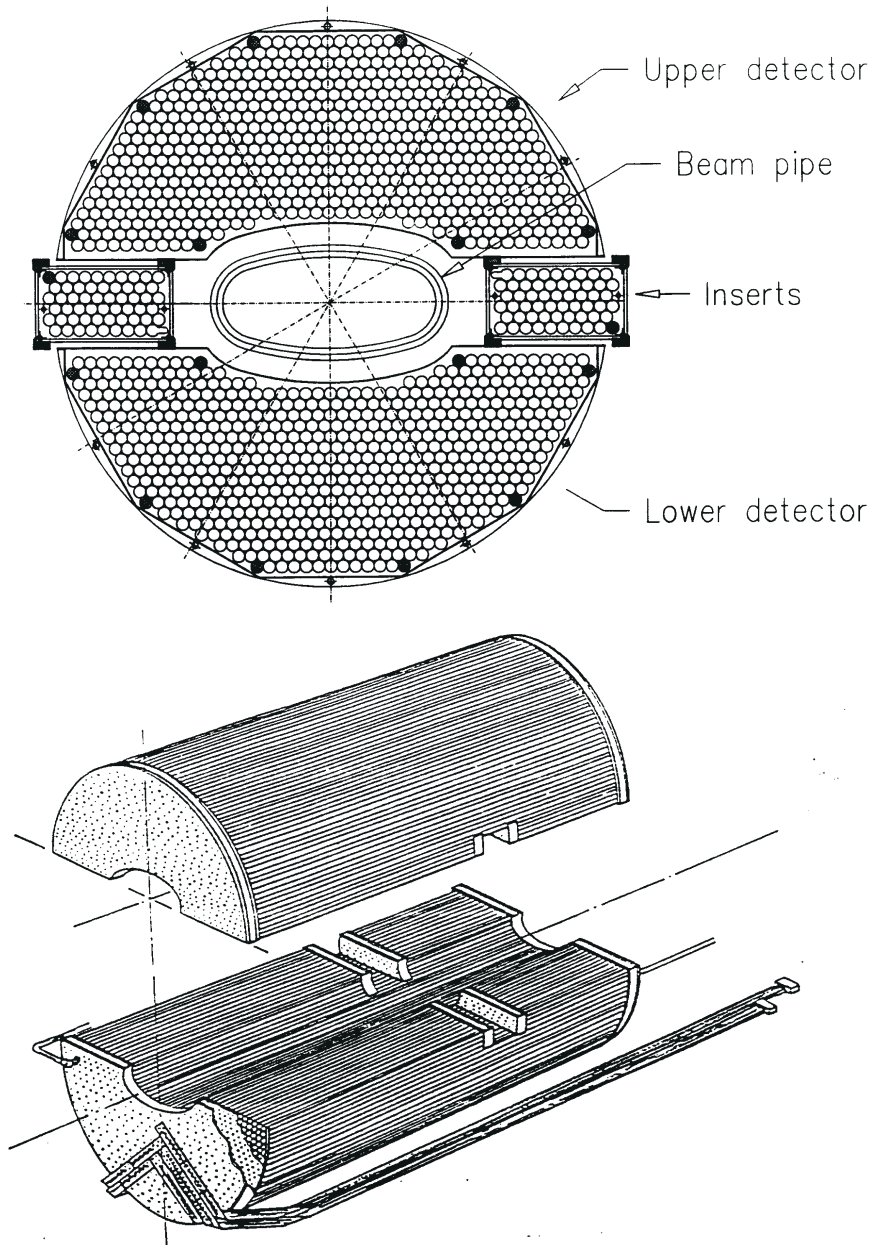


Figure 3.12: *The barrel straw tracker. The top picture shows a projection in the  $xy$  plane, the bottom picture gives a three dimensional view (from [?, ?]).*

Figure 3.13: A typical TDC spectrum for the straws.

The drift-time calibration ( $R(t)$  curve) of the straws was done with elastic events. Assuming uniform illumination for each straw (an equal number of tracks passing by at any distance from the straw wire), the  $R(t)$  curve from first order calibration was obtained by integrating the TDC spectrum (figure 3.13). There was a small difference in the TDC offset for different straws and different pipe scintillators that triggered. The calibration was done in the following way :

1. From the TDC distribution find the T0 and number of channels TN. T0 corresponds to the inner radius of the straws,  $r_0$ , and T0+TN to the outer radius,  $r_{straw}$ . One TDC channel corresponds to one nanosecond.
2. Then, assuming uniform illumination, integrate the TDC spectrum to find the  $R(t)$  curve. The radius corresponding to a given time  $t$  is

$$R(t) = r_0 + (r_{straw} - r_0) \frac{\sum_{t'=t_0}^{t'=t} N(t')}{\sum_{t'=t_0}^{t'=t_N} N(t')}, \quad (3.3)$$

where  $t$  is TDC-TDC0.

3. If the mean value of the difference between measured and calculated radius is different from zero for some TDC channel, correct the  $R(t)$  curve for this difference, at the same time, make sure that the curve is monotonically increasing.

The calibration curve obtained from this procedure is shown in figure 3.14. A resolution of about  $250 \mu\text{m}$  in the barrel straws and about  $350 \mu\text{m}$  in the forward straws was obtained from the drift-time measurement (figure 3.15).

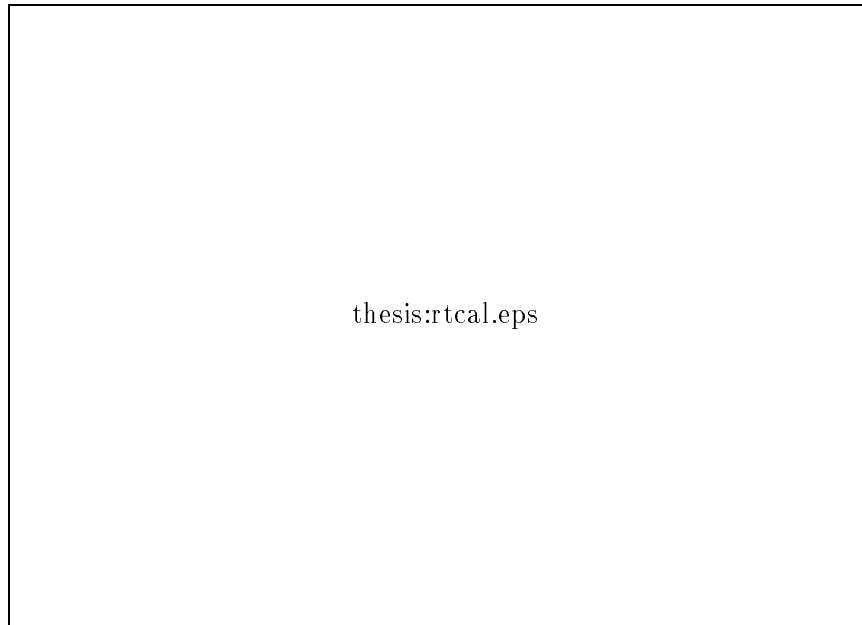


Figure 3.14: *Calibration curve for the straw tracker, showing the distance from the straw wire as a function of the drift time (from [?]).*



Figure 3.15: *The resolution of the barrel straw tracker as a function of the distance from the straw wire (from [?]).*

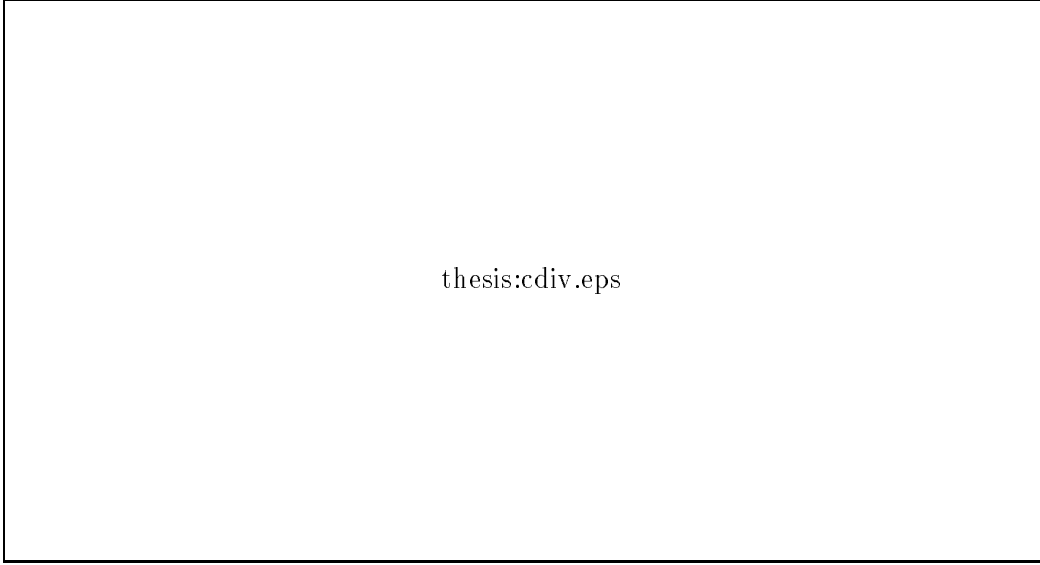


Figure 3.16: *Electronic connection scheme of a wire pair as used for the charge-division readout of the barrel straws (from [?]).*

The principle for the charge division read-out [?] is shown in figure 3.16. The straw wires were connected together in pairs. The position of the current source could be calculated using the total charges  $q_1$  and  $q_2$  received at the preamplifiers PA1, PA2. A signed coordinate  $\xi$ , running along the resistive length, and having its origin at the centre (the midpoint of the jumper resistor), was used. The coordinate of the current source was then given by

$$\xi = \frac{R_2 + R_1}{2\rho} \frac{q_2 - q_1}{q_2 + q_1} + \frac{R_2 - R_1}{2\rho}, \quad (3.4)$$

where  $R_i = (R_{cable,i} + R_{wire,i} + R_{jumper})$  and  $\rho$  the specific resistance of the anode wire. The sign of  $\xi$  would indicate which of the wires were hit.

The physical coordinate  $z$  was given by  $z = z_{end} \pm \xi$  depending on which wire was hit,  $z_{end}$  being the physical coordinate of the forward end of the barrel straws. When differences in amplifier gains  $g_1, g_2$  were taken into account, the difference to sum ratio  $\zeta$  of the measured charges  $Q_1, Q_2$  to the ideal case was

$$\zeta = \frac{Q_2 - Q_1}{Q_1 + Q_2} = \frac{g_2 q_2 - g_1 q_1}{g_2 q_2 + g_1 q_1}, \quad (3.5)$$

The coordinate  $\xi$  could be expanded as a power series in  $\zeta$ , which was cut after the second-order term :

$$\xi = c_1(\zeta - \zeta_0) + c_2(\zeta - \zeta_0)^2, \quad (3.6)$$

where the parameters  $\zeta_0, c_1$ , and  $c_2$  had to be determined for each wire pair. Also the  $z_{end}$  parameter was treated as a free parameter for each wire pair and provided a consistency check at the end of the calibration. To do the charge division calibration, a set of events collected by the  $4\pi$  trigger (section 3.3) in coincidence with a trigger scintillator that triggered on tracks from the target at a lab angle about  $140^\circ$  was used. The four calibration points

that were necessary to determine the four parameters were taken to be the forward and backward physical limit of the active region of each individual wire. These were visible in the  $\zeta$  distribution of all hits on a wire pair.

A resolution of about 1 cm on the  $z$ -coordinate was obtained by this method.

### The silicon dE/dx counters

The forward silicon dE/dx counters [?] were located downstream of the straw tracker. By measuring the energy loss, these counters gave information about the particle velocity  $\beta$ , which helped in distinguishing  $4K$  events from background like  $p\bar{p}\pi^+\pi^-$  (figure 3.18). The forward silicon (figure 3.17) consisted of two planar circular counter arrays, giving two energy loss measurements per track. The lower of the two measurements were used (truncated mean), because of the Landau tail (figure 3.19) this gave a better estimate of  $\beta$  than a single measurement.

The planes were built out of detectors with area 5 cm<sup>2</sup>, each containing four pads with a surface 0.5 · 2.5 cm<sup>2</sup>, mounted on a printed circuit board together with the electronics. One plane had the longer side of the pads parallel to the  $x$ -direction, in the other plane it was parallel to the  $y$ -direction. The thickness of the silicon pads was 280  $\mu$ m. The amount of material encountered by a particle at normal incidence was about 0.03 radiation lengths, including the circuit board and the electronics. The front-end electronics to read the signal of these counters was based on the AMPLEX chip [?], originally developed for the UA2 inner silicon detector, with an elaborate multiplexing scheme to read out the 3676 pads.

The theoretical formula for the the mean rate of ionization energy loss for a charged particle traversing a material is given by the Bethe-Block formula [?]:

$$\frac{dE}{dx} = 0.1535 \text{ MeV}/c^2 \frac{Z\rho}{A\beta^2} \left( \ln \frac{2m_e c^2 \beta^2 \gamma^2 W_{max}}{I^2} - 2\beta^2 \right), \quad (3.7)$$

where  $I, Z, A$  and  $\rho$  are the ionization potential, atomic number, atomic weight, and density (in [kg/m<sup>3</sup>]) of the absorbing material,  $m_e$  is the electron mass,  $W_{max}$  is maximum energy transfer in a single collision,  $\beta = \frac{v}{c}$  of the incident particle, and  $\gamma = \frac{1}{\sqrt{1-\beta^2}}$ .

Since the mean energy loss is proportional to  $1/\beta^2$  for  $\beta\gamma \lesssim 1$ , in the energy range of JETSET a calibration curve of the form

$$\varepsilon = a + b/\beta^2 \quad (3.8)$$

where  $a$  and  $b$  were fitted parameters, could be made to calculate the expected response when a particle of velocity  $\beta$  passed through the dE/x detectors [?]. The calibration curves (figure 3.20) were obtained from elastic and  $p\bar{p}\pi^+\pi^-$  events collected during the data taking, by doing a linear least squares fit to the measured energy loss versus  $1/\beta^2$ . Figure 3.21 show the silicon resolution as a function of  $1/\beta^2$ . The results agreed within errors with test beam results [?], and Monte Carlo simulation studies [?].

When both silicon planes were hit the resolution was  $\Delta\beta/\beta \approx 15\%$  for  $\beta \approx 0.5$ , and  $\Delta\beta/\beta \approx 25\%$  for  $\beta \approx 0.95$  [?].

In the offline PID the silicon dE/dx counters and the threshold Cherenkovs complemented each other, since the former worked best at low  $\beta$ , and the latter would measure the higher  $\beta$  values. In addition the silicon counters were used for track finding and fitting.

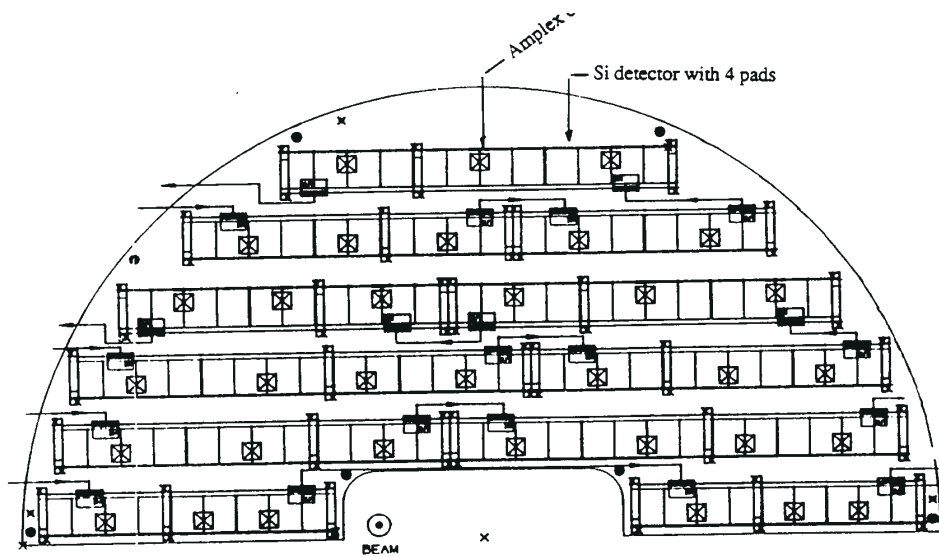


Figure 3.17: Schematic drawing of one half plane of the silicon  $dE/dx$  planes with silicon pads and AMPLEX chips (from [?]).

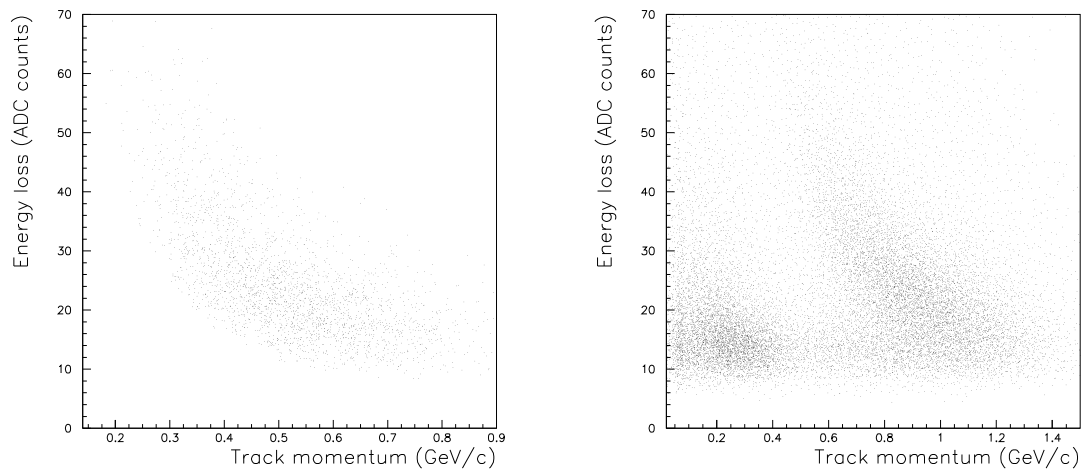


Figure 3.18: Energy loss in silicon detectors as a function of track momentum: kaons (left), protons and pions (right) (from [?]).



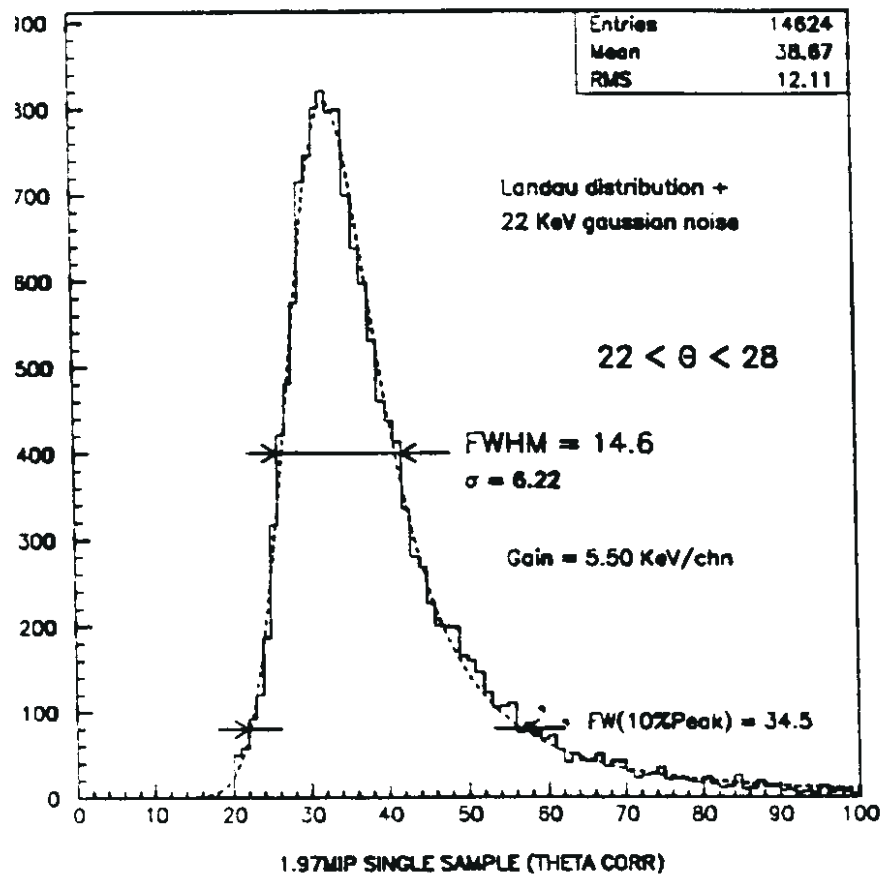


Figure 3.19: Energy loss in silicon detectors from elastic events, the solid curve is the measured one, the dotted one represents theoretical expectations, convoluted with electronic noise known from detector test. (from [?]).

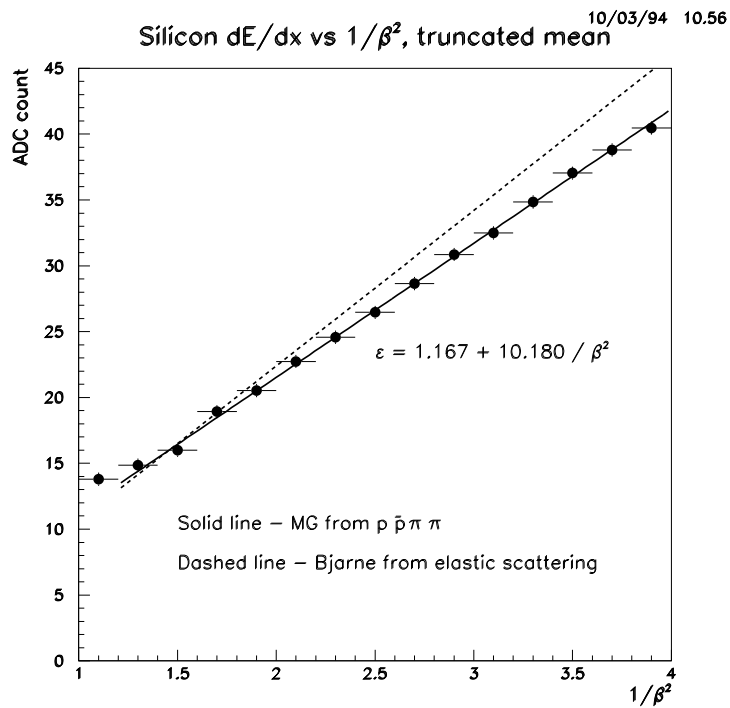
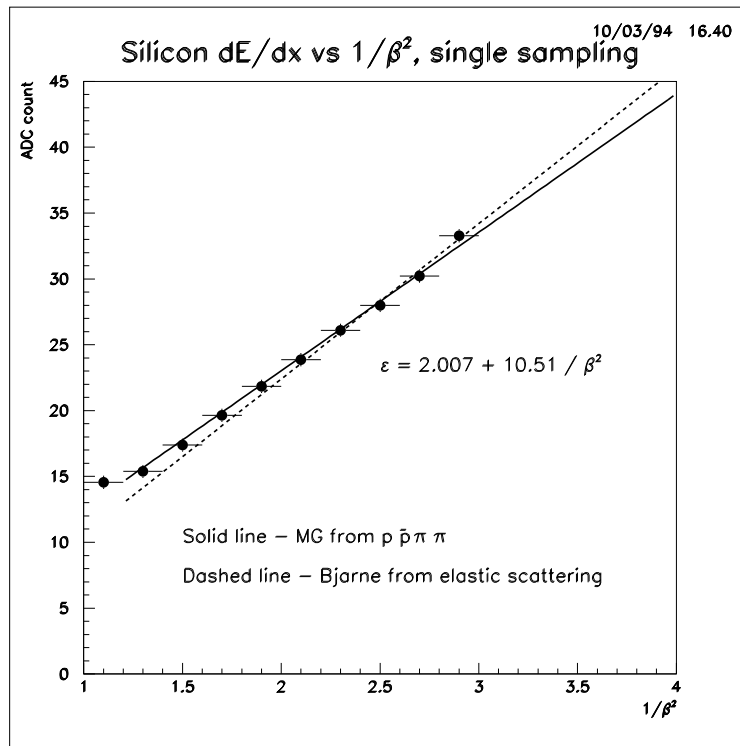


Figure 3.20: Calibration of silicon, single sampling and truncated mean (double sampling), showing the energy loss in silicon (in ADC units) vs  $1/\beta^2$ . The solid line is obtained from  $p\bar{p}\pi^+\pi^-$  events, the dashed line from elastic  $p\bar{p}$  events. From [?].

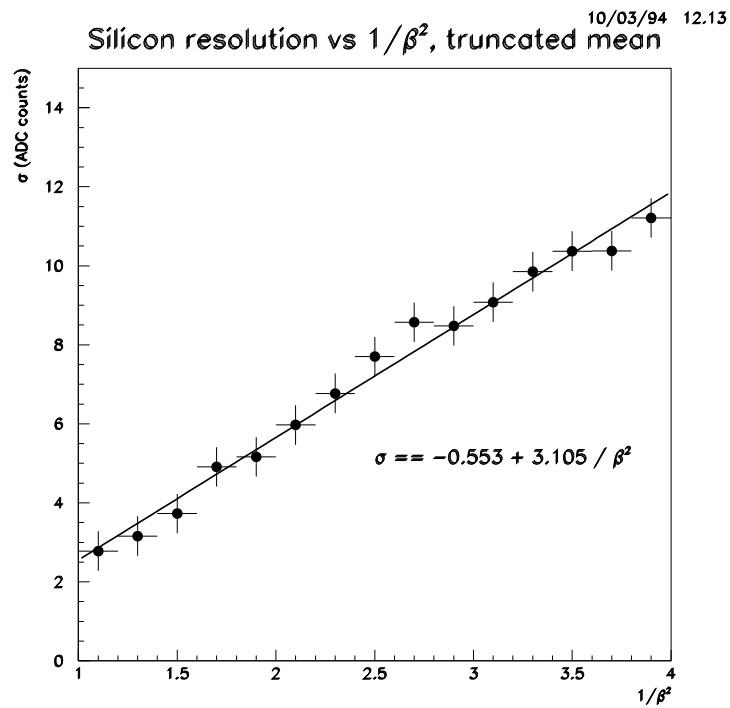
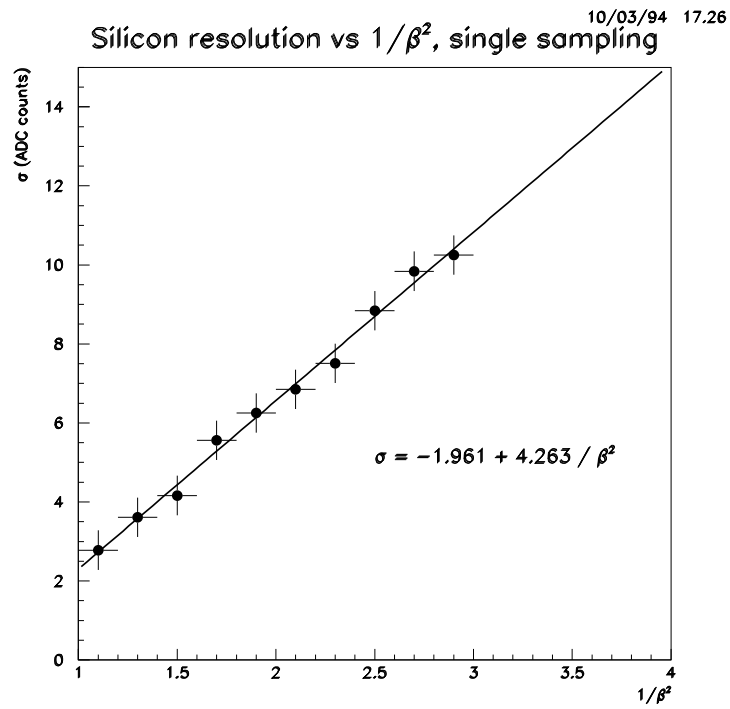


Figure 3.21: Silicon resolution, single sampling and truncated mean (double sampling), showing the resolution (in ADC units) vs  $1/\beta^2$ . From [?].

### The threshold Cherenkov counters

The threshold Cherenkov counters [?] (figure 3.23) were used to reject fast charged pions at the trigger level. The barrel Cherenkov counter was a cylinder with radius of 29 cm, built of 24 wedges with thickness 2 cm and length 60 cm. It was located inside the outer barrel scintillators. The forward Cherenkov counter consisted of 24 pie shaped wedges with an outer radius of 30 cm and thickness 2 cm, and was placed downstream of the silicon dE/dx counters. The walls of all Cherenkov counters were made of UV-transmitting plexiglass sheets, 3 mm thick. Two types of radiators were used: Liquid freon ( $C_6F_{14}$ ), which has refractive index 1.276, corresponding to  $\beta_{threshold} = 0.79$ , and water, which has refractive index 1.33 and  $\beta_{threshold} = 0.752$ . The freon radiator was used at high momentum runs, where the kaons often had  $\beta$  values higher than the threshold in water.

The light output was increased by a factor of  $\approx 3$  by means of a wavelength shifter. All counters were read out with cylindrical UV transmitting plexiglass bars connected to photo-multipliers.

The size of the Cherenkov signal (in ADC channels) was proportional to the number of photo-electrons and was used to estimate the  $\beta$  values of the traversing particles. This was used in the offline PID, and complemented the dE/dx counter by measuring high  $\beta$  values. The detectors were calibrated with elastic events. Figure 3.22 shows the value of the measured  $\beta$  (after calibration of the ADC) versus calculated  $\beta$  (from kinematics). The  $\beta$  resolution turned out to be about 10%.

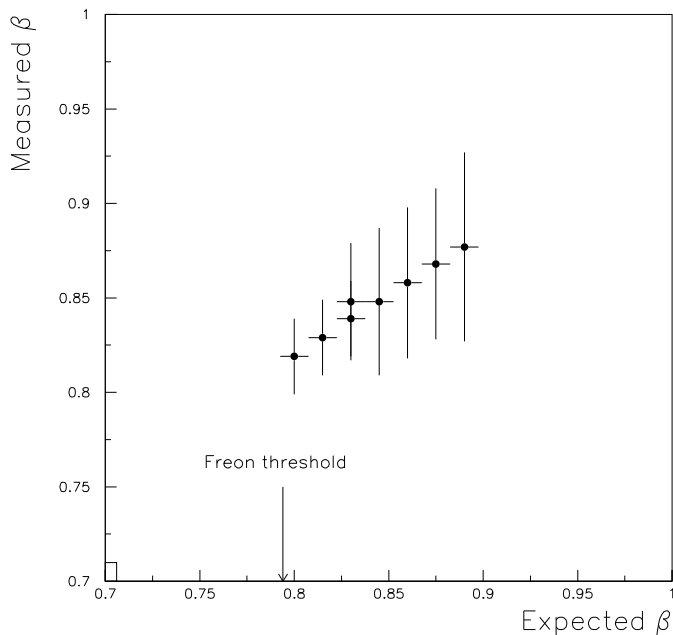


Figure 3.22: Measured versus expected  $\beta$  in the threshold Cherenkov (from [?]).

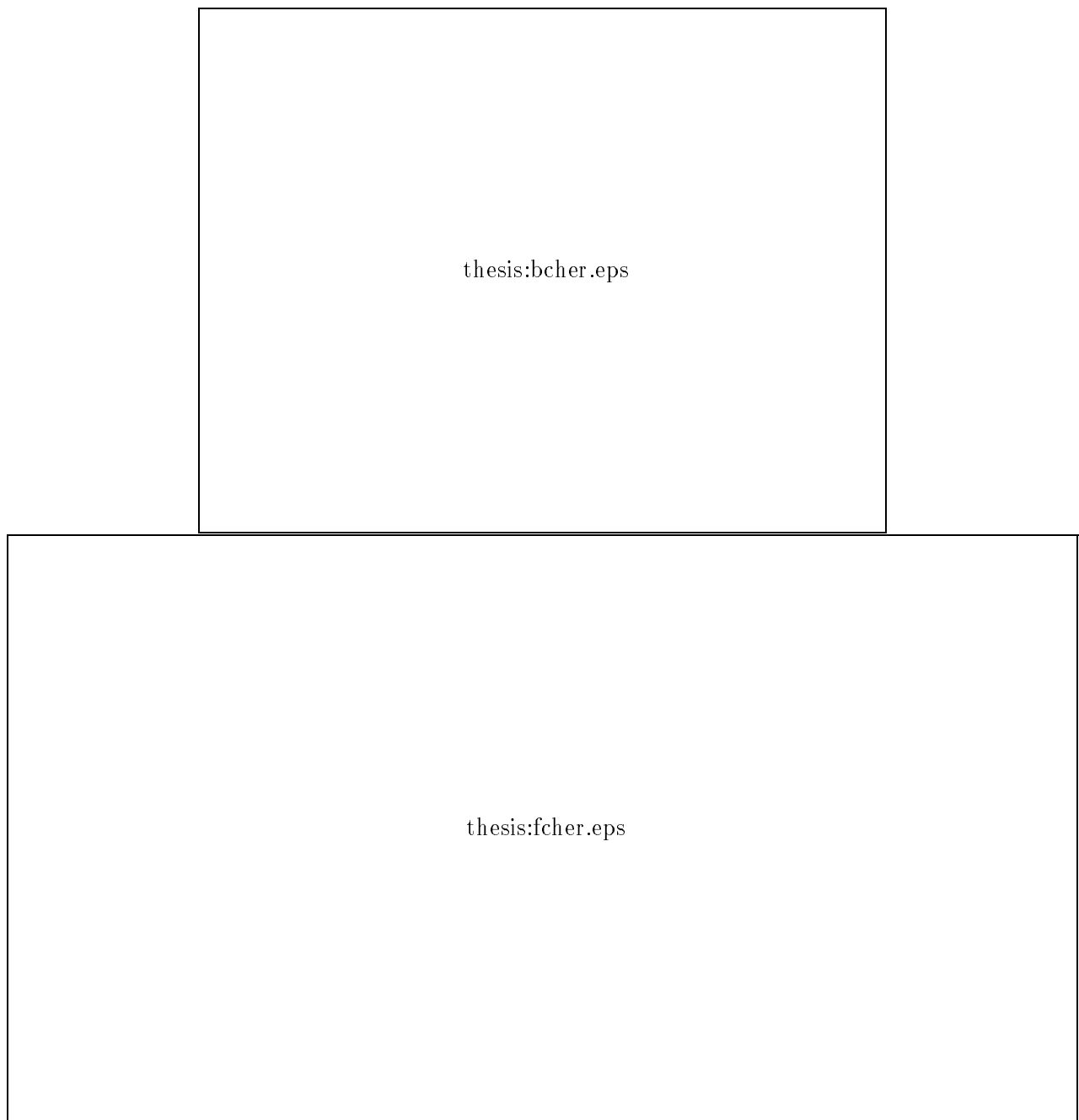


Figure 3.23: *The barrel Cherenkov system (top), and the forward Cherenkov system (bottom). From [?].*

The theoretical formula for the number of photoelectrons emitted for a particle traversing the Cherenkov counter is [?]

$$N_{p.e.} = L \times 370 \text{ cm}^{-1} eV^{-1} \int (1 - \frac{\beta_{thr}^2}{\beta^2}) E dE, \quad (3.9)$$

where  $L$  is the path length in the radiator. The integration is over the photon energies  $E$  where  $\beta > \frac{1}{n(E)}$  ( $n(E)$  is the index of refraction).

Typically, the index of refraction is constant over the useful range of photocathode sensitivity. In that case

$$N_{p.e.} \propto L(1 - \frac{\beta_{thr}^2}{\beta^2}) \quad (\beta > \beta_{thr.}) \quad (3.10)$$

### Calorimeter and barrel gamma veto

The purpose of the forward calorimeter [?] was to measure the energy of photons coming from the decay of neutral mesons like  $\pi^0$ s. This way it could be used to reconstruct events containing neutral particles, like  $p\bar{p} \rightarrow \phi\phi\pi^0$ , and in the analysis of  $p\bar{p} \rightarrow K^+K^-K^+K^-$  it was used to reject events with neutral mesons. This detector was built of plastic scintillation fibers embedded in Pb plates and packed together in towers (figure 3.24) pointing 20 cm upstream of the interaction region. The volume of the towers consisted of 50% fibers, 35% lead, and 15 % epoxy for filling around the fibers. The calorimeter was placed after the outer scintillators and consisted of 300 towers assembled into eight concentric rings around the beam axis. The rings contained 12, 24, or 48 towers. Each tower was shaped like a trapezoid, with different height and width depending on polar angle, but with constant front and rear surface areas of 36 cm<sup>2</sup> and 55 cm<sup>2</sup> respectively, and a length of 20 cm.

A particle being emitted from the interaction area encountered 12.5 radiation lengths of material by traversing the calorimeter; a photon would lose all its energy by electromagnetic interactions in the lead. The emitted light was collected by a conically shaped acrylic light-guide glued to the rear face of each tower and connected to a photomultiplier. The energy resolution was  $\sigma_E/E \approx \frac{0.06}{\sqrt{E(\text{GeV})}}$  [?].

The purpose of the barrel gamma veto counter (fig 3.25) was to detect photons from the decay of neutral mesons and then to veto those events. This detector was also made of lead and plastic scintillator fibers, but with the fibers parallel to the beam. It had a cylindrical geometry similar to the barrel Cherenkov, segmented into 24 wedge-shaped elements in the azimuthal direction. Each element was 6 radiation lengths thick. The readout was done by a 5 cm photomultiplier at one end.

### The RICH counter

The RICH counter (figure 3.26) was installed in the experiment after the first year of data-taking [?]. The purpose of this detector was to measure the  $\beta$  value of the particles by reconstructing the opening angle for Cherenkov light. The photons emitted by the particle passing through the Cherenkov radiative material were projected onto a photon detector, which reconstructed the ring of Cherenkov light, and hence the Cherenkov angle. The RICH

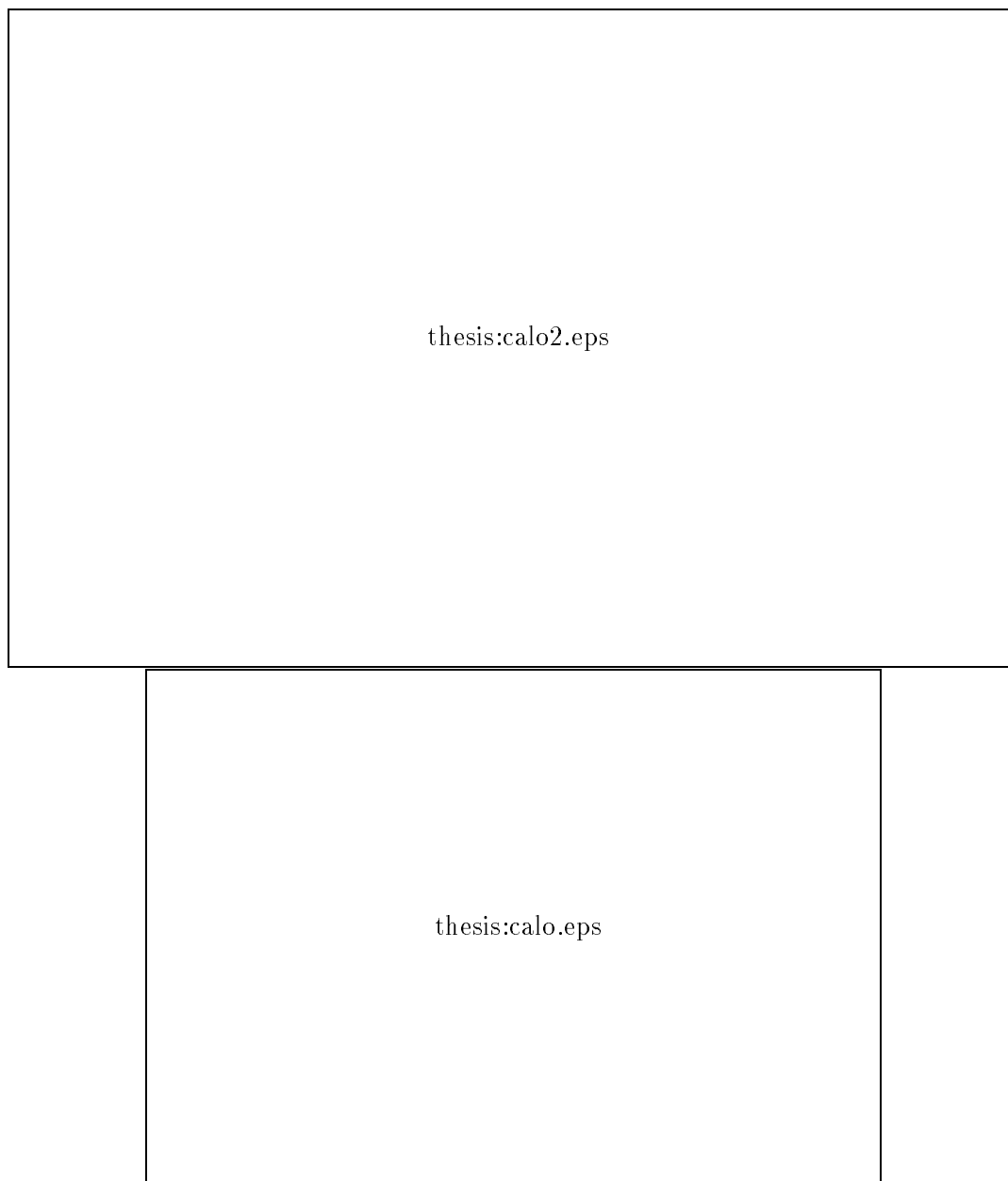


Figure 3.24: *Front and side view of the forward calorimeter (top) and calorimeter module including light guide and photomultiplier (bottom) (from [?]).*

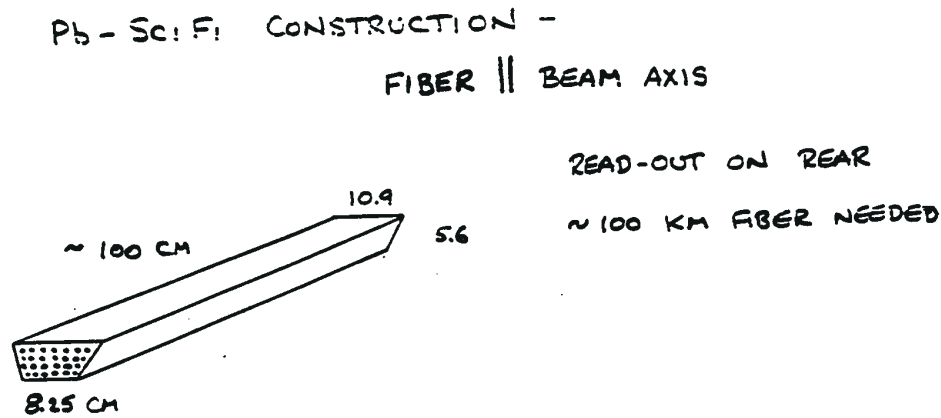


Figure 3.25: An element of the barrel gamma veto counter (from [?]).

detector had a conical shape, and featured 1 cm of quartz (fused silica) radiator ( $\beta_{thr}=0.64$ ), and a photon detector, based on the photosensitive gas TMAE, consisting of a pixel array of proportional chambers. The gap between the radiator and the detector was about 7 cm. The photon detector consisted of 76 modules arranged on a square grid, within a circle of radius 35 cm. Each module contained  $8 \times 8$  detector cells, where each cell had dimensions  $8 \text{ mm} \times 8 \text{ mm} \times 20 \text{ mm}$ , with a single wire passing along the long axis. In the middle there was a hole where  $2 \times 3$  modules had been left out to make room for the beam pipe. The RICH was placed between the silicon dE/dx and the forward threshold Cherenkov, and could reconstruct  $\beta$  for tracks with a polar angle between 20 and 35 degrees. A resolution of  $\frac{\Delta\beta}{\beta} \approx 2\%$  was obtained. The main limit of the  $\beta$  resolution was shown to be the finite tracking resolution of the JETSET tracker, which dominated over the chromatic dispersion and photon detection resolution of the RICH counter.

### The silicon luminosity monitor system

This system [?] was installed in 1992, after the first year of data taking. The purpose was to monitor the luminosity, both online and offline, by triggering on elastic events where the recoil proton hit the silicon luminosity detector. The system was divided in 4 different detectors, located in the barrel region, installed symmetrically with respect to the beam, at the  $\phi$ -angles shown in table 3.5. Each detector covered a region in azimuthal angle  $\phi$  of about 5 degrees, and contained 10 silicon strips, each with a thickness of  $500 \mu\text{m}$  and an area of  $24 \text{ mm} \times 6 \text{ mm}$ , arranged so the total area of the detector was  $24 \text{ mm} \times 60 \text{ mm}$ , and with the longer side of the detector parallel to the beam. The polar angle covered was between 59 and 72 degrees.



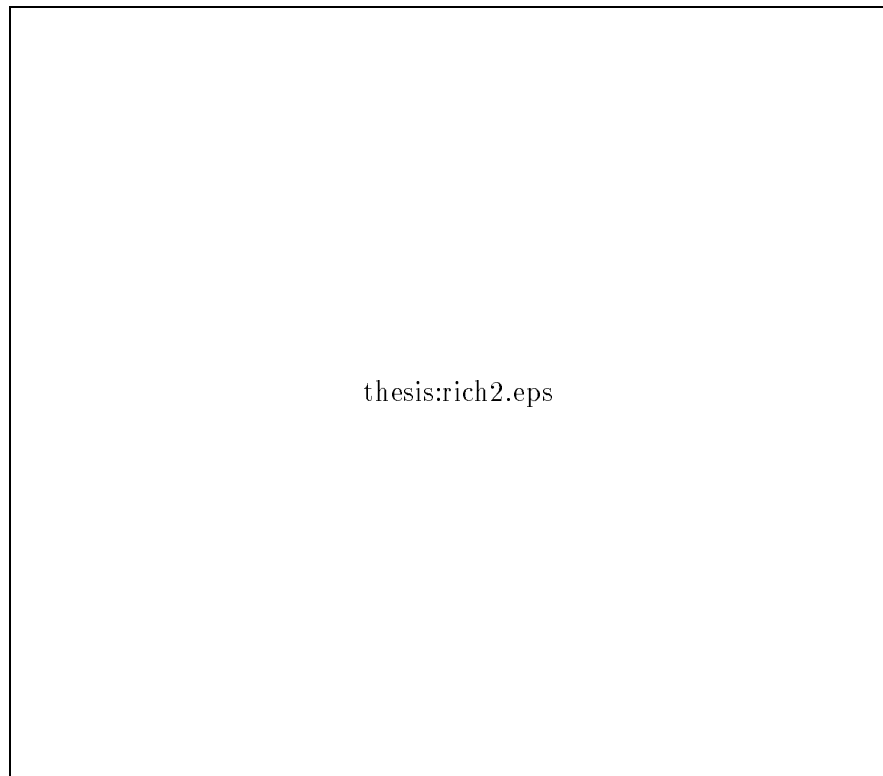


Figure 3.26: *View of one half of the RICH counter (from [?]).*

Detector	$\phi$
1	38.20
2	340.8
3	145.3
4	202.6

Table 3.5: *Azimuthal angles for the silicon strip detectors.*

### The barrel silicon

The purpose of this detector was to provide dE/dx information for tracks in the barrel region [?]. This system was installed in 1992, and it has not been used in most of the analysis presented in this thesis. It was installed between the barrel straws and the barrel Cherenkovs, at a radial distance of about 21 cm. The silicon crystals had an area  $4.5 \text{ mm} \times 22.6 \text{ mm}$  and were parallel to the beam axis. The electronics were similar to those of the forward silicon.

### The $z$ -chamber

This chamber was a multi-wire proportional chamber, with wires perpendicular to the beam axis, and a hexagonal shape, at a radial distance of about 23 cm. This detector was introduced to provide a measurement of the  $z$ -coordinate (coordinate along the beam axis) for the barrel tracks. It was useful for the calibration of the  $z$ -coordinate measurement via charge division from the barrel straws tracker.

## 3.3 Triggering

With a luminosity of  $\mathcal{L} \approx 10^{30} \text{ cm}^{-2} \text{ s}^{-1}$  and a total cross section  $\sigma(p\bar{p} \rightarrow \text{anything}) = 100 \text{ mb}$  there were about  $10^5$   $p\bar{p}$  interactions occurring each second. The trigger reduced this number to an acceptable event rate of about 100 Hz. This was done by concentrating on the following salient characteristics of the  $p\bar{p} \rightarrow 4K$  and  $p\bar{p} \rightarrow \phi\phi \rightarrow 4K$  events: They had four and only four prongs, they were forward of  $65^\circ$  in the lab frame, at least three of the four particles were almost always forward of  $45^\circ$  (see figures 3.27 and 3.28), they had moderate  $\beta$  values (figures 3.29 and 3.29), and no photons. The cross sections for the most important background reactions are shown in figure 3.4. From figures 3.27 to 3.30 it can be seen that by making cuts on the particle velocity  $\beta$ , and on the polar angle  $\theta$ , a large part of the background events with four charged particles will be removed. This was done by the trigger conditions on the pipe scintillator and Cherenkov multiplicity.

There were also cuts to check momentum conservation (not all tracks on one side), and criteria on the outer scintillator multiplicity to ascertain that the events had four clean tracks going through the detector.

The reaction  $\bar{p}p \rightarrow \bar{p}p\pi^+\pi^-$  had an event signature looking very much like  $\bar{p}p \rightarrow 4K$  and had to be removed offline. At high momenta (1.9 GeV/c) a large percentage of this reaction was expected in the trigger sample. The offline cut on barrel gamma veto and calorimeter removed events with neutral particles like  $\bar{p}p \rightarrow 2\pi^+2\pi^-\pi^0$ , which were also a large part of the trigger sample at high momenta.

The trigger conditions for  $4K$  events were [?]

- Pipe scintillator multiplicity of four charged particles, either all four in the forward (15-45 degrees) scintillators, or three in the forward and one in the barrel (45-65 degrees) scintillators. A total of 4 or 5 hits in the sum of forward and barrel pipes, and 0 or 1 hit in the barrel pipe scintillator was accepted. Symbolically this can be expressed

$$(4 \leq AP \leq 5) \cap (BP \leq 1), \quad (3.11)$$

where AP= All Pipes, BP =Barrel Pipes.

- A barrel and forward veto condition demanded that there were no hits in the outer barrel scintillator if no barrel pipe scintillators were hit, and that there were no hits in the cylindrical scintillator placed around the beam pipe in the extreme forward part of the detector. This is expressed symbolically as follows:

$$((BP > 0) \cup \overline{(2/3BJ)}) \cap \overline{FV}. \quad (3.12)$$

2/3BJ means the “2/3 Jülich barrel” signal signifying that two out of the three layers in the outer barrel hodoscope fired.

FV = Forward Veto.

- A maximum multiplicity of one or two of the threshold Cherenkov counters, depending on the incident antiproton momentum. Here a variety of logical conditions were used:

$$\begin{aligned} (FC \leq 2) \cap (BC \leq 2), & \quad (3.13) \\ (FC \leq 2) \cap (BC \leq 1), \\ (AC \leq 2) \cap (BC \leq 1), \\ (FC \leq 1) \cap (BC \leq 1), \\ (AC \leq 1). \end{aligned}$$

AC= All Cherenkov, BC = Barrel Cherenkov, FC = Forward Cherenkov.

Table 3.6 shows the Cherenkov trigger conditions during the 1991 run, where both freon and water were used in the Cherenkovs.

- An azimuthal interval  $\Delta\phi < 180^\circ$  between two successive particles. If the pipe scintillators are divided into four quadrants Q1-Q4, including both barrel and forward counters, this can be approximated by the following condition:

$$(Q1 \cup Q2) \cap (Q2 \cup Q3) \cap (Q3 \cup Q4) \cap (Q4 \cup Q1). \quad (3.14)$$

- The forward and barrel outer scintillator multiplicity had to satisfy the following conditions:

$$(2/3FJ \cap (FJ \geq 1) \cap (BJ = 0 \cup (2/3BJ \cap BJ \leq 2))). \quad (3.15)$$

FJ = “most of three” the multiplicity of the forward Jülich hodoscope layer with maximum hits.

BJ = “most of three” the multiplicity of the barrel Jülich hodoscope layer with maximum hits.

This cut ensured that there was at least one hit in the outer forward scintillators.

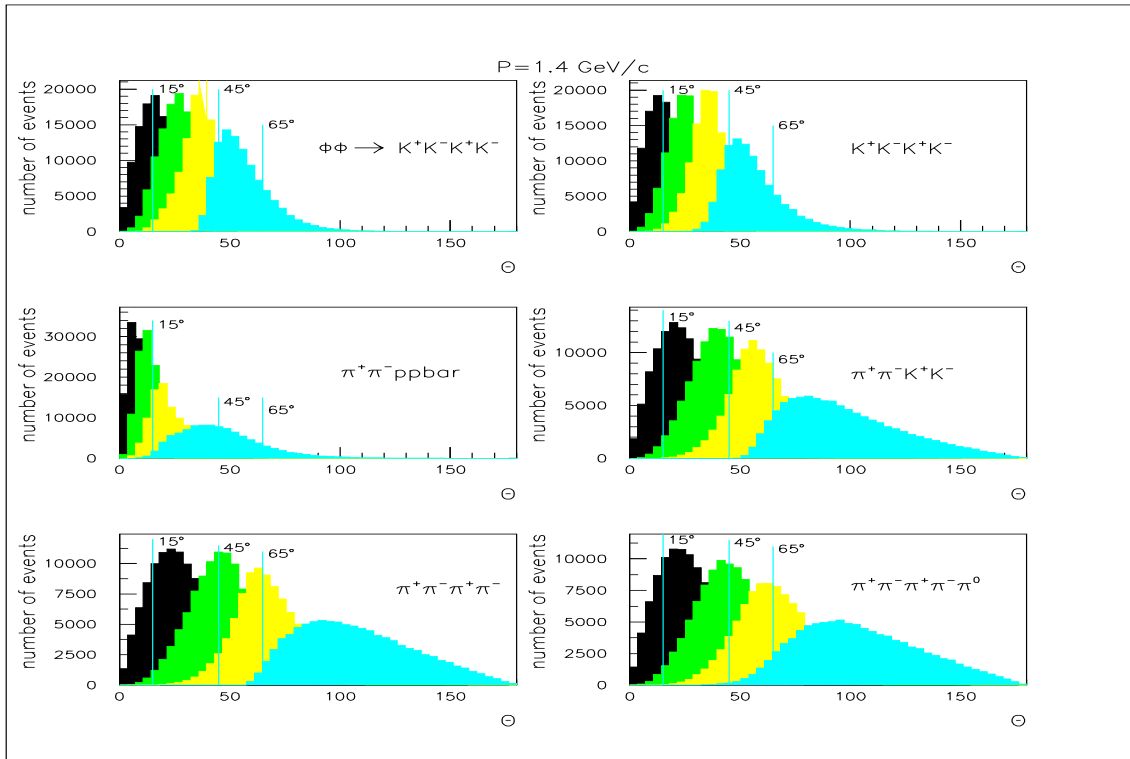


Figure 3.27: Distributions of polar angle for the four particles in  $p\bar{p} \rightarrow \phi\phi \rightarrow 4K$ , the nonresonant  $p\bar{p} \rightarrow 4K$ , and background reactions with 4 charged prongs, when the beam momentum is  $1.4 \text{ GeV}/c$ . The tracks are sorted in order of ascending  $\theta$ . The acceptance limits of the pipe scintillators (15-45 degrees and 45-65 degrees) are indicated. From Monte Carlo simulations.

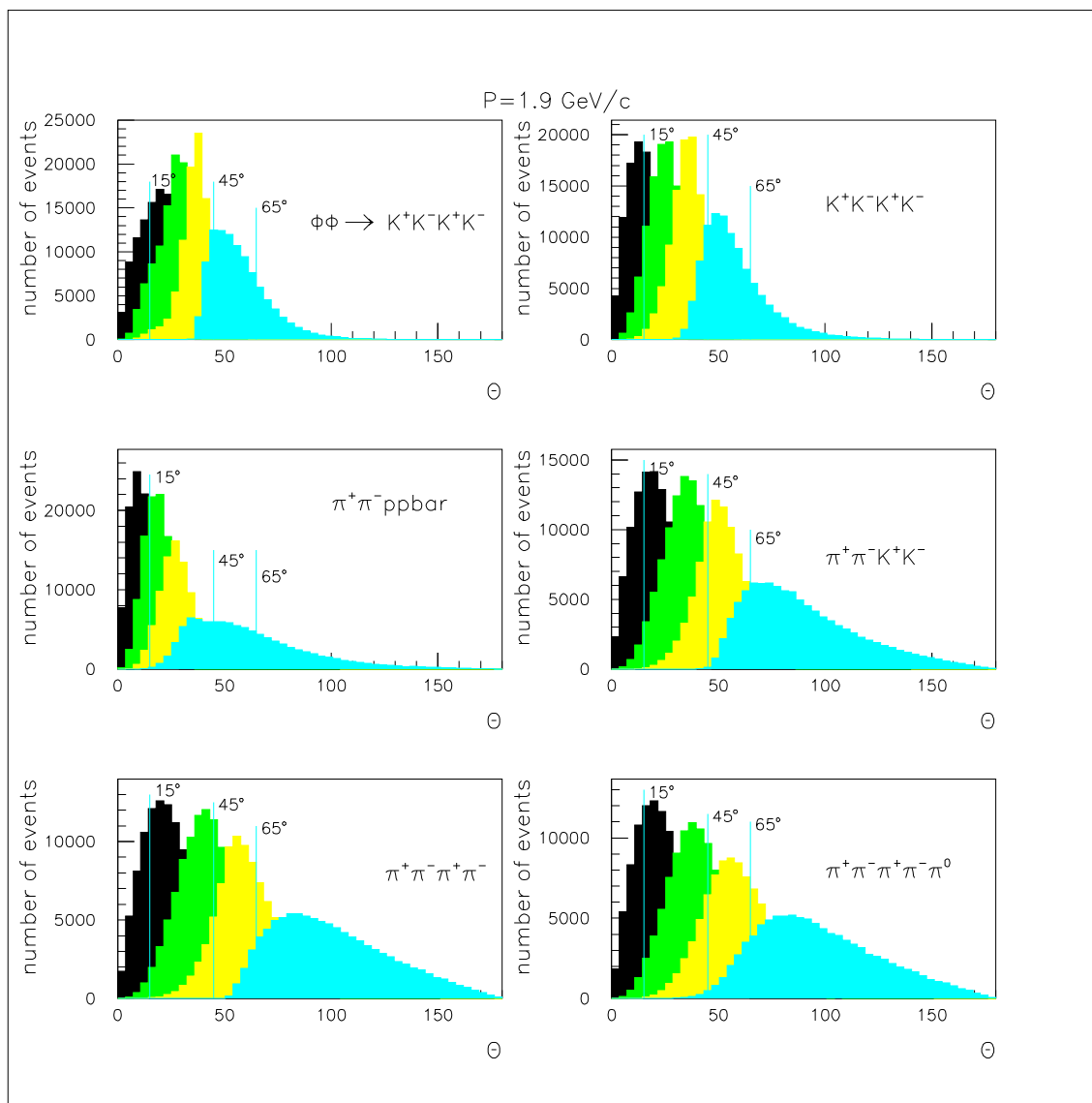


Figure 3.28: Distributions of polar angle for the four particles in  $p\bar{p} \rightarrow \phi\phi \rightarrow 4K$ , the nonresonant  $p\bar{p} \rightarrow 4K$ , and background reactions with 4 charged prongs, when the beam momentum is  $1.9 \text{ GeV}/c$ . The tracks are sorted in order of ascending  $\theta$ . The acceptance limits of the pipe scintillators (15-45 degrees and 45-65 degrees) are indicated. From Monte Carlo simulations.

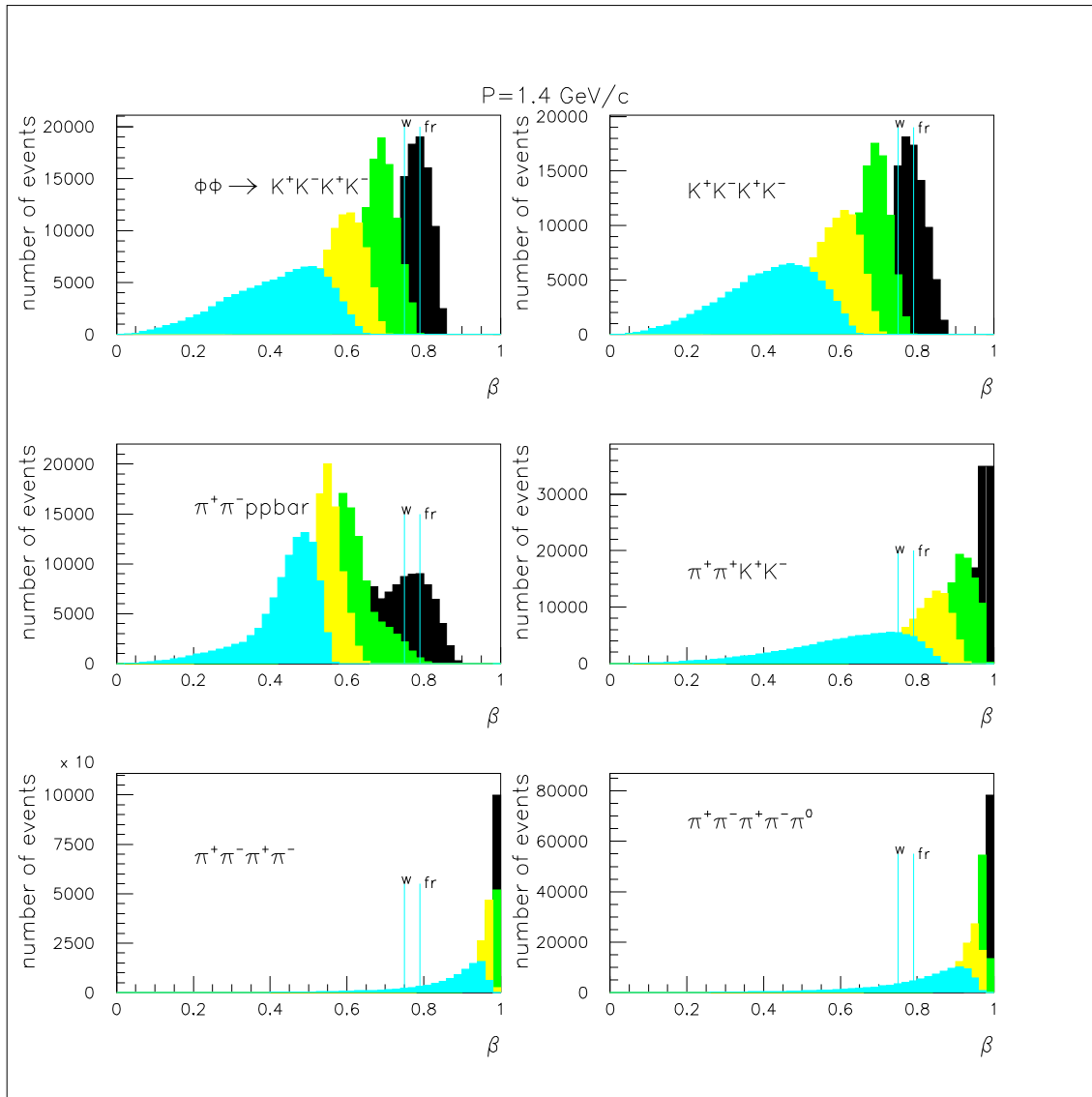


Figure 3.29: Distributions of  $\beta$  for the four particles in  $p\bar{p} \rightarrow \phi\phi \rightarrow 4K$ , the nonresonant  $p\bar{p} \rightarrow 4K$ , and background reactions with 4 charged prongs, when the beam momentum is 1.4 GeV/c. The tracks are sorted in order of ascending  $\beta$ . The  $\beta_{\text{threshold}}$  values for water and freon, both of which have been used in our Cherenkov counters, are indicated. From Monte Carlo simulations.

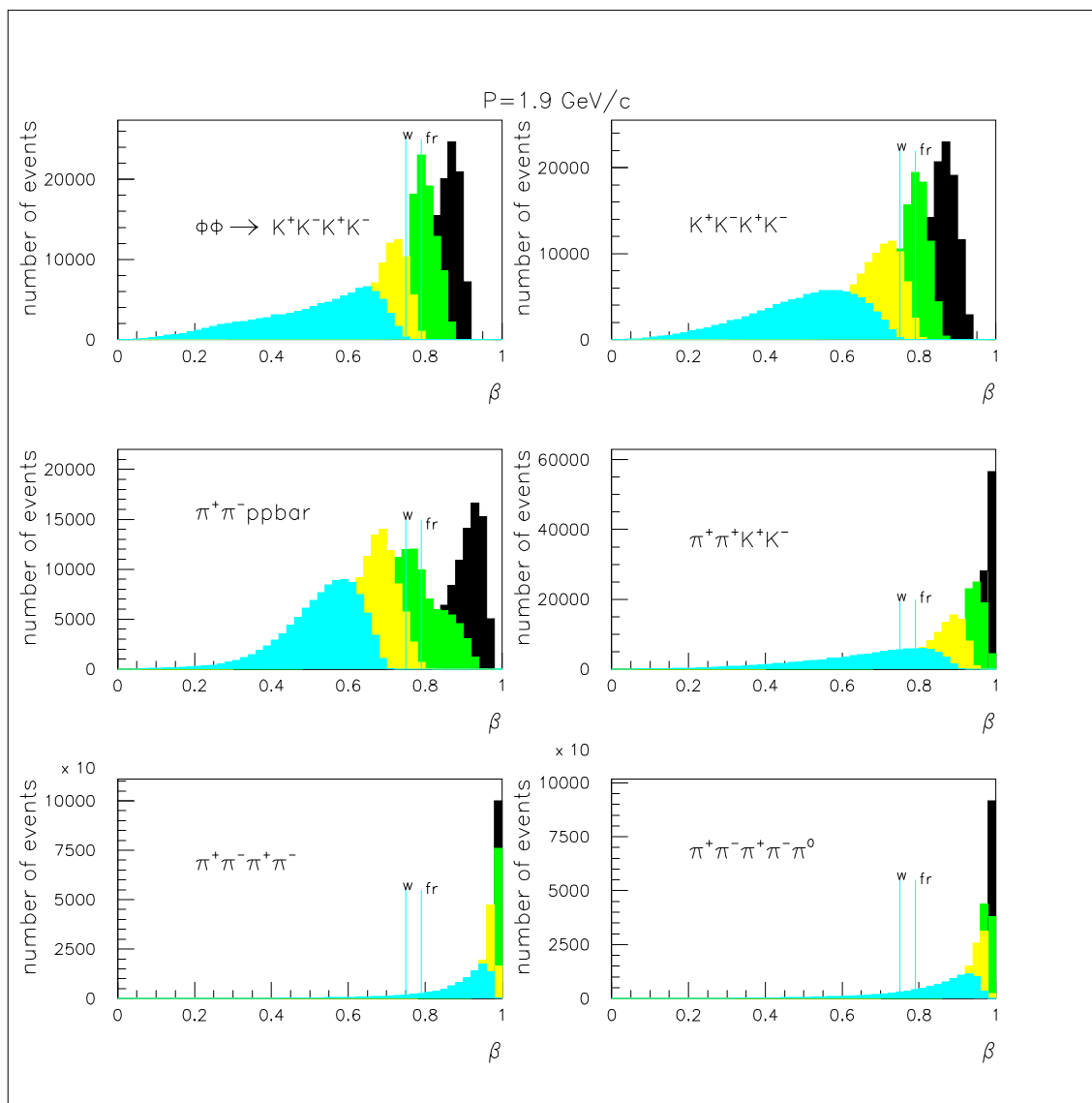


Figure 3.30: Distributions of  $\beta$  for the four particles in  $p\bar{p} \rightarrow \phi\phi \rightarrow 4K$ , the nonresonant  $p\bar{p} \rightarrow 4K$ , and background reactions with 4 charged prongs, when the beam momentum is 1.9 GeV/c. The tracks are sorted in order of ascending  $\beta$ . The  $\beta_{\text{threshold}}$  values for water and freon, both of which have been used in our Cherenkov counters, are indicated. From Monte Carlo simulations.

	Radiator		Threshold( P.E.)		Momentum (GeV/C)	Multiplicity		
	BC	FC	BC	FC		AC	FC	BC
'Large scan'	Freon	Freon	$\leq 1$	$\leq 1$	1.9	$\leq 2$	-	$\leq 1$
					1.7,1.5	-	$\leq 1$	$\leq 1$
					1.8	$\leq 2$	-	$\leq 1$
					1.6,1.4	$\leq 1$	-	$\leq 1$
					1.3,1.2	$\leq 1$	-	$\leq 1$
'Fine scan'	Freon	Water	$\leq 1$	$\leq 5$	all	-	$\leq 1$	$\leq 1$

Table 3.6: *Cherenkov trigger conditions during the 1991 JETSET runs. There were two run periods with a 'large scan' and a 'fine scan', with different radiators in the forward Cherenkov, different photo-electron thresholds, and varying trigger conditions. (BC= barrel Cherenkov, FC = forward Cherenkov, AC= all Cherenkov.)*

Other triggers were also collected. These triggers were prescaled in order to collect the maximum number of 4K events and at the same time provide adequate samples of the others.

- The **4 $\pi$  trigger**, which consisted of the first two conditions in the 4K trigger. The purpose of this trigger was to study the performance of the 4K trigger, especially the efficiency of the Cherenkov detectors.
- The **elastic trigger** requested one forward pipe-scintillator hit, and one in the barrel, and no more than one Cherenkov hit. The conditions from the outer scintillators were the same as for the 4K trigger. The elastic trigger was used for detector (straws, silicon, Cherenkov) calibration and alignment, as well as for calculating the luminosity.
- The  **$K_s K_s$  trigger** required two to three forward Cherenkov signals, one to two barrel Cherenkov signals, and no hits in the pipe scintillators. In addition, three to four hits in the outer scintillators and no hits in the first ring of the forward calorimeter was demanded.
- The **neutral trigger** required no hits in either pipe scintillators or outer scintillators, together with at least one hit each in the forward calorimeter and barrel gamma veto.
- The **luminosity trigger** (from June 1992 onwards) consisted of a coincidence of a silicon strip detector and a pixel (made of a right and a left forward scintillator) in the region allowed by elastic kinematics. This trigger collected elastic events to measure the luminosity (see chapter 6). With this trigger the luminosity could be calculated online.



### 3.4 The data acquisition system

The data acquisition system made use of the CERN-developed, VME based Valet-Plus system. Each of the detector components was controlled by an independent Valet-Plus system [?] with CAMAC and fastbus readout buses. Four Valets dealt with the various detectors, grouped as follows :

1. *Pipe scintillators* and *Cherenkovs* (ADC plus pattern units), and the *RICH*.
2. *Forward Calorimeter*, *Barrel  $\gamma$  veto*, and *Outer scintillators*, with a total of 1000 channels of fastbus ADC and scintillator TDC information.
3. *Straw trackers* with a total of 3000 fastbus channels (ADC and TDC information for charge division and straw drift time), and data from the z-chamber.
4. *Silicon counters* with the zero suppressed multiplexed ADC system (DRAMS).

The signals from the Valets were collected by four T800 transputers and sent to a fifth Valet, called the *event-builder*, which formatted the data into an event and wrote it onto IBM 3812 cartridges. The information for one event was between 1.5 and 2.5 Kbytes, and was written out to tape at a maximum rate of 200 events/sec. The Valets were controlled, and the data were monitored on a cluster of VAX stations. Events were also sent from the event builder Valet to the VAX-cluster where events were decoded online, and an event display program used to monitor the events. Scaler information and information from the LEAR VAX about the beam profile was recorded on tape, as well as in the logbook.

## Chapter 4

# Selection of the reaction $\bar{p}p \rightarrow 4K^\pm$

The analysis chain used to select  $\bar{p}p \rightarrow 4K^\pm$  events consisted of the following steps :

- Reduction from raw tapes, using only the pattern of pipe scintillator hits.
- Geometrical reconstruction, requiring 4 tracks coming from the nominal vertex area.
- First step event selection, requiring that the event contains sufficient detector information to be reconstructed.
- Kinematical reconstruction of the event, assuming  $4K$  masses or some other (background reaction).
- Kinematical cuts.
- Particle Identification (PID) cuts: Compatibility with silicon and Cherenkov detectors.
- Removal of the large  $\bar{p}p \rightarrow \bar{p}p\pi^+\pi^-$  background.
- Stability cuts.

### 4.1 Data collected

The JETSET experiment collected data from 1991 to 1994, with a beam momentum between 1.2 GeV/c and 2.0 GeV/c. The trigger cuts are described in chapter 3. The main aim was to collect  $\bar{p}p \rightarrow 4K$  events; elastic events,  $4\pi$  triggers etc., were collected simultaneously, but with prescaled triggers. There were typically two run periods each year, each run lasting a few weeks. During the various runs different scans were performed.

Coarse scans had steps in the beam momentum of 0.1 GeV/c, to measure the cross sections of  $\bar{p}p \rightarrow \phi\phi \rightarrow K^+K^-K^+K^-$  ,  $\bar{p}p \rightarrow \phi KK \rightarrow K^+K^-K^+K^-$  , and  $\bar{p}p \rightarrow K^+K^-K^+K^-$  as a function of energy over the whole available energy range. Fine scans had steps in beam momentum of 0.015 GeV/c over a small energy range to search for specific resonances in  $\bar{p}p \rightarrow \phi\phi$ .

Beamtime	Beam momentum GeV/c	c.m. energy GeV	4K triggers	4K reduced
April	1.500	2.254	1 152 874	379 098
	2.000	2.430	4 309 023	2 048 167
July	1.900	2.395	5 426 141	2 694.052
	1.700	2.324	4 794 052	2 290 081
	1.500	2.254	1 853 184	855 946
	1.800	2.360	6 803 367	3 385 611
	1.600	2.289	4 129 815	1 924 725
	1.400	2.218	5 592 226	2 430 516
	1.300	2.183	5 641 730	2 458 644
	1.200	2.149	1 709 731	725 019
October	1.500	2.254	2 493 578	1 057 281
	1.405	2.220	3 130 671	1 502 314
	1.435	2.231	6 080 740	2 938 636
	1450	2.236	6 136 854	3 049 675
	1465	2.241	3 241 521	1 565 961
	1.420	2.225	6 477 255	2 766 080
	1.480	2.247	3 766 922	1 820 944
	1.390	2.215	886 074	463 573

Table 4.1: 1991 runs. Beam momenta, total centre-of-mass energy, number of 4K triggers, and number of events after reduction (section 4.2.1).

In tables 4.1 to 4.4 the numbers of 4K triggers, together with the number of events after reduction (section 4.2.1), collected in the various run periods are shown. This chapter describes the analysis to select 4K events from the collected 4K triggers, as well as background and acceptance determinations for this chain.

To justify many of the cuts in this analysis, and to find the resolution of detectors and efficiency of the trigger and analysis, simulated data, produced with a Monte Carlo program using the GEANT [?] package, were used. This program, described in section 4.4, simulated the kinematics of the reaction, and the geometry and response of the detector components.

Beamtime	Beam momentum GeV/c	c.m. energy GeV	4K triggers	4K reduced
June	1.505	2.256	1 103 702	553 513
	1.950	2.413	6 846 195	4 025 516
	1.750	2.342	10 531 630	6 880 473
	1.650	2.307	9 336 572	6 072 357
December	1.506	2.256	12 905 276	8 296 713
	1.465	2.242	16 581 199	10 571 782
	1.405	2.221	15 360 583	9 837 746
	1.435	2.231	11 403 371	7 289 444
	1.390	2.215	9 375 019	5 869 325

Table 4.2: 1992 runs. Beam momenta, total centre-of-mass energy, number of 4K triggers, and number of events after reduction (section 4.2.1).

Beamtime	Beam momentum GeV/c	c.m. energy GeV	4K triggers	4K reduced
May	1.415	2.224	59 900 000	29 932 877
	1.360	2.205	19 358 847	12 114 721
	1.330	2.194	19 368 014	12 131 743
	1.800	2.360	96 200 000	41 647 188
August	2.000	2.430	29 445 657	
	1.400	2.219	9 334 527	
	1.405	2.221	7 244 903	
	1.410	2.222	7 329 674	
	1.415	2.224	7 084 273	
	1.420	2.226	7 938 003	
	1.425	2.228	7 763 273	
	1.430	2.229	8 177 105	
	1.435	2.231	7 544 384	
	1.440	2.233	8 010 652	
	1.445	2.235	7 220 451	
	1.237	2.162	7 199 169	
	1.246	2.165	4 740 405	
	0.850	2.034	893 380	
	1.188	2.145	6 955 317	
1.278	2.176	3 336 506		

Table 4.3: 1993 runs. Beam momenta, total centre-of-mass energy, number of 4K triggers, and number of events after reduction (section 4.2.1). For run periods from August 93 and later, the reduction cuts were implemented in the 4K trigger, thus the number of reduced events is the same as the number of triggered events.

Beamtime	Beam momentum GeV/c	c.m. energy GeV	4K triggers	4K reduced
August	1.500	2.254	8 082 891	
	1.380	2.212	20 429 408	
	1.345	2.200	20 883 045	
	1.315	2.189	19 878 513	
	1.220	2.156	19 954 491	
	1.260	2.170	23 579 642	
	1.180	2.142	16 683 080	
	1.200	2.149	17 815 470	
	1.240	2.163	19 462 399	
	1.280	2.177	18 971 449	
	1.550	2.272	17 058 823	
	1.500	2.254	5 447 684	

Table 4.4: 1994 runs. Beam momenta, total centre-of-mass energy, number of 4K triggers, and number of events after reduction (section 4.2.1). For run periods from August 93 and later, the reduction cuts were implemented in the 4K trigger, thus the number of reduced events is the same as the number of triggered events.

## 4.2 Data analysis

### 4.2.1 Reduction

The first stage of the data analysis consisted of reducing the initial sample by requiring the following three conditions:

- The pipe scintillator pattern had to be 3-1, 4-0, or 4-1. The first number is the multiplicity of the forward pipe scintillators, the second the multiplicity of the barrel pipe scintillators.
- The maximum difference in azimuthal angle  $\phi$ , between two adjacent pipe scintillator hits, was not allowed to exceed  $180^\circ$ .
- If the hit pattern in the pipe scintillators was 4-1, then the barrel pipe scintillator hit had to overlap in  $\phi$  with one of the forward pipe scintillators hit.

These cuts, operating only on the pattern of pipe scintillator hits in the event, comprised necessary conditions for the reconstruction of a final state with four charged particles consistent with momentum conservation.

The events satisfying these conditions were written to special reduction tapes with the same format as the raw data. In addition, scalers and LEAR records were written onto the reduction tapes. The fourth column in tables 4.1 to 4.4 shows the number of events left after reduction. For run periods from August 93 and later, the reduction cuts were implemented in the 4K trigger, thus the reduction tapes were just copies of the raw tapes for these data.

### 4.2.2 Geometrical reconstruction of the events

There was no magnetic field in the JETSET detector, hence the tracks were straight lines. The geometrical reconstruction was performed under the assumption of four charged prongs coming from a common vertex inside the target region.

The track finding and fitting were done using projections. In the forward straw tracker a particle trajectory inside the geometrical acceptance crossed the separate layers of vertical and horizontal straws, which gave projections of the track in the  $zx$  and  $zy$  planes (the  $z$ -axis was parallel to the beam, and the  $x$  and  $y$  axes followed the horizontal and vertical directions perpendicular to the beam respectively). A particle trajectory crossing the barrel tracker gave a projection in the  $xy$  plane and a projection in the  $uz$  plane, where  $u$  is the coordinate along the  $xy$  projection. To find the tracks in the  $zx$ ,  $zy$ , and  $xy$  projections, the angular coordinates of the straws were calculated and ordered. Then tracks with small angular separations were grouped together and fitted to a straight line. The straws were regrouped using bands around the fitted lines, this procedure was repeated until the groups were stable.

#### The track fit

The track fitting was done using the TDC and ADC information from the straw tracker. The TDC signal measured the distance from the wire in the straw centre to the traversing particle, defining a circle around the wire that was tangential to the track (page 83). There was a “left-right” ambiguity since it was not known at which side of the wire the particle trajectory passed. In the barrel, the TDC readout gave a measurement of the distance from the straw centre to the passing track in the  $xy$  projection. The forward straws TDC readouts gave a measurement of the distance to the straw centre in either the  $zx$  or  $zy$  projection. The barrel straws also had ADC readouts, which gave a measurement of the longitudinal ( $z$ ) coordinate where the track crossed a straw (page 85).

The straight lines to be fitted were described by the following two equations:

$$F(x, y) = x \sin \phi - y \cos \phi + l_{xy} = 0, \quad (4.1)$$

$$G(z, x, y) = (z - b)/a - y \sin \phi - x \cos \phi = 0. \quad (4.2)$$

The 4 parameters for the tracks are defined as follows :

$l_{xy}$  = distance from the origin to the closest point on the line in the  $xy$  -plane.

$b$  =  $z$ -coordinate for this point.

$\phi$  = azimuthal angle of the track,  $0 \leq \phi \leq 2\pi$ .

$a = \cot \theta$  where  $\theta$  is the polar angle between the velocity vector and the  $z$ -axis.

These two equations are appropriate when fitting barrel tracks. For forward tracks, where projections in  $zx$  and  $zy$  were measured, it is more convenient to use the following two equations, which describe the track projections in the  $zx$  and  $zy$  planes.

$$F(z, x) = -z \sin \theta_{zx} + x \cos \theta_{zx} - l_{zx} = 0, \quad (4.3)$$

$$F(z, y) = -z \sin \theta_{zy} + y \cos \theta_{zy} - l_{zy} = 0, \quad (4.4)$$

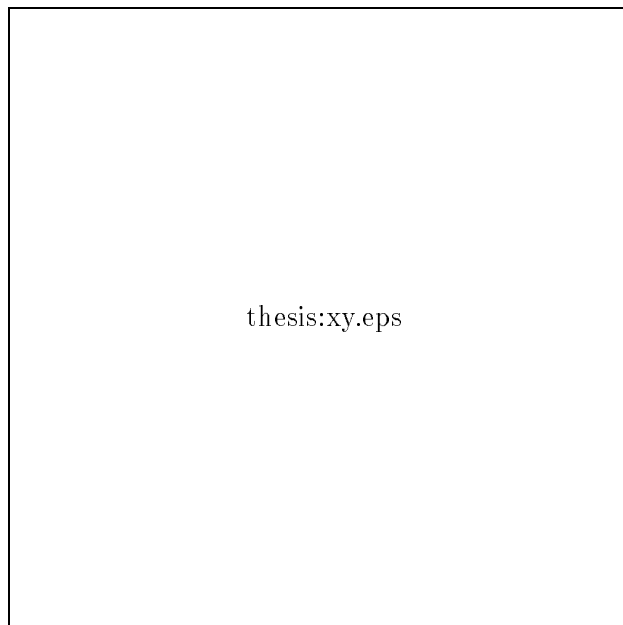


Figure 4.1: *Impact point for a track in the  $xy$  projection.  $x_i^c, y_i^c$  are the coordinates of the straw centre,  $D_i$  the distance from the straw wire to the track.  $x$  and  $y$  are the impact coordinates for a track with azimuthal angle  $\phi$ .*

where  $\theta_{zx}$  is the angle between the  $z$  axis and the track in the  $zx$  projection,  $\theta_{zy}$  is the angle between the  $z$  axis and the track in the  $zy$  projection, and  $l_{zx}, l_{zy}$  the closest distance of the track to the origin in the two projections. The connection between  $a$  and  $\phi$ , and  $\theta_{zx}$  and  $\theta_{zy}$  is

$$\theta_{zx} = \arctan \frac{\cos \phi}{a}, \quad (4.5)$$

$$\theta_{zy} = \arctan \frac{\sin \phi}{a}. \quad (4.6)$$

The method of least squares was used to find the best values of the track parameters [?], hence it was necessary to calculate the expected values of  $D_i$ , the distance of the track from the centre of each straw ( $D_i^{exp}$ ), and  $z_i$  the longitudinal coordinate ( $z_i^{exp}$ ).

The impact points for the tracks in the  $xy$  plane are given by (see figure 4.1).

$$\begin{aligned} x &= x_i^c + \epsilon D_i \sin \phi, \\ y &= y_i^c - \epsilon D_i \cos \phi, \end{aligned} \quad (4.7)$$

where  $x_i^c$  and  $y_i^c$  are the coordinates of the straw centre, and  $D_i$  the distance of the track from the centre of this straw.  $\epsilon$  has a value of +1 or -1, depending on which side of the straw centre the track passed.

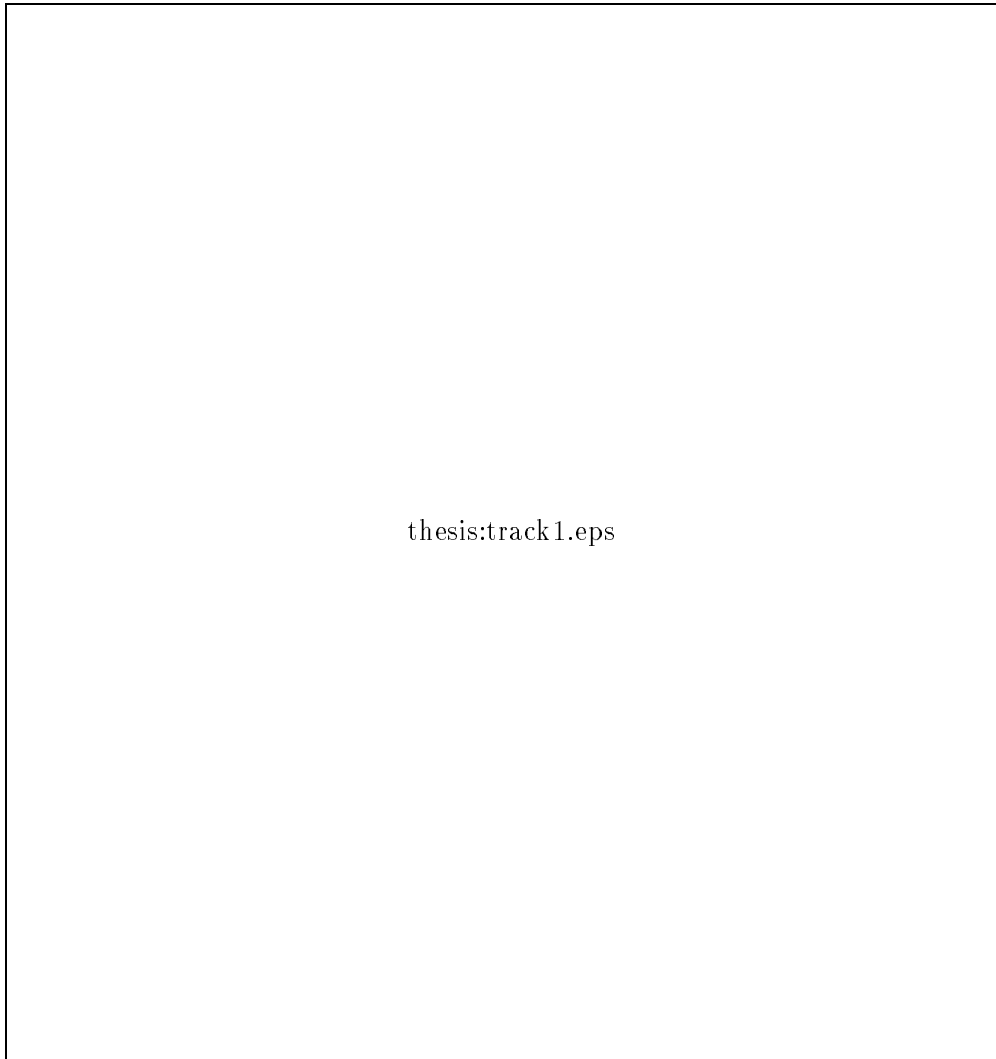


Figure 4.2: *Example of an event with two fitted track in barrel straws, xy projection. The boundary of the straw tracker, which was a cylinder with an elliptical hole in the middle, is indicated by the two large half circles and the inner ellipse. The rectangles adjacent to the ellipse show hits in the barrel and forward pipe scintillators. The circles show the hits in the straws. The radius of each circle show the distance from each straw wire to the traversing tracks, measured by the drift-time.*



Inserting these two values into equations 4.1 and 4.2, and solving for  $D_i$  and  $z_i$  to find the expected value of the barrel straw measurement we get:

$$D_i^{\epsilon xp} = -\epsilon[x_i^c \sin \phi - y_i^c \cos \phi + l_{xy}], \quad (4.8)$$

$$z_i^{\epsilon xp} = a(x_i^c \cos \phi + y_i^c \sin \phi) + b. \quad (4.9)$$

$\epsilon$  was chosen to make  $D_i^{\epsilon xp} > 0$ .

For the straws parallel to the  $y$ -direction the two impact points  $z$  and  $x$  of the track are

$$z = z_i^c + \epsilon D_i^m \sin \theta_{zx}, \quad (4.10)$$

$$x = x_i^c - \epsilon D_i^m \cos \theta_{zx},$$

where  $x_i^c, z_i^c$  are the coordinates for the straw centre and  $\epsilon = \pm 1$  as for the barrel tracks. Inserting this into equation 4.4 gives the expected value

$$D_i^{\epsilon xp} = -\epsilon[z_i^c \sin \theta_{zx} - y_i^c \cos \theta_{zx} + l_{zx}]. \quad (4.11)$$

Doing a similar calculation for the straws parallel to the  $x$ -direction, gives

$$D_i^{\epsilon xp} = -\epsilon[z_i^c \sin \theta_{zy} - y_i^c \cos \theta_{zy} + l_{zy}], \quad (4.12)$$

where  $z_i^c$  and  $y_i^c$  are the coordinates of the straw centre, and  $\epsilon = \pm 1$ .

The straight line fits in the  $xy, zx$ , and  $zy$  projection were done separately.

The sum of squares to be minimized to find the straight lines in each projection was

$$X^2 = \sum_{i=1}^n \frac{(D_i^{\epsilon xp} - D_i^{meas})^2}{(\sigma_i^r)^2}, \quad (4.13)$$

where  $n$  is the number of drift-time measurements in the straw in this projection,  $D_i^{\epsilon xp}$  the expected (calculated) value of the distance from the track to the straw-centre,  $D_i^{meas}$  the measured value of this distance, and  $\sigma_i^r$  the resolution of this measurement.

An iterative procedure was used to find the minimum of  $X^2$ . In the first fit all measured radii were set equal to zero, thus a line going through the straw centers was fitted. In the next fit this was used to determine on which side of the straw centre the track passed, which gave the sign of  $\epsilon$ . If the tracks had only a few straws (less than 6), all the left-right possibilities were fitted and the best one kept. The mean interaction point of the  $p\bar{p}$  interactions was also used in the track fit. The uncertainty of this point was at least 10 times that of the straws (about 0.5 cm), however this extra point was important in fitting tracks with only two or three straws, which was quite common in the forward tracker. The barrel track fit was first done with the  $D$  measurements, giving the parameters in the  $xy$  plane. Then the fit with the  $z$  measurements was done, with the straws assigned in the  $xy$  projection and using the  $\phi$  angle obtained from the  $xy$  fit in equation 4.9. A straight line was fitted through  $u$  and  $z$ .

$$z = au + b, \quad (4.14)$$

$$u = x \cos \phi + y \sin \phi. \quad (4.15)$$

The sum of squares to be minimized was

$$X^2 = \sum_{i=1}^n \frac{(z_i^{\epsilon xp} - z_i^{meas})^2}{(\sigma_i^z)^2}, \quad (4.16)$$

where  $n$  is the number of  $z$  (charge-division) measurements,  $z_i^{exp}$  the expected (calculated) value of  $z$ ,  $z_i^{meas}$  the measured value, and  $\sigma_i^z$  the resolution of this measurement. This is a standard non-iterative fit.

If the observables are normally distributed, and the measurements are independent and non-correlated, the minimum value of  $X^2$  in equations 4.13 and 4.16 follows a chi-squared distribution, and is often denoted  $\chi^2$  [?].

Fitted tracks in the  $xy$ ,  $zx$ , and  $zy$  projection are shown in figures 4.2 and 4.3.

### The vertex fit

The vertex fit was done using the projected tracks. When the tracks were constrained to originate from a common vertex, a better estimate of the track parameters was obtained. In this case the track parameters for the fitted tracks were used as the measured values in a least squares fit. When the tracks were fitted individually, four parameters for each track were obtained, for a total of 16 measured values to use in the vertex fit. When all the tracks are constrained to go through a common vertex, the equation for each track  $j$ , can be written:

$$F^j(x, y) = (x - x_0) \sin \phi^j - (y - y_0) \cos \phi^j = 0, \quad (4.17)$$

$$G^j(z, x, y) = (z - z_0)/a^j - (y - y_0) \sin \phi^j - (x - x_0) \cos \phi^j = 0 \quad (4.18)$$

or in the  $zx, zy$  projections ;

$$F^j(z, x) = (z - z_0) \sin \theta_{zx}^j - (x - x_0) \cos \theta_{zx}^j = 0, \quad (4.19)$$

$$F^j(z, y) = (z - z_0) \sin \theta_{zy}^j - (y - y_0) \cos \theta_{zy}^j = 0. \quad (4.20)$$

In this case, there are 2 parameters for each track, giving the direction, and 3 for the vertex, giving a total of 11 parameters to be fitted.

The connection between the vertex parameters and the parameters for the single tracks is:

$$b = z_0 - a^j (y_0 \sin \phi^j + x_0 \cos \phi^j), \quad (4.21)$$

$$l_{xy}^j = y_0 \cos \phi^j - x_0 \sin \phi^j, \quad (4.22)$$

$$l_{zx}^j = x_0 \cos \theta_{zx}^j - z_0 \sin \theta_{zx}^j, \quad (4.23)$$

$$l_{zy}^j = y_0 \cos \theta_{zy}^j - z_0 \sin \theta_{zy}^j. \quad (4.24)$$

The  $X^2$  to be minimized when there were four forward tracks was

$$X^2 = \sum_{i=1}^3 \frac{v_i - o_i}{\sigma_i^2} + \sum_{j=1}^4 \left( \frac{(l_{zx}^{j,exp} - l_{zx}^{j,meas})^2}{v_{lzx}} + \frac{(l_{zy}^{j,exp} - l_{zy}^{j,meas})^2}{v_{lzy}} \right. \\ \left. + \frac{(\theta_{zx}^{j,exp} - \theta_{zx}^{j,meas})^2}{v_{\theta zx}} + \frac{(\theta_{zy}^{j,exp} - \theta_{zy}^{j,meas})^2}{v_{\theta zy}} \right), \quad (4.25)$$

where  $v_i$  is the vertex coordinates to be fitted ( $x_0, y_0$  and  $z_0$ ),  $o_i$  is the nominal vertex,  $\sigma_i$  the width of the nominal vertex, and  $v_{lzx}, v_{lzy}$  etc. are the squared errors on  $l_{zx}, l_{zy}$  etc. from the track fit.

The distribution of the  $x, y$  and  $z$  of the reconstructed vertex for real data, and of the difference between reconstructed and generated vertex for Monte Carlo events, are shown in figure 4.4 for  $p_{beam} = 1.5$  GeV/c in the July 1991 run.

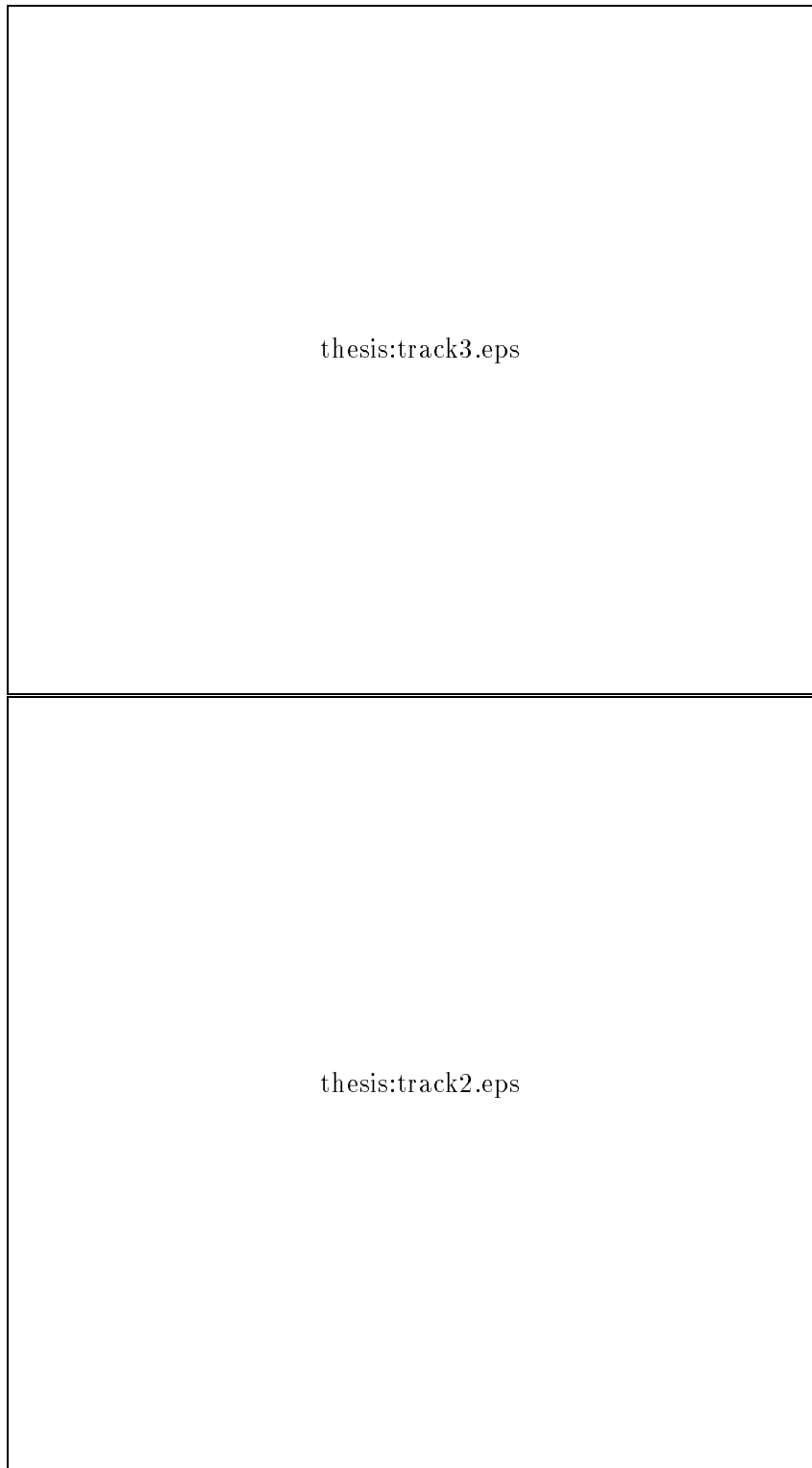


Figure 4.3: *Example of an event with four fitted tracks in the  $zx$  and  $zy$  projection, and fitted vertex. The boundaries of the barrel straw tracker and the relevant forward straw planes are shown. The small lines are hits in the barrel straws, the length of each line indicates the uncertainty in  $z$  from the charge division measurement. The small circles inside the rectangles are hits in the forward straw tracker, with the radii indicating the measured distance of the track from the straw centre. At larger  $z$ -values follow hits in the silicon  $dE/dx$  counters, and furthest away from the vertex, hits in the forward pixels can be seen.*

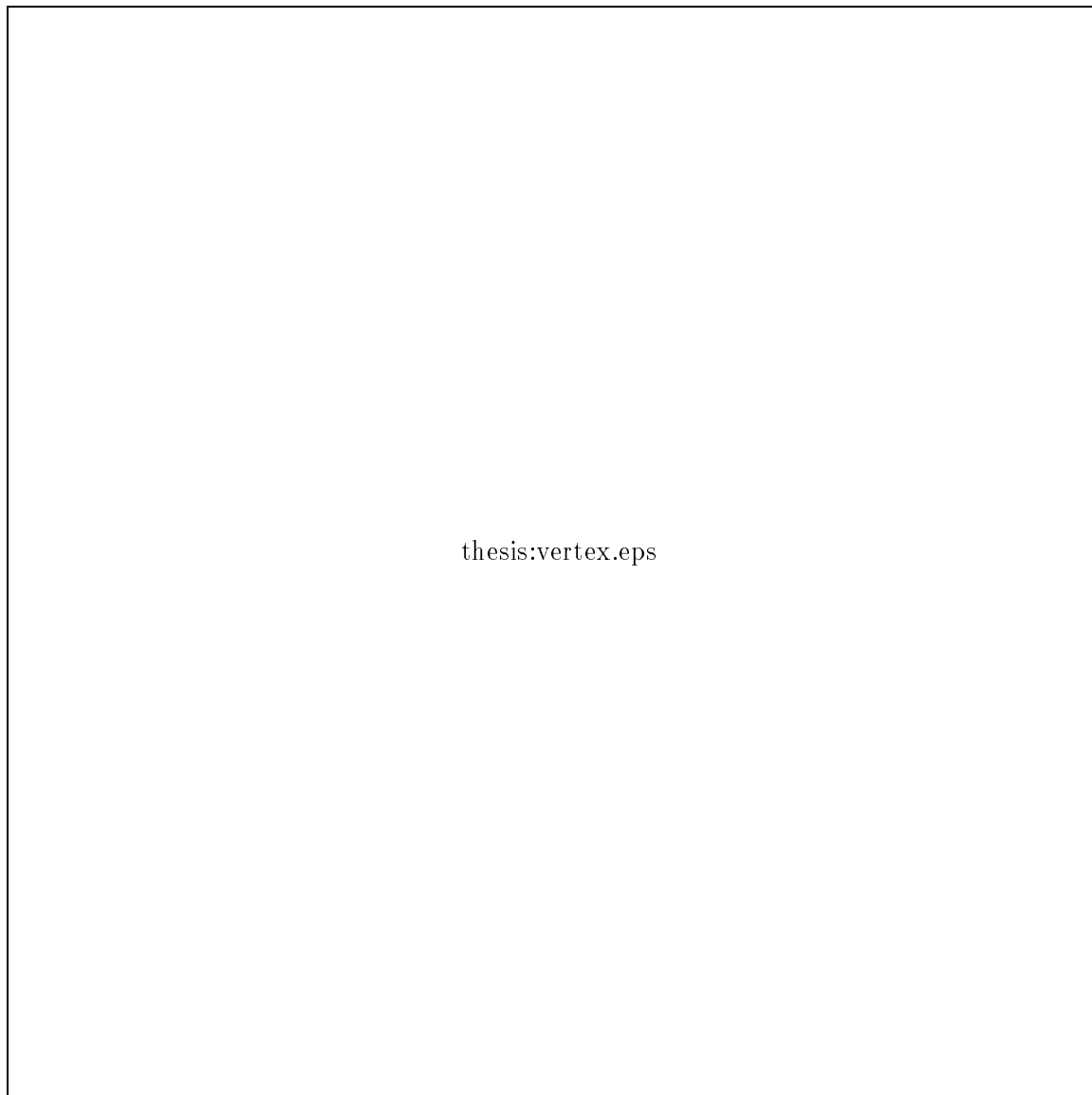


Figure 4.4: *Distribution of reconstructed vertex for real data at  $p_{beam} = 1.5$  GeV/c in the July 1991 run (top), and the difference of reconstructed and generated vertex for Monte Carlo  $\phi\phi$  data at the same momentum (bottom).*

### Track matching

3-dimensional space tracks were obtained by associating the fitted projections. The azimuthal and polar angles,  $\phi$  and  $\theta$ , for the forward tracks were calculated from the projected tracks :

$$\tan \phi = \frac{\tan \theta_{zx}}{\tan \theta_{zy}}, \quad (4.26)$$

$$\tan \theta = \sqrt{\tan^2 \theta_{zx} + \tan^2 \theta_{zy}}. \quad (4.27)$$

In the forward tracker all combinations of projections were compared to hits in the forward pipe scintillators, by introducing an  $X^2$  that measured angular distances in the  $xy$  plane. If a barrel pipe scintillator had been hit, the corresponding barrel track was added. Some forward tracks had been partly observed in the barrel, and these small barrel tracks were associated to the forward tracks. The combinations with the lowest  $X^2$  were kept for later analysis. Sometimes more than one set of four 3-dimensional tracks were found with a low  $X^2$ . They were called **renditions**, and for some events several renditions were written to the DST, with an overall match probability. A minimum of 1% was demanded for the overall match probability for a rendition to be accepted.

In the further description of the analysis, events with three forward tracks and one barrel track are referred to as 3-1, and events with four forward tracks as 4-0.

The tracking resolution in  $\phi$  and  $\theta$  for the accepted events was determined from Monte Carlo simulations and is shown in figure 4.5. Since a large part of the tracking error arose from multiple scattering, the tracking resolution improved at higher momenta, where there was less multiple scattering.

### DST production

The program that performed the geometrical reconstruction was called **Display** [?]. It ran on an HP-715 workstation, and took about 15 ms of CPU time for each event, with a limit of 64 left-right combinations tried in the fitting of track projections. The output of the geometrical reconstruction was written to **geometry DST** tapes. The format of these DSTs was an extension of the raw event format. Additional information supplied included a list of straw hits associated to each track, track parameters before and after the vertex fit, error matrices and  $X^2$  values for the fits, and the overall confidence level for the track matching quality.

### PID detector association

The second stage of the geometrical reconstruction consisted of associating tracks to hits, or clusters of hits, in the PID detectors. This association was done with the **Exotic** [?, ?] program. Each track was shifted and rotated into the local frame of each of the following detectors: Forward silicon, barrel and forward Cherenkovs, barrel and forward outer scintillator (Jülich) pixels, forward calorimeter, and barrel gamma veto.

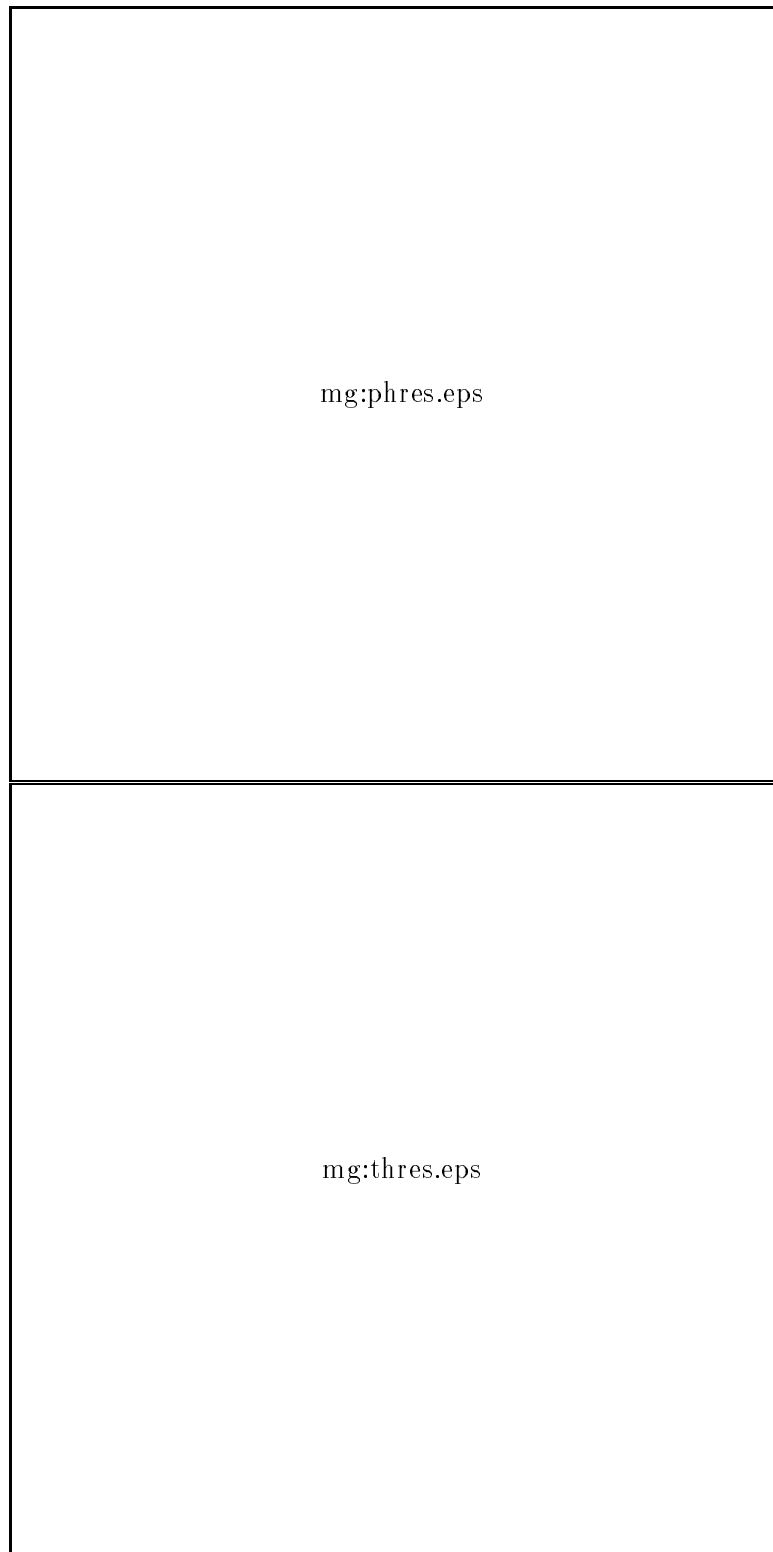


Figure 4.5: Tracking resolution,  $\phi$  (top) and  $\theta$  (bottom), as a function of beam momentum.

The requirement for a hit in the Cherenkov counters was that the track should lie outside  $\pm 1.5^\circ$  in azimuthal angle of the crack between two counters, and more than 1 cm from the counter ends. Either the presence or absence of light in a hit counter gave PID information about the event. The magnitude of the hit, measured in photo electrons, was given by the formula [?]

$$\text{photoelectrons}_i = N_{\text{meas},i} = \frac{\text{ADC}_i - \text{pedestal}_i}{\text{gain}}, \quad (4.28)$$

where  $i$  labels the counter intersected by the track. The *gain* gave the number of ADC counts per photoelectron entering the photo-multiplier. It was the same for all the counters, since the counters were equalized in gain at the beginning of each run. The values for gains and pedestals are reported in [?].

The forward silicon detectors were arranged in two planes with the pads oriented vertically, and two planes oriented horizontally. The two planes with the pads in the same direction complemented each other; each of the planes had about 50 % coverage in the active area. Only one hit in the vertical planes and one hit in the horizontal planes were allowed. If there were more than one hit in the planes of one orientation, the one with the lowest ADC value was ignored, since it was likely to be noise or delta rays. Thus each track could possess up to two silicon hits.

The matching of tracks to PID detectors was done for each rendition of each event.

At this stage of the analysis events with problems in the raw event format, mostly due to problems with the straw and silicon valets, were discarded.<sup>1</sup>

Information about the event relevant for the rest of the analysis was written out in the form of an HBOOK Ntuple [?], containing one entry for each rendition. This Ntuple was called the **4-prong Ntuple**. The selection of the  $p\bar{p} \rightarrow 4K^\pm$  events by first step event selection, kinematical reconstruction, and PID analysis was done with the **GeoBari** program [?, ?], described in the following sections.

### 4.2.3 First step event selection

The following cuts were applied to the 4-prong events before they were passed on to the kinematical reconstruction and PID analysis. Most of these cuts checked that the event contained sufficient detector information to decide whether it was signal or background.

- **Suppression of unwanted runs.** If event rates for various classes of events, or the ratio of event yield to luminosity, showed irregular behaviour for a particular run, events belonging to this run were suppressed. Other reasons to suppress a run could be missing silicon information, or that the run occurred more than once in the reduced sample.
- **Forward straw hit multiplicity** had to be at least 8 hits in each projection for 4-0 events, at least 6 hits for 3-1 and 4-1 events.

---

<sup>1</sup>The loss of events due to problems with the event format, was less than 1% for all runs starting from October 1991. In July 1991 there was a loss of about 5%, in this case a correction to the luminosity was applied to make up for the loss of acceptance.

- **Barrel straw hit multiplicity** had to be at least 5 hits in each projection for 3-1 and 4-1 events.
- **Barrel gamma veto counters** were required to have an energy deposit less than 500 MeV, unless they were correlated to a barrel pipe scintillator hit ( $\pm 30^\circ$  in azimuth angle from a barrel PS).
- No **barrel pixels** with polar angle greater than  $90^\circ$  were allowed.
- No **barrel pixels** in 4-0 events were allowed.
- **Minimum number of silicon samplings.** At least two silicon samplings were required, which corresponded either to two tracks with a single sampling each, or one track with a double sampling.
- **Minimum number of associated Cherenkovs.** At least two associated Cherenkov counters were required. As explained in section 4.2.2, association of a Cherenkov depended only on whether the track intersects the active area of the counter, not whether light is produced or not.
- **Suppression of barrel inserts.** Due to problems with the reconstruction of the tracks in the region of barrel insert straws, these events were suppressed.

#### 4.2.4 Kinematical reconstruction of events

##### Momentum reconstruction

After the reconstruction of the directions of the four particles in the final state, the momenta were calculated using energy and momentum conservation.

$$p_{beam,x} = 0 = p_{1,x} + p_{2,x} + p_{3,x} + p_{4,x}, \quad (4.29)$$

$$p_{beam,y} = 0 = p_{1,y} + p_{2,y} + p_{3,y} + p_{4,y}, \quad (4.30)$$

$$p_{beam,z} = p_{beam} = p_{1,y} + p_{2,y} + p_{3,y} + p_{4,y}, \quad (4.31)$$

$$E_{beam} + E_{target} = \sum_{j=1}^4 E_j, \quad (4.32)$$

where

$p_{beam}, E_{beam}$  = momentum and energy of the incident antiproton.

$p_{beam,i}$  ( $i = x, y, z$ ) = component of the antiproton momentum in the  $x, y$  or  $z$  direction.

$p_j, E_j$  ( $j = 1, 2, 3, 4$ ) = the momentum and energy of each of the four outgoing particles.

$p_{j,i}$  ( $i = x, y, z$ ) = component of the  $j$ th particle's momentum in the  $x, y$  or  $z$  direction.

$m_j$  = the mass of the  $j$ th particle.

This can also be written

$$p_1 c_{1x} + p_2 c_{2x} + p_3 c_{3x} + p_4 c_{4x} = 0, \quad (4.33)$$

$$p_1 c_{1y} + p_2 c_{2y} + p_3 c_{3y} + p_4 c_{4y} = 0, \quad (4.34)$$

$$p_1 c_{1z} + p_2 c_{2z} + p_3 c_{3z} + p_4 c_{4z} = p_{beam}, \quad (4.35)$$

$$\sqrt{p_{beam}^2 + m_p^2} + m_p = \sum_{j=1}^4 \sqrt{m_j^2 + p_j^2}, \quad (4.36)$$



where  $m_p$  is the (anti)proton mass and

$$c_{jx} = \sin \theta_j \cos \phi_j, \quad (4.37)$$

$$c_{jy} = \sin \theta_j \sin \phi_j, \quad (4.38)$$

$$c_{jz} = \cos \theta_j. \quad (4.39)$$

$\theta_j$  and  $\phi_j$  are the reconstructed polar and azimuthal angles of the  $j$ th outgoing particle.

If the masses of the particles are known quantities, this gives four equations and four unknowns. Since the type of reaction was not known a priori, different hypotheses were tried for the final state, for example  $4K$  or  $p\bar{p}\pi^+\pi^-$ , and the system of equations solved for each of those. (For the latter hypotheses, there are 6 different ways the masses can be assigned to tracks.)

To solve the equations, three of the momenta can be expressed by the fourth one:

$$\begin{pmatrix} p_1 \\ p_2 \\ p_3 \end{pmatrix} = M^{-1} \begin{pmatrix} -c_{4x}p_4 \\ -c_{4y}p_4 \\ p_{beam} - c_{4z}p_4 \end{pmatrix}. \quad (4.40)$$

$$M = \begin{pmatrix} c_{1x} & c_{2x} & c_{3x} \\ c_{1y} & c_{2y} & c_{3y} \\ c_{1z} & c_{2z} & c_{3z} \end{pmatrix}. \quad (4.41)$$

The momentum for each particle can then be expressed as a linear function of one of them, for example  $p_4$ .

$$p_j = a_j p_4 + b_j, \quad (4.42)$$

with the constants  $a_j$  and  $b_j$  determined from the angles  $\theta$  and  $\phi$  of the track, and the incident antiproton momentum. When this is inserted into equation 4.36 describing energy conservation,

$$E_x(p_4) = \sum_{j=1}^4 \sqrt{m_j^2 + (a_j p_4 + b_j)^2} - \sqrt{p_{beam}^2 + m_p^2} + m_p - = 0, \quad (4.43)$$

one equation with one unknown is obtained. The second derivative of  $E_x$  with respect to  $p_4$  is always positive,

$$\frac{d^2 E_x}{dp_4^2} = \sum_{j=1}^{n_{track}} a_j^2 \frac{m_j^2}{[(a_j p_4 + b_j)^2 + m_j^2]^{3/2}}, \quad (4.44)$$

therefore equation 4.43 has maximum two solutions. Figure 4.6 shows examples of the functional dependence of  $E_x$  on  $p_4$ . An iterative method was applied to find the minimum of  $E_x$ . It is possible to get 0,1 or 2 physical solutions to equation 4.43 ( $E_x = 0$ ). The minimum value of  $E_x$  was called  $\Delta E$  (figure 4.6), and could be either positive or negative. If it was negative, there were two algebraic solutions for the four particle momenta, corresponding to  $E_x = 0$ . If  $\Delta E$  was positive there was no algebraic solution, but the solution corresponding to the minimum of  $E_x$  was selected. If one or more of the reconstructed momenta were negative for a solution, this solution was rejected. If there were two solutions, the best one was selected on the basis of agreement with the response of the silicon and Cherenkov detectors.

The resolution of the reconstructed momentum as a function of beam momentum, determined from Monte Carlo events, is shown in figure 4.7.

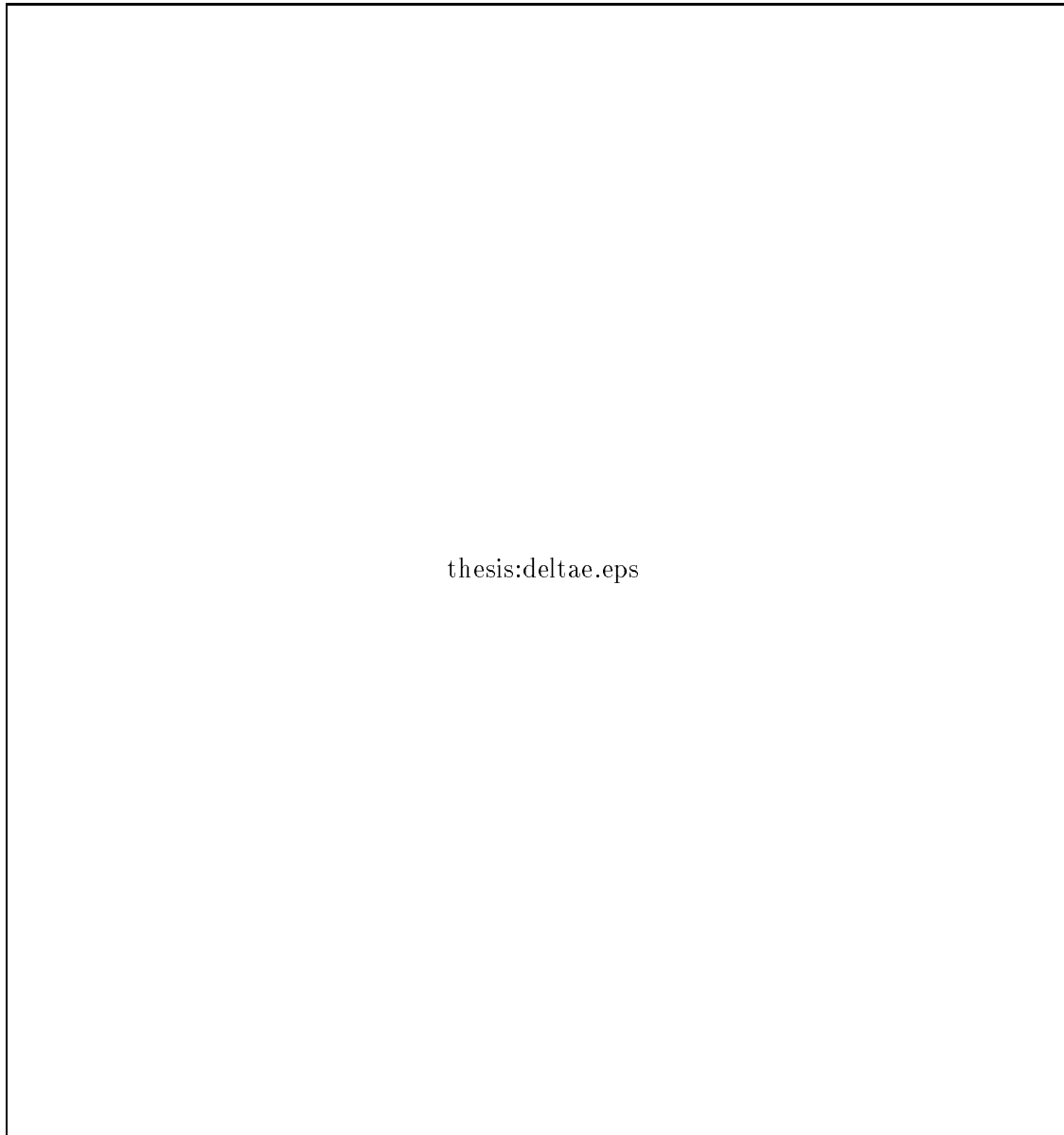


Figure 4.6: *Examples of the functional dependence between  $E_x$  and the fourth particle's momentum,  $p_4$ , for 0, 1 or 2 solutions, and definition of  $\Delta E$  (from [?]).*

### The $\phi\phi$ kinematical fit

The  $\phi\phi$  fit [?] selected  $\bar{p}p \rightarrow \phi\phi \rightarrow K^+K^-K^+K^-$  events on kinematical grounds. The fit used six constraint equations: energy and momentum conservation, and the conditions that the two  $K^+K^-$  pair invariant masses were equal to the  $\phi$  mass. The measured variables in this fit were the three direction cosines for each outgoing particle and the  $\phi$  meson masses, while the unknown variables were the momenta.

The quantity that was minimized in the fit was

$$X^2 = (\underline{y} - \underline{\eta})V^{-1}(\underline{y} - \underline{\eta}) + 2\underline{\lambda}f(\underline{\eta}, \underline{\xi}) + 2\underline{\tau}g(\underline{\xi}) + 2\underline{\delta}d(\underline{\eta}), \quad (4.45)$$

where

$\underline{\eta}, \underline{\xi}$  are measured and unknown variables respectively,

$f, g, d$  constraint equations,

$\underline{\lambda}, \underline{\tau}, \underline{\delta}$  are Lagrangian multipliers,

and  $V$  is the covariance matrix for the measured quantities.

The output from the fit was an  $X_{min}^2$ , which was converted to a probability that the event was of the type  $\bar{p}p \rightarrow \phi\phi \rightarrow K^+K^-K^+K^-$ , assuming that  $X_{min}^2$  followed a  $\chi^2$  distribution. The fit also gave new fitted directions and momenta. An improved resolution on directions and momenta (figure 4.7) was seen in Monte Carlo  $\phi\phi$  events after the fit.

The fit probability for Monte Carlo  $\phi\phi$ ,  $4K$  and  $\phi KK$  events, as well as for real data at 1.5 GeV/c, is shown in figure 4.8. Table 4.5 shows the fractions of Monte Carlo and real events with a fit probability higher than 5% (these were defined as  $\phi\phi$  fit events in our analysis). The  $\phi\phi$  kinematical fit was used to select events with a high probability of being of the type  $\bar{p}p \rightarrow \phi\phi \rightarrow K^+K^-K^+K^-$ . This way we obtained a sample of events with a high fraction of  $4K$  compared to the original 4-prong sample. The  $\phi\phi$  fit was used as a tool to study and set the various cuts used in the  $4K$  event selection.

The sample obtained from this fit contained an unknown amount of background. Therefore the  $\phi\phi$  fit was not used in determining the number of  $\phi\phi$  events for cross section calculations.

Event type	4-prong events (%)	Sel. events (%)
$\phi\phi$ , MC	59.0	79.5
$\phi KK$ , MC	13.3	20.5
$4K$ , MC	8.1	11.3
$p\bar{p}\pi^+\pi^-$ , MC	0.5	3.4
Real data	1.4	42.0

Table 4.5: Fraction of Monte Carlo and real events, with fit probability higher than 5%, before and after  $4K$  selection cuts. beam momentum 1.5 GeV/c (1.6 GeV/c for  $p\bar{p}\pi^+\pi^-$ ).

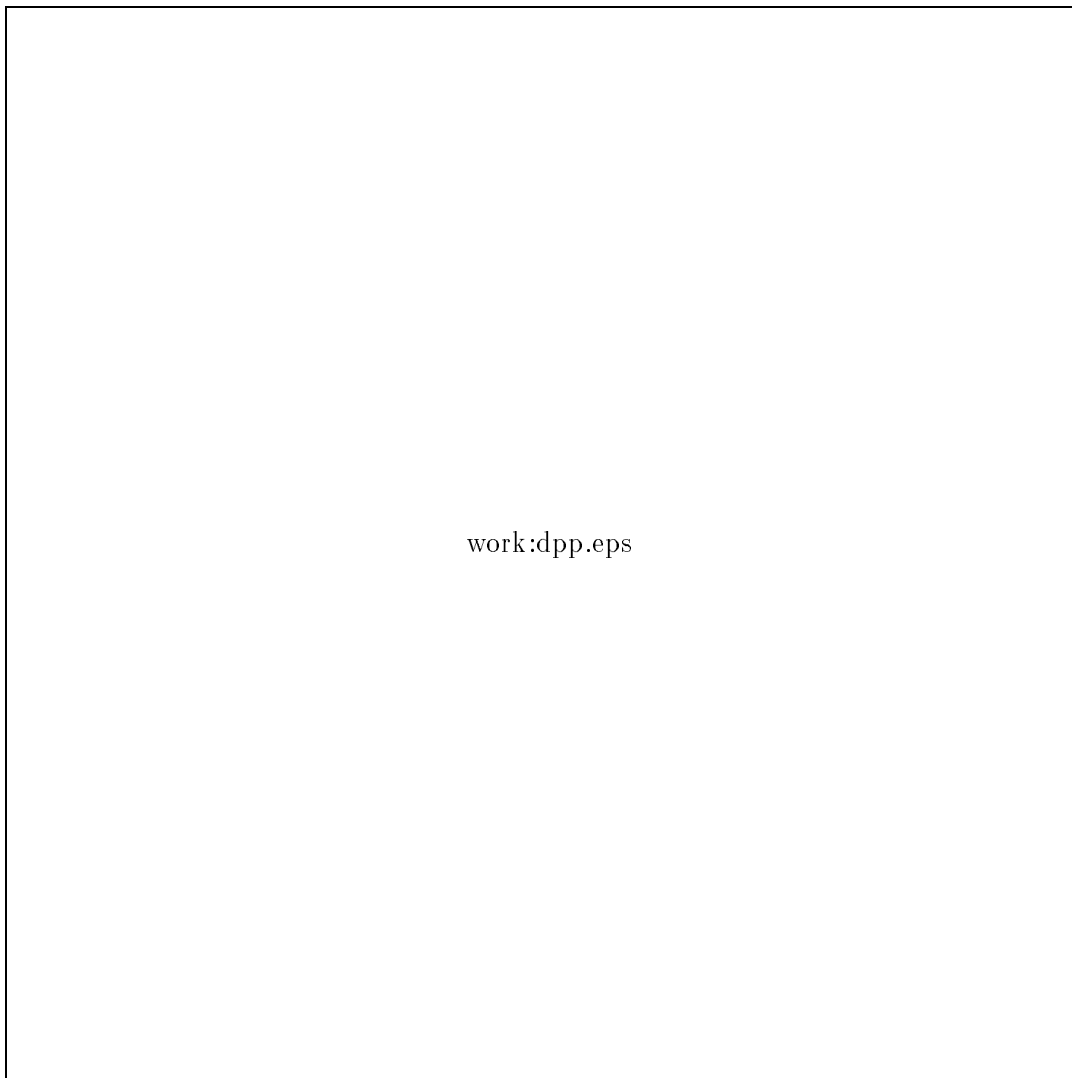


Figure 4.7:  $\Delta(p)/p$  versus track momentum for  $\phi\phi$  Monte Carlo events, circles are with kinematical fit, solid dots without.

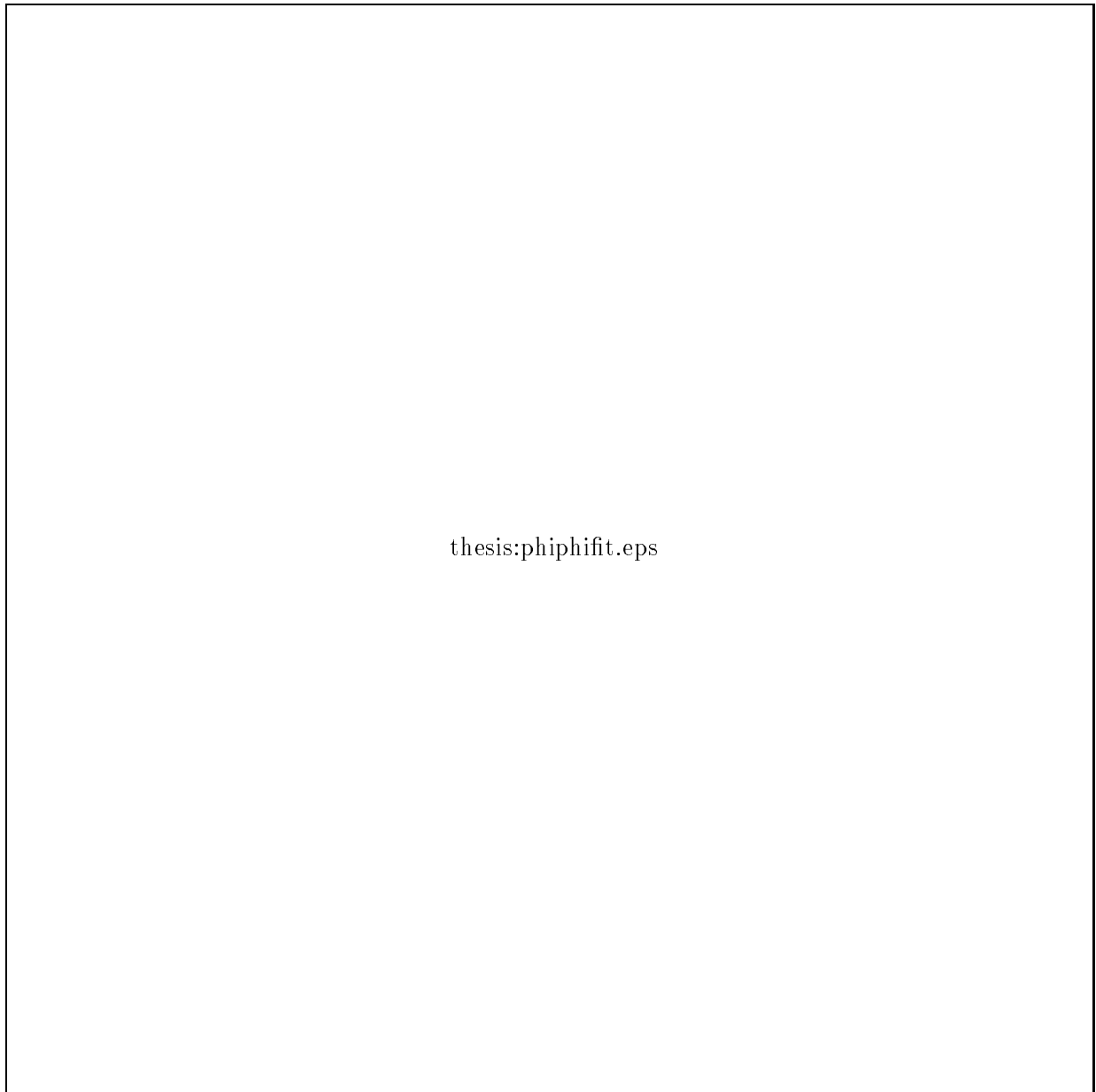


Figure 4.8: *Fit probability from the  $\phi\phi$  fit to Monte Carlo events and real data, after kinematical and PID cuts. Logarithmic scale. The hatched part of the histograms shows events passing the  $\phi\phi$  fit.*

## 4.3 Extraction of the 4K events

### 4.3.1 General guidelines for 4K event selection

The cuts used to extract 4K events from the 4-prong events were required to have a noticeable effect in terms of rejecting background events and selecting 4K events.

The Monte Carlo distributions for 4K,  $\phi\phi$ , and  $\phi KK$  events were used to set the cut values. Additional confirmation was obtained by studying the  $\phi\phi$  fit events, the subclass of the real data with a  $\phi\phi$  fit probability higher than 5%.

The cuts were justified by the distribution of the  $\Delta E$  variable (section 4.2.4) before and after each cut. The signal events populate a narrow peak around  $\Delta E = 0$ , as seen in Monte Carlo 4K,  $\phi\phi$ , and  $\phi KK$  events (figure 4.11). A good cut should remove more events from the unphysical tail at  $\Delta E > 0$ , than from the peak around 0.

The reaction  $p\bar{p} \rightarrow p\bar{p}\pi^+\pi^-$  received special attention. Since this reaction has an event signature similar to 4K, the standard 4K extraction was not sufficient to remove this background. All events were therefore kinematically reconstructed with the  $p\bar{p}\pi^+\pi^-$  mass hypotheses, and kinematical and particle identification cuts applied, in order to be able to identify and reject  $p\bar{p}\pi^+\pi^-$  events.

### 4.3.2 Kinematical cuts

#### $\Delta E$ cut

The  $\Delta E$  distribution for all 4-prong events, reconstructed with the 4K mass hypothesis, at a beam momentum 1.5 GeV/c, is shown in figure 4.9. This can be compared with the distributions of  $\Delta E$  for  $\phi\phi$ , 4K, and  $\phi KK$  Monte Carlo events in figure 4.11, and with the distribution of real 4-prong events that passed the  $\phi\phi$  kinematical fit in figure 4.10. The  $\Delta E$  distribution for  $p\bar{p}\pi^+\pi^-$  events, reconstructed with the  $p\bar{p}\pi^+\pi^-$  mass hypothesis, is shown in figure 4.12. When the correct kinematical hypothesis is chosen, the events populate a narrow peak around  $\Delta E = 0$ . As seen in figure 4.9, the background accumulates mainly on the positive (unphysical) side of the peak, which justifies a cut  $\Delta E \leq \Delta E_{max}$ . A limit of  $\Delta E_{max} = 20$  MeV for the 4K channels and 40 MeV for  $p\bar{p}\pi^+\pi^-$  was chosen.

The  $\Delta E$  distribution for  $p\bar{p}\pi^+\pi^-$  Monte Carlo, reconstructed as 4K, is shown in figure 4.13. The majority of these events are on the negative (physical) side of the signal peak and would not be removed by the  $\Delta E < 20$  MeV cut on 4K channels. Therefore this reaction needed the special treatment mentioned above.

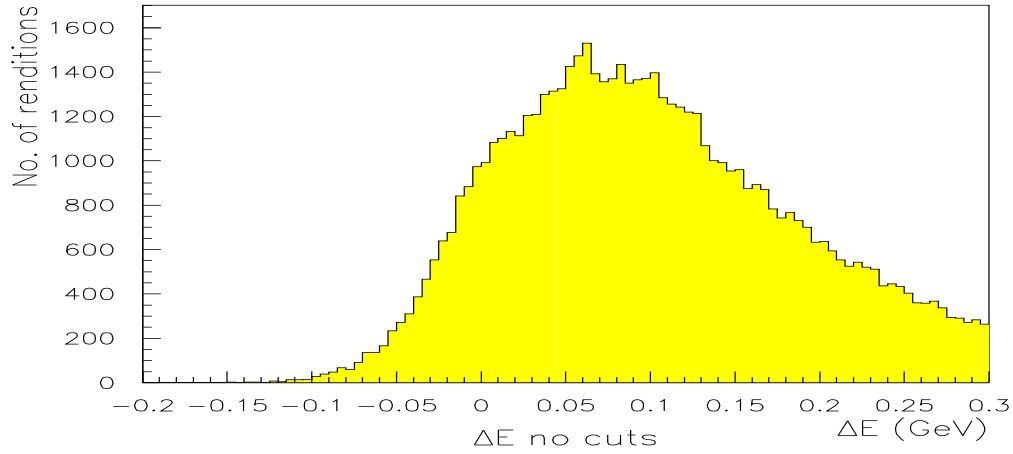


Figure 4.9:  $\Delta E$  for all 4-prong events, reconstructed with the 4K mass hypothesis, at 1.5 GeV/c beam momentum.

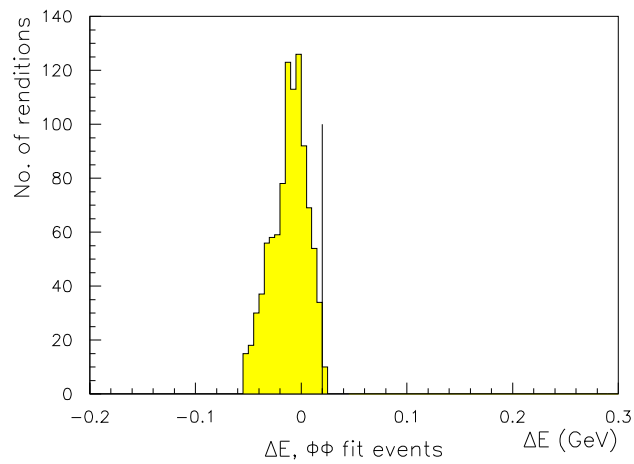


Figure 4.10:  $\Delta E$  for events that passed the  $\phi\phi$  kinematical fit at 1.5 GeV/c beam momentum (reconstructed with the 4K mass hypothesis but no 4K selection cuts). The vertical line indicates the  $\Delta E$  cut for the 4K analysis.

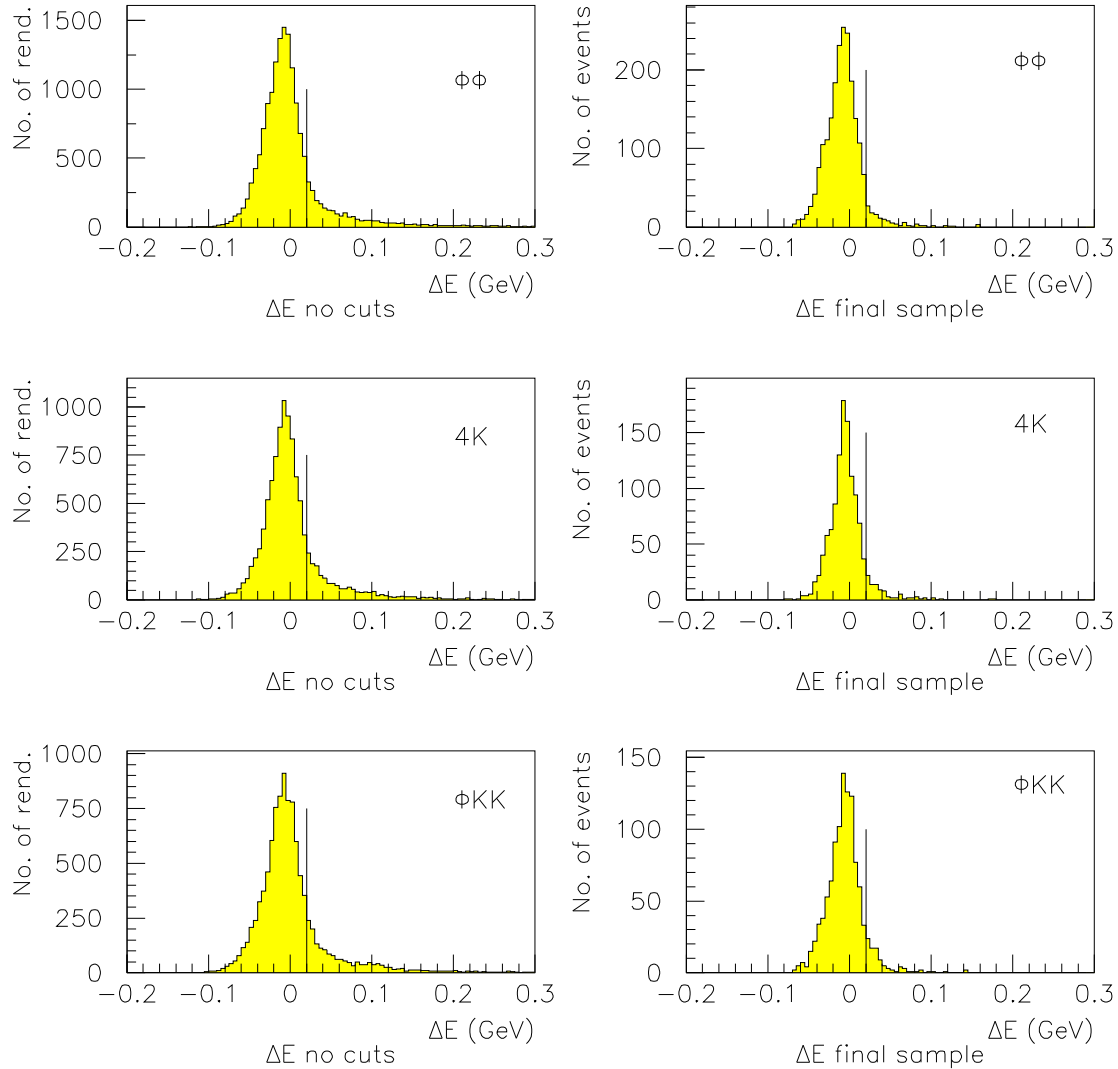


Figure 4.11:  $\Delta E$  for Monte Carlo  $\phi\phi$ ,  $\phi KK$  and 4K events, reconstructed with the 4K mass hypothesis, at 1.5 GeV/c beam momentum, before (left) and after (right) 4K selection cuts with the  $\Delta E$  cut suppressed. The vertical lines indicate where the  $\Delta E$  cut for the 4K analysis cuts the spectrum. The histograms to the left contain all the events in the 4-prong Ntuple, and may contain several renditions for an event, in the final sample to the right the best rendition for each event is selected from kinematics and PID cuts.



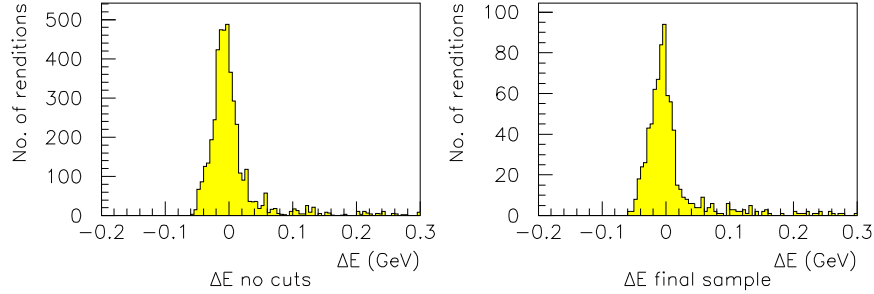


Figure 4.12:  $\Delta E$  for Monte Carlo  $p\bar{p}\pi^+\pi^-$  events, reconstructed with the  $p\bar{p}\pi^+\pi^-$  mass hypothesis at 1.6 GeV/c beam momentum, before (left) and after (right)  $p\bar{p}\pi^+\pi^-$  selection cuts (with the  $\Delta E$  cut suppressed). The vertical lines indicate where the  $\Delta E$  cut for the  $p\bar{p}\pi^+\pi^-$  analysis cuts the spectrum. The histograms to the left contain all the events in the 4-prong Ntuple, and may contain several renditions for an event, for each rendition the mass hypothesis with lowest  $\Delta E$  is selected. In the final sample to the right, the best rendition and mass hypothesis for each event is selected from kinematics and PID cuts.

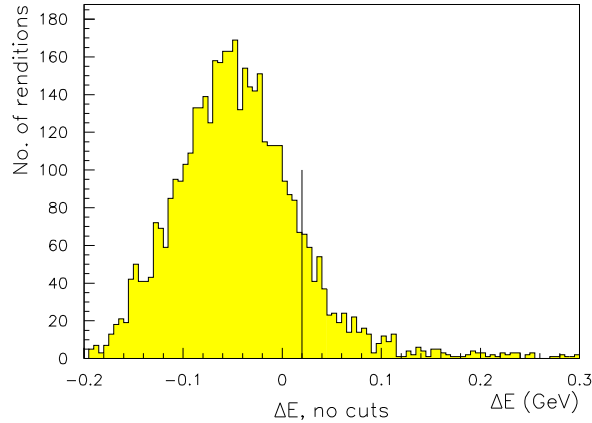


Figure 4.13:  $\Delta E$  for Monte Carlo  $p\bar{p}\pi^+\pi^-$  events at 1.6 GeV/c beam momentum (4K trigger cuts, and reconstructed with the 4K mass hypothesis, no 4K selection cuts). The vertical line indicates where the  $\Delta E$  cut for the 4K analysis cuts the spectrum.

### Minimum momentum cut

A particle with a low momentum had a high probability of being stopped in the detector before reaching the Cherenkov, due to energy loss. If the reconstructed momentum was too low, the mass hypothesis was most likely false, and hence should be rejected. The distribution of the reconstructed momentum for all 4-prong events can be seen in figure 4.14.

The energy loss of kaons in the detector was studied in Monte Carlo events. From this a cut  $p_{min}$  of 200 MeV/c in the forward and 150 MeV/c in the barrel was derived. This is confirmed by the momentum distributions for Monte Carlo events shown in figures 4.15 and 4.17, and for  $\phi\phi$  fit events (figure 4.16).

The minimum momentum cut was efficient in reducing background, also  $p\bar{p}\pi^+\pi^-$ , but removed little of the 4K and  $\phi\phi$  signal.

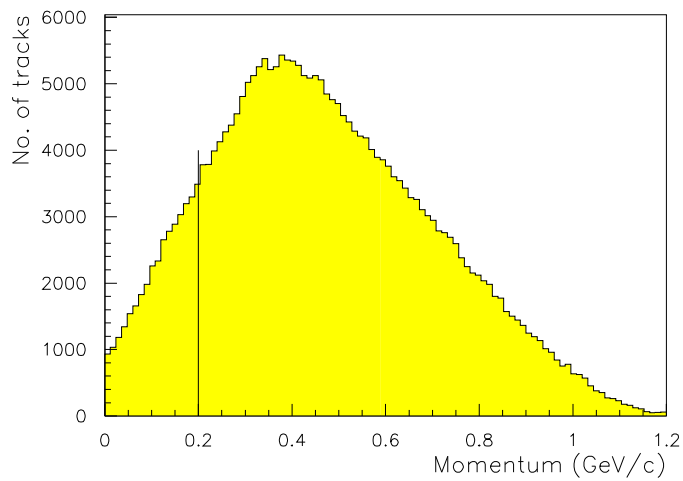


Figure 4.14: *Momentum distribution for all 4-prong events, reconstructed with the 4K mass hypothesis, at 1.5 GeV/c beam momentum. The histogram contains the reconstructed momenta for one or two solutions per rendition. The vertical line indicates the minimum momentum cut for forward tracks.*

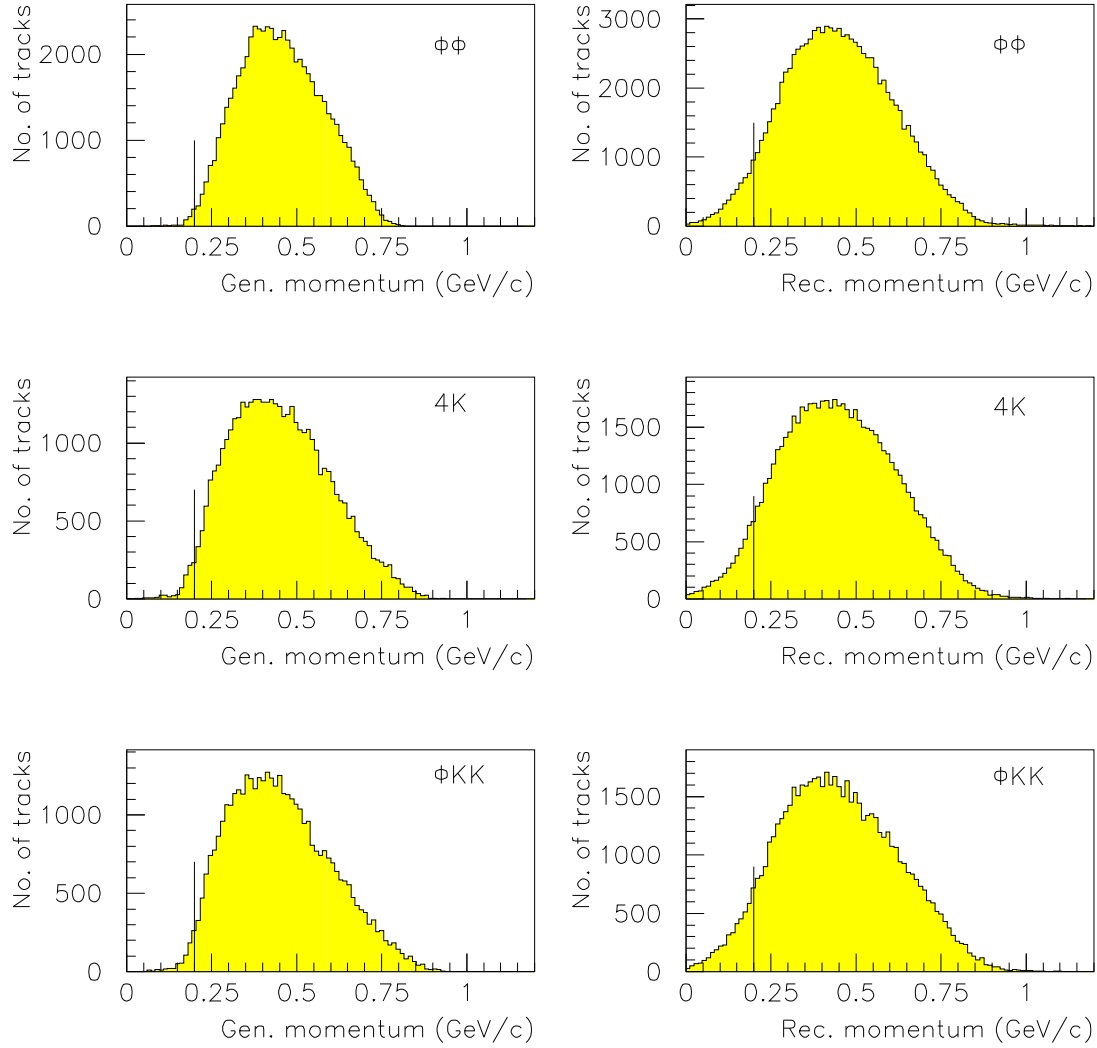


Figure 4.15: *Momentum distribution for Monte Carlo  $\phi\phi$ ,  $4K$ , and  $\phi KK$  events, reconstructed with the  $4K$  mass hypothesis, at  $1.5 \text{ GeV}/c$  beam momentum, (no  $4K$  selection cuts). Generated momenta (at the vertex) to the left, reconstructed to the right. The histograms to the right contain the reconstructed momenta for one or two solutions per rendition. The vertical lines indicate the minimum momentum cut for forward tracks.*

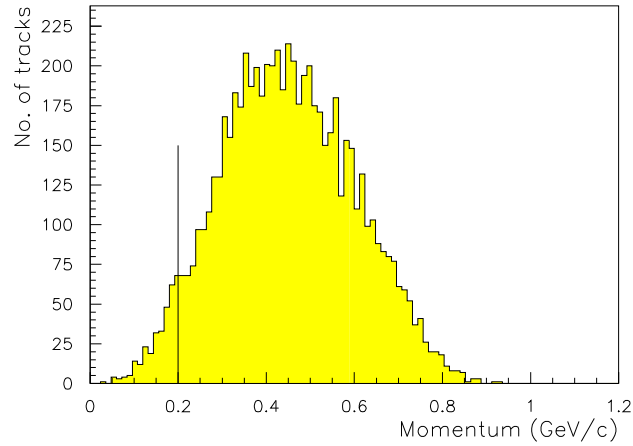


Figure 4.16: *Momentum distribution for 4-prong events with  $\phi\phi$  fit probability greater than 5%, and reconstructed with the 4K mass hypothesis, at 1.5 GeV/c beam momentum (no 4K selection cuts). The histogram contains the reconstructed momenta for one or two solutions per rendition. The vertical line indicates the minimum momentum cut for forward tracks.*

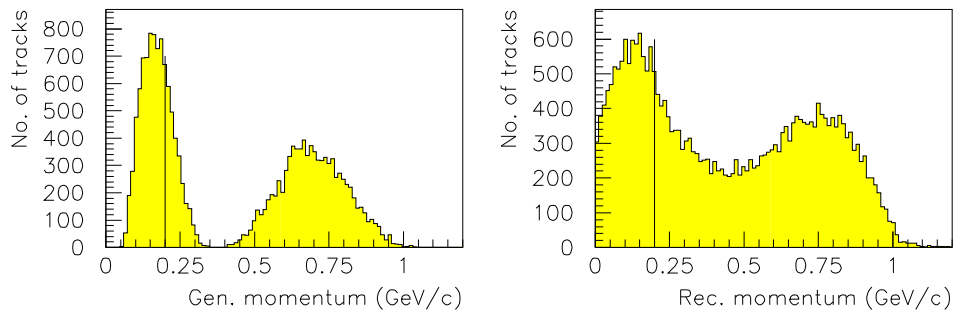


Figure 4.17: *Momentum distribution for Monte Carlo  $p\bar{p}\pi^+\pi^-$  events, reconstructed with the 4K mass hypothesis (no 4K selection cuts). Generated momenta to the left, reconstructed to the right. The vertical lines indicate the minimum momentum cut for forward tracks in the 4K analysis.*

### 4.3.3 Particle identification cuts

#### Material corrections

The particle identification in JETSET used silicon dE/dx detectors and Cherenkov counters to measure the velocity,  $\beta$ . This  $\beta$  value was compared with the one calculated from the kinematical reconstruction to determine whether the event should be kept or rejected. However, the reconstructed  $\beta$  was the one at the origin, while the  $\beta$  value measured by the PID detectors was lower, due to ionization energy loss when the particle passed through the various detector components. To correct for this, the energy loss for a particle with the reconstructed  $\beta$  coming from the origin was calculated. The energy loss depended only on the angle and the velocity of the particle. To find the angular dependence a broad spectrum of charged kaons from the origin into all directions of the detector was generated with the GEANT Monte Carlo program, and the final momentum when they passed through the front surface of the Cherenkov counters was checked [?].

#### Silicon compatibility cuts

The silicon dE/dx detectors (section 3.2) were used in the particle identification by measuring the energy loss in the detectors when a particle passed through them, and comparing this to the expected energy loss, calculated from the solutions to the kinematical reconstruction. As described in section 3.2, the energy loss was proportional to  $\frac{1}{\beta^2}$ , and a calibration curve of the form

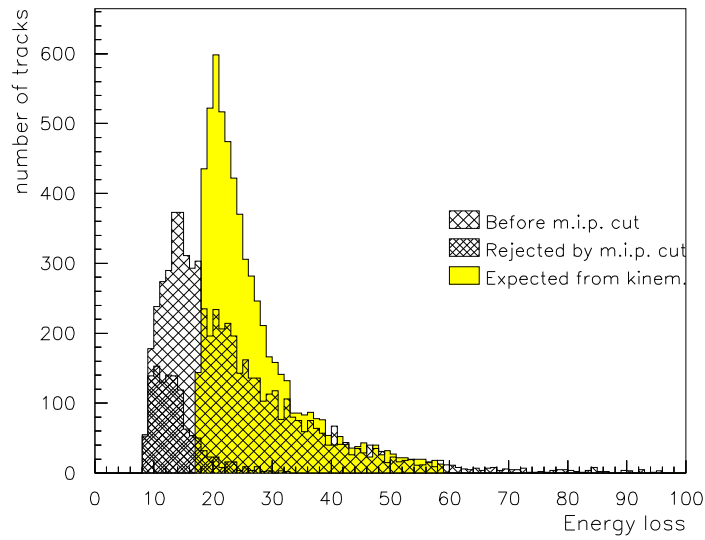
$$\varepsilon = a + b/\beta^2 \quad (4.46)$$

was used.

The expected energy loss from this calibration curve versus  $1/\beta^2$  from the kinematical reconstruction is shown in figure 4.18 for both Monte Carlo and real data. In the same figure the measured energy loss in the silicon counters versus  $1/\beta^2$  from the kinematical reconstruction is shown. The real data show an excess of low energy loss measurements with low  $\beta$ , compared to the Monte Carlo data. A cut at  $dE/dx_{meas} < (6/\beta^2)$ , corresponding to the line shown in figure 4.18, was applied. All solutions with a dE/dx measurement falling below this line were rejected. The effect of this cut on the data and Monte Carlo is shown in figure 4.19. Real data events were more likely than Monte Carlo events to have a low energy loss compared to what was expected from kinematics. The rejected measurements lie mostly on the low side of the spectrum. The events that were rejected by this cut were most likely to be from multi-pion background reactions; the relativistic particles from these events would have the minimum value of the energy loss according to the Bethe-Block formula, that is, the cut rejected events with minimum ionizing particles, and it was therefore called the **m.i.p. cut**. No cut was made on the maximum value of the energy loss. Because of the Landau tail (figure 3.19) some measurements will give a much higher value than predicted from the Bethe-Block formula (or the calibration curves).

Figure 4.18: *Energy loss in silicon (arbitrary units) vs.  $1/\beta^2$  for real data and Monte Carlo  $\phi\phi$  at 1.5 GeV/c beam momentum, reconstructed with the 4K mass hypothesis, showing the expected (left) and measured (right) energy loss. Measurements below the m.i.p. cut (the solid line) caused the kinematical hypothesis to be rejected.*

Measured  $dE/dx$  silicon, real data



Measured  $dE/dx$  silicon, Monte Carlo  $\phi\phi$

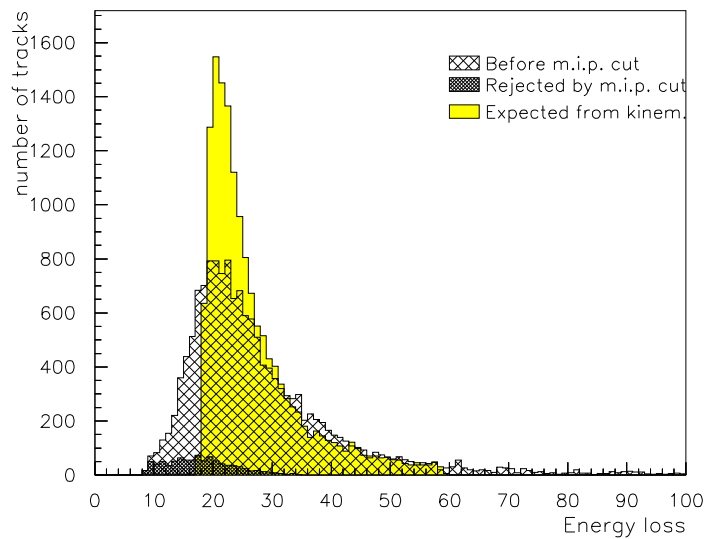


Figure 4.19: Energy loss in silicon(arbitrary units) for real data (top) and Monte Carlo  $\phi\phi$  events (bottom), at a beam momentum  $1.5 \text{ GeV}/c$ . The expected energy loss from the kinematical solutions and the measurements rejected by the m.i.p. cut are shown.

The second silicon cut was a cut on the silicon confidence level, computed from the following sum of squares:

$$X^2 = \sum_{i=1}^n \left( \frac{\varepsilon_{meas.,i} - \varepsilon_{calc.,i}}{\sigma_i} \right)^2, \quad (4.47)$$

where  $n$  is the number of tracks with a silicon measurement,  $\varepsilon_{meas.,i}$  the measured energy loss, either from a single sampling or the truncated mean,  $\sigma_i$  is the r.m.s. measurement error on  $\varepsilon_{meas.,i}$ , and  $\varepsilon_{calc.,i}$  is the expected silicon response from equation 4.46. This  $X^2$  follows a chi-squared distribution with  $n$  degrees of freedom, and was converted into a confidence level, which is the integral of the tail of the  $\chi^2$  distribution beyond the calculated value [?, ?]:

$$\alpha_s = \int_{X^2}^{\infty} f(t|n) dt = \int_{X^2}^{\infty} \frac{1}{2^n \Gamma(\frac{n}{2})} \cdot \frac{t^{\frac{n}{2}-1}}{2} \cdot e^{-t/2} dt. \quad (4.48)$$

$\alpha_s$  is interpreted as the degree of compatibility between the measurement and hypothetical solution. The distribution of the confidence level  $\alpha_s$  is shown in figure 4.20 for Monte Carlo and real data. Events were rejected if the confidence level was lower than 5%.

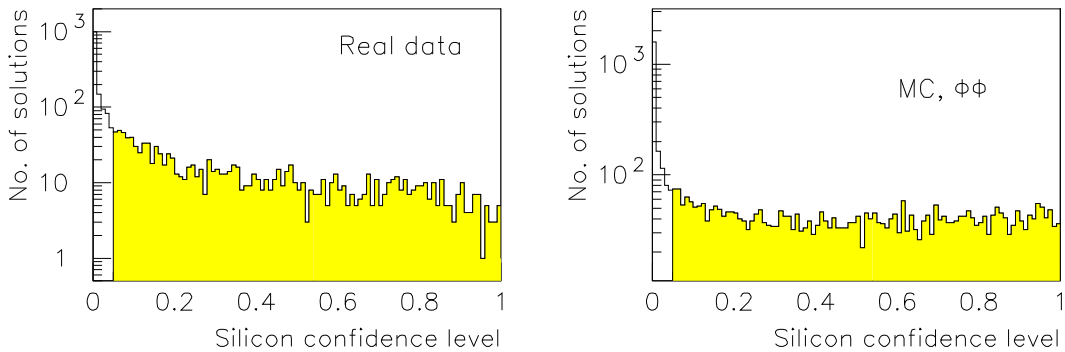


Figure 4.20: *Silicon confidence level for real data and Monte Carlo  $\phi\phi$  events, reconstructed with the 4K mass hypothesis, at a beam momentum 1.5 GeV/c. Note logarithmic scale. The white part of the histograms show the events rejected by the silicon probability cut. The histograms contain the solutions retained after the minimum momentum cut*



### Cherenkov compatibility cut

The Cherenkov counters (section 3.2) were used in the particle identification in a similar way to the silicon counters, that is by comparing the response, measured in number of photoelectrons, from the detectors when a particle passed through them, to the expected number of photoelectrons, calculated from the solutions to the kinematical reconstruction. The measured number of photoelectrons,  $N_{meas.}$ , was calculated from the ADC output by equation 4.28.

The expected number of photoelectrons was a product of three factors [?]

$$N_{exp.,i} = g(\beta)f(\theta)\frac{(\text{normalization factor})_i}{\text{gain}}. \quad (4.49)$$

The first factor represented the dependence of the number of photoelectrons on the particle velocity  $\beta$ . The number of photoelectrons produced by the Cherenkov effect is given by equation 3.10. The function  $g(\beta)$  was normalized to unity for  $\beta = 1$  :

$$g(\beta) = \frac{1 - \frac{\beta_{thr}^2}{\beta^2}}{1 - \beta_{thr}^2} \quad (\beta > \beta_{thr}). \quad (4.50)$$

The second factor gave the dependence of the signal on the lab polar angle  $\theta$ . Test beam results had shown that the light output resulting from the collection of Cherenkov radiation through radiator and walls was given by the following empirical formula:

$$f(\theta) = a + b \cdot \theta + c \cdot \theta^2. \quad (4.51)$$

The constants were chosen so that  $f(\theta)$  was the average yield for a particle with  $\beta = 1$ . The third factor represented a normalization for each individual counter. The normalization factor gave the expected signal in terms of ADC channels for counter  $i$ , per photoelectron. This was divided by the gain to give  $N_{exp.}$  units of photoelectrons.

To determine the overall confidence level for the Cherenkov compatibility, a confidence level  $\alpha_i$  was determined for each of the measured tracks. A track was regarded as measured if it crossed the area of the Cherenkov counters, and did not necessarily have to produce a signal. There were four possibilities [?]:

1.  $N_{exp.} = 0, N_{meas.} = 0$ : The reconstructed  $\beta$  was below threshold, and no signal measured. Expectation and measurement were in perfect agreement and a confidence level:

$$\alpha_i = 1.0, \quad (4.52)$$

was assigned.

2.  $N_{exp.} = 0, N_{meas.} > 0$ : The reconstructed  $\beta$  was below threshold, but a signal had been measured. In this case the compatibility of the measurement with a Gaussian noise signal centered around 0, and  $\sigma$  approximately equal to one photoelectron, was determined [?].

$$\alpha_i = 2 \cdot \frac{1}{\sigma\sqrt{2\pi}} \cdot \int_{N_{meas.}}^{\infty} e^{-(x^2/2\sigma^2)} dx. \quad (4.53)$$

3.  $N_{exp.} > 0, N_{meas.} = 0$ : The reconstructed  $\beta$  was above threshold, but no signal had been measured. The compatibility of the expected signal with zero was evaluated from the Poisson formula,

$$\alpha_i = e^{-N_{exp.}}. \quad (4.54)$$

4.  $N_{exp.} > 0, N_{meas.} > 0$ . The reconstructed  $\beta$  was above threshold, and a signal had been measured. The compatibility of expected and measured number of photoelectrons were evaluated assuming multi-poisson statistics for  $N_{exp}$  [?]. The confidence level was calculated as the integral of the tails of the Poisson distribution from the measured value, and from its reflection through the mean  $N_{exp.}$ .

The confidence levels from the individual Cherenkov measurements were combined to give a parameter  $\beta$ :

$$\beta = -2 \ln \prod_{i=1}^n \alpha_i, \quad (4.55)$$

where  $n$  is the number of measured tracks.

The parameter  $\beta$  follows a  $\chi^2$  distribution with  $2n$  degrees of freedom [?] and was converted to a combined confidence level for the kinematical solution being tested:

$$\alpha_c = \int_{\beta}^{\infty} f(t | 2n) dt = \int_{\beta}^{\infty} \frac{1}{2^? \left(\frac{2n}{2}\right)} \cdot \frac{t^{\frac{2n}{2}-1}}{2} \cdot e^{-t/2} dt. \quad (4.56)$$

The distribution of the confidence level  $\alpha_c$  is shown in figure 4.21 for Monte Carlo and real data. Events were rejected if the confidence level, thus determined, was smaller than 5%.

### Choice of solution

In some cases both solutions of the kinematical reconstruction of a mass hypothesis passed all the kinematical and PID cuts. To choose the best solution, the confidence level from silicon and Cherenkovs were combined to an overall confidence level,  $\alpha$ :

$$\alpha = \alpha_s \alpha_c \cdot [1 - \ln(\alpha_s \alpha_c)]. \quad (4.57)$$

The distribution of this confidence level is shown in figure 4.22 for Monte Carlo and real data. No cut was made on this variable, but the solution with the highest confidence level was selected for the further analysis.

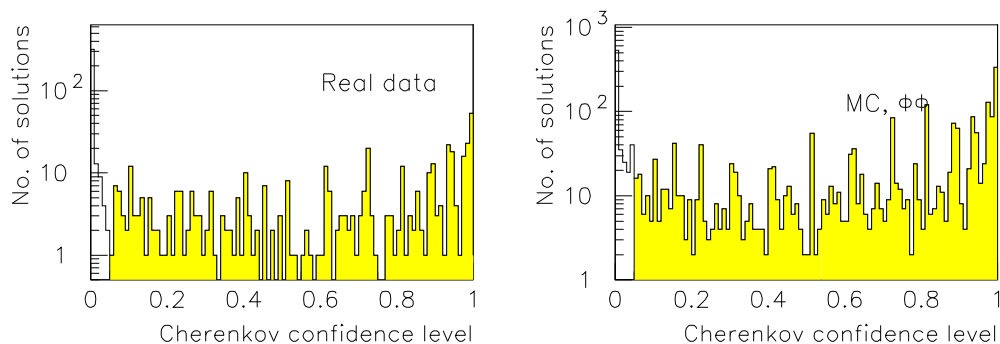


Figure 4.21: *Cherenkov confidence level for real data and Monte Carlo  $\phi\phi$  events, reconstructed with the  $4K$  mass hypothesis, at a beam momentum  $1.5 \text{ GeV}/c$ . Note logarithmic scale. The white part of the histograms show the events rejected by the Cherenkov probability cut. The histograms contain the solutions retained after the silicon probability cut.*

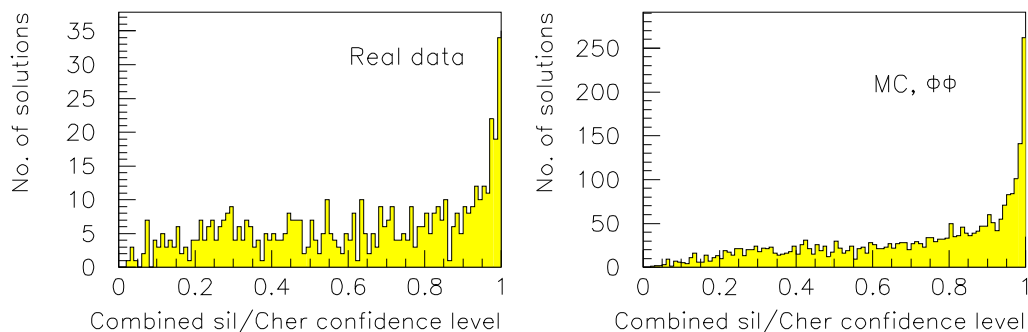


Figure 4.22: *Combined silicon-Cherenkov confidence level for real data and Monte Carlo  $\phi\phi$  events, reconstructed with the  $4K$  mass hypothesis, at a beam momentum  $1.5 \text{ GeV}/c$ . The histograms contain the solutions accepted by the silicon and Cherenkov cuts.*

### Rejection of $p\bar{p}\pi^+\pi^-$ events

If a kinematical solution for an event passed the  $\Delta E$  cut and the PID cuts for  $p\bar{p}\pi^+\pi^-$  events, this event was rejected in the 4K analysis. This cut was particularly efficient at high energies, where the  $p\bar{p}\pi^+\pi^-$  cross section is large. Figure 4.28 shows the  $\Delta E$  after the first step selection, and for the rejected and accepted events after each of the PID cuts for events analysed as  $p\bar{p}\pi^+\pi^-$  at 1.9 GeV/c beam momentum.

Measured energy loss versus  $1/\beta^2$ , and the silicon and Cherenkov confidence level, using the reconstructed  $\beta$  from the  $p\bar{p}\pi^+\pi^-$  mass hypotheses, for real data that had been accepted as  $p\bar{p}\pi^+\pi^-$  at beam momentum 1.9 GeV/c are shown in figures 4.23 to 4.25.

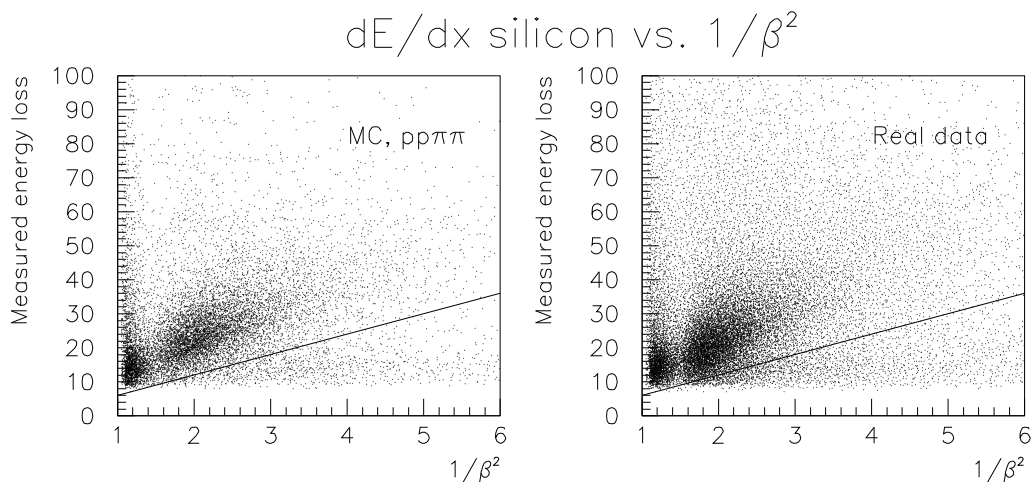


Figure 4.23: Measured silicon energy loss (arbitrary units) vs.  $1/\beta^2$  for real data reconstructed with the  $p\bar{p}\pi^+\pi^-$  mass hypothesis and Monte Carlo  $p\bar{p}\pi^+\pi^-$  at 1.9 GeV/c beam momentum. Measurements below the *m.i.p.* cut (the solid line) caused the kinematical hypothesis to be rejected.

#### 4.3.4 The complete analysis chain. Final decision

The events that were finally accepted as 4K event candidates had gone through the following analysis chain: First the raw 4K triggers were processed. Events satisfying the reduction cuts (section 4.2.1) were written to a new set of tapes. These reduced tapes were then read by the Display program (section 4.2.2), which did the track and vertex reconstruction. The events were accepted if the program could reconstruct 4 tracks coming from a common vertex, and the track parameters were written to a geometry DST tape, together with a copy of the raw event data. For some events, more than one set of 3 dimensional tracks were found, these were called renditions. Each rendition was written to the geometry DST together with its match probability. The geometry DST was then read by the Exotic program (section 4.2.2),

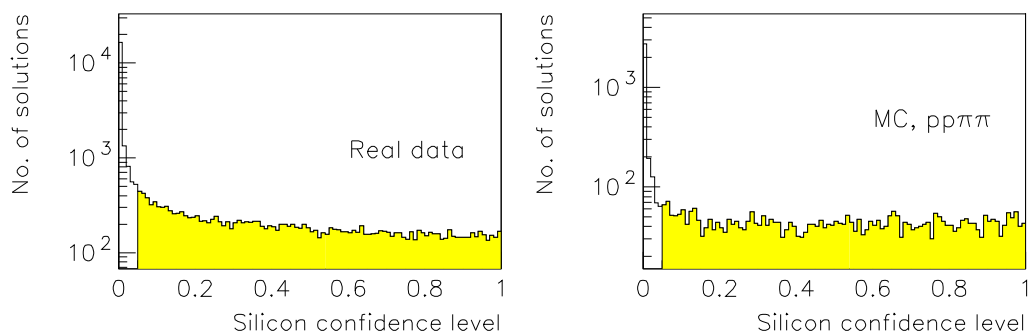


Figure 4.24: Silicon confidence level for real data and Monte Carlo  $p\bar{p}\pi^+\pi^-$  events, reconstructed with the  $p\bar{p}\pi^+\pi^-$  mass hypothesis, at a beam momentum 1.9 GeV/c. Note logarithmic scale. The white part of the histograms shows the events rejected by the silicon probability cut. The histograms contain the solutions retained after the minimum momentum cut.

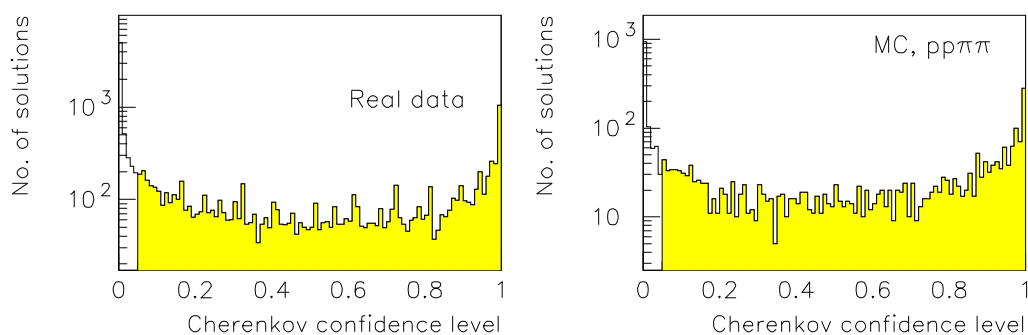


Figure 4.25: Cherenkov confidence level for real data and Monte Carlo  $p\bar{p}\pi^+\pi^-$  events, reconstructed with the  $p\bar{p}\pi^+\pi^-$  mass hypothesis, at a beam momentum 1.9 GeV/c. Note logarithmic scale. The white part of the histograms show the events rejected by the Cherenkov probability cut. The histograms contain the solutions retained after the silicon probability cut.

which associated the tracks to hits in other detectors, and checked for problems in the event data structure. An HBOOK Ntuple, called the 4-prong Ntuple, which contained summary information relevant for the further analysis was created. Each entry in the Ntuple corresponded to a rendition, with sequential renditions containing the same run and event number corresponding to a single event. The 4-prong Ntuple was read by the GeoBari program (section 4.2.3) which was the final step in the analysis to select the 4K event candidates. This program consisted of first step selection, kinematics and PID cuts, and a **final decision**. Each entry in the Ntuple (each rendition) had first to go through the first step selection cuts (section 4.2.3). Then the kinematical reconstruction (section 4.2.4) was applied for 7 different mass hypotheses, 4K and the 6 different  $p\bar{p}\pi^+\pi^-$  combinations. For each of these, the kinematical and particle identification cuts were repeated.

If the mass hypothesis passed the  $\Delta E$  cut (section 4.3.2), all the solutions (0,1 or 2), were tested for the minimum momentum cut (section 4.3.2), and for silicon and Cherenkov compatibility (section 4.3.3). An overall confidence level was formed by combining the silicon and Cherenkov confidence level. If both solutions for a mass hypothesis passed the kinematics and PID cuts, the one with the highest confidence level was selected. If at least one of the solutions for the 4K mass hypothesis passed the kinematics and PID cuts, the event was tagged as a 4K candidate. If at least one of the solutions for one of the 6  $p\bar{p}\pi^+\pi^-$  mass hypotheses passed the cuts, the event was tagged as a  $p\bar{p}\pi^+\pi^-$  candidate. There were some ambiguous events that were tagged both as 4K and  $p\bar{p}\pi^+\pi^-$  candidates. In order to suppress the large  $p\bar{p}\pi^+\pi^-$  background, especially at larger momenta where the  $p\bar{p}\pi^+\pi^-$  cross section is much larger than the 4K cross section, these events were rejected in the 4K analysis. In a few cases, more than one rendition for an event passed all the cuts. In that case the rendition with the highest probability from the track matching was selected. The remaining sample, which we call the 4K selected events, contained one entry per accepted event.

### Justification of the 4K analysis

To show that the analysis described above selected mostly 4K events, and removed mostly background, we did the analysis without activating the  $\Delta E$  cut (section 4.3.2). The distribution of this variable for all the 4-prong events from real data and Monte Carlo events are shown in figures 4.9 to 4.13 and this can be used to justify each of the analysis cuts, as described in section 4.3.1. The  $\Delta E$  distribution for events left after each cut in the 4K analysis are shown in figure 4.26. The  $\Delta E$  distributions for all the events that passed the first step selection, and rejected and accepted events after the kinematics and PID cuts described above, are shown in figure 4.27 for events reconstructed with the 4K mass hypothesis, and in figure 4.28 for events reconstructed with the  $p\bar{p}\pi^+\pi^-$  mass hypothesis.

For both mass hypotheses the cuts remove events mostly from the unphysical region at  $\Delta E > 0$  while keeping events in the peak at  $\Delta E \approx 0$ .

The distributions of momentum, polar angle, and sum of polar angles for the events selected by the 4K analysis are shown in figures 4.29 and 4.30 together with the Monte Carlo 4K and  $\phi\phi$  distributions. The distributions of these variables for all 4-prong events and for  $\phi\phi$  fit events are shown in figures 4.32 and 4.31.

The distributions for events selected by the 4K analysis show a better agreement with Monte Carlo and  $\phi\phi$  fit events, than the raw data.

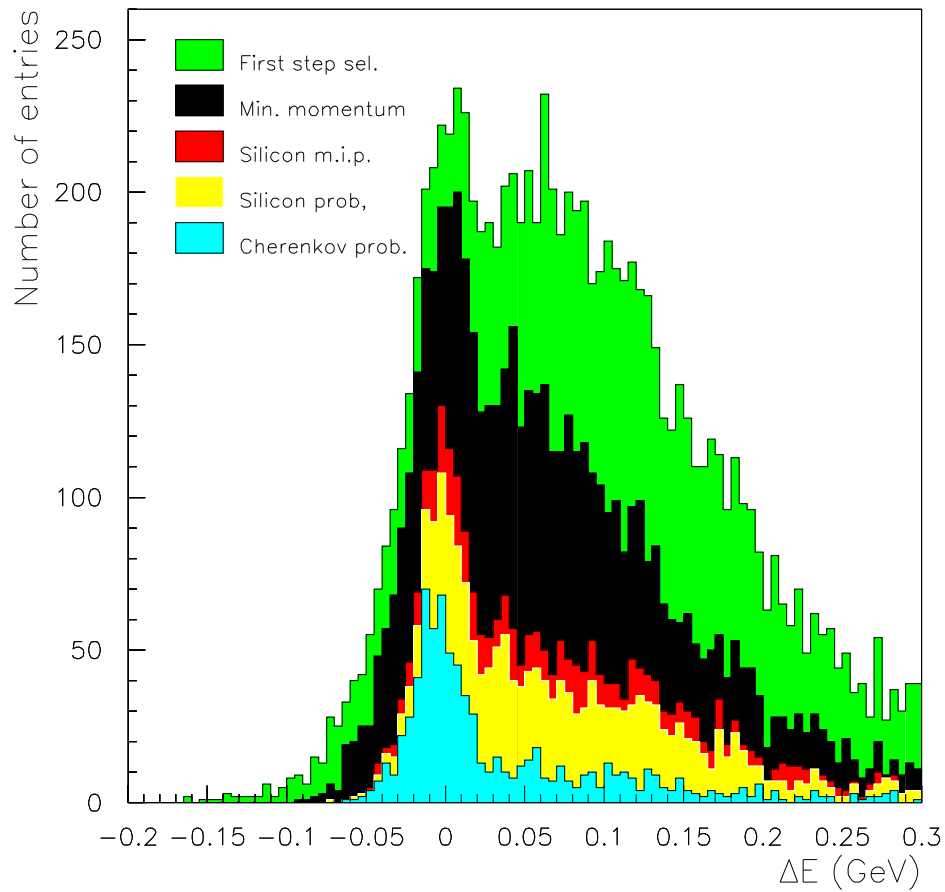


Figure 4.26:  $\Delta E$  distributions for real data, reconstructed with the  $4K$  mass hypothesis, showing  $\Delta E$  for the remaining events after first step selection, minimum momentum cuts, and silicon and Cherenkov cuts. Beam momentum 1.5 GeV/c.

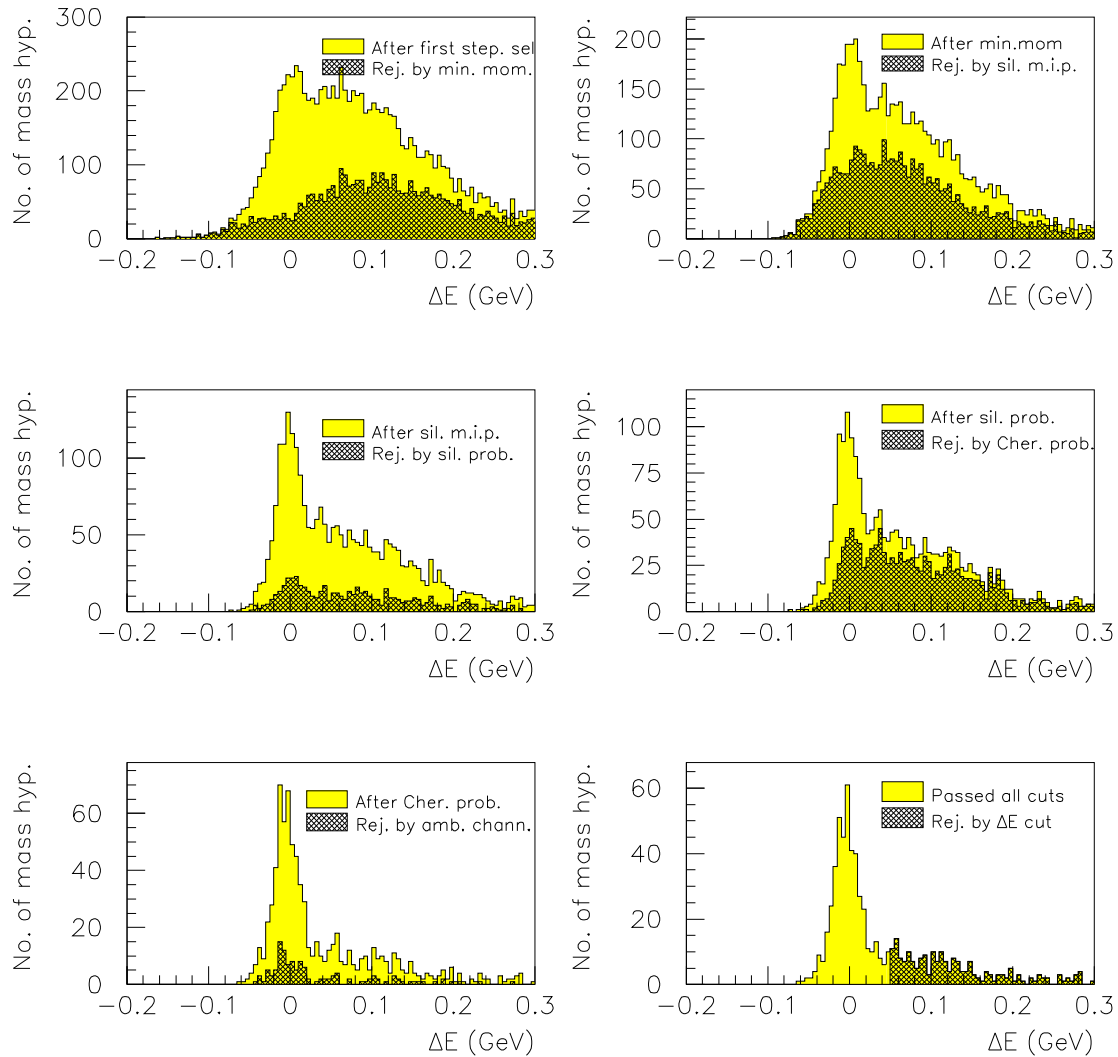


Figure 4.27:  $\Delta E$  distributions for real data events reconstructed with the 4K mass hypothesis, at beam momentum 1.5 GeV/c. The distributions for events accepted and rejected by each of the cuts on the 4-prong ntuple are shown.



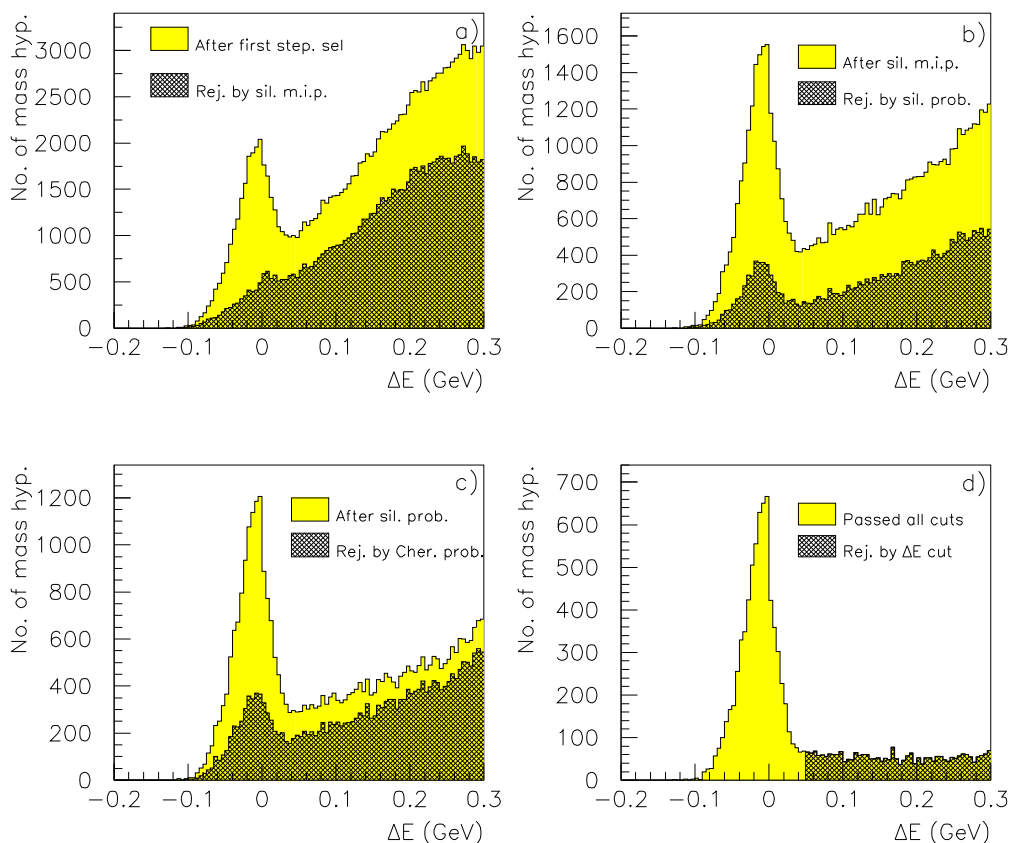


Figure 4.28:  $\Delta E$  distributions for real data events reconstructed with the  $p\bar{p}\pi^+\pi^-$  mass hypothesis, at beam momentum 1.9 GeV/c. The distributions for events accepted and rejected by each of the cuts on 4-prong ntuple are shown. Plot a)-c) may contain several  $p\bar{p}\pi^+\pi^-$  mass hypotheses for each rendition of an event. The large background is mainly from mass hypotheses with the wrong assignments of the 4 masses. In plot d) the best mass hypothesis and rendition are selected. The events that passed all the cuts (d) were rejected in the  $4K$  analysis.

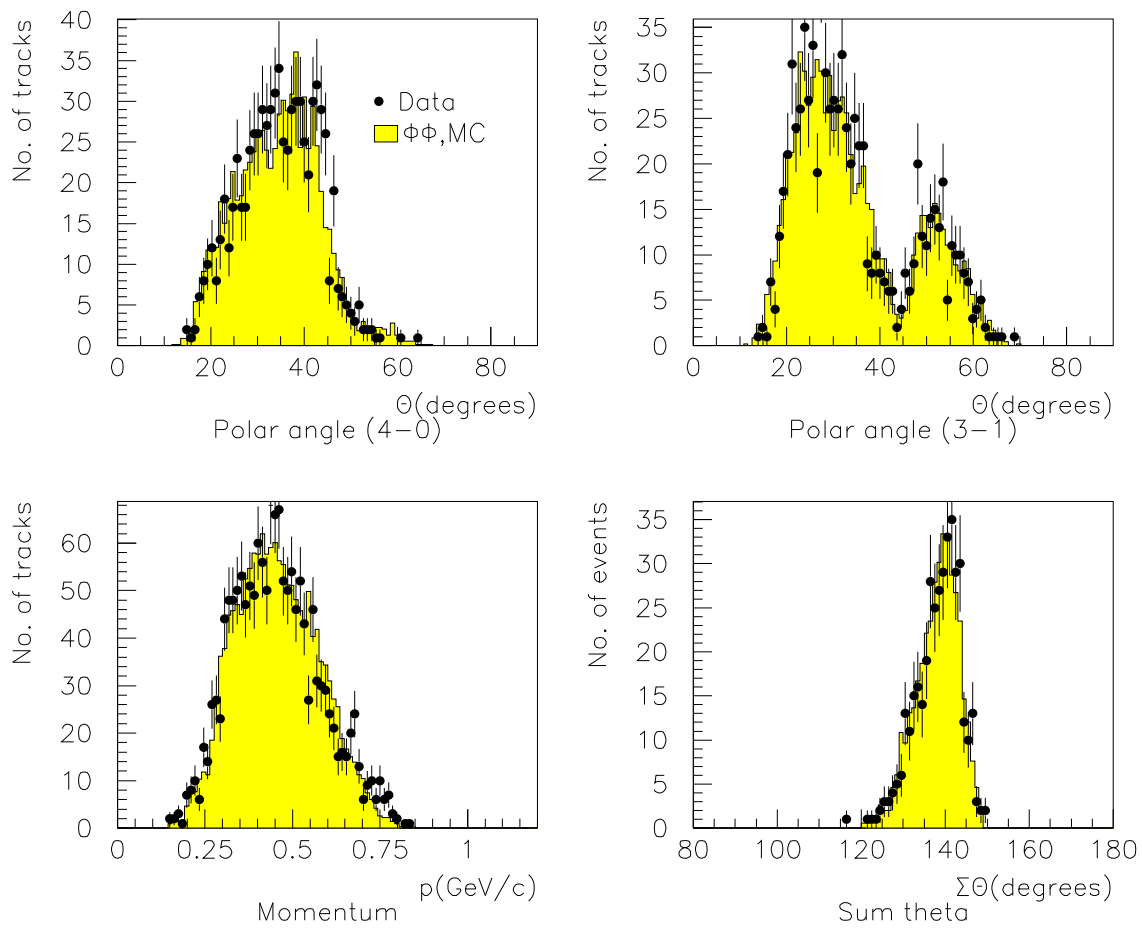


Figure 4.29: Distributions of polar angle  $\theta$  for 3-1 events and 4-0 events, momentum distribution for all tracks, and the sum of polar angles, for real events and  $\phi\phi$  Monte Carlo that passed the 4K event selection at beam momentum 1.5 GeV/c.

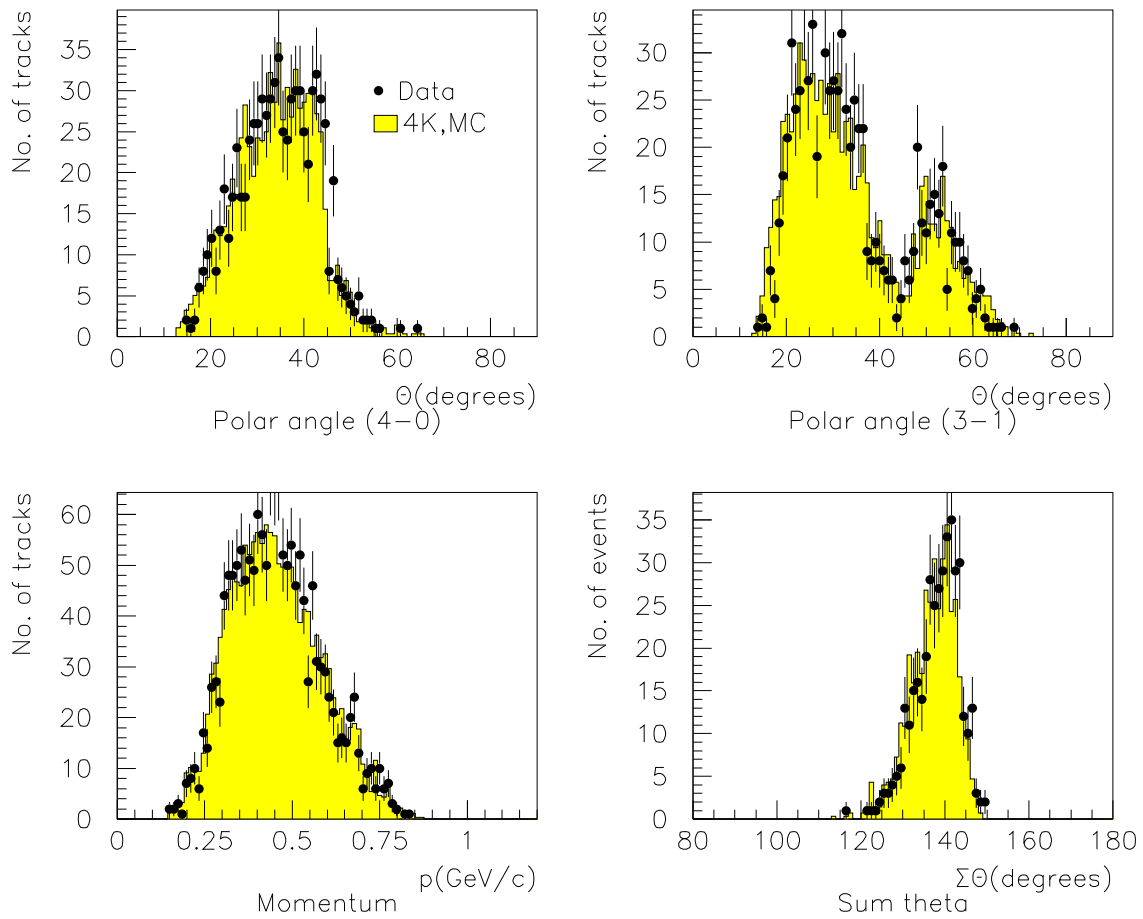


Figure 4.30: Distributions of polar angle  $\theta$  for 3-1 events and 4-0 events, momentum distribution for all tracks, and the sum of polar angles, for real events and 4K Monte Carlo that passed the 4K event selection at beam momentum 1.5  $\text{GeV}/c$ .

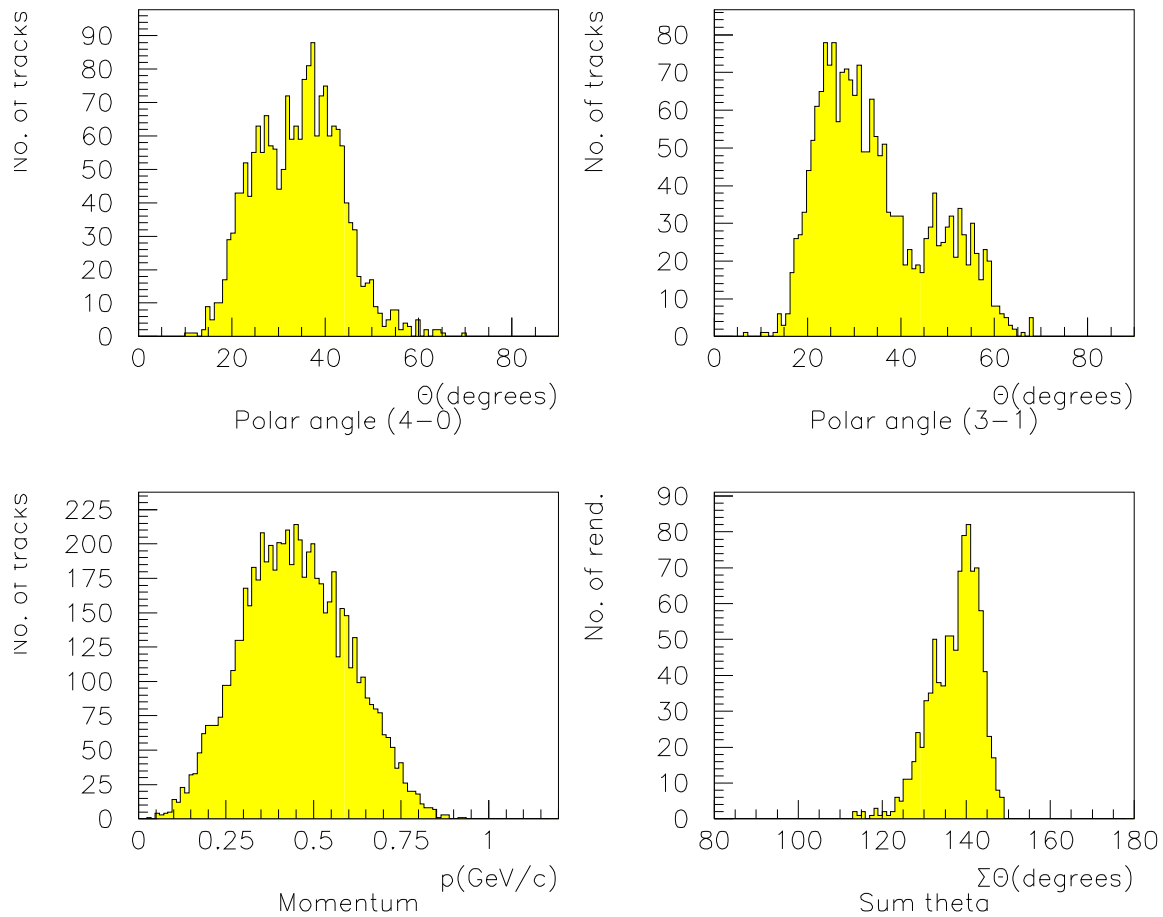


Figure 4.31: Distributions of polar angle  $\theta$  for 3-1 events and 4-0 events, momentum distribution for all tracks, and the sum of polar angles, for all 4-prong events with  $\phi\phi$  fit probability greater than 5% at beam momentum 1.5 GeV/c. Momentum reconstruction is done with the 4K mass hypothesis.

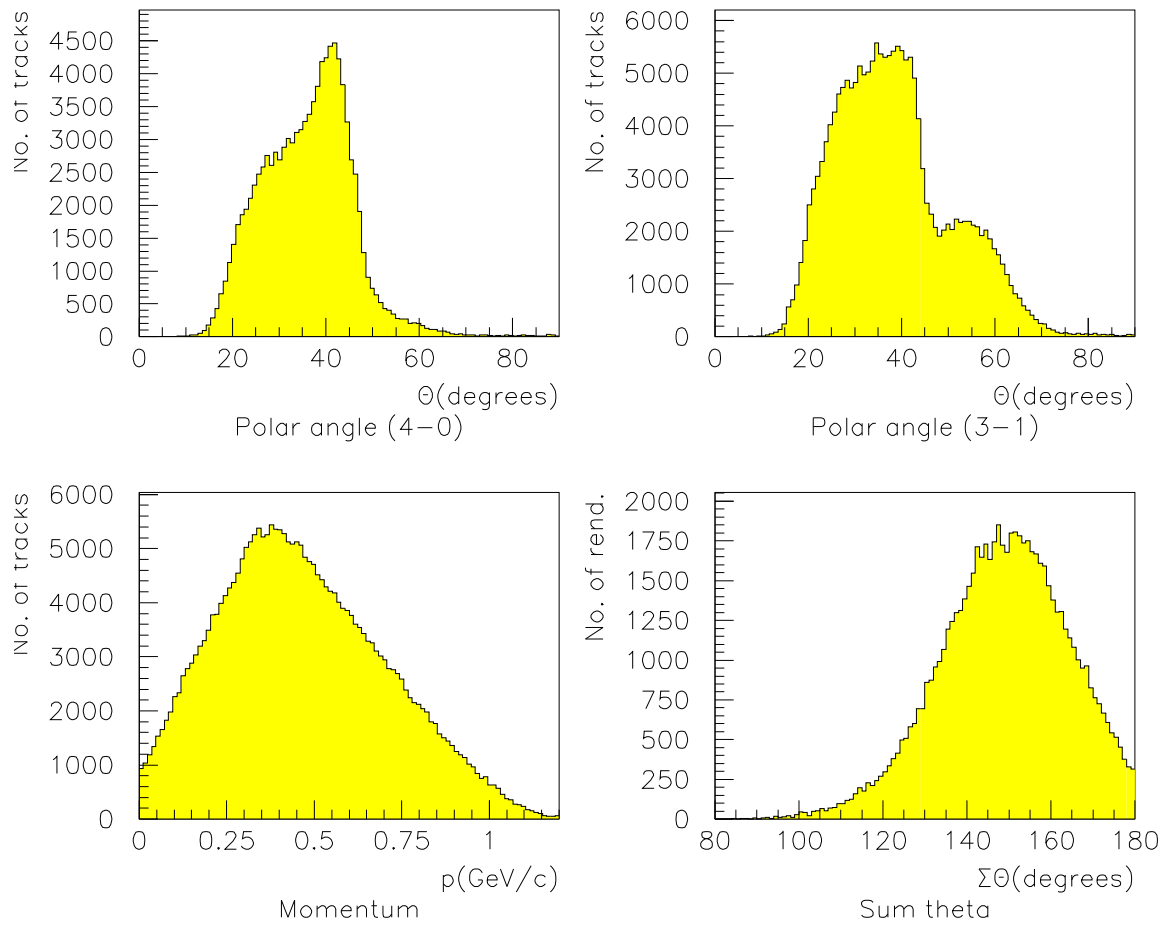


Figure 4.32: Distributions of polar angle  $\theta$  for 3-1 events and 4-0 events, momentum distribution for all tracks, and the sum of polar angles, for all 4-prong events at beam momentum 1.5 GeV/c. Momentum reconstruction is done with the 4K mass hypothesis.

### 4.3.5 Background subtraction

The 4K event sample selected by the method described above contained an unknown amount of background events, where background could be either events from other channels mistaken as 4K, or 4K events that were incorrectly reconstructed.

To estimate the number of background events, we made use of the  $\Delta E$  distribution. When the cut on  $\Delta E$  was not applied, the selected sample contained a tail extending into the unphysical region ( $\Delta E > 0$ ), that is not seen in the Monte Carlo (figure 4.33). The cut on  $\Delta E$  suppressed background events in this unphysical region. To estimate how much background was left in the sample after this cut was applied, the  $\Delta E$  cut was suspended and the full  $\Delta E$  distribution fitted to signal plus background (figure 4.33). This way the background was extrapolated from the unphysical into the physical region.

The expected shape of the signal was obtained from Monte Carlo  $\phi\phi$  and 4K data (figure 4.11). The real data were fitted to a sum of the central peak, where only the height was allowed to vary compared to the Monte Carlo data, plus a background parameterized as [?]

$$(E - E_0)^\alpha \times e^{-\beta E - \gamma E^2}. \quad (4.58)$$

$\alpha$ ,  $\beta$ , and  $\gamma$  are free parameters.

The number of background events was calculated as the integral of the background curve from  $-\infty$  to  $\Delta E_{max}$ , the value of the  $\Delta E$  cut. Note that this method only gives an estimate of the number of background events in the sample and does not give any information about individual events.

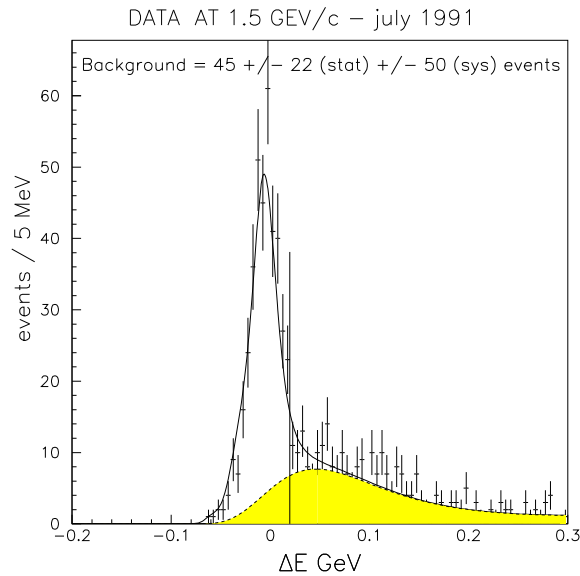


Figure 4.33: *Fit of the  $\Delta E$  distribution of the selected 4K sample to a signal peak plus background.*

### 4.3.6 Statistics

Tables 4.6 to 4.9 show the analysis statistics for real data and Monte Carlo data, analysed with the  $4K$  analysis chain, at three different beam momenta. Statistics for real data and Monte Carlo analysed with the  $p\bar{p}\pi^+\pi^-$  analysis chain are shown in table 4.10. The steps from triggers to DST show number of events after each step, but from the geometrical reconstruction (events written to the 4-prong ntuple), and first step selection, the total number of renditions passing the cuts are shown. The results from the kinematics show number of renditions with the  $4K$  mass hypotheses passing the  $\Delta E$  cut, followed by the total number of  $4K$  solutions for these renditions after the  $p_{min}$  cut, and the three particle identification cuts. The numbers under the heading *final decision* show number of renditions passing the  $4K$  cuts, number of renditions left after the  $p\bar{p}\pi^+\pi^-$  event candidates are rejected, and events left after rendition selection.

In the last row the estimated background, calculated with the method explained in section 4.3.5, is given.

For each of the reactions  $\phi\phi$ ,  $\phi KK$ , and  $4K$ , 100 000 Monte Carlo events were generated. Trigger and reduction cuts were imposed on the Monte Carlo events after tracking.

Reduction I cuts are those described in section 4.2.1. Reduction II cuts are the first 6 cuts in the *first step event selection*, described in section 4.2.3. The statistics for  $\phi\phi$  fit events are shown in table 4.7. A larger fraction of these events is selected by the analysis.

In chapter 6, number of events after PID for all beam momenta for the 1991 to 1993 JETSET runs, as well as the estimated number of background events, are reported.

## 4.4 Acceptance

The acceptance for the experiment for the reaction  $i$  is defined as

$$A_i = \frac{\text{Number of accepted events, reaction, } i}{\text{Total number of events produced, reaction, } i}. \quad (4.59)$$

To calculate the cross section, it was necessary to determine this number. This was done by simulating the detector, and all the physics processes occurring inside it, with a Monte Carlo program [?, ?] based on the GEANT package [?].

$\phi\phi$ ,  $\phi KK$ , and  $4K$  events were generated isotropically in phase space. The Monte Carlo program then tracked the particles through the detector. The geometry and material structure of the detector, as well as the efficiency and resolution of each detector, was described in the program. The GEANT package then applied the effects of physics processes like decay, multiple scattering, hadronic interactions, and energy loss to the tracks. Hits in the detectors were recorded, and the events were written to raw event files similar to the real data events. These files were then analysed with the program used to extract  $4K$  events, that has been described in this chapter. This program also simulated the online trigger conditions.

Reaction type	Real data	$\phi\phi$ MC	4K MC	$\phi KK$ MC
4K triggers processed	1853184			
Monte Carlo events generated		100000	100000	100000
Events after reduction	855 946	"	"	"
Reconstructed (written to DST)	71 627	15 555	10 659	10 189
Events with OK format	71626	"	"	"
Written to 4-prong ntuple	71044	15926	10517	10099
<b>Selection</b>				
Renditions after bad.run suppr.	62765	15926	10517	10099
Renditions after trigger check	62765	6633	4124	3847
Renditions after red.I	62765	6018	3721	3493
Renditions after red.II	13390	4944	3012	2802
Renditions after min. silic.	11594	4801	2932	2727
Renditions after min Cher.	11391	4781	2921	2715
Renditions after barrel ins.	10406	4543	2742	2583
Renditions after pipe scint.ass.	10342	4540	2739	2581
<b>Kinematics</b>				
4K mass hyp. after $\Delta E$ cut	2482	3906	2348	2240
4K solutions after min.mom. cut	2599	5927	3460	3165
<b>Particle identification</b>				
4K solutions after sil. m.i.p. cut	1166	4241	2389	2131
4K solutions after sil. prob.	926	3469	1950	1716
4K solutions after Cher. prob.	581	2813	1609	1398
<b>Final decision</b>				
4K mass hyp. after all PID cuts	481	2317	1303	1187
Renditions after amb. channel rejection	469	2263	1290	1174
Events after rendition selection.	393	1957	1087	1002
Non-4K background	$39 \pm 24 \pm 44$	-	-	"

Table 4.6: Number of real data events and Monte Carlo events passing trigger and 4K analysis cuts, at beam momentum 1.5 GeV/c.



Reaction type	Real data	$\phi\phi$ MC	4K MC	$\phi KK$ MC
Written to 4-prong ntuple	972	9393	851	1348
<b>Selection</b>				
Renditions after bad.run suppr.	862	9393	851	1348
Renditions after trigger check	862	4051	363	557
Renditions after red.I	862	3731	334	523
Renditions after red.II	443	3101	280	447
Renditions after min. silic.	429	3048	275	440
Renditions after min Cher.	424	3038	275	437
Renditions after barrel ins.	403	2890	270	422
Renditions after pipe scint.ass.	403	2890	270	422
<b>Kinematics</b>				
4K mass hyp. after $\Delta E$ cut	402	2866	270	419
4K solutions after min.mom. cut	624	4566	451	659
<b>Particle identification</b>				
4K solutions after sil. m.i.p. cut	435	3359	298	458
4K solutions after sil. prob.	355	2765	233	382
4K solutions after Cher. prob.	259	2243	204	299
<b>Final decision</b>				
4K mass hyp. after all PID cuts	208	1833	156	247
Renditions after amb. channel rejection	200	1789	153	243
Events after rendition selection.	165	1556	123	205

Table 4.7: Number of real data events and Monte Carlo events with  $\phi\phi$  fit probability higher than 5 % passing trigger and 4K analysis cuts, at beam momentum 1.5 GeV/c.

Reaction type	Real data	$\phi\phi$ MC	4K MC	$\phi KK$ MC
4K triggers processed	1709731			
Monte Carlo events generated		100000	100000	100000
Events after reduction	725019	"	"	"
Reconstructed (written to DST)	45519	8653	8739	7804
Events with OK format	43274	"	"	"
Written to 4-prong ntuple	40468	7627	7913	7110
<b>Selection</b>				
Renditions after bad.run suppr.	40033	7627	7913	7110
Renditions after trigger check	40033	2836	2919	2549
Renditions after red.I	40033	2581	2658	2298
Renditions after red.II	7608	1848	1886	1597
Renditions after min. silic.	5819	1743	1764	1490
Renditions after min Cher.	5705	1732	1750	1479
Renditions after barrel ins.	5136	1625	1627	1384
Renditions after pipe scint.ass.	5106	1622	1623	1381
<b>Kinematics</b>				
4K mass hyp. after $\Delta E$ cut	867	1444	1360	1174
4K solutions after min.mom. cut	748	1884	1672	1465
<b>Particle identification</b>				
4K solutions after sil. m.i.p. cut	186	1146	999	869
4K solutions after sil. prob.	136	857	752	631
4K solutions after Cher. prob.	77	691	607	545
<b>Final decision</b>				
4K mass hyp. after all PID cuts	66	592	536	483
Renditions after amb. channel rejection	66	592	536	483
Events after rendition selection.	51	515	459	420
Non-4K background	$5 \pm 7 \pm 8$	-	-	-

Table 4.8: Number of real data events and Monte Carlo events passing trigger and 4K analysis cuts, at beam momentum 1.2 GeV/c.

Reaction type	Real data	$\phi\phi$ MC	4K MC	$\phi KK$ MC
4K triggers processed	5426141			
Monte Carlo events generated		100000	100000	100000
Events after reduction	2694052	"	"	"
Reconstructed (written to DST)	369035	20153	12022	12261
Events with OK format	368118	"	"	"
Written to 4-prong ntuple	376464	22563	12621	12710
<b>Selection</b>				
Renditions after bad.run suppr.	195812	22563	12621	12710
Renditions after trigger check	195812	12463	6497	6535
Renditions after red.I	195812	11420	5968	6053
Renditions after red.II	63216	10127	5154	5236
Renditions after min. silic.	57593	9886	5017	5093
Renditions after min Cher.	55684	9826	4994	5069
Renditions after barrel ins.	52461	9363	4742	4825
Renditions after pipe scint.ass.	52263	9359	4738	4823
<b>Kinematics</b>				
4K mass hyp. after $\Delta E$ cut	22538	8092	4102	4120
4K solutions after min.mom. cut	15547	13208	6351	6199
<b>Particle identification</b>				
4K solutions after sil. m.i.p. cut	6561	10531	4862	4672
4K solutions after sil. prob.	4590	8895	4054	3868
4K solutions after Cher. prob.	1861	5761	2857	2800
<b>Final decision</b>				
4K mass hyp. after all PID cuts	1668	4704	2358	2364
Renditions after amb. channel rejection	1109	4286	2226	2267
Events after rendition selection.	964	3532	1917	1904
Non-4K background	$334 \pm 33 \pm 263$	-	-	-

Table 4.9: Number of real data events and Monte Carlo events passing trigger and 4K analysis cuts, at beam momentum 1.9 GeV/c.

Reaction type	Real data	$p\bar{p}\pi^+\pi^-$ MC
4K triggers processed	2694052	
Monte Carlo events generated)		400000
Events after reduction	2694052	"
Reconstructed (written to DST)	369035	10252
Events with OK format	368118	"
Written to 4-prong ntuple	376464	9979
<b>Selection</b>		
Renditions after bad.run suppr.	195 812	9979
Renditions after trigger check	195 812	5408
Renditions after red.I	195 812	4973
Renditions after red.II	63216	4497
Renditions after min. silic.	57593	4450
Renditions after min Cher.	56845	4427
Renditions after barrel ins.	52461	4200
Renditions after pipe scint.ass.	52263	4198
<b>Kinematics</b>		
4K mass hyp. after $\Delta E$ cut	28042	5402
4K solutions after min.mom. cut	27319	5303
<b>Particle identification</b>		
4K solutions after sil. m.i.p. cut	18705	3787
4K solutions after sil. prob.	14066	3165
4K solutions after Cher. prob.	9052	2264
<b>Final decision</b>		
4K mass hyp. after all PID cuts	8814	2211
Renditions after amb. channel rejection	7356	1868
Events after rendition selection.	7356	1868
Non- $p\bar{p}\pi^+\pi^-$ background	$207 \pm 78 \pm 500$	-

Table 4.10: Number of real data events and Monte Carlo events passing trigger and  $p\bar{p}\pi^+\pi^-$  analysis cuts, at beam momentum 1.9 GeV/c.

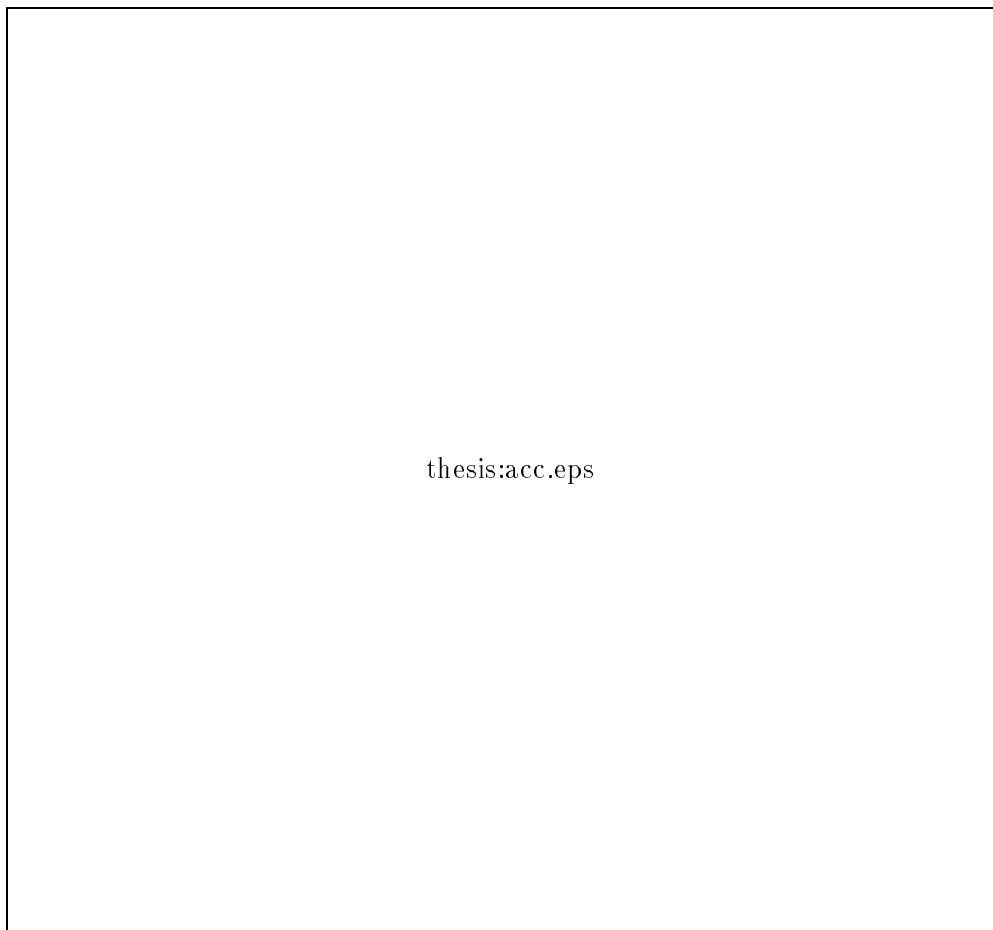


Figure 4.34: *The geometrical acceptance, and the efficiency of trigger, barrel gamma veto, and PID cuts (from [?]).*

For each beam momentum setting at each of the run periods 100 000 events for each of the channels  $\phi\phi$ ,  $\phi KK$ , and  $4K$  were generated. Any changes in the detector, like dead channels, noise, and different discriminator thresholds were inserted into the program [?]. The resulting values for the acceptance are reported in chapter 7.

Factors entering the acceptance were (figure 4.34):

- **Geometrical acceptance.** This is the efficiency of the program to find 4 tracks coming from the vertex. The  $4K$  events could be lost at this stage because the direction of tracks was outside the angular acceptance of the tracker, or because the track finding and matching algorithm could not manage to reconstruct the tracks. To determine the correct tracking efficiency, straw efficiencies, resolutions, and noise rates were simulated in the Monte Carlo program [?]. Other factors that contributed to loss of efficiency were physical processes like multiple scattering, energy loss, and decays.

- **The efficiency of the online trigger.** The trigger cuts are described in section 3.3. In particular, the trigger efficiency was sensitive to the the response of the Cherenkov counter. The Cherenkov trigger accepted events with a maximum multiplicity of hits (section 3.3) above discriminator threshold. To correctly estimate the trigger efficiency, which was dependent on the precise setting of the electronic threshold, the Monte Carlo ADC values were multiplied by a normalization factor dependent on the counter and run period [?].

The Cherenkov efficiency determined from Monte Carlo was also dependent on the type of hadronic interaction generator used in the simulation program. The physics of slow hadrons is complicated to simulate, and the GEANT program has two different programs to generate the hadronic interactions, FLUKA [?], and GHEISHA [?]. Use of the two different programs gave a difference of almost a factor 2 in trigger efficiency. Comparisons of the momentum distributions of kaons with and without a hit in the Cherenkov in Monte Carlo and real data, showed that GHEISHA gave the best agreement to real data [?]. Also, minimum bias data were collected in May 93, at beam momentum 1.415 GeV/c and 1.8 GeV/c, without the Cherenkov conditions. The cross sections calculated from these data are in agreement with the rest of the data within the statistical error.

- **The reduction and first step selection cuts.** These cuts operated on the pattern of pipe scintillator hits, and multiplicity, of various detectors. Most of these cuts gave no loss of final signal, and therefore could not affect the acceptance. An exception is the barrel gamma veto cut. The effect of this cut is shown in figure 4.34.
- **Efficiency of the kinematics and PID cuts.** The efficiency of these cuts depended on the resolution, efficiency, and noise of the Cherenkov and silicon dE/dx detectors. In addition the tracking resolution was important, since the momenta and velocities used in the cuts were calculated from the directions. To obtain the correct resolution in the Monte Carlo the straw hits were smeared out according to a Gaussian distribution with the width corresponding to the straw resolution.

To check that the efficiency of the kinematics and PID cuts was correctly determined in the Monte Carlo, the efficiency of the PID can also estimated from the  $\phi\phi$  fit events. From tables 4.6 and 4.7 we get number of 4-prong events after trigger and reduction cuts, and number of final events for MC  $\phi\phi$  events, and real  $\phi\phi$  fit events. An efficiency of  $0.41 \pm 0.03$  is obtained, which is in agreement with the value of  $0.43 \pm 0.007$  from MC data.

The acceptance was not uniform in the polar angle in the centre of mass system of the outgoing  $\phi$  mesons. Figure 4.35 shows the distribution of  $\cos \Theta_{cm}$ , the polar angle of the  $\phi$  mesons in the CM frame, together with the corresponding curve for phase space Monte Carlo  $\phi\phi$  events, for collected data at a beam momentum between 1.4 -1.45 GeV/c. The acceptance decreases with increasing  $\cos \Theta_{cm}$  and is zero for  $\cos \Theta_{cm} > 0.8$ . This is due to the limited forward acceptance of the detector.

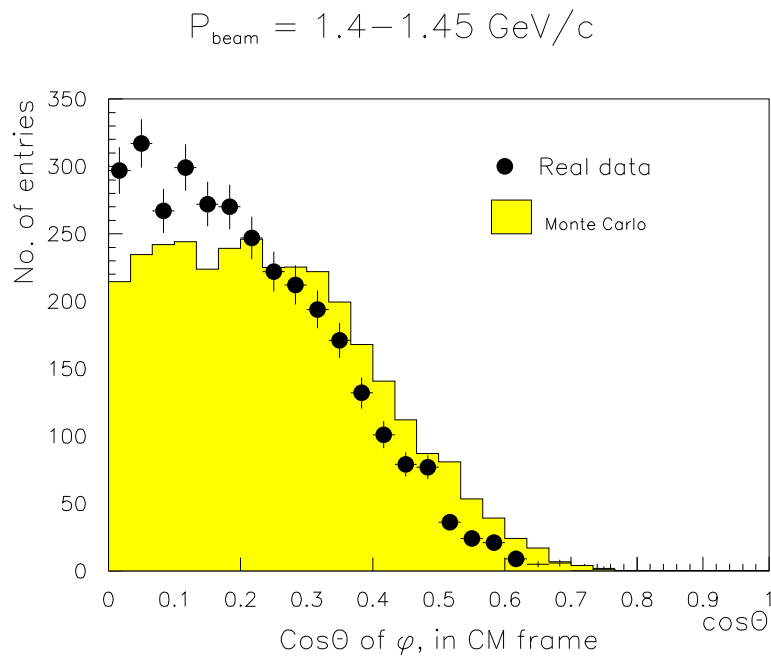


Figure 4.35: Polar angle,  $\theta$ , of the  $\phi$  meson in the c.m. frame, beam momentum 1.4 -1.45 GeV/c.

### Monte Carlo simulation of background channels

A Monte Carlo simulation was done of possible background events to the  $4K$  signal. Generated events of each reaction were tracked through the detector by the GEANT Monte Carlo program, the events were then written to tape, and went through the same analysis chain as the rest of the data. Figure 4.36 shows the cross section of each of these channels times geometrical acceptance, trigger acceptance, kinematical acceptance, and the full acceptance at 1.4 GeV/c.

The estimated background of 20% from non- $4K$  events agrees with the background estimate from the  $\Delta E$  fit.

Figure 4.36: *Cross section times acceptance for the  $\phi\phi$  channel and background channels at 1.4 GeV/c. From [?].*



## Chapter 5

# Extraction of $\phi\phi$ events

The  $4K$  event sample selected by the analysis chain described in the previous chapter contains a mixture of the following types of events :

- $p\bar{p} \rightarrow 4K$  (nonresonant)
- $p\bar{p} \rightarrow \phi K K \rightarrow 4K$
- $p\bar{p} \rightarrow \phi\phi \rightarrow 4K$
- Background reactions, for example  
 $p\bar{p} \rightarrow p\bar{p}\pi^+\pi^-$ ,  $p\bar{p} \rightarrow 4\pi^\pm\pi^0$ ,  $p\bar{p} \rightarrow 2K^\pm 2\pi^\pm\pi^0$ ,  
and other reactions involving pions.<sup>1</sup>

In this chapter, the method for extracting the number of  $p\bar{p} \rightarrow \phi\phi$  events in the  $4K$  event sample, which is required to calculate the  $p\bar{p} \rightarrow \phi\phi$  cross section, is examined.

Optimally, we would also like to estimate how many of the remaining events are  $p\bar{p} \rightarrow 4K$  (nonresonant) and how many are  $p\bar{p} \rightarrow \phi K K \rightarrow 4K$  in order to calculate these cross sections as well.

### Invariant mass distributions

The events we are studying have a final state consisting of 4 particles, which we assume are  $K^+K^-K^+K^-$ ,<sup>2</sup> with the charge assignments unknown. The kaons can be combined into pairs, and the invariant mass for each pair calculated, in three different ways for each event.

$$M(K_2, K_3) \leftrightarrow M(K_1, K_4), \quad M(K_1, K_3) \leftrightarrow M(K_2, K_4), \quad M(K_1, K_2) \leftrightarrow M(K_3, K_4). \quad (5.1)$$

---

<sup>1</sup>The cross sections of the relevant background reactions are given in figure 3.4. A large part of the background events, except those with the  $p\bar{p}\pi^+\pi^-$  final state are removed by the trigger cuts (section 3.3). The amount of background left in the sample after all  $4K$  selection cuts is considered in section 4.4.

<sup>2</sup>Kaon masses are assumed when doing the kinematical reconstruction and when calculating invariant masses

Figure 5.1: Goldhaber plot and invariant mass in the  $\phi$  band for Monte Carlo  $\phi\phi$ ,  $4K$  and  $\phi KK$  events at 1.5 GeV/c beam momentum (after  $4K$  selection cuts). The horizontal and vertical lines indicate the  $\phi$  bands. The one-dimensional histograms to the right show the projection of the Goldhaber plot containing only the entries within the two bands. The  $\phi\phi$  and  $\phi KK$  histograms have been fitted to a Breit Wigner resonant peak plus a background. The  $4K$  histogram has been fitted to only a background shape.

A two-dimensional scatter plot with the invariant mass of the two kaon pairs in each combination plotted against each other is called a **Goldhaber plot**. The plot contains three entries for each event, since the charges of the particles are unknown all three possible combinations must be taken into account. If the event is a  $p\bar{p} \rightarrow \phi\phi \rightarrow 4K$  event then one of the  $K^+K^-$  combinations will have both invariant masses equal to the  $\phi$  mass, which will contribute to a peak in the Goldhaber plot at  $M_1 = M_2 = m_\phi = 1.019 \text{ GeV}/c^2$ . Figures 5.1 and 5.2 show Goldhaber plots for  $\phi\phi$ ,  $4K$ ,  $\phi KK$ , and  $p\bar{p}\pi^+\pi^-$  Monte Carlo events.

Similar plots were shown in chapter 2 (figure 2.32), but in these plots the generated momenta were used to calculate the invariant masses, the difference between figure 5.1 and 2.32 is due to the limited acceptance and reconstruction resolution of the JETSET apparatus which has been simulated by the JETSET GEANT Monte Carlo program, used when generating figure 5.1.

The wrong combinations of kaons for  $\phi\phi$  events show up in the Goldhaber plots as an accumulation near the diagonal edge of phase space. The one-dimensional plots shown are projections of the Goldhaber plot selecting those entries where the other entry has a mass equal to the  $\phi$  mass  $\pm 0.02 \text{ GeV}/c^2$ . This way much of the combinatorial background is removed from  $\phi\phi$  events. The nonresonant  $4K$  events will be produced uniformly in phase space, giving a uniform distribution of the Goldhaber plot. The mass distribution from the nonresonant  $4K$  Monte Carlo events that have gone through the GEANT program is approximately uniform, showing that the non-uniform acceptance of the experiment does not give rise to structures in the mass plot.

The Goldhaber plots and their projections in the  $\phi$  band for all 4-prong events in the real data events and for the selected events are shown in figures 5.3 and 5.4. A clear  $\phi\phi$  peak is seen in the selected events.

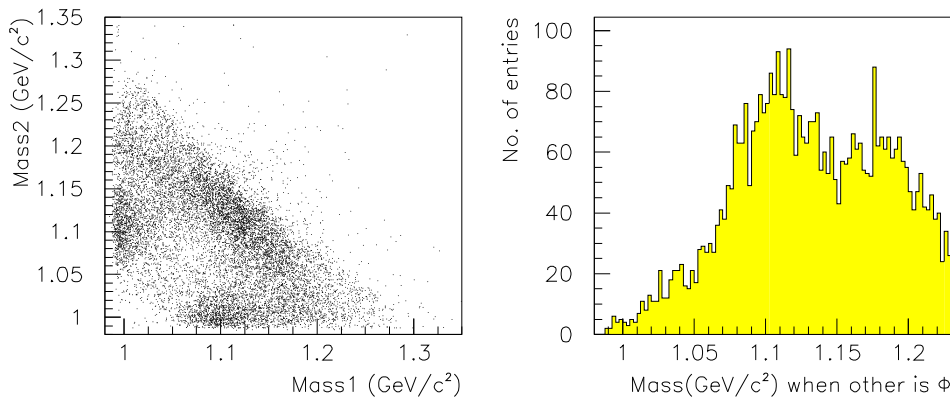


Figure 5.2: Goldhaber plot and invariant mass in the  $\phi$  band for Monte Carlo  $p\bar{p}\pi^+\pi^-$  events at  $1.6 \text{ GeV}/c$  beam momentum, reconstructed with the  $4K$  mass hypothesis (no  $4K$  selection cuts).

### Separation of $\phi\phi$ , $\phi KK$ and $4K$ events

To estimate the relative admixture of  $\phi\phi$ ,  $\phi KK$ , and  $4K$  events, the Goldhaber plots for the 1.5 GeV/c selected data sample (figure 5.4) are compared to the expected distributions from Monte Carlo events (figure 5.1). The  $\phi\phi$  peak can clearly be seen in the data as a clustering of events at  $M_1 = M_2 = m_\phi$ . There is no obvious sign of the two bands at  $M_1 = m_\phi$  and  $M_2 = m_\phi$  which are characteristic for the  $\phi KK$  events.

The presence of  $\phi KK$  in the data can be looked for in the invariant mass distributions **outside** the  $\phi$  band, that is, the projection of the Goldhaber plot when the other entry has a mass different from the  $\phi$  mass. Figure 5.5 shows this distribution for real data and Monte Carlo. The  $\phi$  peak seen in the  $\phi KK$  Monte Carlo events is not obvious in the real data at 1.5 GeV/c. However, at beam momenta 1.7 GeV/c and higher the  $\phi KK$  peak is clearly seen in the data (figures 7.16 to 7.18). It is therefore necessary to take this channel into account. Several different methods were tested on the real data and Monte Carlo data to estimate the number of  $\phi\phi$  and if possible  $\phi KK$  and  $4K$  in the sample.

- To find the number of  $\phi\phi$  event, we can make a cut in the Goldhaber plot, accepting events where both entries fall within a square with sides  $2\Delta M$  ( $\Delta M = 0.02 \text{ GeV}/c^2$ ) with a centre at the  $\phi$  mass ( $m_\phi = 1.019 \text{ GeV}/c^2$ ).

$$(M_1 - m_\phi) < \Delta_M \cap (M_2 - m_\phi) < \Delta M \quad (5.2)$$

A certain fraction of  $\phi KK$ ,  $4K$  and background events will be accepted by this cut, since the cross sections for  $4K$  and  $\phi KK$  are not known a priori, this can not be corrected for.

- Another method is to fit the one-dimensional invariant mass distributions (the projection of the Goldhaber plots inside the  $\phi$  bands) to the following functional form

$$f(x) = a \cdot (x - 2m_K)^{0.35} \cdot (b - x)^c \cdot \left(1 + d \cdot \frac{?^2}{(x - M)^2 + ?^2/4}\right), \quad (5.3)$$

which is a sum of a Breit-Wigner resonant shape with mass  $M$  and width  $?$  plus background.  $a, b, c, d$  are free parameters, while  $m_K$  is the kaon mass. This way the number of non  $\phi\phi$  background events falling under the the  $\phi\phi$  peak can be estimated. This removes most of the  $4K$  but not the  $\phi KK$  background.

- We can also choose to accept as  $p\bar{p} \rightarrow \phi\phi$  the events that have a  $\phi\phi$  fit probability greater than 5%. This method also renders the problem of an unknown amount of nonresonant  $4K$ ,  $\phi KK$ , and other background accepted by the cut.
- The method that was chosen is the **Channel likelihood** method (described below). This method uses a maximum likelihood fit to find the fraction of  $\phi\phi$ ,  $\phi KK$ , and non-resonant channels in the Goldhaber plot.

The results from each of these methods are shown in table 5.1.

Figure 5.3: *Goldhaber plot and invariant mass in the  $\phi$  band for all 4-track events at 1.5 GeV/c beam momentum.*

Figure 5.4: *Goldhaber plot and invariant mass in the  $\phi$  band for events selected with the 4K analysis at 1.5 GeV/c beam momentum.*

Data type	Real data	$\phi\phi$ MC	$4K$ MC	$\phi KK$ MC
Total number of '4K' events	393	1957	1087	1002
Events after mass cut	193	1630	165	276
Events after background subtraction	$172 \pm 9$	$1683 \pm 3$	$9 \pm 59$	$172 \pm 115$
Events with $\phi\phi$ fit prob. > 5%	165	1556	123	205
$\phi\phi$ after channel likelihood	$187 \pm 18$	$1957 \pm 70$	$0 \pm 12$	$39 \pm 31$

Table 5.1: Results from different methods of estimating the number of  $\phi\phi$  events in the event sample selected by the  $4K$  analysis, for real data and Monte Carlo at a beam momentum 1.5 GeV/c. The various methods are described in the text.

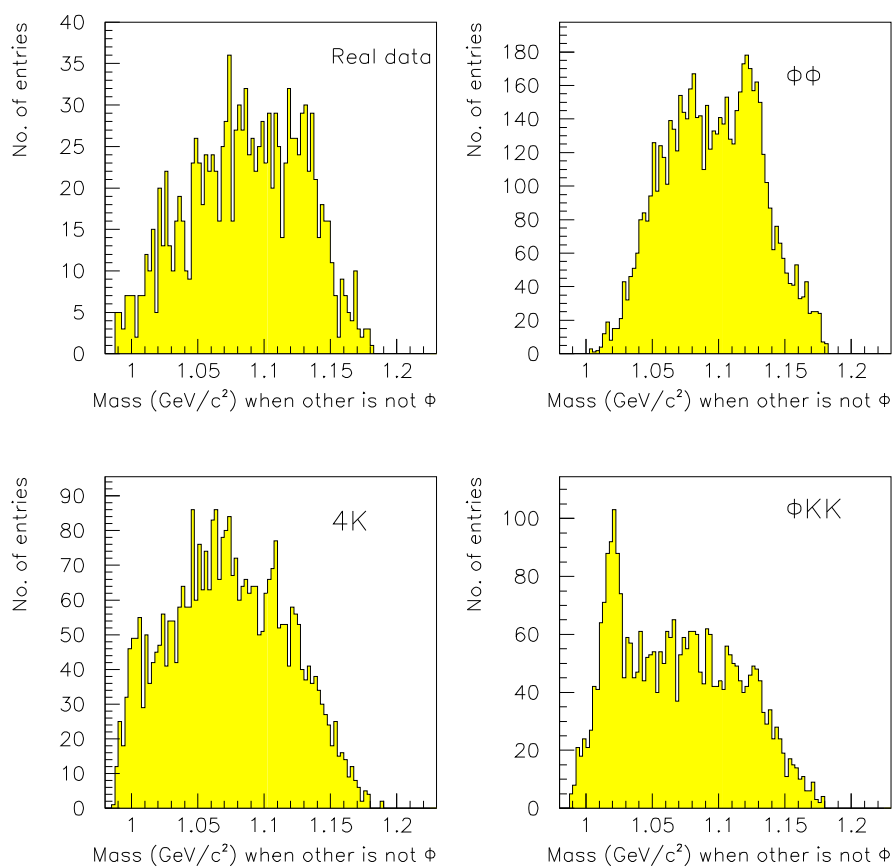


Figure 5.5: Invariant mass outside the  $\phi$  band for Monte Carlo and real data selected with the  $4K$  analysis 1.5 GeV/c beam momentum.

### The channel likelihood method

The purpose of the channel likelihood method [?, ?] was to find the number of  $\phi\phi$ ,  $\phi KK$  events, and “phase-space events”,<sup>3</sup> in the selected  $4K$  sample. This was done by fitting the invariant mass plot, the Goldhaber plot, to a sum of three functions, corresponding to the expected distributions for the three channels. The method of maximum likelihood was applied.

With this method, the likelihood function to be maximized is

$$\mathcal{L} = \prod_{j=1}^n \left( \sum_{i=0}^m \alpha_i W_{ij} \right), \quad (5.4)$$

where  $n$  is the total number of events and  $m$  is the number of resonant channels = 2 ( $\phi\phi$ ,  $\phi KK$ ),  $i = 0$  corresponds to the nonresonant phase space channel.  $\alpha_i W_{ij}$  is the relative probability of event  $j$  having come from channel  $i$ .

The three parameters to be fitted are the  $\alpha_i$ ,  $i = 0, 2$ . They are the fractions of each of the channels  $\phi\phi$ ,  $\phi KK$  and phase space events in the sample ( $\alpha_i = n_i/n$ , where  $n_i$  is number of events, channel  $i$ ) and are subject to the following constraint :

$$\sum_{i=0}^m \alpha_i = 1. \quad (5.5)$$

$W_{ij}$  is a function describing channel  $i$ . It is a function of the 6 invariant mass combinations,  $M_{12}, M_{34}, M_{14}, M_{23}, M_{13}, M_{24}$ , for an event, and is the product of detector acceptance and the phase space density for the channel.

$$W_{ij} = \frac{A_j \cdot R_{ij}}{N_i}, \quad (5.6)$$

where  $A_j$  is the acceptance for event  $j$ , which is the same for all three  $4K$  channels,  $R_{ij}$  is the phase space density function, and  $N_i$  is the normalization integral  $N_i = \int d\Omega_{ps} A(\Omega) R_i(\Omega)$  where  $\Omega$  is an element of 8-dimensional phase space.

The channels  $\phi\phi$  and  $\phi KK$  are described by the invariant mass distributions, which follow the  $\phi\phi$  lineshape. A Breit Wigner resonant shape was found to give the best description of the data.

$$R_{\phi\phi,j} = BW(M_{12})BW(M_{34}) + BW(M_{13})BW(M_{24}) + BW(M_{14})BW(M_{23}), \quad (5.7)$$

$$R_{\phi KK,j} = BW(M_{12}) + BW(M_{34}) + BW(M_{13}) + BW(M_{24}) + BW(M_{14}) + BW(M_{23}). \quad (5.8)$$

where  $M_{12}$  is the invariant mass of kaon 1 and 2, in event  $j$  etc.

The channel 0 is uniformly distributed in phase space

$$R_{0j} = 1. \quad (5.9)$$

$BW$  is a Breit-Wigner function for the  $\phi$  resonance, with parameters determined from  $\phi\phi$  Monte Carlo. These expressions include all the combinations in the invariant mass plot.

---

<sup>3</sup>The events classified as “phase space” were events distributed uniformly in phase space, this included nonresonant  $4K$  and background

Channels	Input fractions	Output fractions
$\phi\phi, \phi KK, 4K$	0.0,0.0 100.0	0.0 (1.1),5.75 (4.5),94.3 (4.6)
$\phi\phi, \phi KK, 4K$	16., 0.0 , 83.3	18.4 (2.0), 0.9 (5.6), 80.7 (5.6)
$\phi\phi, \phi KK, 4K$	33.3, 0.0,66.7	36.2 (2.2), 0.3 (4.7), 63.6 (4.5)
$\phi\phi, \phi KK, 4K$	50.0, 0.0, 50.0	53.7(2.1) 0.1(3.7), 46.2(3.5)
$\phi\phi, \phi KK, 4K$	100.0, 0.0, 0.0	100.0(3.6) 0.0(5.3), 0.0(4.2)
$\phi\phi, \phi KK, 4K$	0.0, 100.0, 0.0	3.9(3.1) 92.0 (8.4), 4.1(6.1)
$\phi\phi, \phi KK, 4K$	0.0, 33.3, 66.6.0	1.2(1.4) 32.4(5.4), 66.4(5.1)
$\phi\phi, \phi KK, 4K$	25.0, 25.0, 50.0	30(1.9) 17.5(4.2), 52.5(4.0)
$\phi\phi, \phi KK, 4K$	21.4, 7.1, 71.5	24.7(2.1) 3.4(5.1), 71.9(5.0)

Table 5.2: *Results from the channel likelihood fit at beam momentum 1.4 GeV/c. Various admixtures of Monte Carlo  $\phi\phi$ ,  $\phi KK$  and  $4K$  events were used. The errors from the channel likelihood fit are given in parenthesis. From [?].*

The maximization of  $\mathcal{L}$  is done by maximizing the log likelihood function:

$$\sum_{j=1}^n \log[\alpha_{\phi\phi}(\frac{R_{\phi\phi}}{N_{\phi\phi}/N_0}) + \alpha_{\phi KK}(\frac{R_{\phi KK}}{N_{\phi KK}/N_0}) + (1 - \alpha_{\phi\phi} - \alpha_{\phi KK})]. \quad (5.10)$$

The ratios  $N_{\phi\phi}/N_0$  and  $N_{\phi KK}/N_0$  were estimated from GEANT Monte Carlo data.

The nonresonant “phase space” fraction contained both nonresonant  $4K$ , and non- $4K$  background events. Monte Carlo studies had shown that the non- $4K$  background events were distributed uniformly in the mass plot, therefore they were classified together with the nonresonant  $4K$  events as a class of events denoted simply as nonresonant, or “phase space”. To find the number  $4K$  nonresonant events, the estimated number of background (section 4.3.5) were subtracted from the nonresonant events. The results from the channel likelihood method at each beam momentum setting are reported in chapter 7.

The channel likelihood method was tested on Monte Carlo generated events in a large variety of signal to background conditions and was always found to provide the correct answer within the statistical errors [?]. An example of the results from these tests are shown in table 5.2. The relative fractions of  $\phi\phi$ ,  $\phi KK$  and nonresonant background calculated by the channel likelihood method for the 1.5 GeV/c, July 1991, data were  $47.6 \pm 4\%$   $\phi\phi$ ,  $22.8 \pm 7.1\%$   $\phi KK$ , and  $29.6 \pm 6.2\%$  nonresonant background. Figure 5.6 shows invariant mass plots for the Monte Carlo data where  $\phi\phi, \phi KK$  and  $4K$  nonresonant events are combined in the same ratios as found from the channel likelihood, which is compared to the distributions for real data. A fraction  $\approx 30\%$  of  $\phi KK$  in the data is compatible with the Monte Carlo, even if this signal can not be seen clearly in the mass plots.



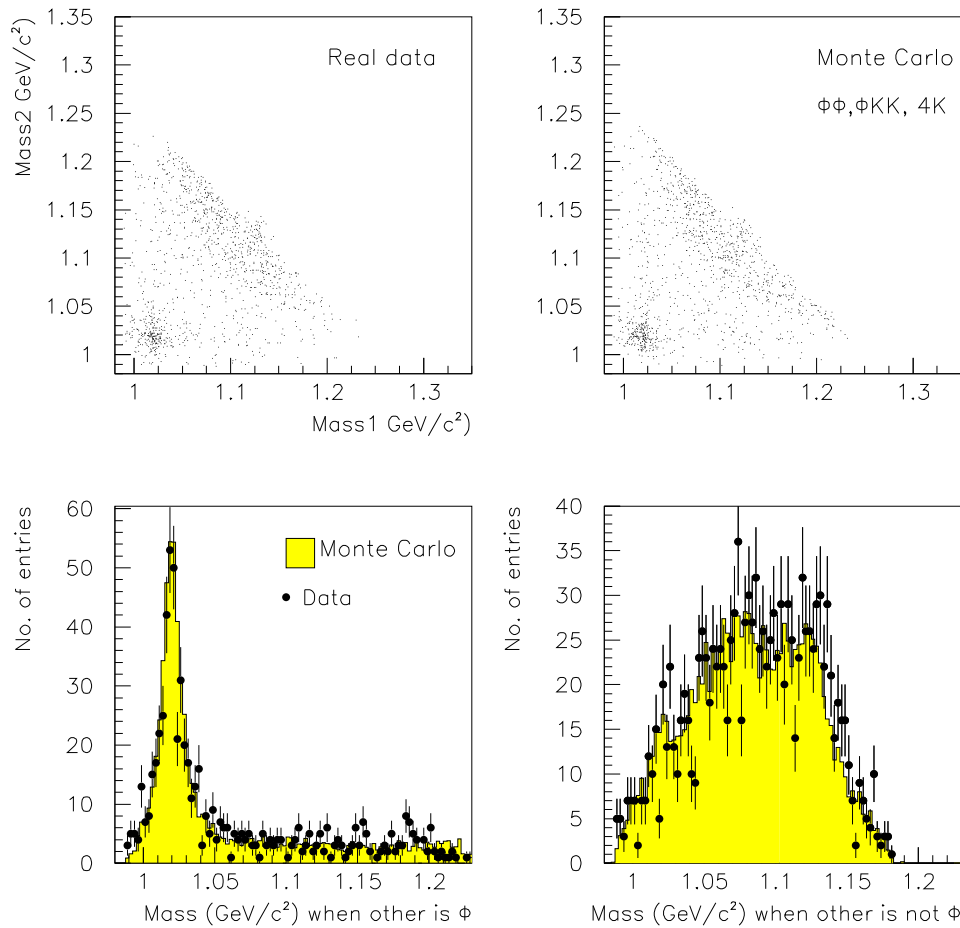


Figure 5.6: Comparisons of Goldhaber plots and invariant mass in and outside the  $\phi$  band for Monte Carlo and real data at 1.5  $\text{GeV}/c$  beam momentum. Monte Carlo  $\phi\phi$ ,  $\phi KK$  and  $4K$  events have been combined in the same fractions as the results from the channel likelihood for real data.

## Chapter 6

# Luminosity

Chapter 4 and 5 described how to obtain two of the factors in the cross section calculation for  $\phi\phi$ ,  $\phi KK$ , and  $4K$ , that is, the number of events and the acceptance. The third factor is the luminosity.

$$\mathcal{L} = N \cdot \nu \cdot \rho_{eff}, \quad (6.1)$$

where  $\rho_{eff}$  is the effective jet density,  $N$  is the number of antiprotons in the LEAR ring, and  $\nu$  is the revolution frequency of the antiprotons.

Two different approaches were used to determine the luminosity:

- The luminosity was determined from formula 6.1, by studying the beam attenuation with time .
- The elastic  $p\bar{p}$  channel, where the cross section  $\sigma_{ela}$  is known, was used to calculate the integrated luminosity from the formula

$$L = \frac{N_{events}}{(\sigma_{ela} \cdot efficiency)}. \quad (6.2)$$

Two methods were used to count the elastic events. **The pixel trigger** counted elastic scattering events at a polar angle around  $90^\circ$  in the c.m. system by the rate of coincidence between opposite pixels in the outer trigger scintillators. **The silicon monitor trigger** used small microstrip detectors placed at a lab polar angle  $\theta_{lab} \approx 65^\circ$  in the barrel to detect the recoil proton from low angle elastic scattering.

### The silicon monitor

This method for calculating the luminosities consisted of counting number of triggers for forward elastic events, using the silicon luminosity detectors in the barrel region, combined with forward pixels [?]. The silicon luminosity monitor system (section 3.2) consisted of four silicon detectors located in the barrel region at a polar angle 59 to 72 degrees, each covering a region in  $\phi$  of about 5 degrees. In an elastic  $p\bar{p}$  event the proton could hit one of the

the silicon detectors while the antiproton would be detected in a forward pixel. The elastic trigger consisted of a coincidence of a silicon strip detector and a pixel (made of a right and a left forward scintillator) in the region allowed by the kinematics of the event. The luminosity was then given by equation 6.2.

The differential elastic cross section [?] was integrated over the active area of the strips. Monte Carlo calculations showed that 20-30 % of the elastic triggers were lost due to interactions of the antiprotons with the detector before reaching the forward pixels [?].

The background of non-elastic scatterings was taken into account and corrected for by measuring coincidences between the silicon strips and non-correlated pixel clusters.

### The elastic pixel triggers

To measure elastic antiproton-proton scattering at a polar angle  $90^\circ$  in the center of mass [?], a coincidence logic was set up between the outer curved scintillators in the forward direction. This trigger required hits in two opposite pixels defined by the elastic kinematics. Each pixel was defined by the overlap of two curved scintillators.

Offline, background events were rejected by simple multiplicity requirements, followed by track finding and fitting; the tracks were required to be consistent with elastic kinematics. The trigger acceptance and the analysis efficiency was calculated from Monte Carlo events generated by the simulation program described in section 4.4. The luminosity was then calculated from equation 6.2.

### The beam attenuation method

The number of antiprotons in the beam decayed as

$$N = N_0 e^{-\sigma \rho_{eff} \nu t}, \quad (6.3)$$

where  $N_0$  is number of antiprotons at  $t = 0$ , and  $\rho_{eff}$  is the effective jet density, which includes the actual jet density times the overlap integral with the stored antiproton beam, given in atoms/cm<sup>2</sup>.

The revolution frequency  $\nu$  is a function of the energy setting:  $\nu = \beta c/L$ .  $L$  is the LEAR circumference (78.54 m).

The factor  $\sigma$  consists of the strong interaction total cross section and the fraction of the Rutherford scattering cross section beyond the acceptance of the machine.

The strong interaction term can be parameterized as

$$\sigma_{si} = \frac{55.3 \text{ GeV}/c \cdot \text{mb}}{P_p} + 60.5 \text{ mb} \quad (6.4)$$

by using the known  $p\bar{p}$  cross sections.

The LEAR machine average acceptance angle for recapture of scattered antiprotons is  $\theta_0 = 5.48$  mrad.

The integral of the Rutherford scattering above the cutoff angle is given as

$$\sigma_{Ruth}(\theta > \theta_0) = \frac{4\pi \cdot r_p^2}{(\gamma - 1/\gamma)^2 \theta_0^2}, \quad (6.5)$$

where  $r_p$  is the classical proton radius =  $1.5 \cdot 10^{-16}$  cm, and  $\gamma = \frac{1}{\sqrt{1-v^2/c^2}}$ .

Table 6.1 shows the value of the relevant factors as a function of the momentum.



Table 6.1: *Momentum dependent factors for the luminosity determination by the beam attenuation method (from [?]).*

From equation 6.3 the effective jet density can be calculated when the number of antiprotons is known :

$$\rho_{eff} = \frac{-\ln(N_{corr}/N_0)}{\sigma(P_{\bar{p}})\nu(P_{\bar{p}})t_{corr}}. \quad (6.6)$$

In this calculation it is necessary to correct for the time when the jet target was turned off, and for beam losses other than due to interactions with the target,  $N_{corr}$  and  $t_{corr}$  are the number of antiprotons and the time, corrected for these effects.

The integrated luminosity is obtained by integrating equation 6.1 [?],

$$\int \mathcal{L} dt = \frac{N_0}{\sigma} [1 - e^{-\sigma \rho_{eff} \nu t_{corr}}]. \quad (6.7)$$

The advantage of this method is that it is independent of the JETSET apparatus, and unlike the other two methods it does not require any knowledge about the detector, trigger and reconstruction efficiency. The disadvantage is that optimum pumping conditions in the vicinity of the target and good stability of the LEAR stochastic cooling system for long periods of time are required.

### Comparison between the methods

When the luminosities obtained by the pixel trigger and the silicon strip monitor were corrected for acceptance losses in the detector, the results from the two methods differed from 1% to 30% [?]. This is more than the statistical error of about 1 %, but within the systematic errors of approximately 15% for each method.

The beam decay method gave a higher value than the other two methods. This is because the beam decay method did not account for losses of the beam that were not due to interactions with the JETSET target, it also required optimum vacuum conditions, and therefore only gave an upper limit on the luminosity.

A difference as large as 20 % in the ratio of run-to-run and period-to-period luminosities between the three methods was observed.

### Relative luminosity determination

The following method [?] was used to establish a relative luminosity scale between the different runs. The rate  $s_i$ , in a scaler  $i$ , a logical combination of signals from detector elements at a certain time  $t$  and antiproton beam momentum  $p$ , is given by:

$$s_i = \sigma_i(p)\epsilon_i(p,t)\nu(p)N(t)\rho_{eff} + o_i(t), \quad (6.8)$$

where  $\sigma_i$  is the total cross section for all processes that satisfy the logical condition of scaler  $i$ ,  $\epsilon_i$  is the scaler efficiency,  $\nu$  is the revolution frequency of LEAR,  $N(t)$  is the number of antiprotons in the machine, and  $\rho_{eff}$  is the effective jet density. The offset  $o_i$  is the rate in scaler  $i$  when the jet is turned off.

To measure the jet density and thereby the luminosity, a scaler with a negligible offset  $o_i$  and efficiency which had a weak dependence on  $p$  and  $t$  was required. In practice this meant a coincidence scaler, which had to be insensitive to small drifts in thresholds and gains of the detector elements it consisted off.

The quantity  $c_i$  is defined as

$$c_i = \frac{s_i}{N(t)} \cdot 10^3. \quad (6.9)$$

At a given antiproton momentum, all of the time dependence of  $c_i$  is due to  $\rho_{eff}$ .

The scaler that best satisfied the above conditions was the one that counted the condition AP(all pipes) =2. The counting rate  $c_i$  for this scaler was observed to be stable over long run periods of the JETSET experiment, implying both the constancy of  $\rho_{eff}$  with time and the stability of the product  $\sigma_i\epsilon_i\nu$  with beam momentum and time. From equations 6.1 and 6.8 the luminosity is then given as

$$\mathcal{L} = \frac{s_i}{\sigma \cdot \epsilon}. \quad (6.10)$$

An excellent measurement of the relative luminosity between the runs, with an error at the level of  $\pm 2\%$ , was obtained with this method. When searching for structure in the excitation curve the relative luminosity is more important than the absolute luminosity.

To set an overall scale, the product  $\sigma \cdot \epsilon$  had to be provided, this was obtained from the pixel trigger results of July 1991 [?].

The resulting luminosities from this method are reported in chapter 7.

## Chapter 7

# Cross sections

The formulas to calculate the cross sections for the reactions  $\bar{p}p \rightarrow \phi\phi$ ,  $\bar{p}p \rightarrow \phi KK$  and  $\bar{p}p \rightarrow 4K^\pm$  (NR)<sup>1</sup> at a certain centre-of-mass energy are:

$$\sigma(\bar{p}p \rightarrow \phi\phi) = \frac{N_{\phi\phi}}{A_{\phi\phi} \cdot L \cdot BR(\phi \rightarrow K^+K^-)^2}, \quad (7.1)$$

$$\sigma(\bar{p}p \rightarrow \phi KK) = \frac{N_{\phi KK}}{A_{\phi KK} \cdot L \cdot BR(\phi \rightarrow K^+K^-)}, \quad (7.2)$$

$$\sigma(\bar{p}p \rightarrow 4K(NR)) = \frac{N_{4K}}{A_{4K} \cdot L}, \quad (7.3)$$

where

$N_{\phi\phi}$ ,  $N_{\phi KK}$ ,  $N_{4K}$  are the number of events of the type  $\phi\phi$ ,  $\phi KK$ , or  $4K(NR)$ ,  
 $A_{\phi\phi}$ ,  $A_{\phi KK}$ ,  $A_{4K}$  are the acceptances for  $\phi\phi$ ,  $\phi KK$ , or  $4K(NR)$  events.  
 $L$  is the integrated luminosity.

### Calculation of cross section

The tables on the pages 176 to 185 list the following quantities, used to calculate the cross sections, for each value of the beam momentum setting, for each run from 1991 to 1993:

- **Luminosity.** The integrated luminosity for this period (chapter 6).
- **Events after PID.** The total number of  $4K$  event candidates after the  $4K$  selection,  $N_{total}$  (chapter 4).
- **Background.** The estimated number of background events  $N_{bck}$  (section 4.3.5).

---

<sup>1</sup>NR=nonresonant

- **Fractions** of events. The fractions of  $\phi\phi$ ,  $\phi KK$ , and nonresonant events ( $\alpha_{\phi\phi}, \alpha_{\phi KK}, \alpha_0$ ) in the total  $4K$  sample obtained from the channel likelihood method (chapter 5).
- **Yields of  $\phi\phi$ ,  $\phi KK$ , nonresonant “phase space” events, and nonresonant  $4K$  events.** The yields of  $\phi\phi$  and  $\phi KK$  events are calculated by multiplying the fitted fractions from channel likelihood by the number of total  $4K$  candidates,  $N_{\phi\phi} = \alpha_{\phi\phi} \cdot N_{total}$ ,  $N_{\phi KK} = \alpha_{\phi KK} \cdot N_{total}$ . The number of “phase space” events found by the channel likelihood method  $N_{ph.sp.} = \alpha_0 \cdot N_{tot}$  is the total sum of nonresonant  $4K$  and background events. The number of nonresonant  $4K$  events,  $N_{4K,NR}$ , is the number of nonresonant “phase space” events, with the number of background events subtracted  $N_{4K,NR} = N_{ph.sp.} - N_{bck}$ .
- **Acceptances**, calculated from Monte Carlo  $\phi\phi$ ,  $\phi KK$ , and  $4K$  simulated events (section 4.4).

The last columns show the calculated cross sections with statistical and systematic errors. Note that the estimated cross sections represent a uniform extrapolation into the angular regions of vanishing acceptance. As shown in figure 4.35 the acceptance is zero for  $\cos \Theta_{cm} > 0.8$ . The reported cross sections may be interpreted as the differential cross sections integrated over the accepted solid angle  $\Omega$  and multiplied by a factor  $4\pi/\Omega$ . This corresponds to the total cross section if the  $\phi$ s are produced and decay isotropically.

The total luminosity for each beam momentum from 1991 to 1993 is shown in figure 7.1. The acceptance for  $\phi\phi$ ,  $\phi KK$ , and  $4K$  as a function of momentum, is shown in figures 7.2 to 7.4. The resulting cross sections and the ratio of  $\phi\phi$  to  $4K$  total cross sections are shown in figures 7.5 to 7.10.

The estimate of the relative admixture of  $\phi\phi$ ,  $\phi KK$ ,  $4K$ , and background is based on the invariant mass and  $\Delta E$  distributions. The two-dimensional invariant mass plot, and the one-dimensional projection inside and outside of the  $\phi$  band, as well as the  $\Delta E$  distributions are shown for all the July 1991 data from 1.2 GeV/c to 1.9 GeV/c in figures 7.11 to 7.18. Figures 7.19 and 7.20 give a graphic representation of the estimated number of  $\phi\phi$ ,  $\phi KK$ ,  $4K$  and background events for each of these data sets, in the form of pie diagrams. Note that at the higher beam momenta, the  $\phi$  peak is seen also in the projection of the invariant mass plot outside the  $\phi$  band. This indicates the presence of  $\phi KK$  in the sample (see figure 2.33), and agrees with the results from channel likelihood which gives a large fraction of  $\phi KK$  at these beam momenta.

## Errors

The errors given for the cross sections include contributions from the following sources:

- **Luminosity.** The systematic error on the luminosity is of the order of 15 %. This is the error on the absolute scale. The relative point-to-point error is 2%. The statistical error is less than 1 % and has been neglected in the error calculations.
- **Events after PID.** The total yield of events after PID,  $N_{total}$ , has a statistical error  $\Delta N_{total} = \sqrt{N_{total}}$ .

- **Background.** The statistical and systematic errors from the background determinations by the  $\Delta E$  fit are given.
- **Fractions.** The statistical error on the fit fractions  $\alpha$  arising from the channel likelihood method are given. In addition a systematic error of 5% has been determined from varying the  $\phi$  width.
- **Yield.** The yield of events of type  $i$  ( $i = \phi\phi, \phi KK, 4K$ ),  $n_i$ , has a statistical error,  $\Delta n_i$ . Since number of events of each type are  $n_i = \alpha_i \cdot N_{total}$ , the statistical error from channel likelihood and the error on the total number of events must be added in quadrature:

$$\Delta n_i = \sqrt{(N_{total} \cdot \Delta \alpha_i)^2 + (\alpha_i \cdot \Delta N_{total})^2}. \quad (7.4)$$

- **Acceptance.** The systematic error on the acceptance arises from the efficiency of the online trigger and is estimated to be of the order 15 %. The statistical error is much smaller, about 1-2 % and has been neglected.

The **statistical errors** on the cross sections  $\sigma_i$  for reaction  $i$  are calculated as:

$$\Delta \sigma_i = \frac{\sigma_i \cdot \Delta n_i}{n_i}. \quad (7.5)$$

Since the statistical errors on luminosity and acceptance are negligible, they have been ignored in the calculation of statistical errors on cross sections.

To get the **systematic errors** on the cross section, the systematic errors from fit fraction (5%), luminosity (15%), and acceptance (15%), are added in quadrature.

$$\Delta \sigma(syS) = \sigma \cdot \sqrt{\left(\frac{\Delta \alpha}{\alpha}\right)^2 + \left(\frac{\Delta L}{L}\right)^2 + \left(\frac{\Delta A}{A}\right)^2}. \quad (7.6)$$

For the  $4K$  cross section the error from the background subtraction is added.

$$\Delta \sigma_{NR}(syS) = \sigma \cdot \sqrt{\left(\frac{\Delta \alpha}{\alpha}\right)^2 + \left(\frac{\Delta L}{L}\right)^2 + \left(\frac{\Delta A}{A}\right)^2 + \left(\frac{\Delta n_{bck}}{n_{4K}}\right)^2} \quad (7.7)$$



Momentum GeV/c	Luminosity $\text{nb}^{-1}$	Events after PID	Background	
1.5 (Apr.91)	6.9	160	$10 \pm 14 \pm 9$	
Channel	Fraction %	Yield	Acceptance %	cross section ( $\mu\text{b}$ )
$\phi\phi$	$61.1 \pm 6.2$	$98 \pm 12$	1.41	$4.17 \pm 0.53 \pm 0.91$
$\phi KK$	$12.6 \pm 10.3$	$20 \pm 17$	0.65	$0.92 \pm 0.75 \pm 0.20$
nonres.	$26.3 \pm 9.4$	$42 \pm 15$		
nonres. 4K		$32 \pm 15$	0.79	$0.59 \pm 0.28 \pm 0.21$

Momentum GeV/c	Luminosity $\text{nb}^{-1}$	Events after PID	Background	
2.0 (Apr.91)	14.5	1645	$476 \pm 45 \pm 284$	
Channel	Fraction %	Yield	Acceptance %	cross section ( $\mu\text{b}$ )
$\phi\phi$	$11.2 \pm 1.2$	$184 \pm 20$	2.14	$2.46 \pm 0.27 \pm 0.54$
$\phi KK$	$25.2 \pm 3.1$	$415 \pm 52$	1.27	$4.58 \pm 0.57 \pm 1.00$
nonres.	$63.7 \pm 2.9$	$1048 \pm 54$		
nonres. 4K		$572 \pm 54$	1.23	$3.21 \pm 0.30 \pm 1.74$

Momentum GeV/c	Luminosity $\text{nb}^{-1}$	Events after PID	Background	
1.9 (Jul.91)	7.8	964	$334 \pm 33 \pm 263$	
Channel	Fraction %	Yield	Acceptance %	cross section ( $\mu\text{b}$ )
$\phi\phi$	$9.4 \pm 1.7$	$91 \pm 17$	3.53	$1.37 \pm 0.25 \pm 0.30$
$\phi KK$	$31.2 \pm 4.3$	$301 \pm 43$	1.90	$4.13 \pm 0.58 \pm 0.90$
nonres.	$59.4 \pm 4.0$	$573 \pm 43$		
nonres. 4K		$239 \pm 43$	1.92	$1.59 \pm 0.29 \pm 1.79$

Momentum GeV/c	Luminosity $\text{nb}^{-1}$	Events after PID	Background	
1.7 (Jul.91)	17.9	1272	$199 \pm 42 \pm 232$	
Channel	Fraction %	Yield	Acceptance %	cross section ( $\mu\text{b}$ )
$\phi\phi$	$21.4 \pm 1.8$	$272 \pm 24$	2.78	$2.27 \pm 0.20 \pm 0.49$
$\phi KK$	$32.9 \pm 4.0$	$418 \pm 52$	1.34	$3.55 \pm 0.44 \pm 0.77$
nonres.	$45.7 \pm 3.6$	$581 \pm 49$		
nonres. 4K		$382 \pm 49$	1.42	$1.50 \pm 0.19 \pm 0.97$

Momentum GeV/c	Luminosity $\text{nb}^{-1}$	Events after PID	Background	
1.5 (Jul.91)	9.0	393	$39 \pm 24 \pm 44$	
Channel	Fraction %	Yield	Acceptance %	cross section ( $\mu\text{b}$ )
$\phi\phi$	$47.6 \pm 4.0$	$187 \pm 18$	1.96	$4.40 \pm 0.43 \pm 0.96$
$\phi KK$	$22.8 \pm 7.1$	$90 \pm 28$	1.00	$2.03 \pm 0.64 \pm 0.44$
nonres.	$29.6 \pm 6.2$	$116 \pm 25$		
nonres. 4K		$77 \pm 25$	1.09	$0.79 \pm 0.25 \pm 0.48$

Momentum GeV/c	Luminosity $\text{nb}^{-1}$	Events after PID	Background	
1.8 (Jul.91)	22.3	2010	$561 \pm 57 \pm 472$	
Channel	Fraction %	Yield	Acceptance %	cross section ( $\mu\text{b}$ )
$\phi\phi$	$16.9 \pm 1.3$	$340 \pm 27$	3.33	$1.90 \pm 0.15 \pm 0.41$
$\phi KK$	$34.1 \pm 3.0$	$685 \pm 62$	1.68	$3.73 \pm 0.34 \pm 0.81$
nonres.	$49.0 \pm 2.7$	$985 \pm 58$		
nonres. $4K$		$424 \pm 58$	1.77	$1.07 \pm 0.15 \pm 1.22$

Momentum GeV/c	Luminosity $\text{nb}^{-1}$	Events after PID	Background	
1.6 (Jul.91)	20.0	929	$107 \pm 36 \pm 150$	
Channel	Fraction %	Yield	Acceptance %	cross section ( $\mu\text{b}$ )
$\phi\phi$	$30.5 \pm 2.4$	$283 \pm 24$	2.34	$2.51 \pm 0.21 \pm 0.55$
$\phi KK$	$28.1 \pm 4.8$	$261 \pm 45$	1.17	$2.27 \pm 0.39 \pm 0.50$
nonres.	$41.5 \pm 4.3$	$386 \pm 42$		
nonres. $4K$		$279 \pm 42$	1.27	$1.10 \pm 0.16 \pm 0.64$

Momentum GeV/c	Luminosity $\text{nb}^{-1}$	Events after PID	Background	
1.4 (Jul.91)	27.8	705	$97 \pm 33 \pm 106$	
Channel	Fraction %	Yield	Acceptance %	cross section ( $\mu\text{b}$ )
$\phi\phi$	$58.6 \pm 3.0$	$413 \pm 26$	1.52	$4.06 \pm 0.26 \pm 0.88$
$\phi KK$	$0.8 \pm 5.2$	$6 \pm 37$	0.82	$0.05 \pm 0.33 \pm 0.01$
nonres.	$40.6 \pm 4.9$	$286 \pm 36$		
nonres. $4K$		$189 \pm 36$	0.91	$0.75 \pm 0.14 \pm 0.45$

Momentum GeV/c	Luminosity $\text{nb}^{-1}$	Events after PID	Background	
1.3 (Jul.91)	28.9	385	$50 \pm 21 \pm 56$	
Channel	Fraction %	Yield	Acceptance %	cross section ( $\mu\text{b}$ )
$\phi\phi$	$65.8 \pm 4.6$	$253 \pm 22$	0.97	$3.75 \pm 0.32 \pm 0.82$
$\phi KK$	$4.0 \pm 8.2$	$15 \pm 32$	0.62	$0.18 \pm 0.36 \pm 0.04$
nonres.	$30.2 \pm 7.0$	$116 \pm 28$		
nonres. $4K$		$66 \pm 28$	0.66	$0.35 \pm 0.14 \pm 0.30$

Momentum GeV/c	Luminosity $\text{nb}^{-1}$	Events after PID	Background	
1.2 (Jul.91)	9.2	51	$5 \pm 7 \pm 8$	
Channel	Fraction %	Yield	Acceptance %	cross section ( $\mu\text{b}$ )
$\phi\phi$	$60.5 \pm 15.0$	$31 \pm 9$	0.51	$2.73 \pm 0.77 \pm 0.59$
$\phi KK$	$22.6 \pm 23.3$	$12 \pm 12$	0.42	$0.61 \pm 0.63 \pm 0.13$
nonres.	$16.9 \pm 16.8$	$9 \pm 9$		
nonres. $4K$		$4 \pm 9$	0.46	$0.09 \pm 0.20 \pm 0.19$

Momentum GeV/c	Luminosity $\text{nb}^{-1}$	Events after PID	Background	
1.500 (Oct.91)	7.7	245	$35 \pm 18 \pm 26$	
Channel	Fraction %	Yield	Acceptance %	cross section ( $\mu\text{b}$ )
$\phi\phi$	$44.0 \pm 5.0$	$108 \pm 14$	2.14	$2.71 \pm 0.35 \pm 0.59$
$\phi KK$	$35.5 \pm 8.6$	$87 \pm 22$	1.11	$2.07 \pm 0.52 \pm 0.45$
nonres.	$20.6 \pm 7.1$	$50 \pm 18$		
nonres. $4K$		$15 \pm 18$	1.20	$0.17 \pm 0.19 \pm 0.28$

Momentum GeV/c	Luminosity $\text{nb}^{-1}$	Events after PID	Background	
1.405 (Oct.91)	5.2	149	$16 \pm 12 \pm 18$	
Channel	Fraction %	Yield	Acceptance %	cross section ( $\mu\text{b}$ )
$\phi\phi$	$59.6 \pm 6.6$	$89 \pm 12$	1.72	$4.12 \pm 0.56 \pm 0.90$
$\phi KK$	$19.3 \pm 9.9$	$29 \pm 15$	0.91	$1.24 \pm 0.64 \pm 0.27$
nonres.	$21.1 \pm 8.3$	$31 \pm 13$		
nonres. $4K$		$15 \pm 13$	0.98	$0.30 \pm 0.25 \pm 0.36$

Momentum GeV/c	Luminosity $\text{nb}^{-1}$	Events after PID	Background	
1.435 (Oct.91)	11.9	329	$45 \pm 21 \pm 37$	
Channel	Fraction %	Yield	Acceptance %	cross section ( $\mu\text{b}$ )
$\phi\phi$	$48.8 \pm 4.5$	$161 \pm 17$	1.81	$3.09 \pm 0.33 \pm 0.67$
$\phi KK$	$29.5 \pm 8.5$	$97 \pm 28$	0.91	$1.83 \pm 0.54 \pm 0.40$
nonres.	$21.8 \pm 7.1$	$72 \pm 24$		
nonres. $4K$		$27 \pm 24$	1.03	$0.22 \pm 0.19 \pm 0.31$

Momentum GeV/c	Luminosity $\text{nb}^{-1}$	Events after PID	Background	
1.450 (Oct.91)	12.0	349	$42 \pm 99 \pm 56$	
Channel	Fraction %	Yield	Acceptance %	cross section ( $\mu\text{b}$ )
$\phi\phi$	$47.1 \pm 4.4$	$164 \pm 18$	1.91	$2.97 \pm 0.32 \pm 0.65$
$\phi KK$	$26.0 \pm 8.1$	$91 \pm 29$	1.00	$1.54 \pm 0.49 \pm 0.34$
nonres.	$26.9 \pm 6.9$	$94 \pm 25$		
nonres. $4K$		$52 \pm 25$	1.10	$0.39 \pm 0.19 \pm 0.43$

Momentum GeV/c	Luminosity $\text{nb}^{-1}$	Events after PID	Background	
1.465 (Oct.91)	6.5	214	$11 \pm 17 \pm 22$	
Channel	Fraction %	Yield	Acceptance %	cross section ( $\mu\text{b}$ )
$\phi\phi$	$49.9 \pm 5.6$	$107 \pm 14$	1.96	$3.48 \pm 0.45 \pm 0.76$
$\phi KK$	$23.8 \pm 9.9$	$51 \pm 21$	1.05	$1.52 \pm 0.64 \pm 0.33$
nonres.	$26.3 \pm 8.4$	$56 \pm 18$		
nonres. $4K$		$45 \pm 18$	1.18	$0.59 \pm 0.24 \pm 0.31$

Momentum GeV/c	Luminosity $\text{nb}^{-1}$	Events after PID	Background	
1.420 (Oct.91)	12.2	336	$8 \pm 19 \pm 31$	
Channel	Fraction %	Yield	Acceptance %	cross section ( $\mu\text{b}$ )
$\phi\phi$	$62.8 \pm 4.4$	$211 \pm 19$	1.79	$4.01 \pm 0.35 \pm 0.87$
$\phi KK$	$17.0 \pm 7.1$	$57 \pm 24$	0.91	$1.05 \pm 0.44 \pm 0.23$
nonres. nonres. $4K$	$20.2 \pm 6.0$	$68 \pm 20$ $60 \pm 20$	1.02	$0.48 \pm 0.16 \pm 0.27$

Momentum GeV/c	Luminosity $\text{nb}^{-1}$	Events after PID	Background	
1.480 (Oct.91)	7.9	249	$23 \pm 18 \pm 34$	
Channel	Fraction %	Yield	Acceptance %	cross section ( $\mu\text{b}$ )
$\phi\phi$	$46.2 \pm 5.3$	$115 \pm 15$	2.06	$2.93 \pm 0.38 \pm 0.64$
$\phi KK$	$31.2 \pm 9.8$	$78 \pm 25$	1.12	$1.79 \pm 0.57 \pm 0.39$
nonres. nonres. $4K$	$22.6 \pm 8.2$	$56 \pm 21$ $33 \pm 21$	1.21	$0.35 \pm 0.22 \pm 0.36$

Momentum GeV/c	Luminosity $\text{nb}^{-1}$	Events after PID	Background	
1.390 (Oct.91)	1.7	36	$4 \pm 6 \pm 7$	
Channel	Fraction %	Yield	Acceptance %	cross section ( $\mu\text{b}$ )
$\phi\phi$	$40.9 \pm 14.9$	$15 \pm 6$	1.60	$2.25 \pm 0.90 \pm 0.49$
$\phi KK$	$0.3 \pm 32.8$	$0 \pm 12$	0.81	$0.02 \pm 1.75 \pm 0.00$
nonres. nonres. $4K$	$58.8 \pm 27.4$	$21 \pm 10$ $17 \pm 10$	1.00	$1.01 \pm 0.62 \pm 0.47$

Momentum GeV/c	Luminosity $\text{nb}^{-1}$	Events after PID	Background	
1.505 (Jun.92)	2.9	61	$17 \pm 9 \pm 8$	
Channel	Fraction %	Yield	Acceptance %	cross section ( $\mu\text{b}$ )
$\phi\phi$	$44.0 \pm 10.5$	$27 \pm 7$	1.85	$2.08 \pm 0.55 \pm 0.45$
$\phi KK$	$16.5 \pm 19.3$	$10 \pm 12$	0.93	$0.76 \pm 0.89 \pm 0.17$
nonres. nonres. $4K$	$39.5 \pm 16.5$	$24 \pm 10$ $7 \pm 10$	1.03	$0.24 \pm 0.35 \pm 0.27$

Momentum GeV/c	Luminosity $\text{nb}^{-1}$	Events after PID	Background	
1.950 (Jun.92)	7.7	821	$377 \pm 34 \pm 264$	
Channel	Fraction %	Yield	Acceptance %	cross section ( $\mu\text{b}$ )
$\phi\phi$	$9.6 \pm 1.6$	$79 \pm 13$	2.90	$1.46 \pm 0.25 \pm 0.32$
$\phi KK$	$22.9 \pm 4.4$	$188 \pm 37$	1.63	$3.05 \pm 0.60 \pm 0.66$
nonres. nonres. $4K$	$67.5 \pm 4.2$	$554 \pm 39$ $177 \pm 39$	1.76	$1.31 \pm 0.29 \pm 1.97$

Momentum GeV/c	Luminosity $\text{nb}^{-1}$	Events after PID	Background	
1.750(Jun.92)	14.5	885	$207 \pm 36 \pm 244$	
Channel	Fraction %	Yield	Acceptance %	cross section ( $\mu\text{b}$ )
$\phi\phi$	$15.0 \pm 1.9$	$133 \pm 17$	2.78	$1.37 \pm 0.18 \pm 0.30$
$\phi KK$	$34.8 \pm 4.6$	$308 \pm 42$	1.32	$3.28 \pm 0.45 \pm 0.71$
nonres.	$50.2 \pm 4.2$	$444 \pm 40$		
nonres. $4K$		$237 \pm 40$	1.46	$1.12 \pm 0.19 \pm 1.18$

Momentum GeV/c	Luminosity $\text{nb}^{-1}$	Events after PID	Background	
1.650(Jun.92)	13.7	599	$121 \pm 30 \pm 140$	
Channel	Fraction %	Yield	Acceptance %	cross section ( $\mu\text{b}$ )
$\phi\phi$	$24.3 \pm 2.9$	$146 \pm 18$	2.35	$1.88 \pm 0.24 \pm 0.41$
$\phi KK$	$35.2 \pm 6.3$	$211 \pm 39$	1.23	$2.55 \pm 0.47 \pm 0.56$
nonres.	$40.5 \pm 5.5$	$243 \pm 34$		
nonres. $4K$		$122 \pm 34$	1.30	$0.68 \pm 0.19 \pm 0.80$

Momentum GeV/c	Luminosity $\text{nb}^{-1}$	Events after PID	Background	
1.506 (Dec.92)	16.2	537	$113 \pm 28 \pm 127$	
Channel	Fraction %	Yield	Acceptance %	cross section ( $\mu\text{b}$ )
$\phi\phi$	$40.2 \pm 3.3$	$216 \pm 20$	2.12	$2.61 \pm 0.24 \pm 0.57$
$\phi KK$	$17.5 \pm 6.1$	$94 \pm 33$	1.05	$1.13 \pm 0.40 \pm 0.25$
nonres.	$42.3 \pm 5.6$	$227 \pm 32$		
nonres. $4K$		$114 \pm 32$	1.16	$0.61 \pm 0.17 \pm 0.69$

Momentum GeV/c	Luminosity $\text{nb}^{-1}$	Events after PID	Background	
1.465 (Dec.92)	34.3	1022	$204 \pm 37 \pm 228$	
Channel	Fraction %	Yield	Acceptance %	cross section ( $\mu\text{b}$ )
$\phi\phi$	$47.2 \pm 2.4$	$482 \pm 29$	1.90	$3.07 \pm 0.18 \pm 0.67$
$\phi KK$	$12.7 \pm 4.3$	$130 \pm 44$	0.98	$0.79 \pm 0.27 \pm 0.17$
nonres.	$40.2 \pm 4.0$	$411 \pm 43$		
nonres. $4K$		$207 \pm 43$	1.09	$0.55 \pm 0.11 \pm 0.62$

Momentum GeV/c	Luminosity $\text{nb}^{-1}$	Events after PID	Background	
1.404 (Dec.92)	36.8	880	$140 \pm 52 \pm 178$	
Channel	Fraction %	Yield	Acceptance %	cross section ( $\mu\text{b}$ )
$\phi\phi$	$59.9 \pm 2.7$	$527 \pm 29$	1.50	$3.96 \pm 0.22 \pm 0.86$
$\phi KK$	$10.1 \pm 4.6$	$89 \pm 41$	0.84	$0.59 \pm 0.27 \pm 0.13$
nonres.	$30.0 \pm 4.1$	$264 \pm 37$		
nonres. $4K$		$124 \pm 37$	0.90	$0.37 \pm 0.11 \pm 0.54$

Momentum GeV/c	Luminosity $\text{nb}^{-1}$	Events after PID	Background	
1.435 (Dec.92)	24.4	670	$99 \pm 35 \pm 127$	
Channel	Fraction %	Yield	Acceptance %	cross section ( $\mu\text{b}$ )
$\phi\phi$	$48.5 \pm 3.0$	$325 \pm 23$	1.69	$3.27 \pm 0.24 \pm 0.71$
$\phi KK$	$9.5 \pm 5.3$	$64 \pm 36$	0.92	$0.58 \pm 0.32 \pm 0.13$
nonres.	$41.9 \pm 4.9$	$281 \pm 34$		
nonres. $4K$		$182 \pm 34$	1.02	$0.73 \pm 0.14 \pm 0.53$

Momentum GeV/c	Luminosity $\text{nb}^{-1}$	Events after PID	Background	
1.390 (Dec.92)	16.4	428	$64 \pm 23 \pm 86$	
Channel	Fraction %	Yield	Acceptance %	cross section ( $\mu\text{b}$ )
$\phi\phi$	$45.8 \pm 4.1$	$196 \pm 20$	1.49	$3.33 \pm 0.34 \pm 0.73$
$\phi KK$	$9.8 \pm 7.0$	$42 \pm 30$	0.77	$0.68 \pm 0.48 \pm 0.15$
nonres.	$44.5 \pm 6.4$	$190 \pm 29$		
nonres. $4K$		$126 \pm 29$	0.95	$0.81 \pm 0.18 \pm 0.58$

Momentum GeV/c	Luminosity $\text{nb}^{-1}$	Events after PID	Background	
1.415 (May93)	12.6	494	$132 \pm 30 \pm 146$	
Channel	Fraction %	Yield	Acceptance %	cross section ( $\mu\text{b}$ )
$\phi\phi$	$45.9 \pm 3.6$	$227 \pm 20$	2.04	$3.66 \pm 0.33 \pm 0.80$
$\phi KK$	$2.3 \pm 6.7$	$11 \pm 33$	1.13	$0.16 \pm 0.47 \pm 0.04$
nonres.	$51.8 \pm 6.3$	$256 \pm 33$		
nonres. $4K$		$124 \pm 33$	1.28	$0.77 \pm 0.21 \pm 0.92$

Momentum GeV/c	Luminosity $\text{nb}^{-1}$	Events after PID	Background	
1.360 (May93)	32.4	899	$194 \pm 34 \pm 235$	
Channel	Fraction %	Yield	Acceptance %	cross section ( $\mu\text{b}$ )
$\phi\phi$	$51.4 \pm 2.7$	$462 \pm 28$	1.48	$4.00 \pm 0.25 \pm 0.87$
$\phi KK$	$2.0 \pm 5.0$	$18 \pm 45$	0.90	$0.13 \pm 0.31 \pm 0.03$
nonres.	$46.6 \pm 4.6$	$419 \pm 44$		
nonres. $4K$		$225 \pm 44$	0.94	$0.74 \pm 0.14 \pm 0.79$

Momentum GeV/c	Luminosity $\text{nb}^{-1}$	Events after PID	Background	
1.330 (May93)	39.8	847	$192 \pm 37 \pm 227$	
Channel	Fraction %	Yield	Acceptance %	cross section ( $\mu\text{b}$ )
$\phi\phi$	$58.8 \pm 2.9$	$498 \pm 30$	1.26	$4.12 \pm 0.25 \pm 0.90$
$\phi KK$	$3.1 \pm 5.3$	$26 \pm 45$	0.74	$0.18 \pm 0.31 \pm 0.04$
nonres.	$38.2 \pm 4.8$	$324 \pm 42$		
nonres. $4K$		$132 \pm 42$	0.87	$0.38 \pm 0.12 \pm 0.66$

Momentum GeV/c	Luminosity $\text{nb}^{-1}$	Events after PID	Background	
1.800 (May93)	16.9	2407	$983 \pm 64 \pm 856$	
Channel	Fraction %	Yield	Acceptance %	cross section ( $\mu\text{b}$ )
$\phi\phi$	$10.5 \pm 1.1$	$253 \pm 27$	3.81	$1.63 \pm 0.17 \pm 0.35$
$\phi KK$	$24.5 \pm 2.8$	$590 \pm 68$	1.82	$3.90 \pm 0.45 \pm 0.85$
nonres.	$65.0 \pm 2.6$	$1565 \pm 70$		
nonres. $4K$		$582 \pm 70$	1.87	$1.84 \pm 0.22 \pm 2.74$

Momentum GeV/c	Luminosity $\text{nb}^{-1}$	Events after PID	Background	
2.000 (Aug.93)	38.5	8312	$3864 \pm 112 \pm 3111$	
Channel	Fraction %	Yield	Acceptance %	cross section ( $\mu\text{b}$ )
$\phi\phi$	$6.4 \pm 0.4$	$532 \pm 34$	3.26	$1.76 \pm 0.11 \pm 0.38$
$\phi KK$	$13.7 \pm 1.3$	$1139 \pm 109$	1.95	$3.09 \pm 0.30 \pm 0.67$
nonres.	$80.0 \pm 1.3$	$6650 \pm 130$		
nonres. $4K$		$2786 \pm 130$	2.01	$3.60 \pm 0.17 \pm 4.10$

Momentum GeV/c	Luminosity $\text{nb}^{-1}$	Events after PID	Background	
1.400 (Aug.93)	14.6	520	$152 \pm 31 \pm 147$	
Channel	Fraction %	Yield	Acceptance %	cross section ( $\mu\text{b}$ )
$\phi\phi$	$51.3 \pm 3.5$	$267 \pm 21$	1.76	$4.31 \pm 0.35 \pm 0.94$
$\phi KK$	$3.1 \pm 6.3$	$16 \pm 33$	0.94	$0.24 \pm 0.49 \pm 0.05$
nonres.	$45.5 \pm 5.9$	$237 \pm 32$		
nonres. $4K$		$85 \pm 32$	1.08	$0.54 \pm 0.20 \pm 0.94$

Momentum GeV/c	Luminosity $\text{nb}^{-1}$	Events after PID	Background	
1.405 (Aug.93)	11.8	427	$84 \pm 27 \pm 102$	
Channel	Fraction %	Yield	Acceptance %	cross section ( $\mu\text{b}$ )
$\phi\phi$	$48.7 \pm 3.8$	$208 \pm 19$	1.77	$4.13 \pm 0.38 \pm 0.90$
$\phi KK$	$5.3 \pm 7.0$	$23 \pm 30$	0.96	$0.41 \pm 0.54 \pm 0.09$
nonres.	$46.0 \pm 6.5$	$196 \pm 29$		
nonres. $4K$		$112 \pm 29$	1.09	$0.87 \pm 0.23 \pm 0.82$

Momentum GeV/c	Luminosity $\text{nb}^{-1}$	Events after PID	Background	
1.410 (Aug.93)	13.1	470	$90 \pm 23 \pm 114$	
Channel	Fraction %	Yield	Acceptance %	cross section ( $\mu\text{b}$ )
$\phi\phi$	$49.9 \pm 3.6$	$235 \pm 20$	1.79	$4.15 \pm 0.35 \pm 0.90$
$\phi KK$	$0.6 \pm 6.5$	$3 \pm 31$	0.94	$0.05 \pm 0.51 \pm 0.01$
nonres.	$49.6 \pm 6.2$	$233 \pm 31$		
nonres. $4K$		$143 \pm 31$	1.04	$1.05 \pm 0.23 \pm 0.87$

Momentum GeV/c	Luminosity $\text{nb}^{-1}$	Events after PID	Background	
1.415 (Aug.93)	12.3	429	$93 \pm 27 \pm 105$	
Channel	Fraction %	Yield	Acceptance %	cross section ( $\mu\text{b}$ )
$\phi\phi$	$54.7 \pm 3.8$	$235 \pm 20$	1.79	$4.42 \pm 0.37 \pm 0.96$
$\phi KK$	$4.8 \pm 6.6$	$21 \pm 28$	1.00	$0.34 \pm 0.47 \pm 0.07$
nonres. nonres. $4K$	$40.5 \pm 6.2$	$174 \pm 28$ $81 \pm 28$	1.06	$0.62 \pm 0.21 \pm 0.82$

Momentum GeV/c	Luminosity $\text{nb}^{-1}$	Events after PID	Background	
1.420 (Aug.93)	13.5	480	$100 \pm 27 \pm 120$	
Channel	Fraction %	Yield	Acceptance %	cross section ( $\mu\text{b}$ )
$\phi\phi$	$50.3 \pm 3.6$	$241 \pm 20$	1.78	$4.17 \pm 0.35 \pm 0.91$
$\phi KK$	$3.3 \pm 6.7$	$16 \pm 32$	1.05	$0.23 \pm 0.46 \pm 0.05$
nonres. nonres. $4K$	$46.5 \pm 6.2$	$223 \pm 31$ $123 \pm 31$	1.16	$0.79 \pm 0.20 \pm 0.79$

Momentum GeV/c	Luminosity $\text{nb}^{-1}$	Events after PID	Background	
1.425 (Aug.93)	13.6	488	$117 \pm 32 \pm 130$	
Channel	Fraction %	Yield	Acceptance %	cross section ( $\mu\text{b}$ )
$\phi\phi$	$37.8 \pm 3.6$	$184 \pm 19$	1.93	$2.92 \pm 0.31 \pm 0.64$
$\phi KK$	$16.7 \pm 7.1$	$81 \pm 35$	0.98	$1.25 \pm 0.53 \pm 0.27$
nonres. nonres. $4K$	$45.5 \pm 6.4$	$222 \pm 33$ $105 \pm 33$	1.14	$0.68 \pm 0.21 \pm 0.85$

Momentum GeV/c	Luminosity $\text{nb}^{-1}$	Events after PID	Background	
1.430 (Aug.93)	12.8	479	$127 \pm 29 \pm 130$	
Channel	Fraction %	Yield	Acceptance %	cross section ( $\mu\text{b}$ )
$\phi\phi$	$40.2 \pm 3.7$	$193 \pm 20$	1.98	$3.15 \pm 0.32 \pm 0.69$
$\phi KK$	$19.5 \pm 7.4$	$93 \pm 36$	1.06	$1.40 \pm 0.54 \pm 0.31$
nonres. nonres. $4K$	$40.3 \pm 6.5$	$193 \pm 32$ $66 \pm 32$	1.13	$0.46 \pm 0.22 \pm 0.90$

Momentum GeV/c	Luminosity $\text{nb}^{-1}$	Events after PID	Background	
1.435 (Aug.93)	11.3	492	$94 \pm 30 \pm 123$	
Channel	Fraction %	Yield	Acceptance %	cross section ( $\mu\text{b}$ )
$\phi\phi$	$42.6 \pm 3.6$	$210 \pm 20$	1.97	$3.91 \pm 0.37 \pm 0.85$
$\phi KK$	$11.1 \pm 6.6$	$55 \pm 33$	1.10	$0.89 \pm 0.53 \pm 0.20$
nonres. nonres. $4K$	$46.2 \pm 6.0$	$227 \pm 31$ $133 \pm 31$	1.17	$1.01 \pm 0.24 \pm 0.96$



Momentum GeV/c	Luminosity $\text{nb}^{-1}$	Events after PID	Background	
1.440 (Aug.93)	11.9	526	$99 \pm 26 \pm 126$	
Channel	Fraction %	Yield	Acceptance %	cross section ( $\mu\text{b}$ )
$\phi\phi$	$43.1 \pm 3.1$	$227 \pm 19$	2.02	$3.91 \pm 0.33 \pm 0.85$
$\phi KK$	$9.3 \pm 5.7$	$49 \pm 30$	1.09	$0.77 \pm 0.47 \pm 0.17$
nonres.	$47.6 \pm 5.4$	$250 \pm 30$		
nonres. $4K$		$151 \pm 30$	1.22	$1.04 \pm 0.21 \pm 0.90$

Momentum GeV/c	Luminosity $\text{nb}^{-1}$	Events after PID	Background	
1.445 (Aug.93)	11.1	420	$88 \pm 23 \pm 119$	
Channel	Fraction %	Yield	Acceptance %	cross section ( $\mu\text{b}$ )
$\phi\phi$	$45.5 \pm 3.9$	$191 \pm 19$	2.05	$3.48 \pm 0.34 \pm 0.76$
$\phi KK$	$20.3 \pm 7.0$	$85 \pm 30$	1.15	$1.36 \pm 0.47 \pm 0.30$
nonres.	$34.3 \pm 6.2$	$144 \pm 27$		
nonres. $4K$		$56 \pm 27$	1.25	$0.40 \pm 0.19 \pm 0.86$

Momentum GeV/c	Luminosity $\text{nb}^{-1}$	Events after PID	Background	
1.237 (Aug.93)	11.8	120	$20 \pm 12 \pm 37$	
Channel	Fraction %	Yield	Acceptance %	cross section ( $\mu\text{b}$ )
$\phi\phi$	$70.0 \pm 8.8$	$84 \pm 13$	0.80	$3.69 \pm 0.56 \pm 0.80$
$\phi KK$	$0.5 \pm 15.8$	$1 \pm 19$	0.58	$0.02 \pm 0.56 \pm 0.00$
nonres.	$29.5 \pm 12.4$	$35 \pm 15$		
nonres. $4K$		$15 \pm 15$	0.63	$0.21 \pm 0.20 \pm 0.50$

Momentum GeV/c	Luminosity $\text{nb}^{-1}$	Events after PID	Background	
1.246 (Aug.93)	8.9	100	$41 \pm 11 \pm 33$	
Channel	Fraction %	Yield	Acceptance %	cross section ( $\mu\text{b}$ )
$\phi\phi$	$71.5 \pm 8.3$	$72 \pm 11$	0.82	$4.06 \pm 0.62 \pm 0.89$
$\phi KK$	$3.5 \pm 16.1$	$4 \pm 16$	0.63	$0.13 \pm 0.58 \pm 0.03$
nonres.	$25.0 \pm 13.4$	$25 \pm 14$		
nonres. $4K$		$-16 \pm 14$	0.61	$-0.29 \pm 0.25 \pm -0.61$

Momentum GeV/c	Luminosity $\text{nb}^{-1}$	Events after PID	Background	
1.188 (Aug.93)	17.5	132	$26 \pm 12 \pm 39$	
Channel	Fraction %	Yield	Acceptance %	cross section ( $\mu\text{b}$ )
$\phi\phi$	$67.7 \pm 9.1$	$89 \pm 14$	0.54	$3.92 \pm 0.62 \pm 0.85$
$\phi KK$	$1.3 \pm 18.1$	$2 \pm 24$	0.42	$0.05 \pm 0.66 \pm 0.01$
nonres.	$31.0 \pm 13.7$	$41 \pm 18$		
nonres. $4K$		$15 \pm 18$	0.50	$0.17 \pm 0.21 \pm 0.45$

Momentum GeV/c	Luminosity $\text{nb}^{-1}$	Events after PID	Background	
1.278 (Aug.93)	12.2	170	$37 \pm 14 \pm 48$	
Channel	Fraction %	Yield	Acceptance %	cross section ( $\mu\text{b}$ )
$\phi\phi$	$49.6 \pm 7.5$	$84 \pm 14$	0.99	$2.90 \pm 0.49 \pm 0.63$
$\phi K K$	$35.9 \pm 13.0$	$61 \pm 23$	0.62	$1.64 \pm 0.61 \pm 0.36$
nonres. nonres. $4K$	$14.6 \pm 9.8$	$25 \pm 17$ $-12 \pm 17$	0.71	$-0.14 \pm 0.19 \pm -0.55$

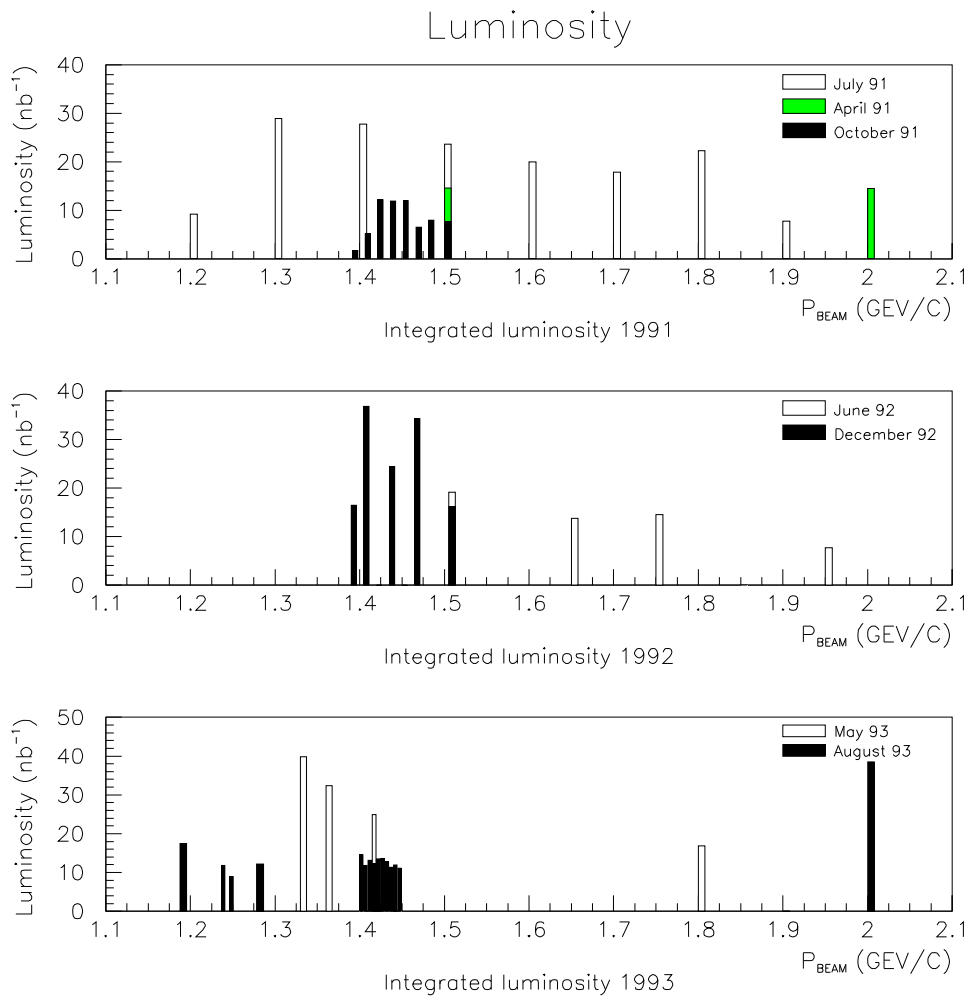


Figure 7.1: *The total integrated luminosity from 1991 to 1993.*

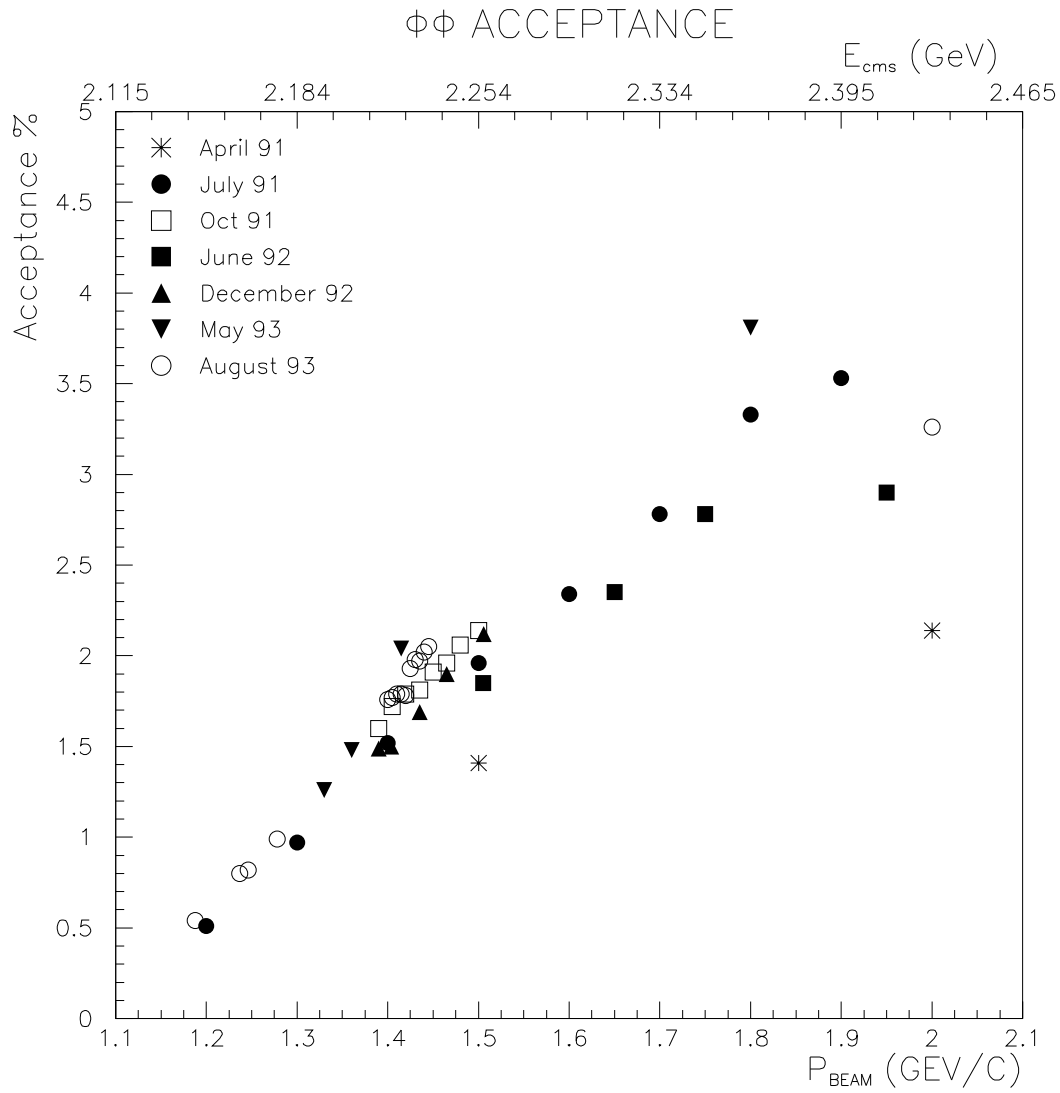


Figure 7.2: *The acceptance of the reaction  $p\bar{p} \rightarrow \phi\phi$  in the JETSET detector (from Monte Carlo).*

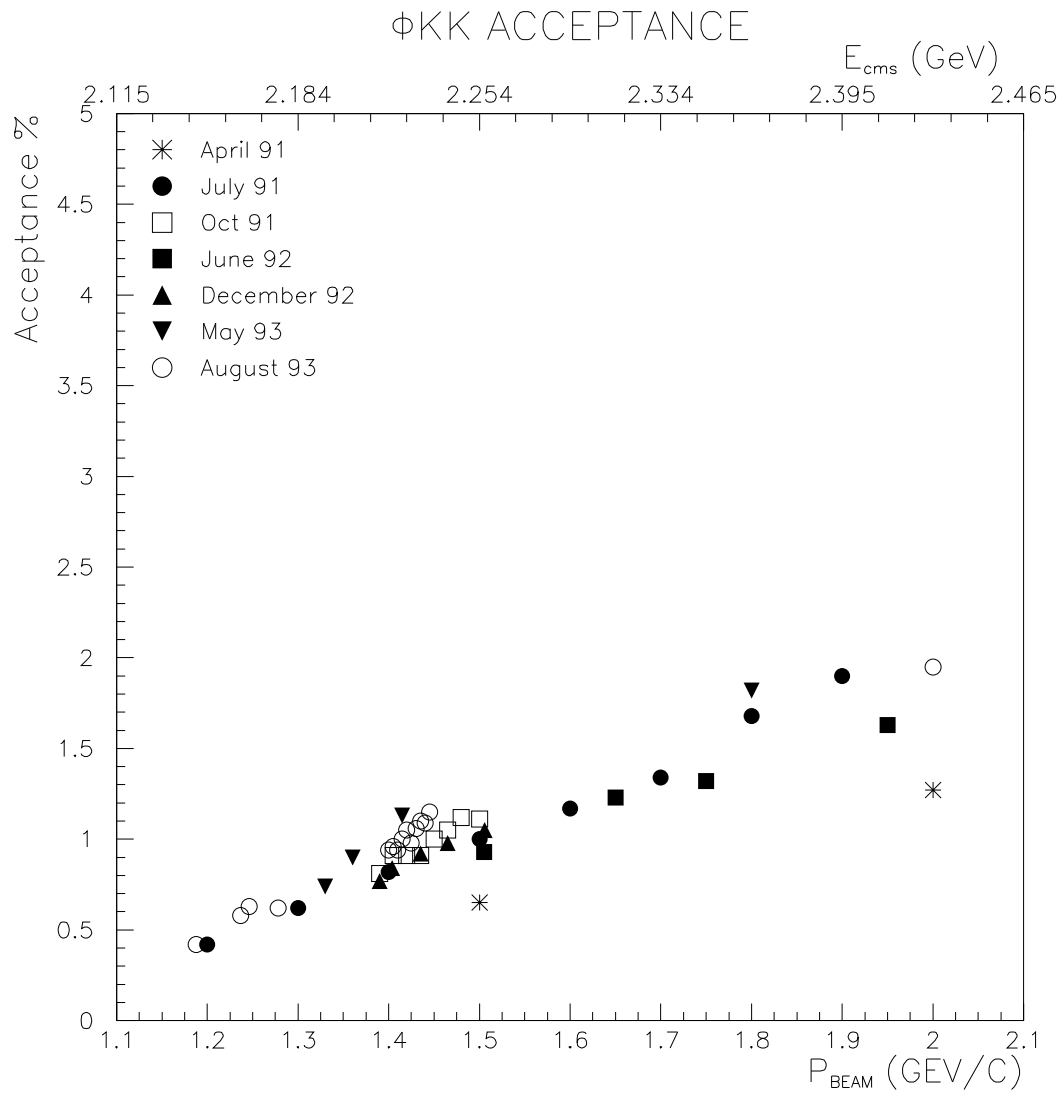


Figure 7.3: The acceptance of the reaction  $p\bar{p} \rightarrow \phi KK$  in the JETSET detector (from Monte Carlo).

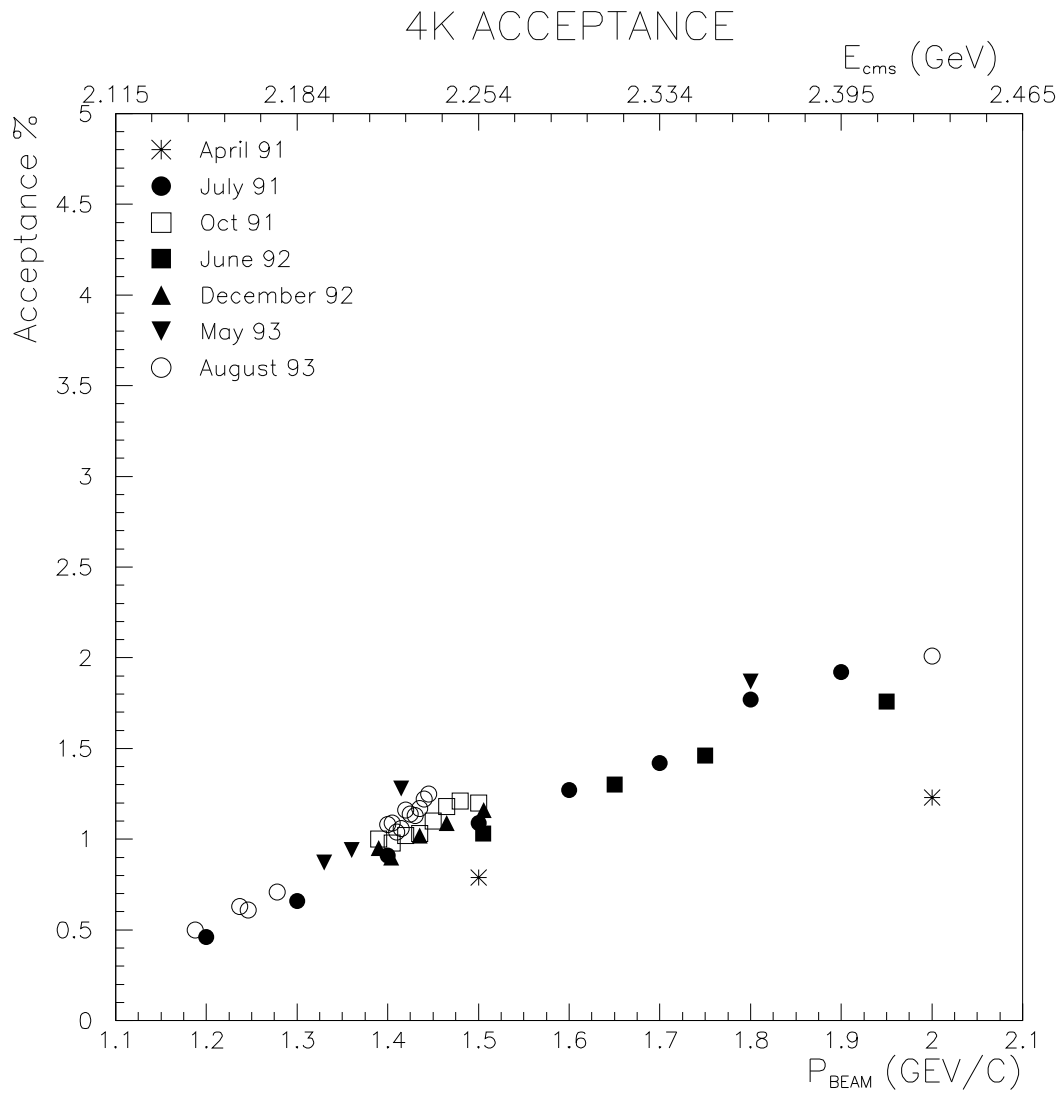


Figure 7.4: *The acceptance of the nonresonant reaction  $p\bar{p} \rightarrow 4K$  in the JETSET detector (from Monte Carlo).*

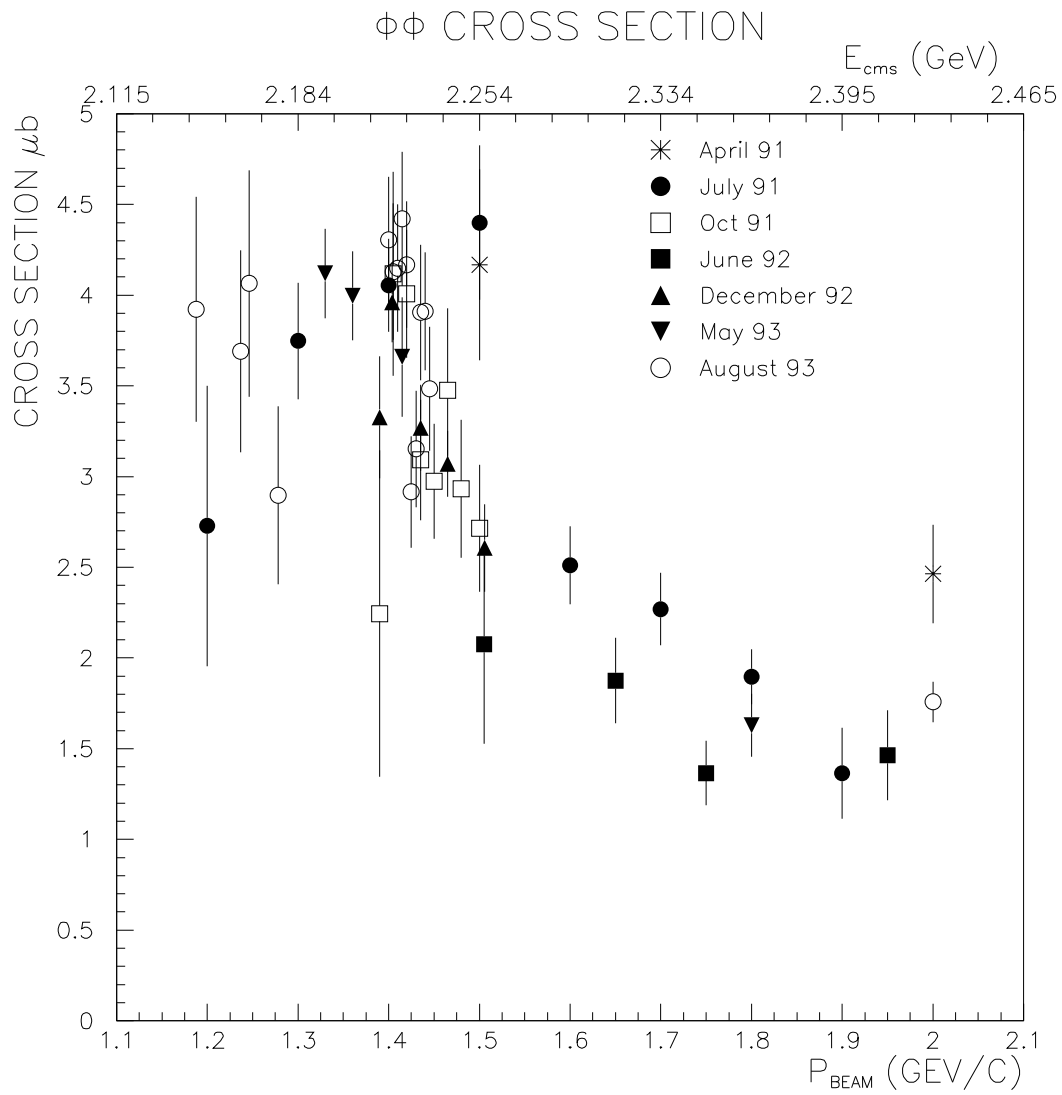


Figure 7.5: Cross section for the reaction  $p\bar{p} \rightarrow \phi\phi$  as measured by JETSET.

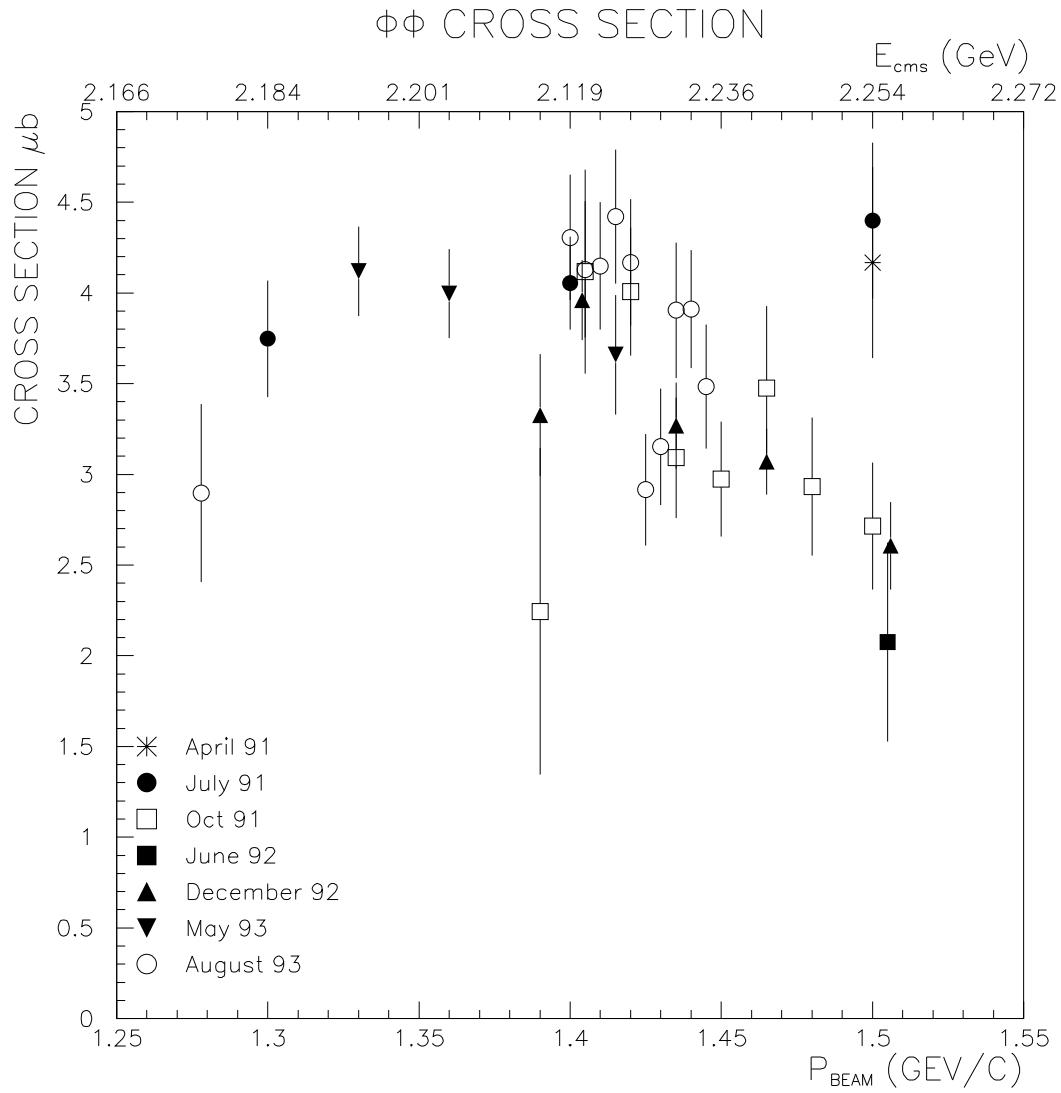


Figure 7.6: Cross section for the reaction  $p\bar{p} \rightarrow \phi\phi$  as measured by JETSET (beam-momentum 1.25-1.55 GeV/c).

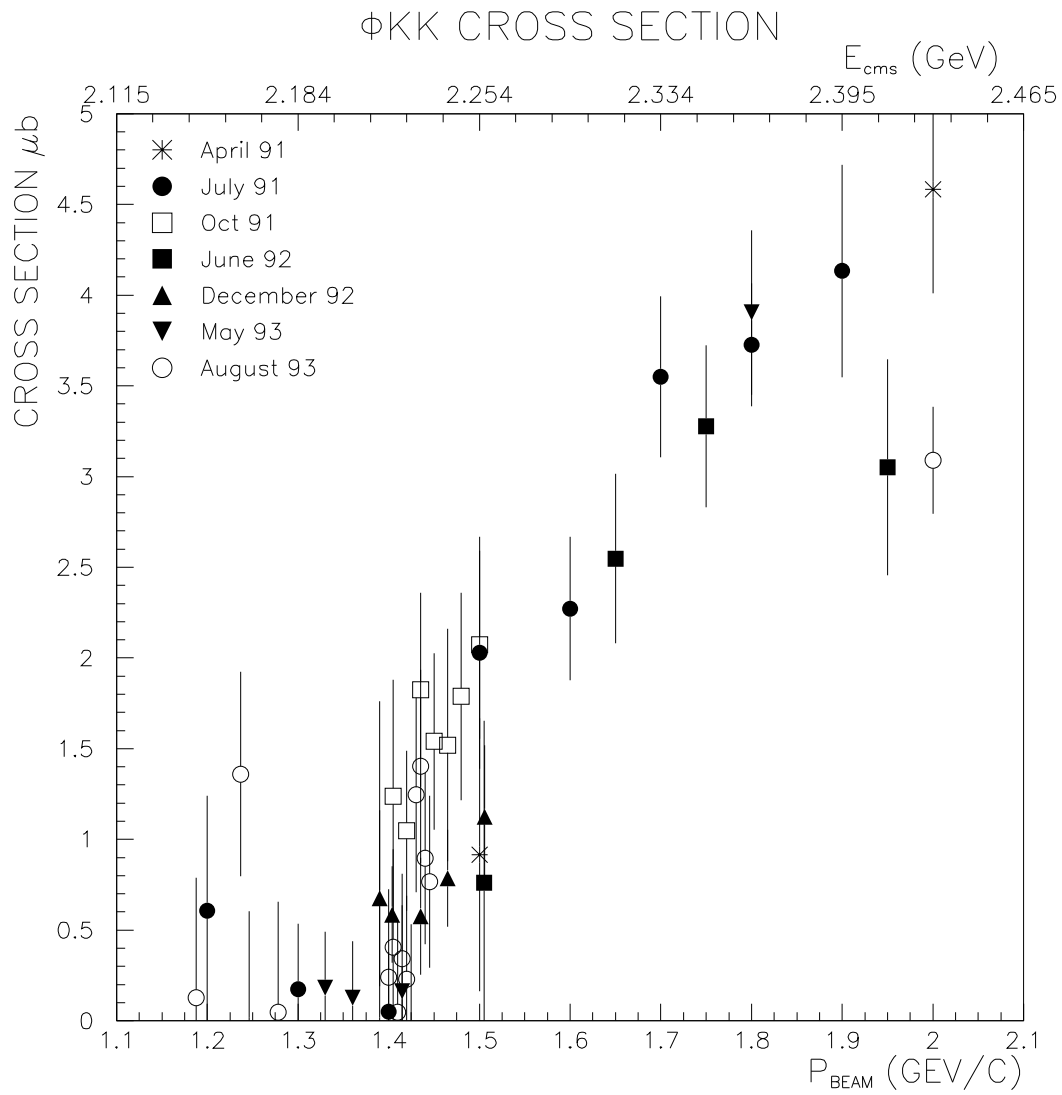


Figure 7.7: Cross section for the reaction  $p\bar{p} \rightarrow \phi KK$  as measured by JETSET.



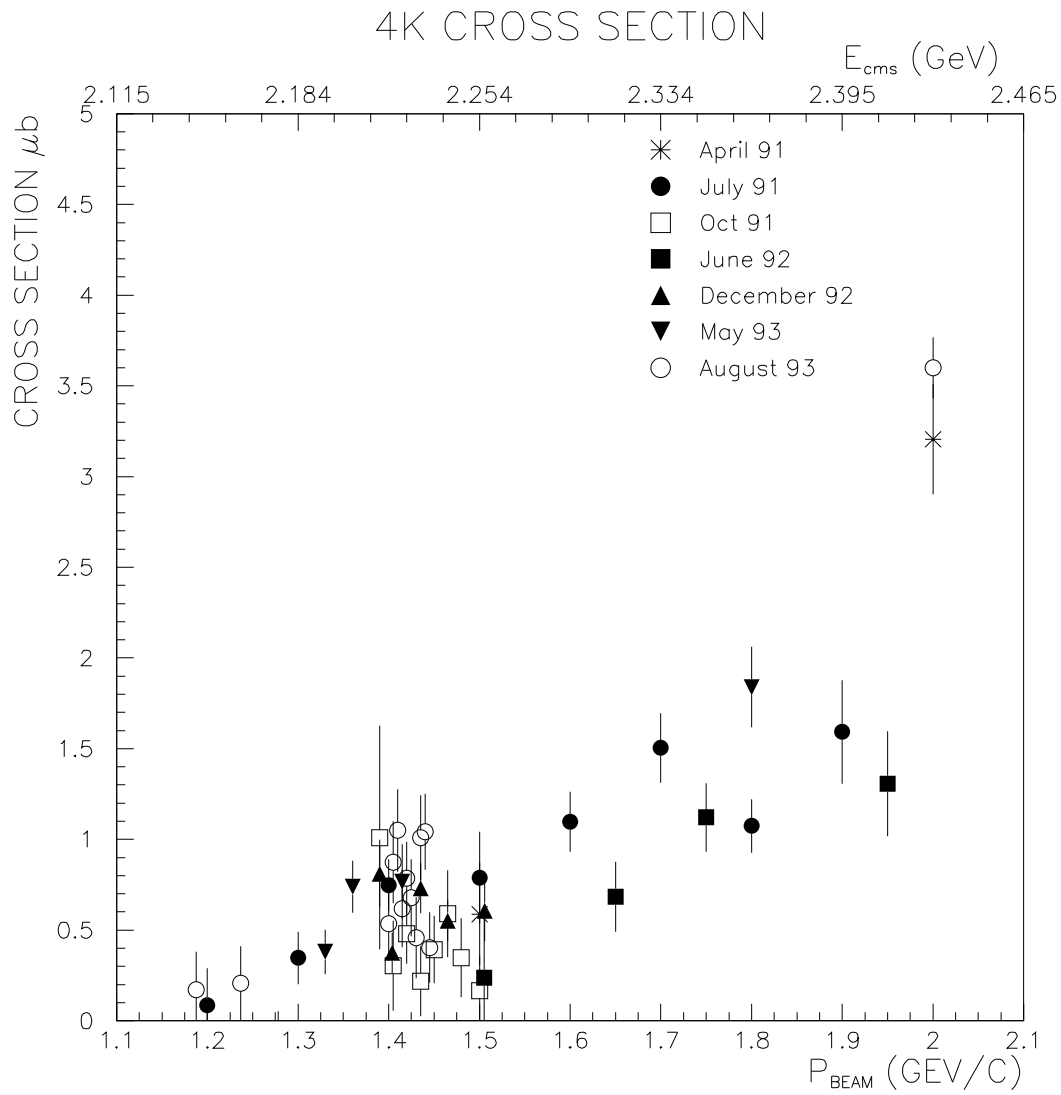


Figure 7.8: Cross section for the nonresonant reaction  $p\bar{p} \rightarrow 4K$  as measured by JETSET.

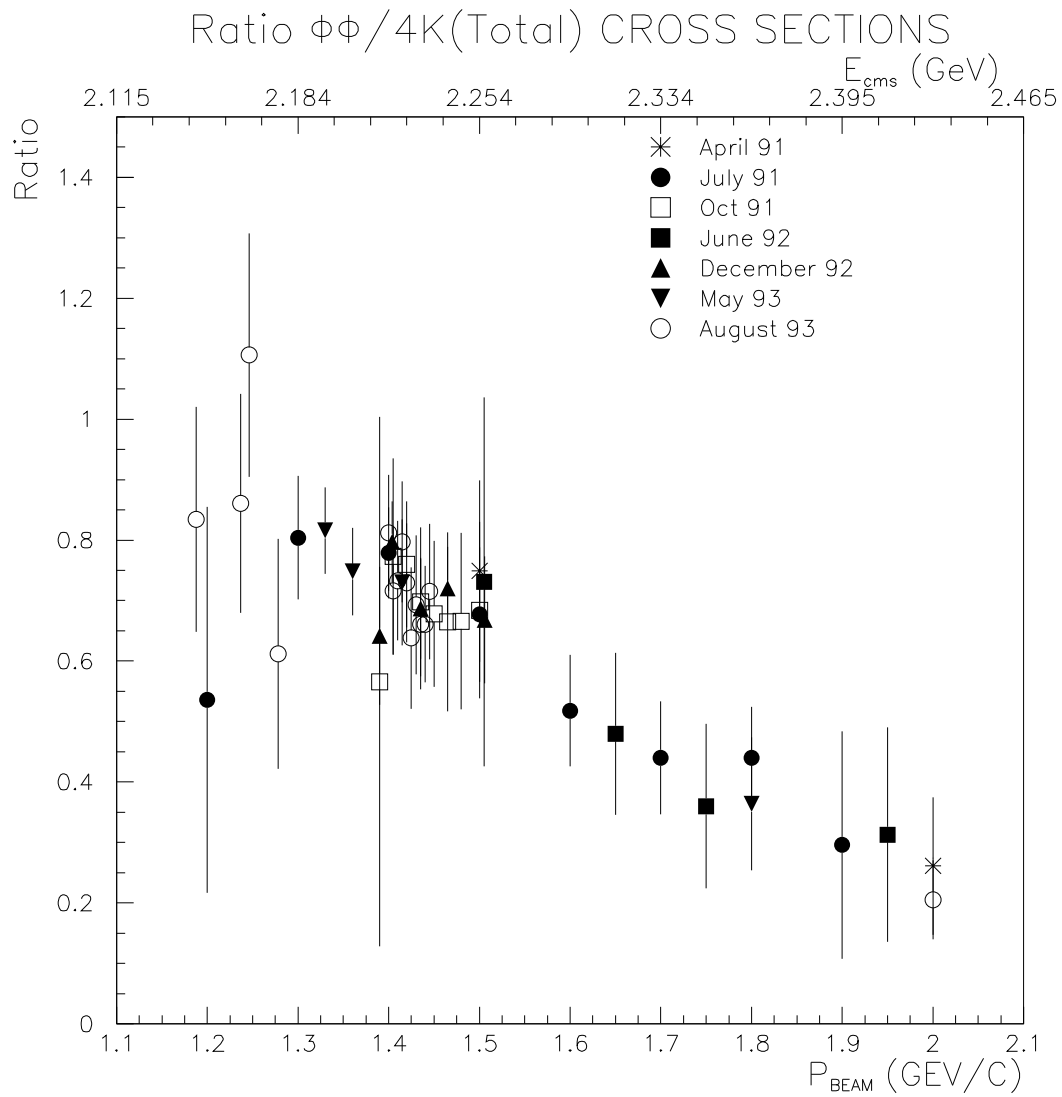


Figure 7.9: The ratio of the  $p\bar{p} \rightarrow \phi\phi$  cross section and the  $p\bar{p} \rightarrow 4K(\text{total})$  cross section as measured by JETSET.

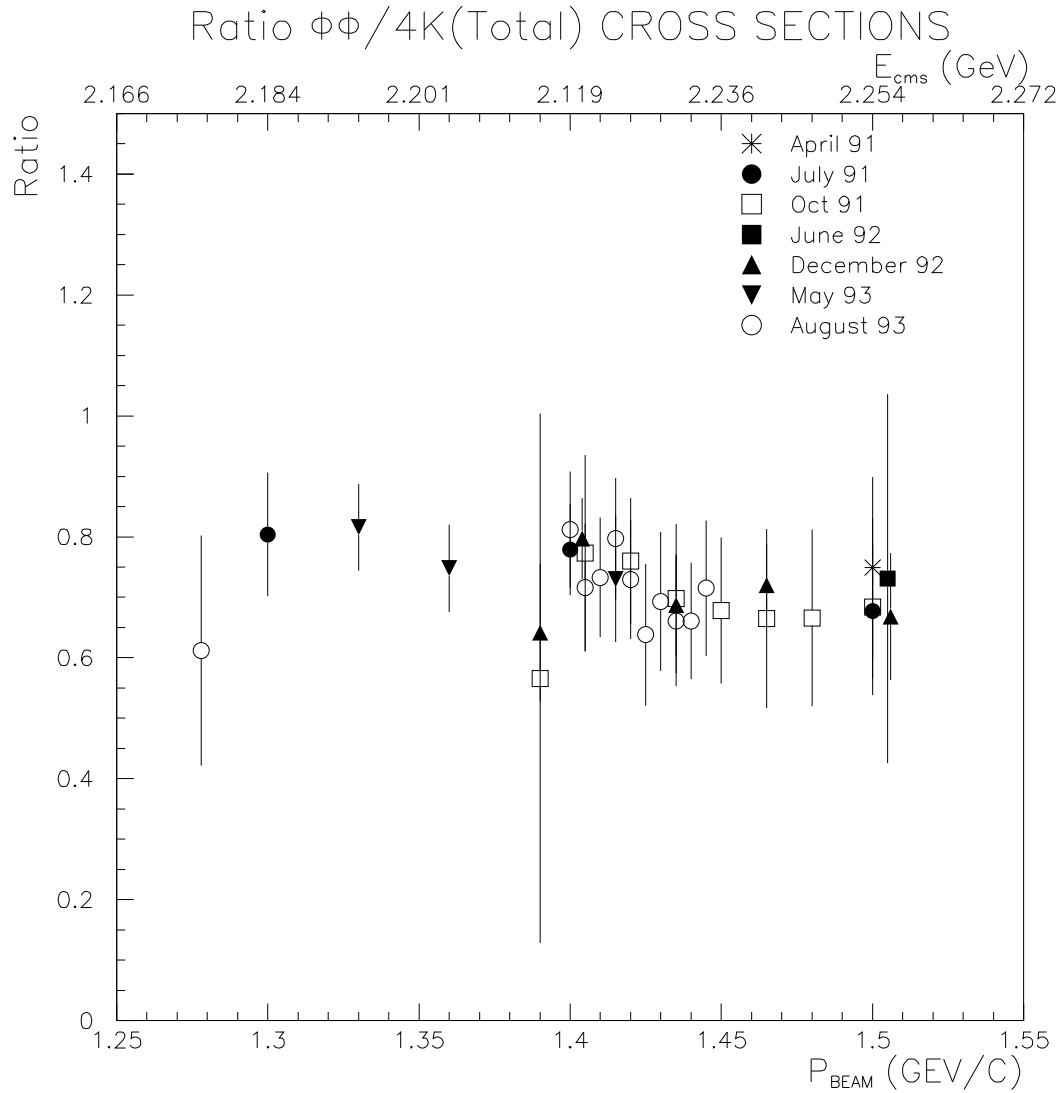


Figure 7.10: *The ratio of the  $p\bar{p} \rightarrow \phi\phi$  cross section and the  $p\bar{p} \rightarrow 4K(\text{total})$  cross section as measured by JETSET (beam-momentum 1.25-1.55 GeV/c).*

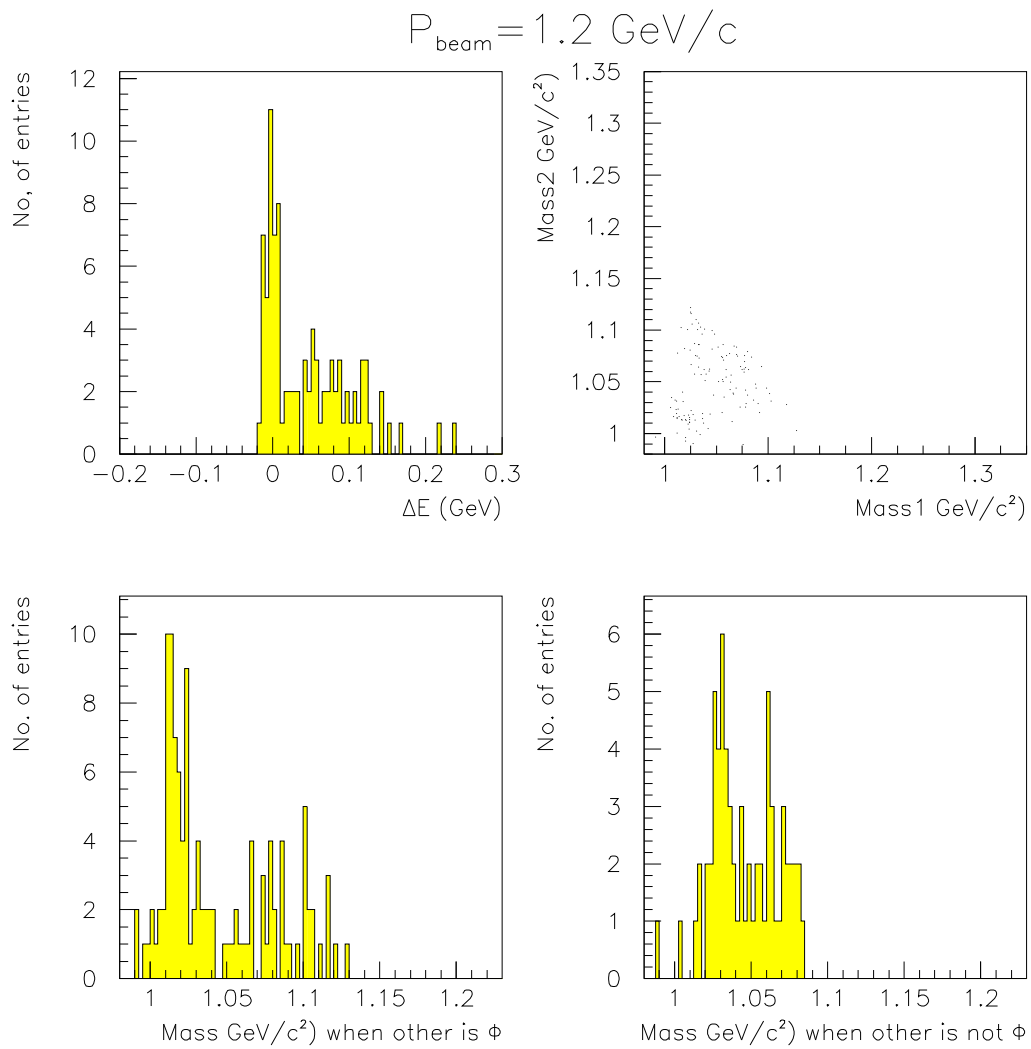


Figure 7.11:  $\Delta E$ , Goldhaber plot, and invariant mass in and out of the  $\phi$  band at beam momentum  $1.2 \text{ GeV}/c$ .

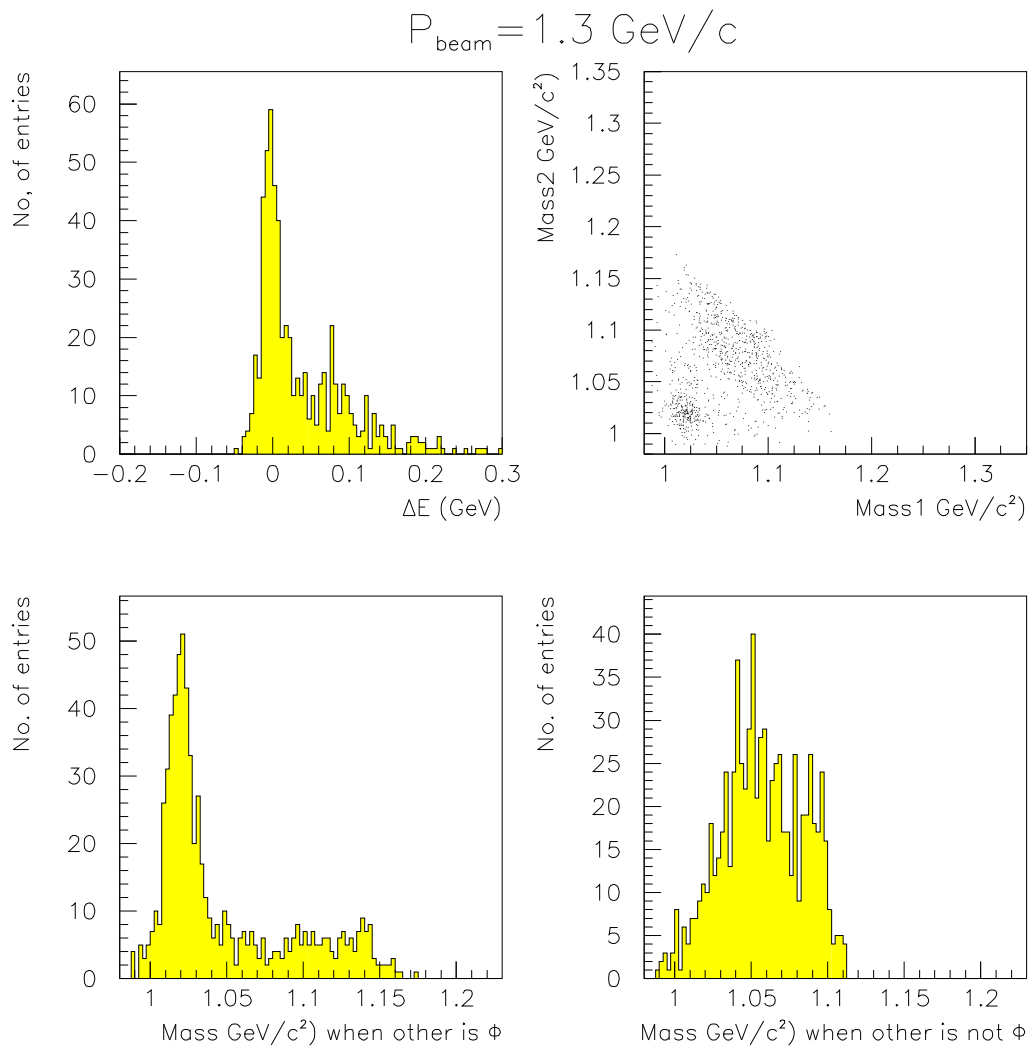


Figure 7.12:  $\Delta E$ , Goldhaber plot, and invariant mass in and out of the  $\phi$  band at beam momentum  $1.3 \text{ GeV}/c$ .

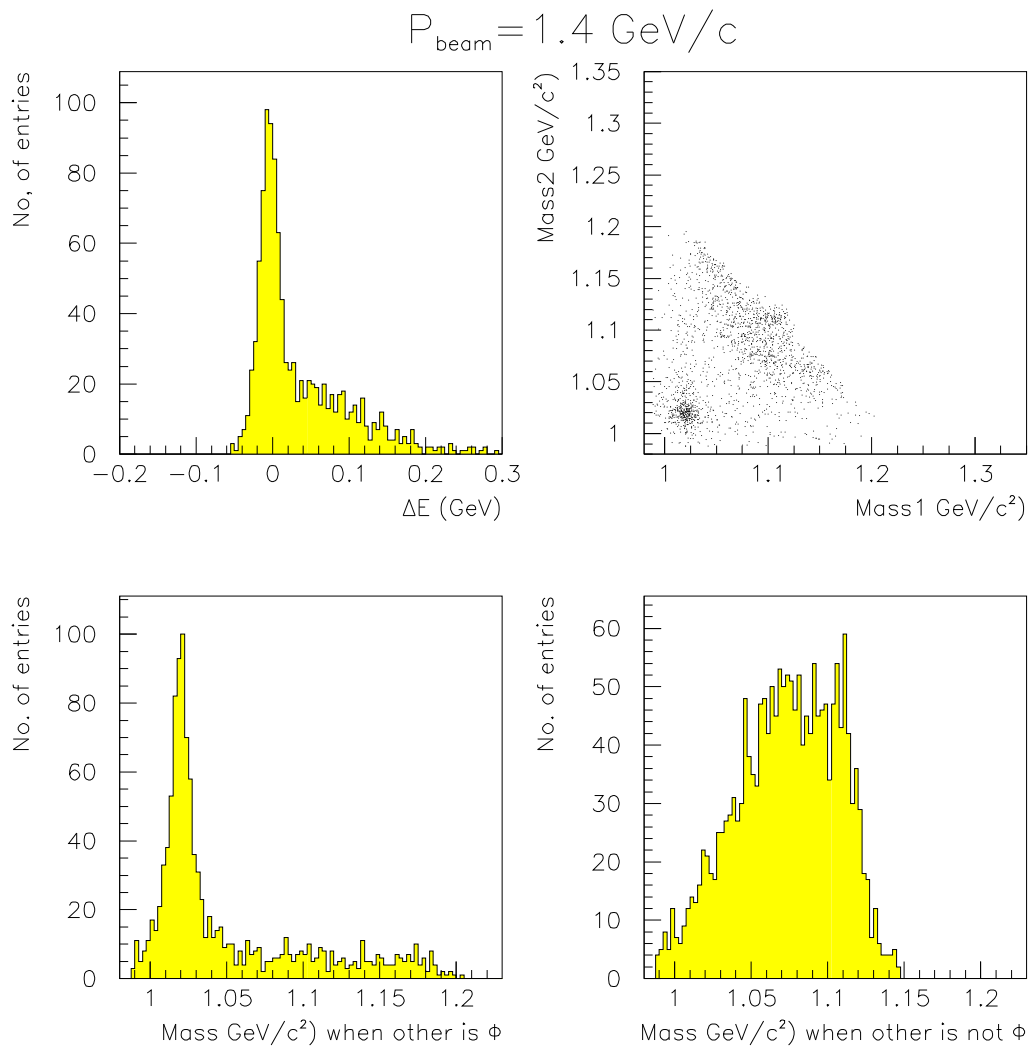


Figure 7.13:  $\Delta E$ , Goldhaber plot, and invariant mass in and out of the  $\phi$  band at beam momentum 1.4 GeV/c.

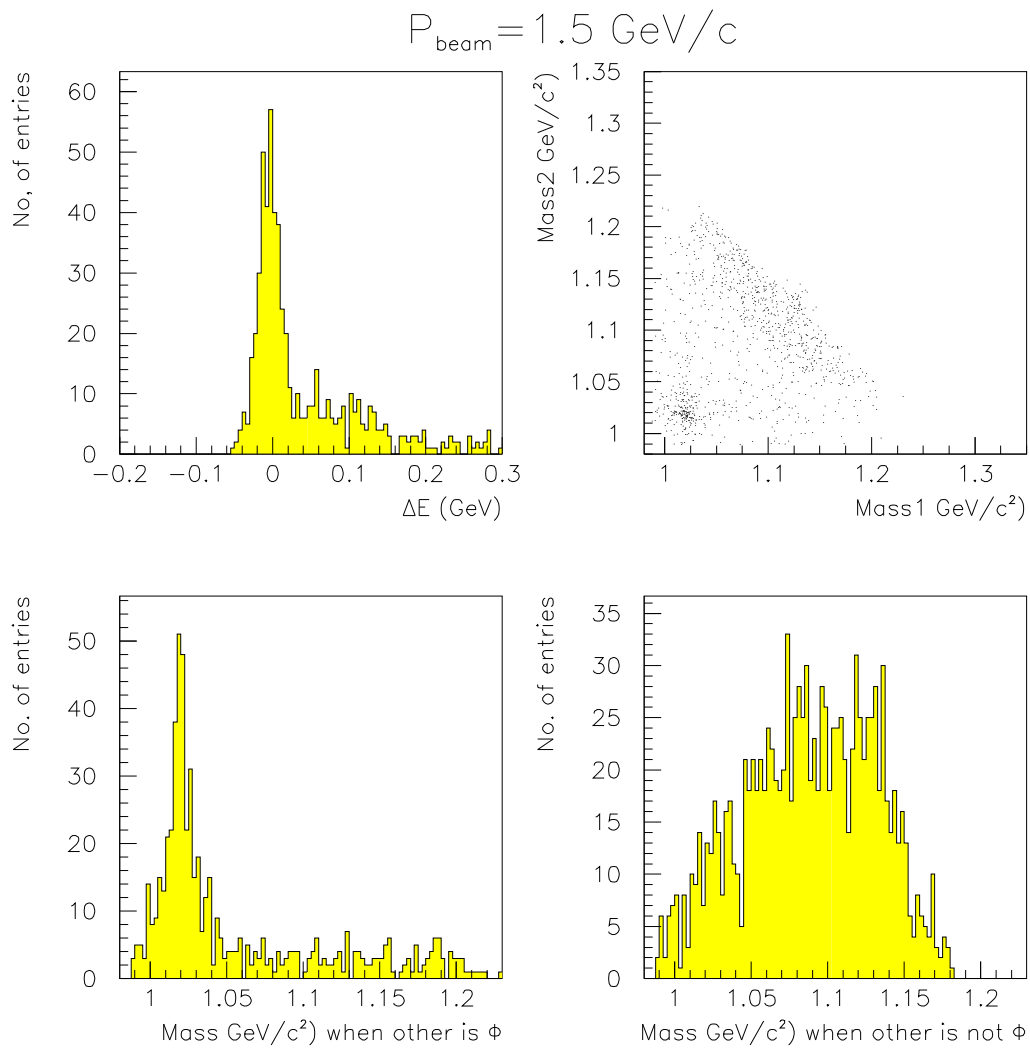


Figure 7.14:  $\Delta E$ , Goldhaber plot, and invariant mass in and out of the  $\phi$  band at beam momentum  $1.5 \text{ GeV}/c$ .

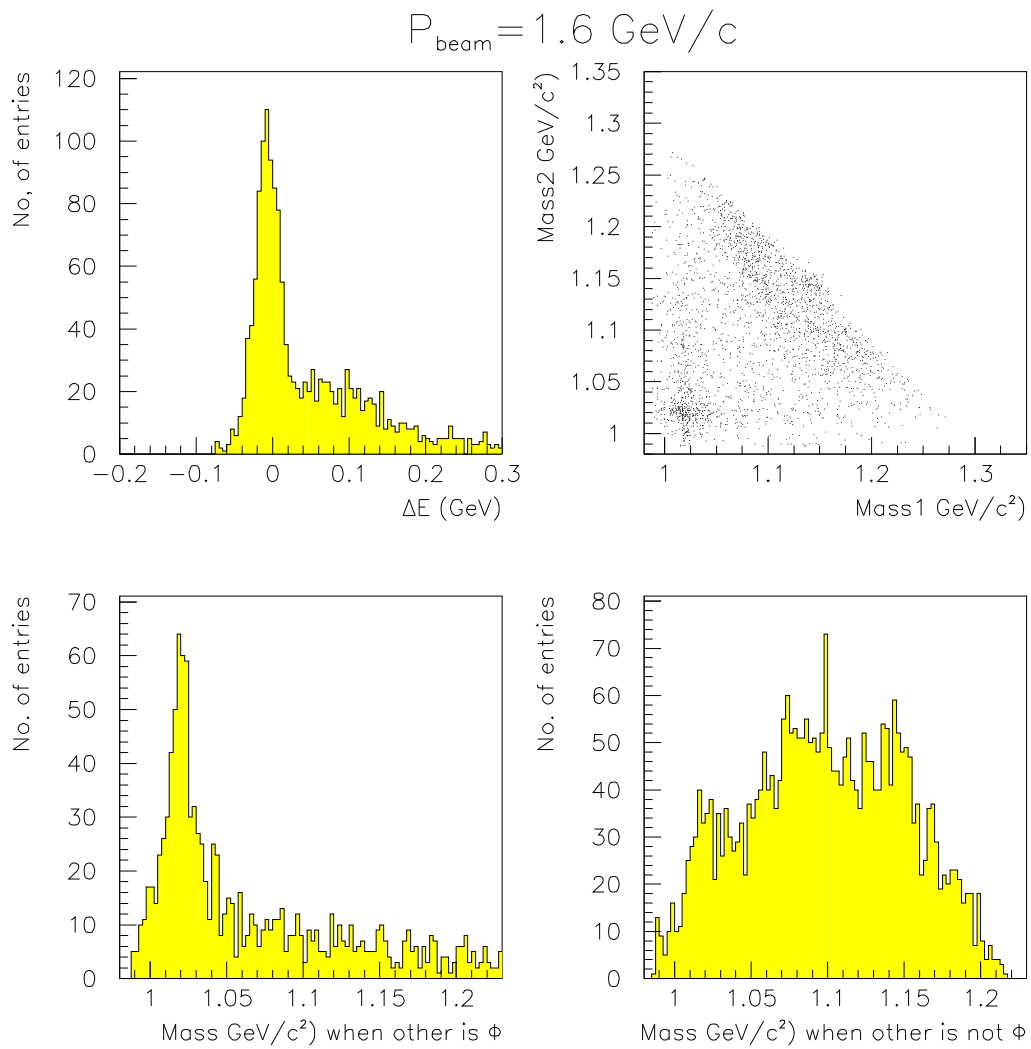


Figure 7.15:  $\Delta E$ , Goldhaber plot, and invariant mass in and out of the  $\phi$  band at beam momentum 1.6 GeV/c.



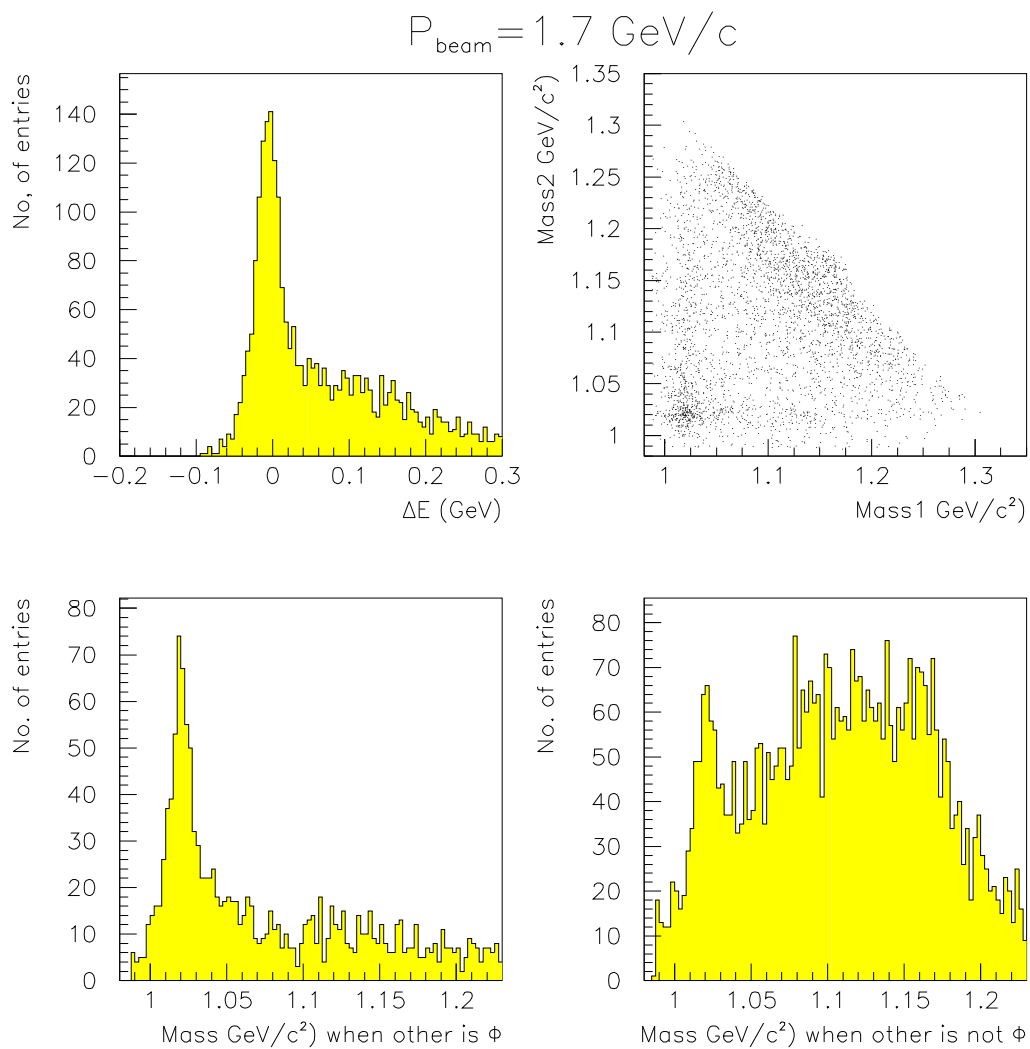


Figure 7.16:  $\Delta E$ , Goldhaber plot, and invariant mass in and out of the  $\phi$  band at beam momentum  $1.7 \text{ GeV}/c$ .

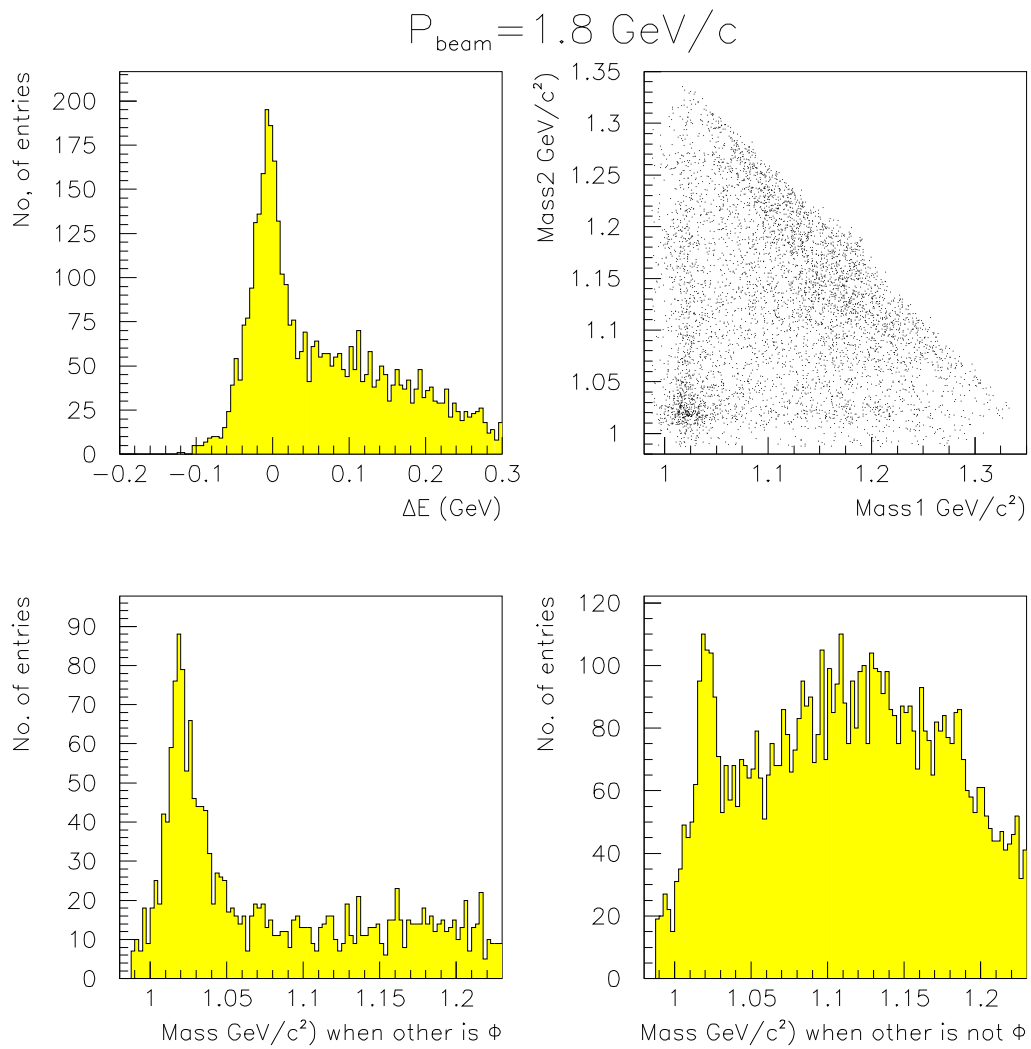


Figure 7.17:  $\Delta E$ , Goldhaber plot, and invariant mass in and out of the  $\phi$  band at beam momentum 1.8 GeV/c.

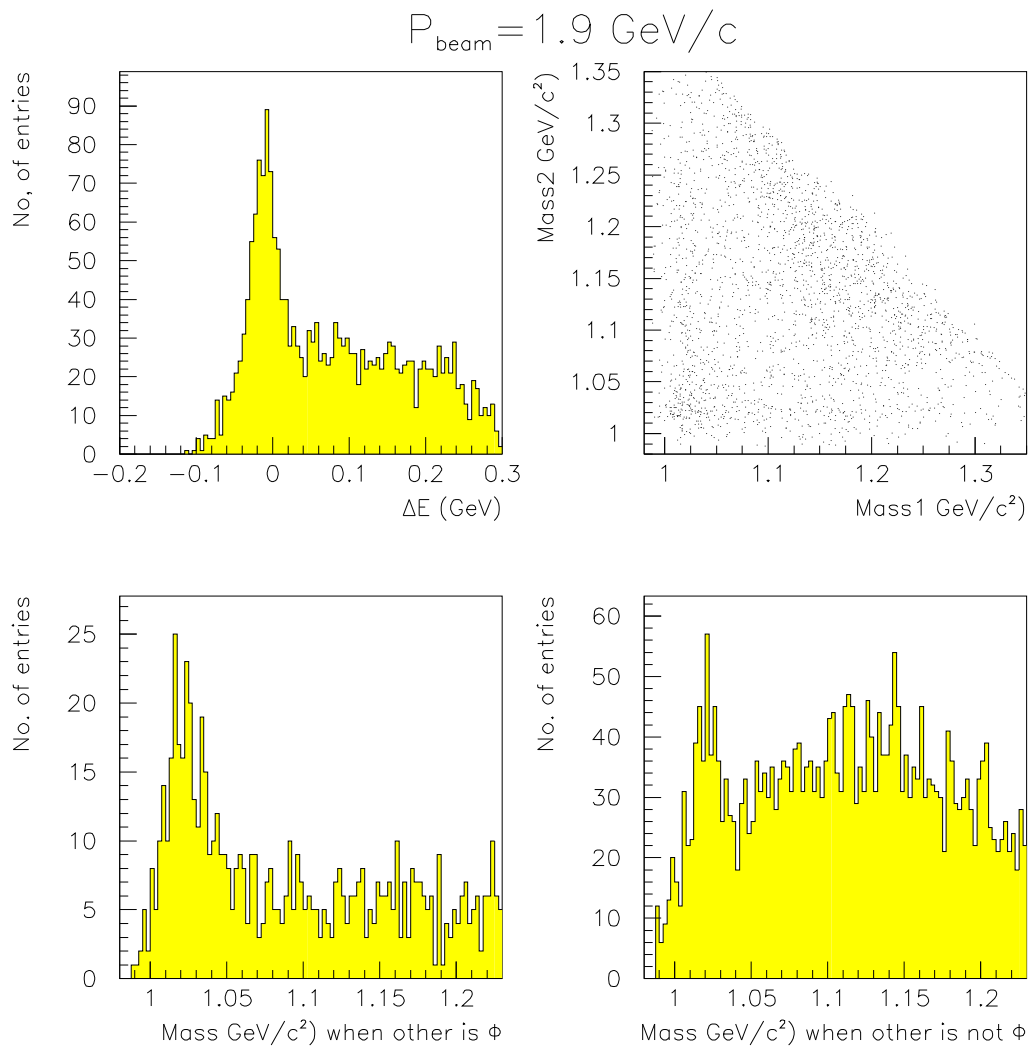


Figure 7.18:  $\Delta E$ , Goldhaber plot, and invariant mass in and out of the  $\phi$  band at beam momentum  $1.9 \text{ GeV}/c$ .

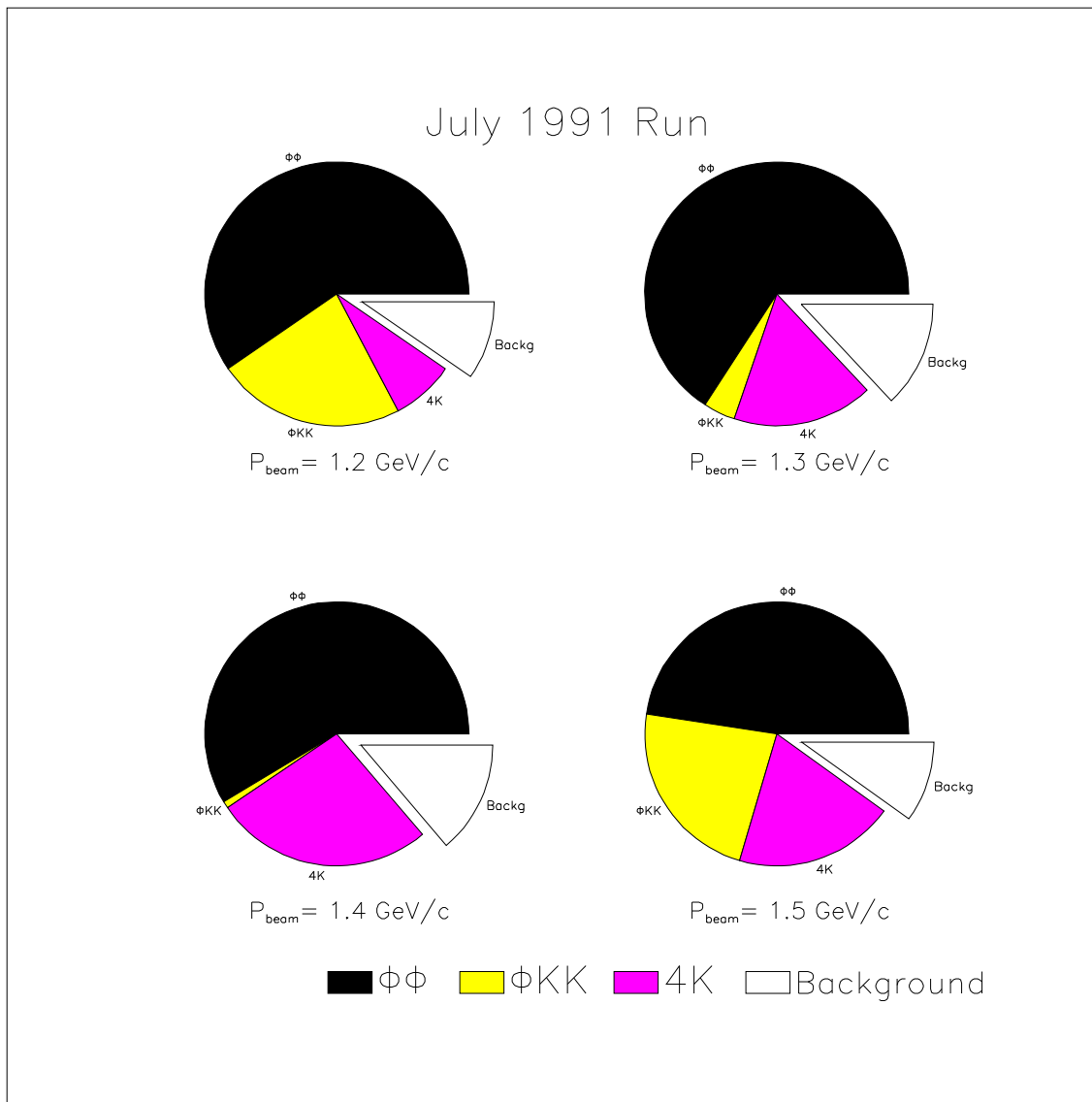


Figure 7.19: Fractions of  $\phi\phi$ ,  $\phi KK$ ,  $4K$  and background in the event sample after PID at beam momentum 1.2-1.5 GeV/c (July 1991 run).

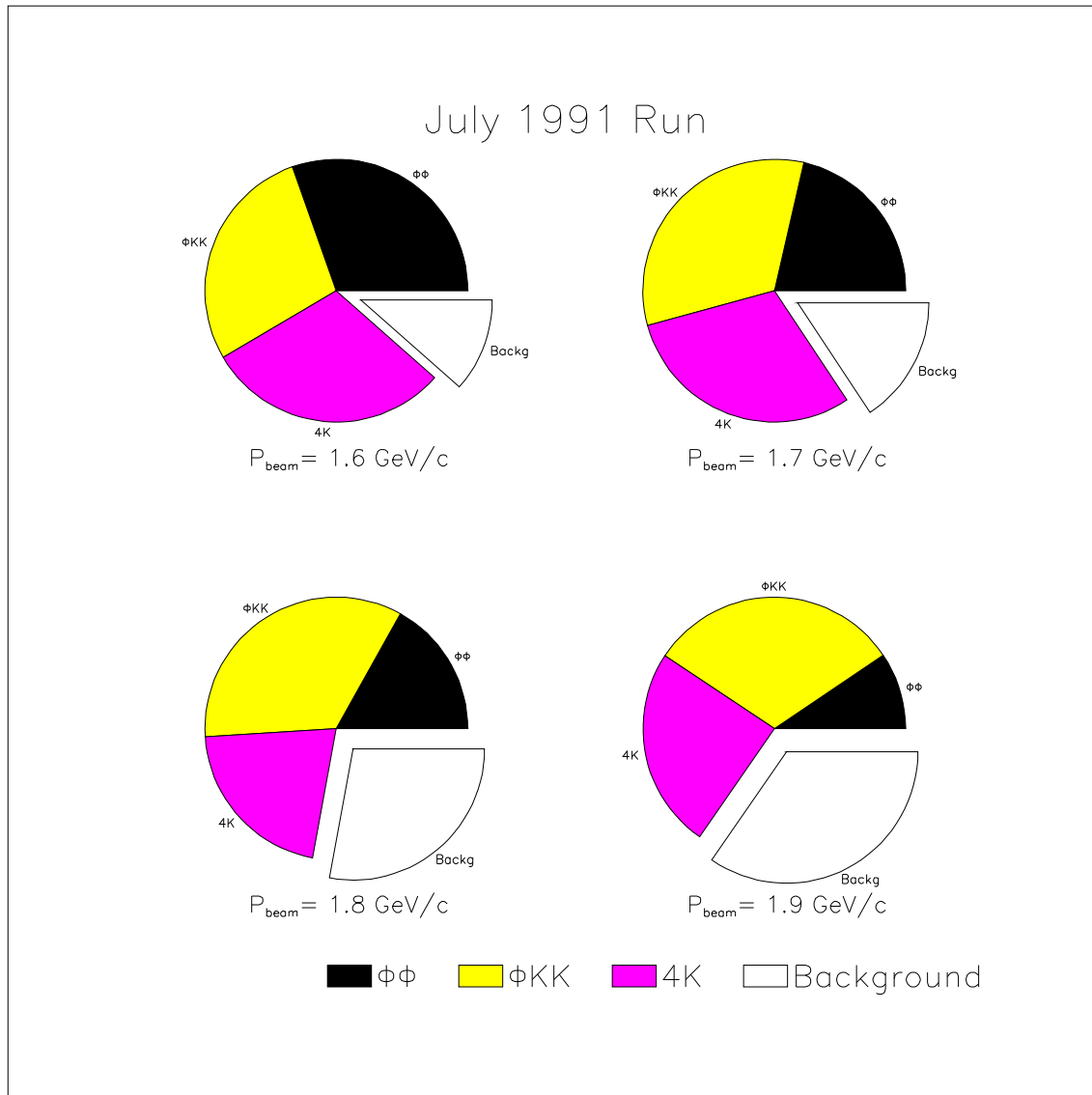


Figure 7.20: Fractions of  $\phi\phi$ ,  $\phi KK$ ,  $4K$  and background in the event sample after PID at beam momentum 1.6-1.9 GeV/c (July 1991 run).

## Chapter 8

# Analysis of angular distributions

The scattering of hadrons at the GeV scale is dominated by the presence of poles in the scattering amplitude near to the real (physical) axis. Each pole corresponds to an unstable hadronic resonance whose decays to lighter hadrons is responsible for the singularity, and can be assigned unique quantum numbers for conserved quantities such as spin ( $J$ ), parity ( $P$ ), charge-conjugation parity ( $C$ ), isospin ( $I$ ), strangeness ( $S$ ) and for  $S=0$ ,  $G$ -parity ( $G$ ). In a formation experiment like JETSET, these resonances would enter as intermediate states  $X$  in the reaction  $p\bar{p} \rightarrow X \rightarrow \phi\phi$  and show up as an enhancement in the cross section whose position and width are dictated by the mass and lifetime of the resonance  $X$ . In general there may be more than one  $X$  contributing to the reaction at a given incident  $\bar{p}$  momentum, in which case the amplitude from each pole must be added coherently.

In addition to structures in the total cross section, important information concerning the existence and nature of intermediate resonances can be inferred by studying the angular distributions of the outgoing  $K$ -mesons. Apart from any assumptions concerning hypothetical intermediate resonances  $X$ , the final-state angular distributions can be decomposed into components of definite orbital angular momentum, spin, and total angular momentum in the final  $\phi\phi$  state. In regions where the total cross section indicates resonant behaviour, one can then look in the partial wave decomposition for a single combination of  $J, P, C$  that is responsible for the peak. If another non-resonant wave is also present, the relative amplitude between resonant and non-resonant wave should reveal a rapid phase motion in the mid-resonance region if the peak is a real resonance effect.

### Experimental angular distributions

The angles of interest are  $\Theta$  and  $\Phi$ , the polar and azimuthal angle of the  $\phi$  mesons in the centre of mass system,  $\theta_1, \phi_1, \theta_2, \phi_2$ , the polar and azimuthal angles of one of the  $K$ -mesons in the rest frame of each  $\phi$  meson, and  $\chi = \phi_1 + \phi_2$ , the azimuthal angle between the decay planes of the  $\phi$ s, (see figures 2.34 and 2.35). Figures 8.1 and 8.2 show the angular distributions for events with a beam momentum 1.4-1.45 GeV (corresponding to a centre-of-mass energy of 2.218-2.236 GeV). This corresponds to the energy where a peak in the  $p\bar{p} \rightarrow \phi\phi$  cross section has been observed by JETSET (figure 7.5). Events where the invariant masses of two kaon

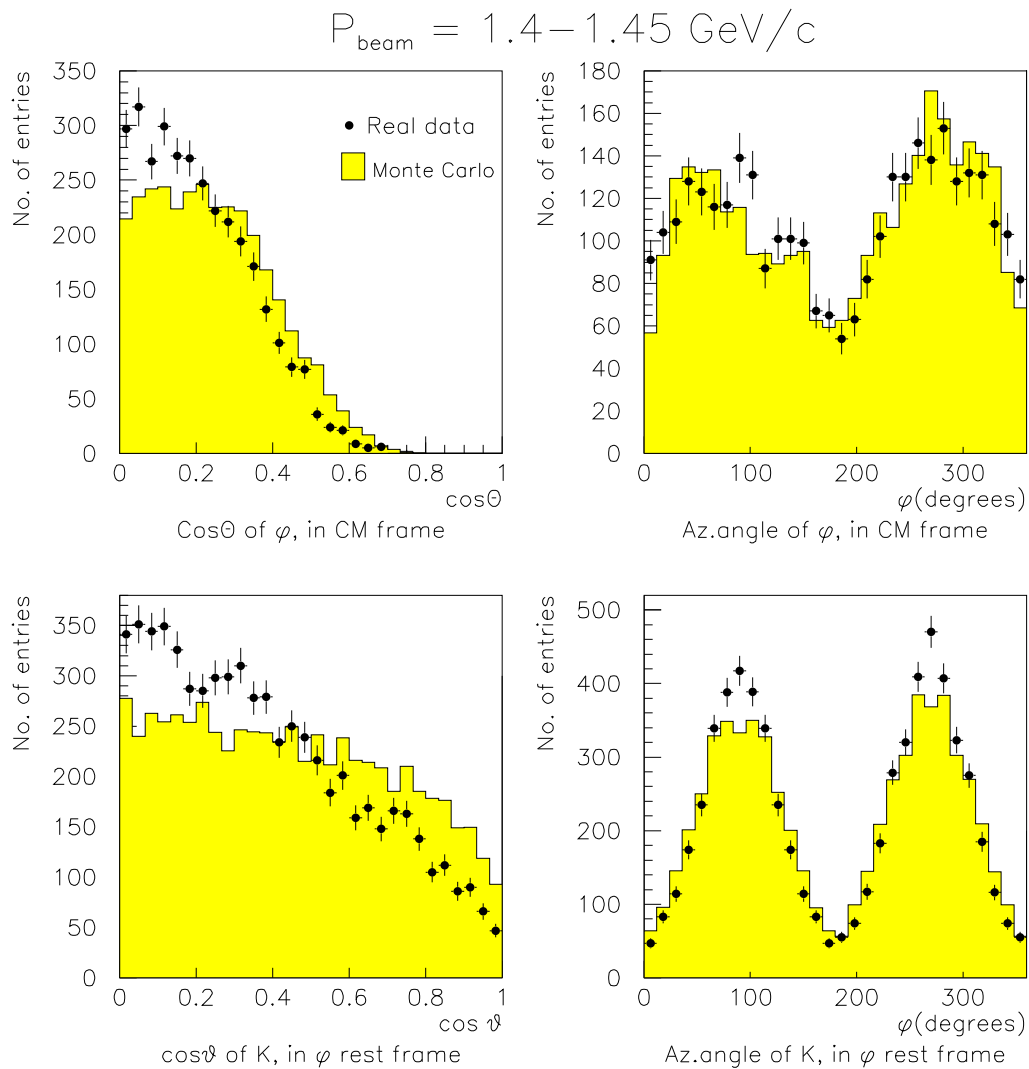


Figure 8.1: Distributions of polar and azimuthal angles in the reaction  $p\bar{p} \rightarrow \phi\phi$ , for real events and isotropic Monte Carlo events.

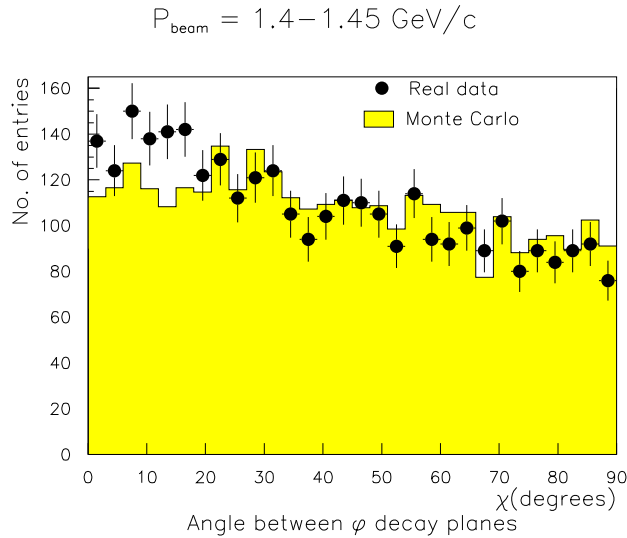


Figure 8.2: *Distribution of the angle  $\chi$  between  $\phi$  decay planes, for real events and isotropic Monte Carlo events.*

pairs was inside the  $\phi\phi$  peak in the Goldhaber plot were selected.

The Monte Carlo events were generated isotropically, which means that the angular distributions for all the generated events were uniform. The Monte Carlo distributions in figures 2.34 and 2.35 therefore show that the acceptance is far from uniform in the various angles. This is due to the limited geometric acceptance of the detector. In particular the acceptance is low at small  $\Theta$  angles, and little information can be obtained from this distribution. The distributions for real data show some deviations from the Monte Carlo data indicating that the real events were not produced isotropically.

Section 2.5.2 described how the parity  $P$  and signature  $(-1)^J$  can be determined from the distribution of the angle  $\chi$ .

$$I(\chi) = 1 + \beta \cos 2\chi, \quad (8.1)$$

The  $\chi$  distribution (figure 8.2) was fitted to the functional form in equation 8.1, and a positive value of  $\beta$  was obtained. According to the rules in section 2.5.2 this indicates that the intermediate state has  $(-1)^J = +1$ , and parity  $P = +1$ . The fit was done without acceptance corrections <sup>1</sup>.

---

<sup>1</sup>Even if the acceptance in  $\chi$  is almost uniform, the nonuniform acceptance in the other angles might distort this distribution for some partial waves, and a correct treatment of the acceptance would include a 6-dimensional acceptance matrix where the acceptance for each event was a function of the 6 angles in the event. This requires a larger number of Monte Carlo events than was available at the time of writing.



### Results from the partial wave analysis

To determine the contribution to the total cross section of the possible partial waves in the reaction  $p\bar{p} \rightarrow \phi\phi$ , the following partial wave analysis was performed [?]:

The log likelihood function from the channel likelihood method (section 5) was expanded to include a sum over the possible  $J^{PC} (L(p\bar{p})S(p\bar{p}), l(\phi\phi)s(\phi\phi))$  combination for the partial waves (table 2.11):

$$\sum_{j=1}^n \log \left[ \sum_{i=1}^m \alpha_{\phi\phi,i} \left( \frac{R_{\phi\phi} \cdot W_i(\Omega)}{N_i \cdot N_{\phi\phi}/N_0} \right) + \alpha_{\phi KK} \left( \frac{R_{\phi KK}}{N_{\phi KK}/N_0} \right) + (1 - \alpha_{\phi\phi} - \alpha_{\phi KK}) \right], \quad (8.2)$$

where  $m$  is the number of partial waves,  $\Omega$  represent the six angles,  $W_i(\Omega)$  is the angular dependence of each partial wave (including acceptance effects), and  $\alpha_{\phi\phi,i}$  is the ratio of  $\phi\phi$  events corresponding to the partial wave  $i$  in the sample. The other quantities are defined in chapter 5. The normalization integrals were obtained from Monte Carlo data. In addition to this extended channel likelihood fit, a partial wave analysis with interfering waves was performed [?]. Consistent results were obtained with the two methods when waves with  $J \leq 4$ ,  $L(p\bar{p}) \leq 5$ , and  $l(\phi\phi) \leq 4$  were included. Three waves were found to contribute to the threshold region of the  $\phi\phi$  spectrum, all having  $J^{PC} = 2^{++}$  (figure 8.3). The sum of the three  $2^{++}$  contributions was fitted to a Breit Wigner shape with the following parameters:

$$m = 2.20 \pm 0.01 \text{ GeV}, \quad (8.3)$$

$$? = 90 \pm 18 \text{ MeV}. \quad (8.4)$$

A rapid phase motion was seen when taking the difference between the waves  $2^{++}(3120)$  and  $2^{++}(3122)$  at  $m_{\phi\phi} \approx 2.2$  GeV. This is in agreement with the Breit- Wigner prediction for a resonance, which says that the phase should move from 0 degrees below resonance, through 90 degrees at mid resonance, to 180 degrees below [?].

Partial wave analysis involves the use of complicated computer codes and it is not easy to produce plots giving convincing evidence that the numerical results are correct. The systematic errors are difficult to estimate because they may be sensitive to the acceptance in very selective ways. Nevertheless PWA is the only way to clearly demonstrate resonance behaviour and to identify the quantum numbers of the resonance. It is also very helpful in disentangling different states in the case of multiple overlapping resonances that contribute to the same channel [?].

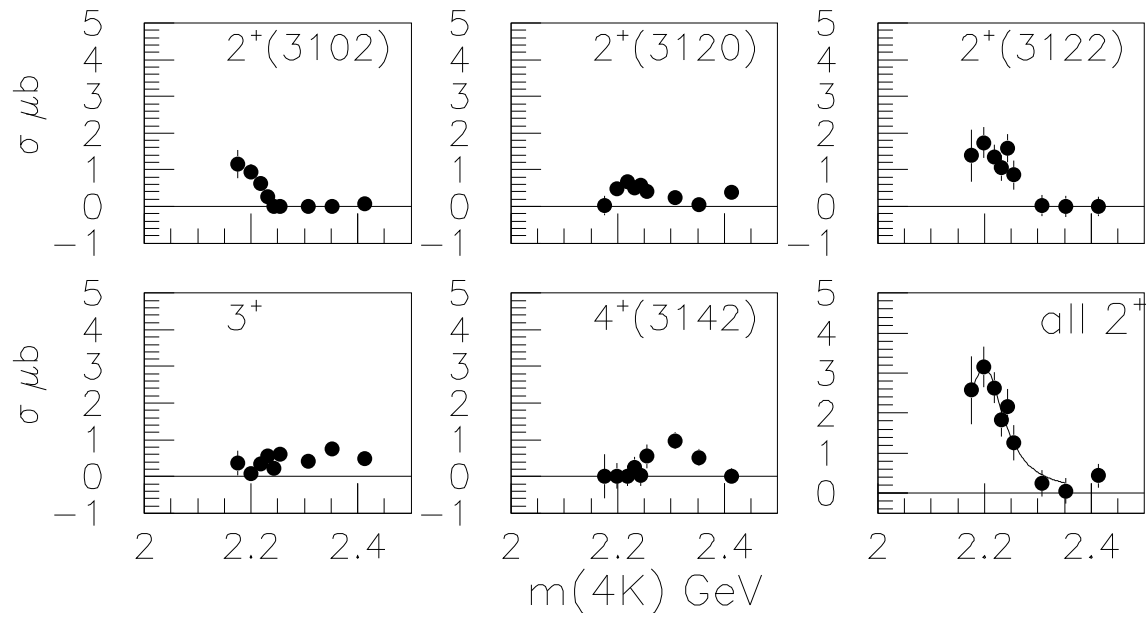


Figure 8.3: Results from partial wave analysis of the  $\phi\phi$  system. The partial waves are labelled in terms of  $J^P(L(p\bar{p})S(p\bar{p})l(\phi\phi)s(\phi\phi))$ . From [?].

# Chapter 9

## Conclusions

The results from our experiment show the following :

- The cross section for  $p\bar{p} \rightarrow \phi\phi$  is of the order 1.5-4  $\mu\text{b}$  in the energy range 2.149-2.430 GeV. The cross section reaches its maximum value at a centre of mass energy of about 2.218 GeV and decreases with higher energies (figure 7.5).  
The  $p\bar{p} \rightarrow 4K^\pm$  cross section increases with energy, from 0.1  $\mu\text{b}$  to 3  $\mu\text{b}$  in the same energy range (figure 7.8). The cross section for  $p\bar{p} \rightarrow \phi KK$  increases even faster, from 0.1  $\mu\text{b}$  to 4.5  $\mu\text{b}$  (figure 7.7).
- The  $\phi\phi$  cross section is dominated by  $J^{PC} = 2^{++}$ , especially close to threshold (figure 8.3). The  $2^{++}$  part of the cross section can be fitted to a resonant Breit Wigner shape with parameters.

$$m = 2.20 \pm 0.01 \text{ GeV}, \quad (9.1)$$

$$\Gamma = 90 \pm 18 \text{ MeV}. \quad (9.2)$$

Comparing these results with the predictions from chapter 2, we observe that  $p\bar{p} \rightarrow \phi\phi$  does not appear to be suppressed, in contradiction to what is predicted from the OZI rule (section 2.3). One possibility could be that the OZI rule is not valid for these kind of reaction, which are not of the single hairpin type (page 41). The empirical evidence for the OZI rule is mostly from single hairpin diagrams. However QCD, and asymptotic freedom, predicts that the rule should be equally valid for reactions like  $p\bar{p} \rightarrow \phi\phi$ .

If the OZI rule is valid for  $p\bar{p} \rightarrow \phi\phi$ , but the reaction can proceed through the  $\omega$  component of the  $\phi$ -meson, a cross section of  $\approx 10 \text{ nb}$  is predicted (page 42). This is two orders of magnitude lower than what is measured.

The cross section for  $p\bar{p} \rightarrow \phi\phi$  is approximately equal to, or higher than that for  $p\bar{p} \rightarrow 4K^\pm$  in the observed energy range, even if the latter reaction is not OZI-suppressed.

The OZI rule could be evaded if  $p\bar{p} \rightarrow \phi\phi$  proceeds through the strangeness component of the proton. The predicted cross section in this case is about 0.8  $\mu\text{b}$ . The reaction is expected to take place with the two protons in spin triplet, and quantum numbers  $J^{PC} = 2^{++}$  for the  $\phi\phi$

system (page 43). If the reaction  $p\bar{p} \rightarrow \phi\phi$  takes place through the two meson intermediate state  $K\bar{K}$ , the cross section is predicted to vary with energy from  $0.6 \mu\text{b}$  to  $3.0 \mu\text{b}$ . Also in this case the reaction would take place with the protons in a spin triplet state, and the total spin of the  $\phi$ -mesons would be either 0 or 2 (page 46).

It is also possible that the reaction  $p\bar{p} \rightarrow \phi\phi$  occurs through a gluonic resonant state. In this case there would be a strong coupling when the total energy is in the vicinity of the resonance mass, which would violate the OZI rule. Theoretical models predict a tensor glueball with mass  $\approx 2.2$  -  $2.3$  GeV (section 2.2.5).

The measurements of cross sections and quantum numbers are compatible with either the strangeness component in proton model, the two meson intermediate state, or a glueball. The resonant shape has mass and  $J^{PC}$  in agreement with predictions for glueballs, but the width is somewhat larger than what is expected. If the reaction takes place through the strangeness component of the proton, what was observed could be an  $s\bar{s}$  resonant state.

The  $p\bar{p} \rightarrow \phi\phi$  cross sections are higher than what were measured in the two previous experiments R704 [?], and the ANL bubble chamber experiment [?] (section 2.4.2). However, these measurements were done at higher energies, so they are not incompatible with a  $p\bar{p} \rightarrow \phi\phi$  cross section decreasing with increasing energies as we observe in our data.

Our results are in agreement with what is previously measured in the  $\phi\phi$  production experiments described in section 2.4.3, which all found the production taking place mostly in  $J^P = 2^+$  wave, and the ratio of  $\phi\phi$  to  $\phi K K$  and  $4K$  final states larger than expected from the OZI rule. However, the width of the resonant shape is smaller than that of the  $g_T$  resonances (equation 2.75), which have been some of the most prominent glueball candidates.

The shape of our observed cross section is similar to what is measured in  $J/\Psi$  decay (section 2.4.4), but the resonance states observed in these reactions had dominantly  $J^P = 0^-$ .

The resonant shape is much wider than what is observed for the  $\xi$  resonance, (section 2.4.5) even if the mass and quantum numbers are similar.

A better understanding of mesonic spectroscopy and of the OZI rule is required before any definite statements can be made about whether our experiment has observed a glueball or something else.